Reservoir Characterization of Kvitebjørn and Valemon HTHP fields, northern North Sea, Offshore Norway

Ali Asghar Shahid

Master Thesis in Petroleum Geoscience
60 Credits

Department of Geoscience
Faculty of Mathematics and Natural Sciences

UNIVERSITY OF OSLO

November / 2021

Supervisor: Nazmul Haque Mondol

Reservoir characterization of high temperature high pressure (HTHP) Valemon and Kvitebjørn fields, Viking Graben, northern North Sea.

Preface

This master thesis is submitted to complete the M.Sc. degree in Petroleum Geosciences at the University of Oslo (UiO). The research was carried out in an unprecedented time due to Covid-19 pandemic and so faced several challenges during the project period. Though the thesis has started efficiently in June 2021 but with hard work and efficient time management, I overcome all challenges to complete the thesis approximately one month earlier than the official deadline. The thesis was conducted at the Department of Geosciences, University of Oslo, Norway under the supervision of Professor Nazmul Haque Mondol.

Acknowledgments

First of all, I like to take this opportunity to express my sincere gratitude to my supervisor Professor Nazmul Haque Mondol, for his immense support, constant motivation, kind behavior, patience, and guidance to complete the thesis.

This thesis gets additional support, encouragement, and guidance from Dr. Manzar Fawad, Researcher at UiO and Md. Jamilur Rahman, Ph.D. Research Fellow at UiO. I want to pay my respect to them, and wish good luck in their future endeavors.

Last but not least, I would like to thank my family, especially my parents, for their immense sacrifices and support that made me achieve my goals. Indeed, without my parents and family support and encouragement, I would not have been at this stage and completing my master's degree.

Ali Asghar Shahid

Abstract

This study focuses on characterization of the High-Temperature High-Pressure (HTHP) Middle-Jurassic sandstone reservoirs of Valemon and Kvitebjørn fields, Viking Graben, northern North Sea using petrophysical analysis, rock physics diagnostics and AVO modelling of six exploration wells 34/10-23, 34/10-42S, 34/11-1, 34/11-4, 34/11-5S and 34/11-6S. Within the six wells, four of them (34/10-23, 34/10-42S, 34/11-4 and 34/11-6S) are located in the Valemon field and two others (34/11-1 and 34/11-5S) and located in the Kvitebjørn field. The reservoir zones in both fields comprise the Cook, Rannoch, Etive, Ness and Tarbert Formation sandstones of Early and Middle Jurassic age. This study focuses on reservoir characterization of Middle-Jurassic Tarbert and Ness Formations.

The reservoir properties, such as, total porosity, clay volume, net-to-gross, permeability and saturation are evaluated for the reservoir units utilizing petrophysical analysis techniques. The target reservoir zones and pay zones are recognized established on the cutoff values for the stated reservoir properties. The rock physics diagnostics approach is principally carried out to evaluate the cement volume, for the quality control of the petrophysical analysis generated results, and to inquire about sensitivity and abnormalities that are generated as a consequence of the lithology and fluid variations.

The rock physics diagnostic cross plots utilized in this study are Acoustic Impedance (AI) versus P-to S-wave velocity-ratio (Vp/Vs), Lambda-Rho (λρ) versus Mu-Rho (μρ), and Total Porosity (φ_t) versus Vp. The cross plots further color-coded with reservoir properties, such as, Clay Volume (V_{clay}), Total Porosity (φ_t), and Gas Saturation (S_g). Moreover, the AVO Modelling is utilize, in order to examine sensitivity by understanding the effects related to fluid substitution produced on the impedance interfaces.

The AVO Modelling performed on top of the Tarbert Formation in the four studied wells (34/10-23, 34/10-42S, 34/11-1 and 34/11-5S) and characterized with respect to AVO classes. Overall, the best and sufficient reservoir properties seen in the Middle-Jurassic Tarbert Formation, which is the thinnest reservoir zone in this study. The Tarbert Formation is identified as the hydrocarbon bearing zone in wells 34/10-23, 34/11-1, 34/11-4, 34/11-5S and 34/11-6S. Additionally, the Middle-Jurassic Ness Formation is also a target reservoir in this study and recognized as hydrocarbon bearing zone in the three studied wells (34/11-1, 34/11-4 and 34/11-6S).

The petrophysical analysis, rock physics diagnostic and AVO Modelling, indicates the well 34/10-42S exhibits reservoir zones with good reservoir properties but it comprises high water saturation, therefore, considered as dry or non-economical well. The Early-Jurassic Cook Formation comprises reservoir properties and consider as reservoir zone in two wells (34/10-42S and 34/11-1). It comprises high water saturation in all the studied wells. Whereas, the Middle-Jurassic Etive and Rannoch Formations exhibit a good reservoir quality but they are relatively less hydrocarbon saturation (high water bearing sandstones) in almost all the studied wells.

The Tarbert Formation interpreted as gas reservoirs in wells 34/10-23 and 34/11-6S and gas/condensate reservoirs in wells 34/11-1, 34/11-4 and 34/11-5S. The Ness Formation interpreted as gas reservoir in well 34/11-6S and gas/condensate reservoirs in wells 34/11-1 and

34/11-4. As expected, the decrease in porosity is evident for the deeply buried Middle Jurassic reservoirs in well 34/11-5S. A high degree of cementation has resulted in low porosity and essentially reduced the fluid sensitivity, which has clearly been documented in various rock physics crossplots (i.e. LMR, Vp versus Vs and Vp/Vs versus AI) and AVO modelling.

A Class-4 AVO is observed for the top Tarbert Formation in wells 34/10-23 and 34/10-42S, associated with less compacted sands, while the top Tarbert Formation in well 34/11-5S has a Class-1 AVO indicative of moderately to highly cemented sandstone. Moreover, the Tarbert Formation in well 34/11-1 comprises AVO Class-3. The AVO modelling is found to have limitations when dealing with deeper HTHP reservoirs of low thickness. The AVO classify the Tarbert Formation in well 34/10-23 as Class-4 due to the low thickness (14m), led to tuning effect. Moreover, Tarbert Formation and overlying cap rock become stiffer due to possible quartz cementation, decreasing the fluid sensitivity. The pressure-depth curves generated for Tarbert and Ness Formations with formation pressure data exhibit both the formations comprise higher formation pressure (overpressure) relative to the Normal hydrostatic pressure curve. The Tarbert formation being low in thickness and comprising HTHP gas reservoir is a complex formation to deal with. Finally, the thesis comprises limited data in characterizing HTHP reservoirs but for geoscientists, it is a great opportunity to evaluate the HTHP reservoirs with more data acquired from advanced tools and technologies, which would make HTHP reservoirs a challenge to prevail over.

Table of Contents

Table of Figures

List of Table

Nomenclature

AI	Acoustic Impedance
AVO	Amplitude versus Offset
API	American Petroleum Institute, scale of radioactivity used for the gamma ray log
BS	Base Sand
BSF	Below Seafloor
DHI	Direct Hydrocarbon Indicator
GOC	Gas-Oil-Contact
GR	Gamma Ray
GWC	Gas-Water-Contact
HC	Hydrocarbon
HTHP	High Temperature High Pressure
K	Bulk Modulus
k	Permeability
KB	Kelly Bushing
LMR	Lambda-Mu-Rho (λ-µ-ρ)
MD	Measured Depth
mD	Millidarcy, measure of permeability
N/G	Net-to-Gross Ratio
OWC	Oil-Water-Contact
PR	Poisson's Ratio
RKB	Relative to Kelly Bushing
RPT	Rock Physics Template
Rw	Water Resistivity
Sw	Water Saturation
Sg	Gas Saturation
TVD	True Vertical Depth
Vp	P-wave velocity
Vs	S-wave velocity
Vsh	Shale Volume
ρ	Density
λ	Incompressibility (rock physics) and wavelength
ν	Poisson's Ratio
ϕ	Porosity
µ	Shear Modulus

Chapter 1: Introduction

1.1 Background Motivation

Norwegian Continental Shelf (NSC) is one of the most well-explored and studied regions — divided into three petroleum provinces, namely "North Sea", "Norwegian Sea" and "Barents Sea" (Figure 1.1). The interest in hydrocarbon exploration in the North Sea was generated through the discovery of the Groningen field in the Netherland in 1958 (Faleide et al., 2010).

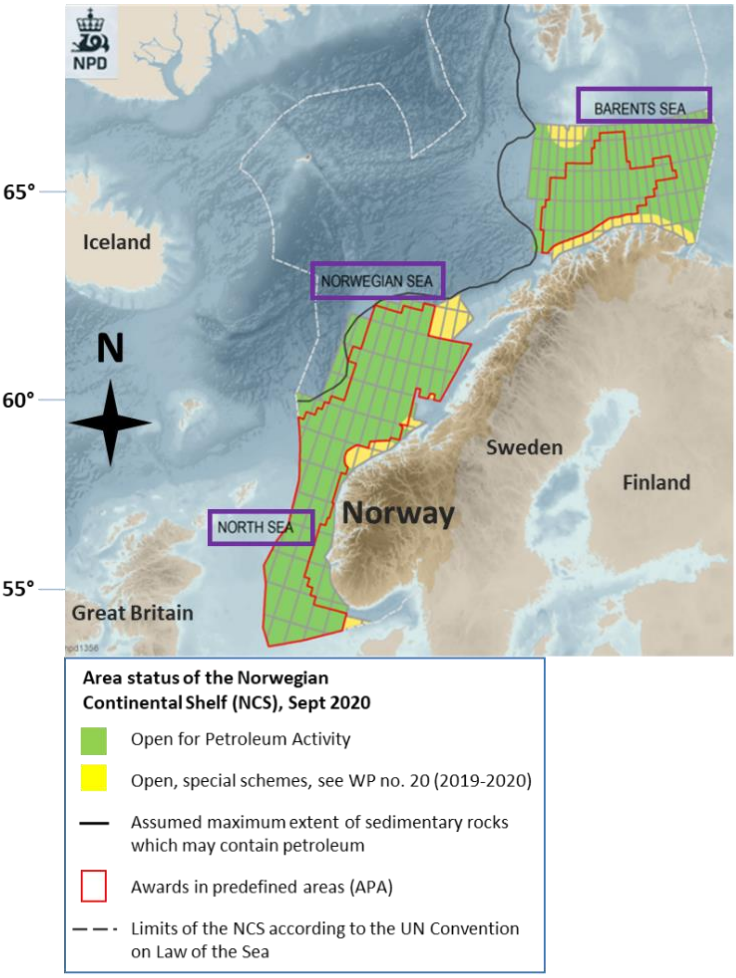

Figure 1. 1: Location of the three petroleum provinces (purple boxes); the North Sea, Norwegian Sea, and Barents Sea in the Norwegian Continental Shelf (NCS) (modified after Norwegian Petroleum Directorate, 2021b).

The North Sea is a mature oil and gas province, which has been open for exploration since the mid-1960s (Figure 1.1). It is located on the left flanks of Jurassic-Cretaceous rift system with existing fields such as Central, Viking and Sogn Grabens (Hansen et al., 2020). According to ExxonMobil the world's population will increase to 9 billion in coming 20 years, with a high increase in energy demand by a substantial rate of 25% (ExxonMobil, 2017). Coal, oil, and gas are expected to roughly meet 80% to the worldwide energy demand by 2040, in which oil and gas will comprise about 60% (ExxonMobil, 2017). In order to decrease emissions, replace coal, and provide consistent, inexpensive and clean energy in the future, the world needs to shift to natural gas and renewable energies (Wojnar T, 2018). The regional fuel energy usage in the past and predictions for the future from British Petroleum (2021) is illustrated in Figure 1.2, which gives us an overview that oil as a fuel ruled in Americas, Africa, and Europe, whereas gas dominated in the Middle East and CIS regions. Moreover, coal dominated the region of Asia Pacific (British Petroleum, 2021).

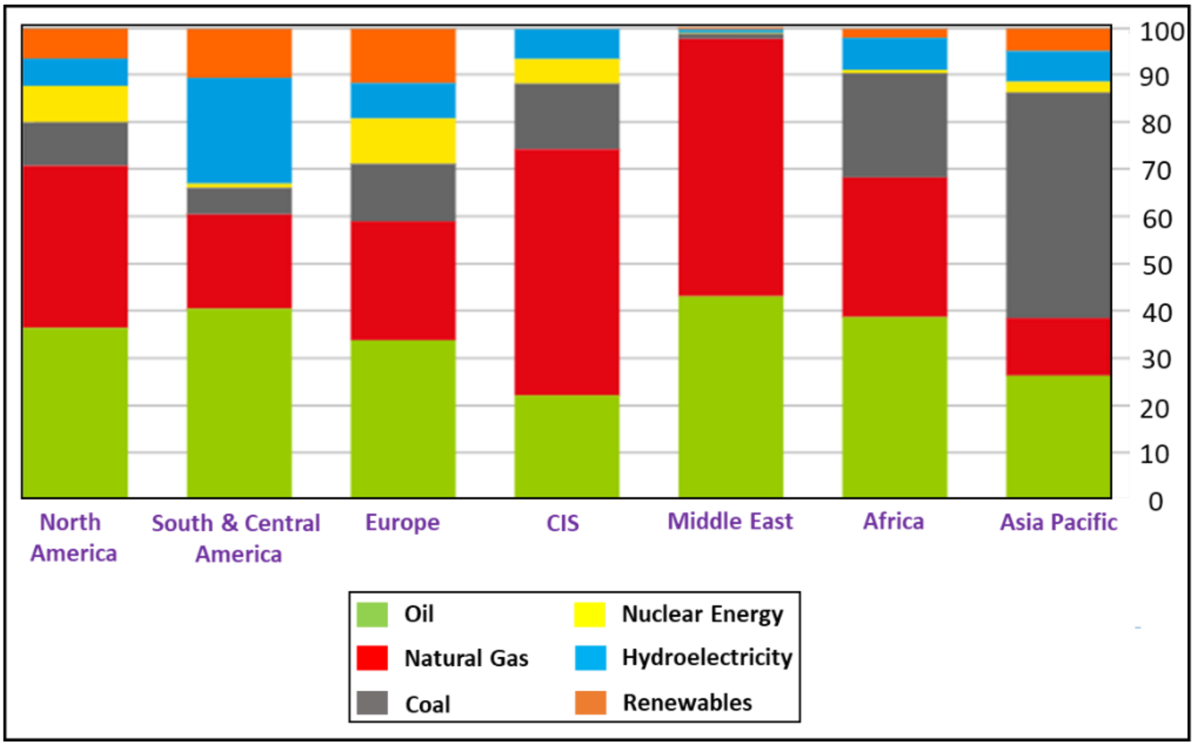

Figure 1. 2: The estimated global energy fuel consumption for the year 2020 (modified after British Petroleum, 2021).

This study is conducted to understand the high temperature high pressure reservoir properties of the Valemon and Kvitebjørn fields in Viking Graben, northern North Sea (Figure 1.3). The research related to reservoir characterization of HTHP reservoirs is still limited, and when there is a gap, there is an opportunity to carry out something new to fill the gap. The exploration of the oil and gas industry into new uncharted areas is driven by the continued growth and high demand for hydrocarbons. Due to the extreme nature of deep waters, high pressure (overpressure), and high temperature, it is difficult to explore hydrocarbons in such areas. Therefore, companies all over the globe are developing new innovative techniques for the exploration of hydrocarbons in high-temperature, high-pressure (HTHP) environments (Zhang et al., 2018).

Two features characterize the formation of an HTHP fields are high pore-pressure (>10000 psi) and high-temperature (>149°C) (Zhang et al., 2018). The HTHP hydrocarbon reservoir is a subsurface formation, containing a certain degree of porosity, and permeability to contain oil and gas under severe HTHP conditions (Zhang et al., 2018).

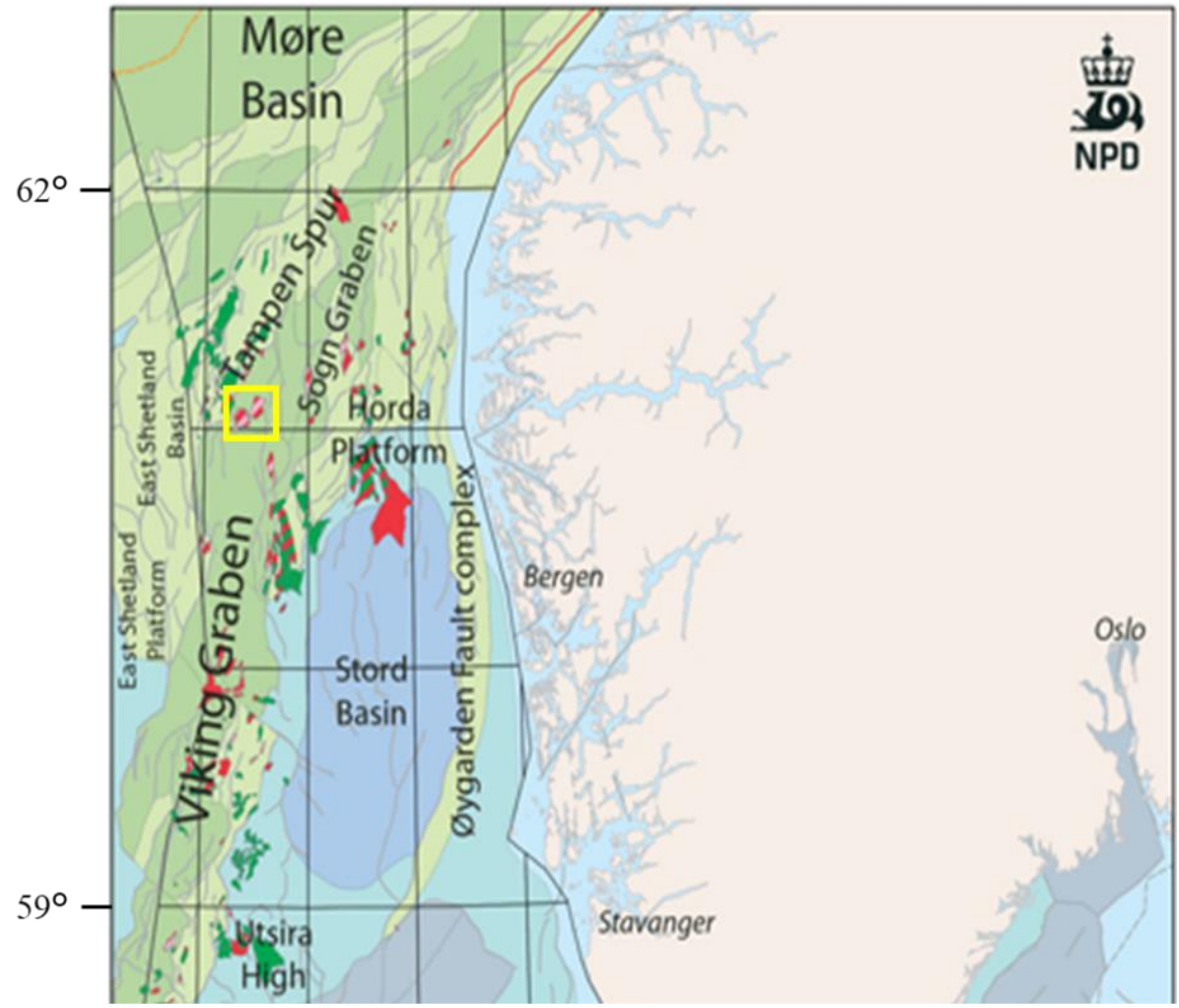

Figure 1. 3: Location of the Viking Graben and studied fields (yellow box) (modified after Norwegian Petroleum Directorate, 2021a).

Petroleum companies have run investigations and found that the HTHP hydrocarbon reservoirs exist worldwide, located in the American continent, the Nile Valley, and the North Sea (Shadravan & Amani, 2012; Zhang et al., 2018). The matrix of HTHP reservoirs is categorized based on the well operating environment aspects (Figure 1.4). Through several researches, it is determined that the following three factors determine the mechanism of the HTHP reservoir formation (Qu et al., 2013; Zhang et al., 2018; Zhe & Li, 2001).

1. that related to formation stress, which includes; disequilibrium compaction and tectonic movement mechanisms
2. that related to fluid volume expansion, a mineral transformation from montmorillonite to illite or plaster to anhydrite, a hydrocarbon generation mechanism, a pyrolysis reaction of liquid hydrocarbon, and a hydrothermal pressurization mechanism.
3. that related to the fluid movement and buoyancy action, including the effects of hydrodynamic force, penetration, reverse osmosis action, buoyancy, and the diffusion mechanisms of concentration.

One of the most studied rift systems on this Earth is the North Sea, which comprises an extensive well database and 3D seismic coverage. This thesis emphasizes the Valemon and Kvitebjørn fields, located in the northern Viking Graben, northern North Sea. Six wells in total are included in the study from both the fields: Kvitebjørn field wells are 34/11-1 and 34/11-5 S, whereas, Valemon field wells are 34/10/23, 34/10-42 S, 34/11-4 and 34/11-6 S.

In the study area to characterize the reservoir quality of the Middle Jurassic succession, the approaches applied to the available well logs are petrophysical analysis, rock physics diagnostics, and AVO forward modelling. The known targets of interest in the study area are the Middle Jurassic Tarbert and Ness Formations from the Brent Group.

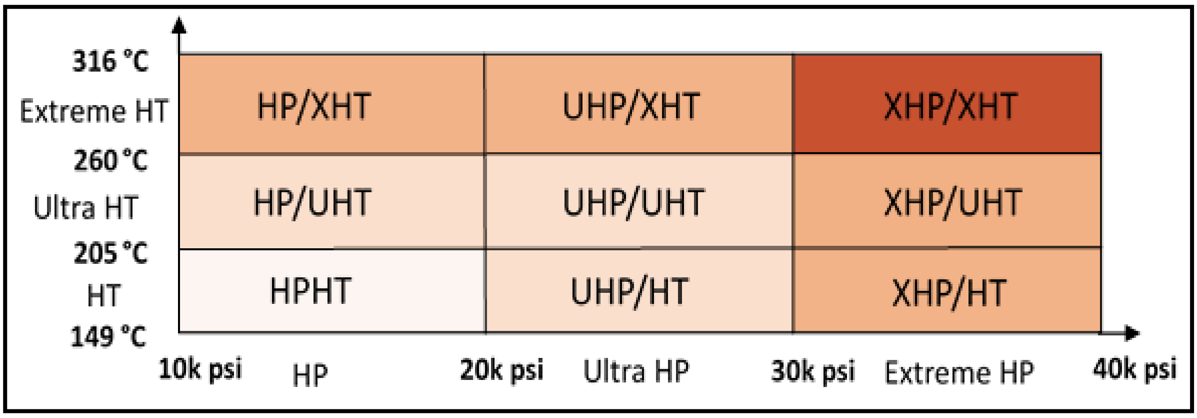

Figure 1. 4: The general classification of HTHP hydrocarbon reservoirs (modified after Shadravan & Amani, 2012).

1.2 Research Objective

The primary objective is to evaluate the reservoir quality of HPHT Middle Jurassic successions of the Valemon and Kvitebjørn fields, northern Viking Graben, northern North Sea area. To distinguish the target hydrocarbon reservoirs, the standard industrial geophysical techniques and softwares are utilized. The work comprises petrophysical rock analysis, rock physics diagnostics and AVO forward Modelling.

The six exploration wells provide with the data to classify the target reservoirs and their properties. The properties here are; determining the volume of clay, net to gross ratio, porosity, permeability, and hydrocarbon saturation. The properties also include the differentiation of lithofacies and pore fluids present in the reservoirs. Well correlations are also included in the study. Quality has been controlled and checked for errors, uncertainty, and sensitivity for the methods and the results.

1.3 Study Area

The area of study is in the northern Viking Graben, northern North Sea (Figure 1.5). In the northern part of the North Sea lies the study field Valemon; this field is situated in the west of the Kvitebjørn field, approximately 160 km west of Bergen (Figure 1.6). The water depth is about 135 meters. In 1985, the Valemon field was discovered, and in 2011, the approval of the development and operations (PDO) plans for the Valemon field were approved (Norwegian Petroleum/Valemon Field, 2021).

The Valemon field produces condensate and gas from the Early Jurassic sandstone in the Cook Formation and Middle Jurassic sandstone of Tarbert and Ness Formations in the Brent Group. The depth of the reservoir is 3,900-4,000 meters exposed to high temperature and high pressure (HTHP). Pressure depletion is the production mechanism of the Valemon field (Norwegian Petroleum/Valemon Field, 2021).

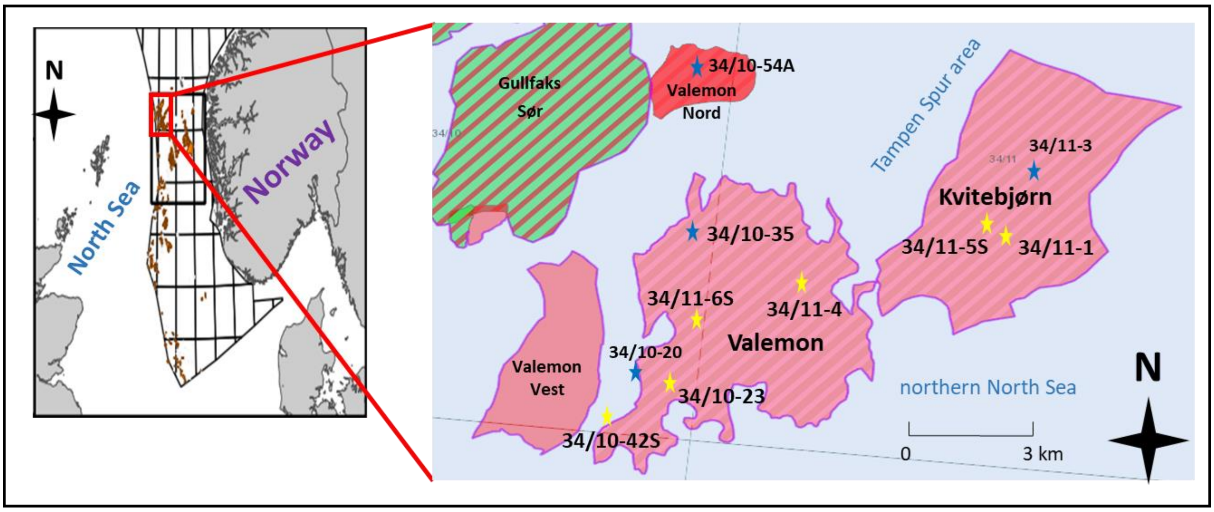

Figure 1. 5: Location map of Valemon and Kvitebjørn fields, along with the available exploration wells. The six wells used mainly in this study are marked by yellow star (modified after Norwegian Petroleum Directorate, 2021c).

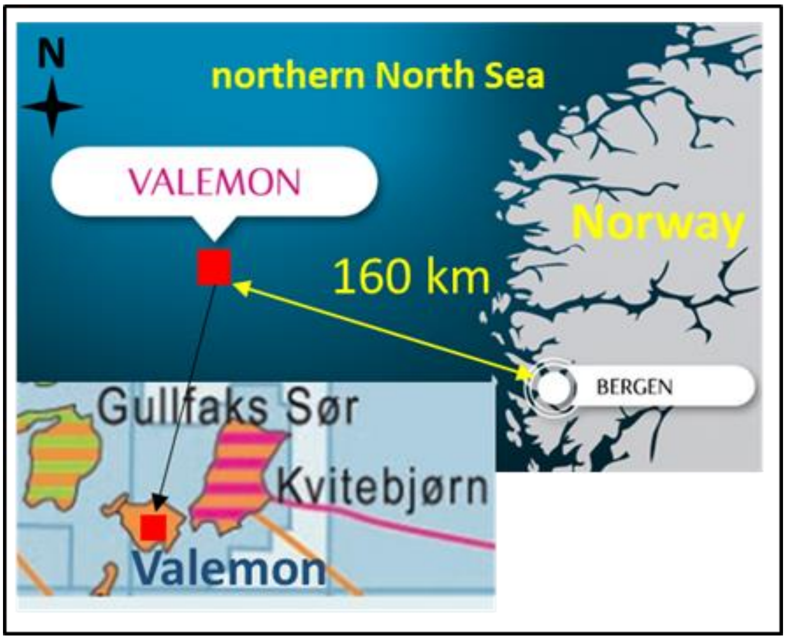

Figure 1. 6: Location of the Valemon field (160 km from Bergen) in the northern North Sea (modified after Norwegian Petroleum/Valemon Field, 2021).

In the Tampen spur area, in the northern part of the North Sea, lies the Kvitebjørn field, which is 15 kilometers southeast of the Gullfaks field (Figure 1.7). Here the water depths are about 190 meters. The Kvitebjørn field was discovered in 1994, and the development and operations (PDO) plans were approved in 2000. The Kvitebjørn field produces condensate and gas from the Middle Jurassic sandstone in the Brent Group (Tarbert and Ness Formations). Secondary reservoirs lie in the Lower Jurassic Cook Formation and the Upper Triassic Statfjord Group (Raude Formation). The depth of this reservoir is about 4,000 meters, with high pressure and high temperature (HPHT).

Figure 1. 7: Location of the Kvitebjørn field in the northern North Sea, has a distance of 15 km from the Gullfaks field (modified after norskolje.museum.no, 2016).

1.4 Database and Software

The database comprises a suite of well log data from seven (07) exploration wells in the study area. The wells used in this thesis are 34/10/23, 34/10-35, 34/10-42S, 34/11-1, 34/11-4, 34/11-5S, and 34/11-6S. The relevant information were also utilized, taken from resources and articles from the NPD (Norwegian Petroleum Directorate) webpage. Data of each well has been obtained from NPD and displayed in Table 1.1. Equinor, formerly Statoil Petroleum AS, has drilled all the studied wells.

The process and analysis of the wells log data; have been primarily done by three software: Interactive Petrophysics (IP), Hampson Russell (HR), and Petrel. Petrophysical analysis, rock physical diagnostics, and AVO forward Modelling were performed using Interactive Petrophysics 2019 (IP), and Hampson Russell Suite 10.5 (HRS). Meanwhile, Petrel has been used for the well correlations and thickness maps generation of target reservoir units. Compared to Hampson and Russell, Interactive Petrophysics has the best functionality for petrophysical analysis. The drawback it faces is the lack of advanced options regarding rock physics diagnostics and AVO forward Modelling.

In addition, Microsoft Word, Microsoft Excel, and Microsoft Power Point were used. These were utilized for generating plots, supplementary calculations, and editing. As part of the rock physics diagnostics, standard and reconstructed rock physics templates are digitized/employed from the literature.

Table 1. 1: General information regarding all studied wells. N/A = Not Available.

Facts	34/10-23	34/10-42S	34/11-4	34/11-6S	34/11-5S	34/11-1
Geological Location	Viking Graben	Viking Graben	Viking Graben	Viking Graben	Viking Graben	Viking Graben
Field	Valemon	Valemon	Valemon	Valemon	Kvitebjørn	Kvitebjørn
Type	Exploration	Exploration	Exploration	Exploration	Exploration	Exploration
Purpose	Wildcat	Appraisal	Appraisal	Wildcat	Appraisal	Wildcat
Content	**Gas**	**Dry**	**Gas / Condensate**	**Gas / Condensate**	**Gas / Condensate**	**Gas / Condensate**
NS Degrees	61° 1' 6.35" N	61° 0' 26.99' N	61° 3' 26.2" N	61° 2' 26.72" N	61° 4' 49.01" N	61° 4' 44.46" N
EW Degrees	2° 19' 1.57" E	2° 17' 3.46" E	2° 22' 46.74" E	2° 20' 19.68" E	2° 29' 59" E	2° 30' 22.74" E
Main Area	North Sea	North Sea	North Sea	North Sea	North Sea	North Sea
Year Completed	13.10.1985	19.09.1999	14.04.1999	26.01.2017	03.07.2006	25.10.1994
Bottom Hole Temperature (°C)	162	155	159	N/A	161	165
1st level of HC/Age	Tarbert / M.Jurassic	-	Ness / M.Jurassic	Tarbert/ M.Jurassic	Tarbert / M.Jurassic	Tarbert / M.Jurassic
2nd level of HC/Age	-	-	Tarbert / M.Jurassic	Ness / M.Jurassic	-	Ness / M.Jurassic
Oldest Penetrated Age	Late Triassic	E.Jurassic	E.Jurassic	E.Jurassic	E.Jurassic	E.Jurassic
Oldest Penetrated Fm	Statfjørd GP	Cook Fm	Cook Fm	Drake Fm	Drake Fm	Statfjørd GP
KB (m)	29	24	24	69	60.5	24
Water depth (m)	135	135	133	133.5	190	191
MD (m RKB)	4764	4520	4438	7126	7380	4580
TVD (m RKB)	4764	4318	4437	4405	4432	4579
MD - TVD (m)	0	202	1	2721	2948	1
Maximum Inclination (°)	0°	27.7°	2.3°	67.3°	70°	3.3°
Current Activity Status	Abandoned	Abandoned	Abandoned	Producing	Plugged	Abandoned

(Note: First four wells in light orange color are from Valemon field and the last two wells in light golden color are from Kvitebjørn field).

1.5 Chapter Description

This thesis comprises seven chapters; the following is the description of each chapter:

Chapter 1 (Introduction): This chapter provides an overview of the northern North Sea area. It includes the exploration history, study area, HTHP reservoir, research objective, the available data, software, and limitations.

Chapter 2 (Geological setting): This chapter discusses the northern North Sea regional tectonic and structural evolution. It also explains the general geology and petroleum systems within the Early to Middle Jurassic successions.

Chapter 3 (Research methodologies and theoretical background): This chapter uses the existing data, published articles, and literature to explain the research methods and theoretical background. The technique of estimating uplift has been included.

Chapter 4 (Petrophysical analysis): This chapter describes the results, interpretation, and limitations of the petrophysical analysis. The reservoir quality is evaluated based on several factors, such as determination and estimation of shale volume, porosity, lithology, permeability, net-to-gross ratio, and hydrocarbon saturation. The linking of depositional footprints to the spatial variation in reservoir properties has been reviewed. The explanation for the diagenetic processes is also included in this chapter.

Chapter 5 (Rock physics diagnostics): This chapter presents the interpretation and limitation of rock physics diagnostics. Various cross plots link reservoir properties with the elastic properties are considered. Information regarding lithology, cementation, sorting, porosity, and/ or fluid content is featured by several cross plots. The uncertainties of applying specific rock physics models are also discussed.

Chapter 6 (AVO Modelling): This chapter deals with AVO forward modelling, particularly results, interpretations, and limitations. The chapter also encompasses AVO seismic forward Modelling, where gas sand classes are determined from the top of the target gas/oil reservoirs. A generation of synthetic seismic is involved in studying the amplitude variations with offset. The fluid substitution effect is also outlined.

Chapter 7 (Summary and Conclusions): This chapter summarizes the quality of all the results and interpretations.

Appendix 1 (Conference Abstracts): During the thesis, two abstracts from the same study were presented, in Norwegian Winter Conference (January 2021) and 5th SEG student conference (November 2021).

Appendix 2 (All well logs display): The remaining well logs are displayed in this section.

1.6 Limitations and Future Work

- Due to the Covid-19 restrictions, sufficient time to work on this research is lacking. The interpretation, generating petrophysics and AVO results, editing all results and other Figures, and writing this thesis, all completed in the time of June to September, 2021).
- Due to lack of time, seismic data was not utilized. Therefore, sufficient information of structures and types of traps are not available.
- Thin section analysis is absent, and the core examination lacks the mineralogical information about the reservoir rocks is nor considered in this study.
- Due to the absence of cores facies, the correlation across the wells was difficult. The facies interpretation from cores in addition to the well logs analysis, could be more helpful for the study and would have provided us more in-sight knowledge for this study.
- Uncertainties are present in rock physics evaluations due to the unavailability of mineralogical information used for rock physics diagnostics.
- Mineralogy and cementation volume from thin-section analysis can be helpful in future research to constraint the reservoir rock properties. Inverted elastic parameters from seismic data can be used for rock physics diagnostics, and the verification from the well log data will add extra value to the study.
- The log data are somewhat limited due to relatively old exploration wells. The available well log data can be seen in Table 1.2. The Photoelectric log and Bit size are available only in the wells 34/11-5S and 34/11-6S. The SP log is available only in the wells 34/10-23 and 34/10-35. Moreover, other than Deep Resistivity log, all resistivity logs are not available in all wells.

Table 1. 2: Available Well Logs.

Well Logs	34/10-23	34/10-42S	34/11-1	34/11-4	34/11-5S	34/11-6S
Caliper	✓	✓	✓	✓	✓	✓
Bit size	✗	✗	✗	✗	✓	✓
Density	✓	✓	✓	✓	✓	✓
Gamma Ray	✓	✓	✓	✓	✓	✓
Neutron Porosity	✓	✓	✓	✓	✓	✓
Photoelectric	✗	✗	✗	✗	✓	✓
Resistivity Micro	✓	✗	✓	✗	✗	✗
Resistivity Shallow	✓	✗	✗	✗	✗	✓
Resistivity Medium	✗	✓	✓	✓	✓	✓
Resistivity Deep	✓	✓	✓	✓	✓	✓
Sonic (P-wave)	✓	✓	✓	✓	✓	✓
Sonic (S-wave)	✓	✓	✓	✓	✓	✓
SP	✓	✗	✗	✗	✗	✗
Deviated Well	✗	✓	✗	✗	✓	✓

(Note: The S-wave is represented with black color tick - it is the estimated S-wave from fluid substitution method in HampsonRussell software).

Chapter 2: Geological Setting

2.1 Regional Tectonic and Structural Evolution

Heterogeneous structure lies in and around the study area towards the northern section of the rift basin of the North Sea (Figure. 2.1). The extensions during the Caledonian and Devonian orogenies are responsible for these structures. The rifting process of the northern North Sea occurred due to the extensional phases, which happened from Late Permian to the Early Triassic ages. During the period of Early Triassic to Middle Jurassic and Early Cretaceous from Late Jurassic, different thermal cooling phases occurred after the extensional stages. During the Cretaceous time, the post rifting subsidence occurred (Odinsen et al., 2000).

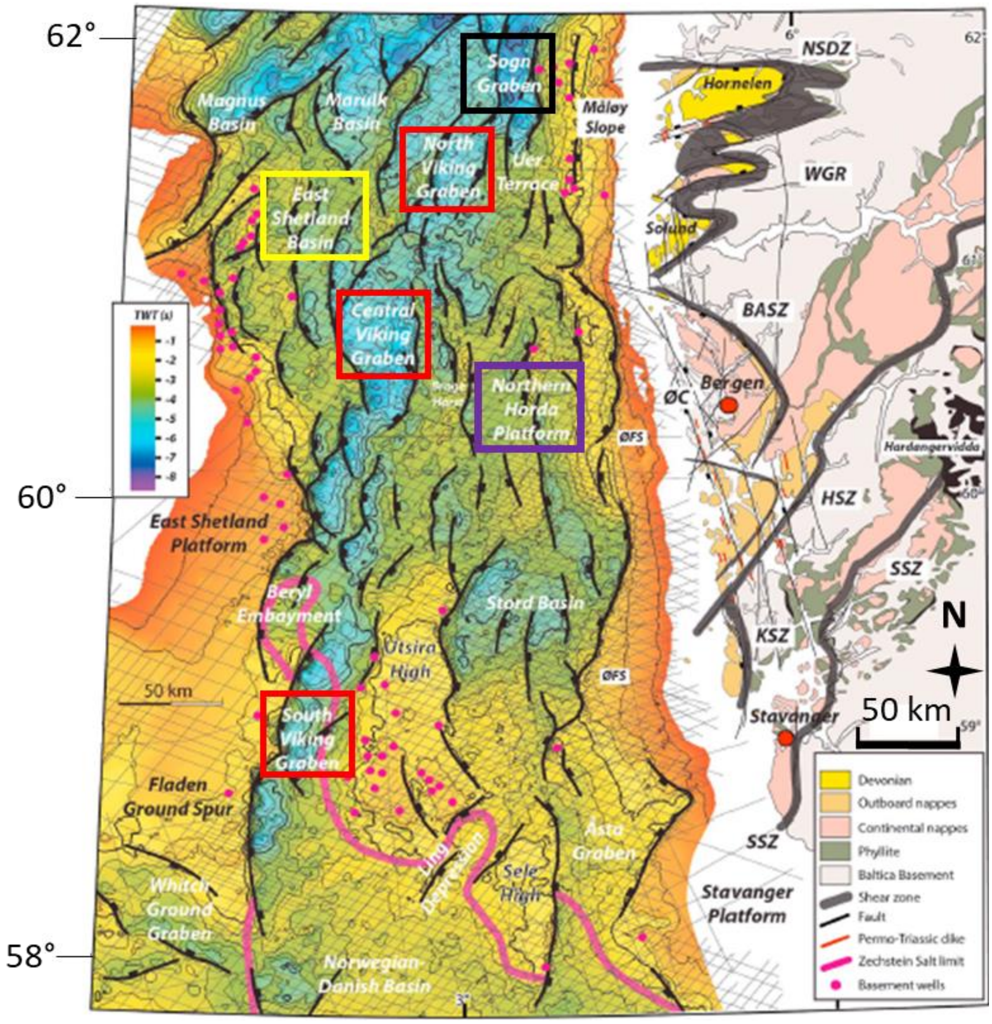

Figure 2.1: The time structural map of base rift surface (base Permo-Triassic rifting) in the North Sea Rift and southwest Norwegian Geology in the northern North Sea area. Along with the location of structural features present in the northern North Sea, such as Viking Graben (red box), Sogn Graben (black box), East Shetland Basin (yellow box) and Northern Horda Platform (purple box) (modified after Fazlikhani et al., 2017).

There are two Grabens within the northern North Sea, which are Viking Graben and Sogn Graben. Viking Graben has the major portion at the northern side of the North Sea. The Graben's limbs mark their boundaries to both East and the West of it. Following the Eastwards, the Graben's limbs mark the boundary with the one Horda Platform, and following westwards, the Graben's limbs mark the boundaries with the East Shetland Basin, and with one Tampen Spur (Faleide et al., 2010) (Figure 2.1).

Due to high hydrocarbon exploration and production, leading to an economic significance, the extensional rift basin because of the Middle Jurassic Brent Group, in particular, is believed to be the most researched extensional rift basin (Folkestad et al., 2014). The northern North Sea rift's development was accomplished after no less than two Late Paleozoic-Mesozoic rift stages. This was created on a basement foundation. It contained Proterozoic and Caledonian rocks and the fabrics of the shear zones caused by extension from the Caledonian and Devonian (Fossen, 2010). The increase of the metamorphism and deformation of the Caledonian was occurring, which was Northwest from this Hardangerfjord Shear Zone (HSZ). At the Northward and Westward of Bergen, the Oygarden Fault Complex is found because of Proterozoic basement (Fazlikhani et al., 2017; Fossen, 1992; Fossen & and Hurich, 2005). Through the Caledonian orogeny (460-400 Ma), and the Variscan orogeny (400-300 Ma), compressional tectonics influenced the northern North Sea's pre-rift crystalline basement (Ziegler, 1975).

The structural lineaments, which are oriented NE-SW and EN-WSW, are connected with these orogenic cycles that existed succeeding through the Devonian and Carboniferous extension activated as normal faults, and this did operate via the relaxation of the crust, and was post-orogenic (Ziegler, 1975). This occurred by creating some of the principal intermontane basins and extensional shear zones, similar to those conserved ashore in Western Norway (Fossen, 1992; Vetti et al., 2012). Two of the main shear zones, which are extensional, are the detachments of the Nordfjord-Sogn and Arc Bergen. These are mapped Western Norway ashore, straightway Eastward of the Horda Platform and Måløy Slope (Fossen & and Hurich, 2005; Smethurst, 2000).

A crustal fabric forms due to the extensional shear zones, which has been defined to have changed the North Sea's basin's creation through transforming the rift system's geometry of the Mesozoic, and controlling the distribution of the subsidence, which is controlled thermally of the Cenozoic (Bartholomew et al., 1993; Smethurst, 2000; Stewart et al., 1992; Ziegler, 1975). A barrier separating the deposits of the Late Permian-Early Triassic rift with pre-rift systems is described by the base rift surface. Sandstones and evaporites belonging to the Permian are included here (e.g., Åsta Graben, Ling Depression, and South Viking Graben), Caledonian nappe units (e.g., Utsira Highland Måløy), and the rocks and formations which belong to the Devonian-Carboniferous (e.g., Sele High and East Shetland Platform). In Figure 2.2, a profile of the subsurface related to the rifting events is shown, which occurred in the northern North Seas that formed East Shetland Basin (red box), Viking Graben (purple box), and Horda Platform (blue box).

The northern North Sea experienced two main rifting episodes and one inter-rifting period during the Late Permo-Triassic to the Early Cretaceous ages. This event happened after the Devonian extinction (Ziegler, 1975). In the northern North Sea, the rift-related faults are aligned towards the NW-SE and NE-SW, strike N-S, and are related to both extension phases (Badley et al., 1988; Odinsen et al., 2000; Roberts et al., 1995). During the Late Permian, the first of the main rift-phase started, which lasted 25-35 Myr, before it came to a halt during the Early

Triassic period (Ter Voorde et al., 2000; Ziegler, 1975). A predominant dip towards the west of the developed faults formed during the rift phase, and eastward's tilted bound half Grabens (Færseth, 1996). The positioning of the North to South striking Permian dykes ashore in Norway was the establishing factor.

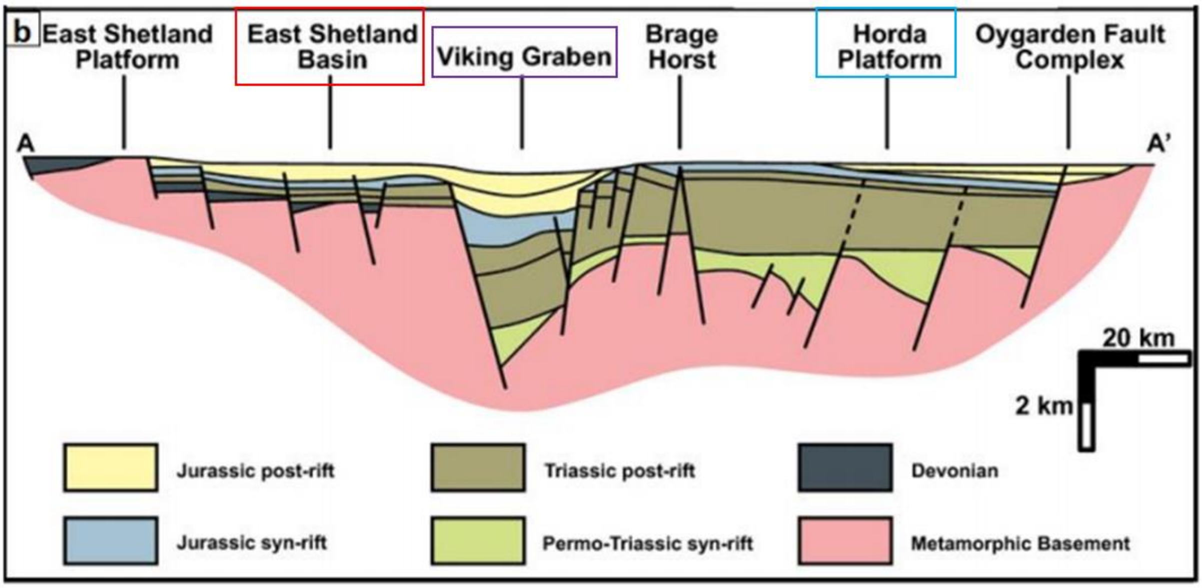

Figure 2. 2: Subsurface profile of the northern North Sea, highlighting East Shetland Basin (red box), Viking Graben (purple box) and Horda Platform (blue box) (modified after Whipp et al., 2014).

After the first rift phase, the faults formed, which then influenced in the second phase, the strain got included in the upper crust (Bellahsen & Daniel, 2005; Henza et al., 2011; Whipp et al., 2014). A second rifting phase occurred after the first, which happened through the Middle Jurassic to the Early Cretaceous. The Viking Graben was formed as a dominant central Graben structure whose first faults in its rifting phases were reactivated (Odinsen et al., 2000). During the rise in Early Jurassic (Aalenian) and Central North Sea Jurassic erosion, the second rift process occurred (Underhill et al., 1993; Ziegler, 1975). During the period of Middle to Late Jurassic, this dome collapsed, and then the activity of the second rift phase began, which lasted until the Early Cretaceous (Coward et al., 2003; Færseth, 1996; Faerseth et al., 1998; Underhill et al., 1993; Ziegler, 1992). The start and suspension of the active faulting across the rift were diachronous (Coward et al., 2003; Cowie et al., 2005).

Within the North, the Viking Graben has a striking from North to South, the Witch Ground Graben which is NNW-SSE striking is lying on the Eastern side. The Central Graben, which is striking at NNW-SSE, lies on the Southern side of the North Sea where the rift activity got restricted onto (Coward et al., 2003; Færseth, 1996; Odinsen et al., 2000; Roberts et al., 1995; Ter Voorde et al., 2000). Some west-dipping faults from the first rift phase (Permian-Triassic) were crosscut from faults dipping east from the rifts, which belong to the second phase lying in the period of Middle to Late Jurassic. This indicated that the new emerging faults during the second rifting event are more dominant than the reactivating faults, which previously existed (Færseth, 1996; Tomasso et al., 2008).

By the time the second rift phase ended, it had already started to migrate northward, as rift activity in the northern North Sea decreased. The expansion linked to the starting of the proto-North Atlantic became the more assertive regional stress (Phillips et al., 2019). Clastic sediments were being deposited along the fault scarps, as the normal faults were still active during the earliest Cretaceous period. Onlap features, particularly at the base Cretaceous Unconformity got terminated at erosional surfaces (Coward et al., 2003).

2.2 Structural Elements

During the Caledonian Orogeny event, basement crystalline rocks, which marked the majority of the North Sea area, had experienced solidification. The northern North Sea, oriented North-South, has a length of 150 to 200 km area of a widespread crust (Fjeldskaar et al., 2004). In the province of the northern North Sea, the Sogn Graben, Viking Graben, which are northwards, are the principal structural components. Both are bounded by the East Shetland Basin and in the East Horda Platform, and to the West by the Tampen Spur (Faleide et al., 2010). The Jurassic-Cretaceous rifting, which was then succeeded with the thermal subsidence and the filling of sediments in the Cretaceous, was the reason these structural elements were formed. The Viking Graben and its margins underline the old rift basin of the Permian-Early Triassic (Faleide et al., 2010). Sedimentary basins in asymmetric half-grabens and large rotated fault blocks characterize this area; these features are associated with the thinning and extension of the crust (Fjeldskaar et al., 2004). There is some evidences, which points towards a possible third tectonic event in the Tertiary (Rüpke et al., 2008); however, it was thought that after the late Jurassic rifting, the tectonic activities had ceased. Figure 2.3 displays key structural elements present in the northern North Sea (Faleide et al., 2010).

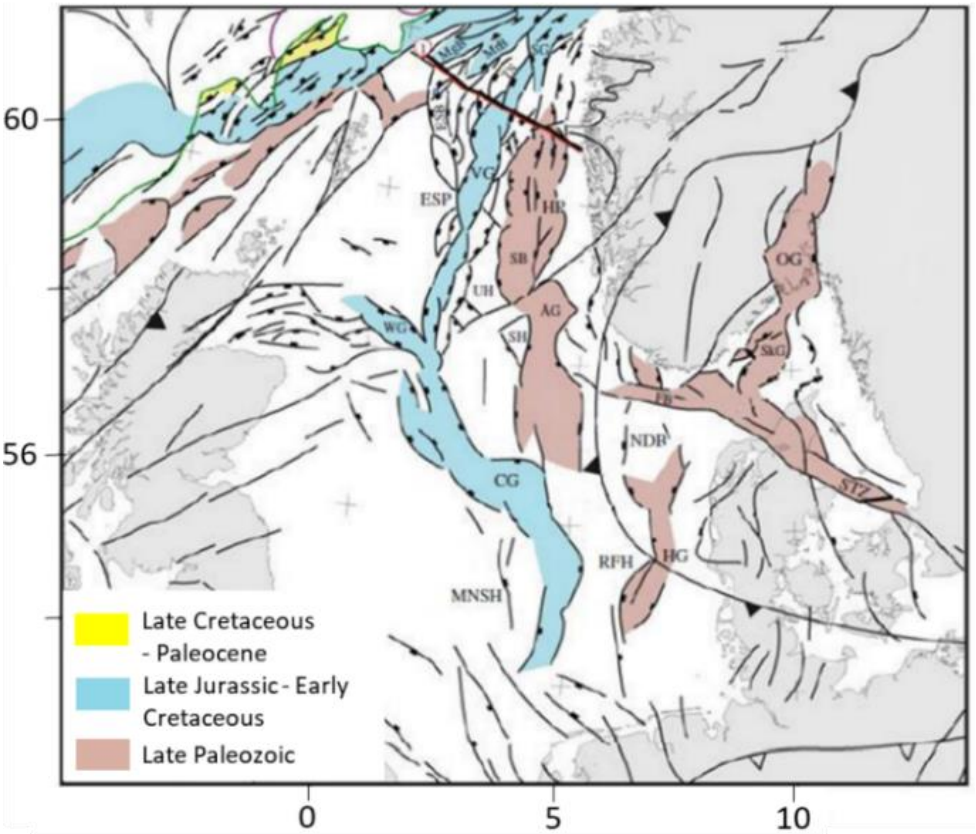

Figure 2. 3: Main structural elements present in the northern North Sea and neighboring areas, along with depositional ages (modified after Faleide et al., 2010).

The first major rifting event, which is the Permian-Triassic event, has affected the architecture of the northern North Sea. The Horda Platform is situated today where the rift axis is thought to be located (Christiansson et al., 2000) (Figure 2.1). During the second major rifting phase, many of the master faults created during this incident were later reactivated. This event took place where the Viking Graben is located; this event is dated to the late Middle Jurassic (Christiansson et al., 2000) (Figure 2.1). During the Upper Jurassic, the rifting phase occurred. Here the fault activity was only focused on the faults along the margins of the Viking Grabens. Due to this, more pronounced graben relief is found, with the development of graben topography, which includes platforms, and platform marginal heights (Gabrielsen et al., 1990). Due to cooling, post-rift subsidence followed the late Jurassic rifting (Marcussen et al., 2010).

With a series of rotated fault blocks, the Tampen spur is a structural high between the Viking Graben in the east and southeast and the Møre Basin in the north and northwest (Nystuen & Fält, 1995). Due to the Late Jurassic major uplift of the area, the margins of the Tampen spur were strongly affected by erosion, which happened during the early Cretaceous period (Jorde & Diesen, 1992). Marked by the red and purple rectangles, the regional seismic profile from the northern North Sea is shown with the Viking Graben and Tampen Spur in Figure 2.4.

2.3 Stratigraphy

The most important period considered is rightly the Late Jurassic period for the development of the petroleum system within the North Sea. This is due to the Kimmeridge Clay Formation and its equivalent Draupne and Heather Formations deposited in the Norwegian North Sea. In the North Sea, these are the main source rocks (Cornford, 1998). During the Jurassic period, the Brent Group was deposited (Figure 2.4). There was a global transgression during the period of the early Jurassic, which resulted in the shift of climate being dry to more tropical (Ramberg et al., 2007). In the northern North Sea Basin, the vast river system is drained northward. The system retreated southwards, and the thermal dome subsided. This event happened after the transgression occurred. The Brent Delta was produced by the sediments, which were being transported through this river system. The Brent Delta is considered one of the major hydrocarbon-bearing reservoir to the Norwegian oil industry. There was a relative sea-level rise due to the rifting event, which occurred during the Jurassic period. The rise in the relative sea level in the northern North Sea results in the dominant deposition of marine sediments, which comprises organic-rich deposits. The Triassic and Jurassic sediments were quickly buried as a result of subsidence and the rise in sea level. Moreover, at the end of the Cretaceous time, the Triassic and Jurassic sediments enclosed the relief structure, developed as a result of rotating fault blocks in the Viking Grabens (Ramberg et al., 2007).

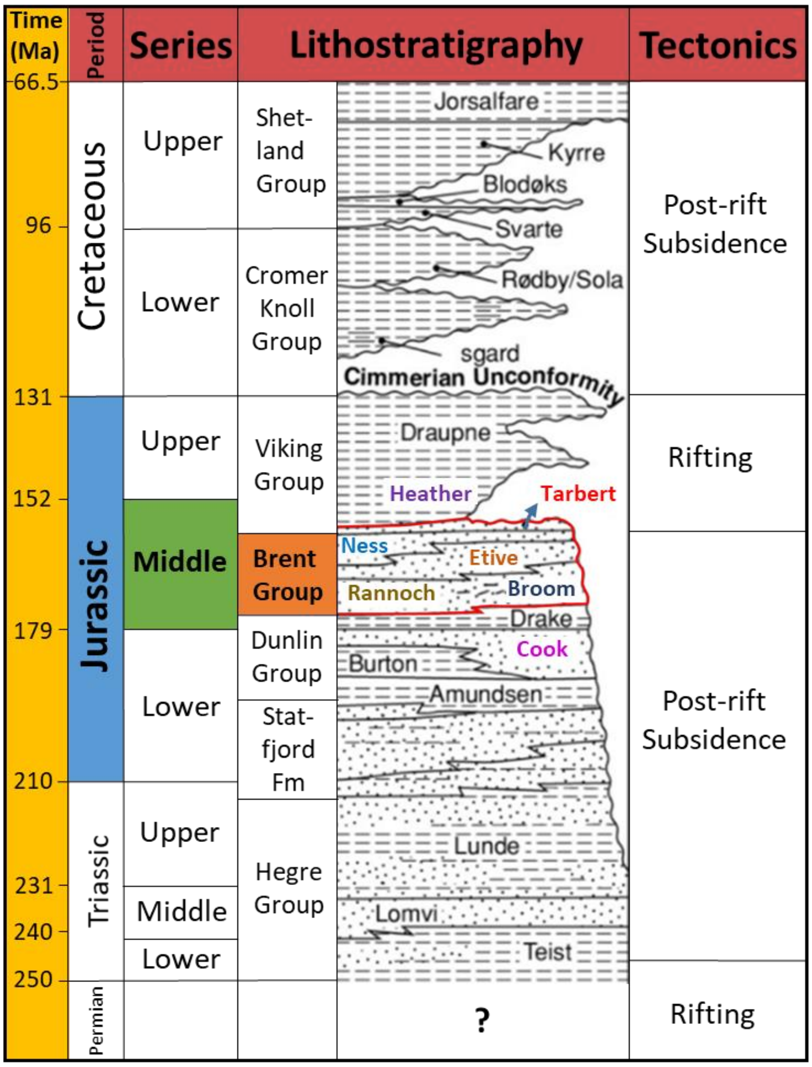

Figure 2.4: General stratigraphy of the northern North Sea area, highlighting Early Jurassic Cook Formation, Middle Jurassic Brent Group, and Upper Jurassic Heather and Draupne Formations (modified after Ketzer et al., 1999).

2.3.1 Statfjord Formation

The North Sea comprises a significant distribution of mudrocks and sandstones related to Statfjord Formation (Ryseth, 2001). The deposition of mudstone and sandstone of the Statfjord Formation occurred on the alluvial plain, controlled by the braided river (Jorde & Diesen, 1992). The Statfjord Formation comprises deposition of continental or paralic sediments related to the Triassic to Early-Jurassic time. Moreover, it exhibit a transitional boundary of continental to marine environments of deposition (Vollset et al., 1984).

2.3.2 Dunlin Group

The age of Dunlin Group is Lower Jurassic (Figure 2.4). The group comprises sediments related to marine environment. This group comprises five formations: Drake, Cook, Burton, Johansen and Amundsen Formations (Vollset et al., 1984). The group ranging from white to light gray sediments of marine argillaceous nature. These sediments are of marine sandstones located at the marginal areas with grain sizes of very fine to medium (Vollset et al., 1984). In the deepest portion of Dunlin Group, a variation in the depositional environment is seen and progressing from being alluvial to marginal marine then to the deep marine depositional environment. This variation or transition in the deposition pattern exhibit boundary within the Dunlin Group and Statfjord Formation (Chamock et al., 2001).

2.3.3 Brent Group

The Brent Group is of Middle-Jurassic age. About 200 research papers have been published on various characteristics associated with the Brent Group, as it contains the majority of Britain's oil reserves (Fjellanger et al., 1996; Richards, 1992). The Brent Group comprising main lithologies of siltstones, conglomerates, grey-brown sandstones, and shales intercalations with minor beds of coal. The group comprises five formations (upper to lower), which are Tarbert, Ness, Etive, Rannoch and Broom Formations (Vollset et al., 1984) (Figure 2.4).

2.3.4 Viking Group

The Viking Group of Upper-Jurassic age comprises Draupne and the Heather Formation (Figure 2.4). The group majorly contains dark gray to black color, marine mudstones, shales and claystones. In age, this group ranges from Bathonian to Ryazanian (Vollset et al., 1984).

2.3.4.1 Heather Formation

The Heather Formation belongs to the Viking Group and comprises grey silty claystone along with the limestone intercalations. The formation deposited in the open marine environment and is Upper-Jurassic age (Vollset et al., 1984). Through the rifting event of the North Sea in the Bathonian to Kimmeridgian time, the deposition of the Heather Formation occurred as syn-rift deposits (Justwan & Dahl, 2005).

2.3.4.2 Draupne Formation

The foremost source rock in the northern North Sea is Draupne Formation (Justwan & Dahl, 2005). The formation is a member of Viking Graben and is of Upper-Jurassic age. The formation comprises claystone of black to dark grey-brown color, which deposited in a marine environment (Vollset et al., 1984).

2.3.5 Cromer Knoll Group

The depositional environment of Cromer Knoll Group is open marine. It comprises mainly of marls, calcareous claystone and siltstones along with the sandstone and limestone intercalations. The group is of Lower-Cretaceous time period (Isaksen & Tonstad, 1989) and contains Lysing, Lange and Lyr Formations (Dalland et al., 1988).

2.3.6 Shetland Group

The Shetland Group is of Upper Cretaceous age, containing marls, mudstones, calcareous shales, and limestone facies. The depositional environment of the Shetland Group is open marine (Isaksen & Tonstad, 1989).

2.4 Petroleum Geology

2.4.1 Source rocks

The northern North Sea comprises two key source rocks that are Draupne and Heather Formations. The Draupne Formation also known as Kimmeridge Clay is the foremost significant oil-prone source rock. Whereas the Heather Formation is a significant gas-prone formation (Goff, 1983; Lafargue & Behar, 1989).

2.4.1.1 Draupne Formation

The deposition of Draupne Formation occurred in the anoxic environments (Isaksen & Tonstad, 1989). This formation is recognized as significant oil-producing source rock of kerogen type II. Moreover, it can generate the gas as the maturity level increases. The average TOC in the formation is about 2.7%, but the amount of TOC exhibits variation in the horizontal and vertical directions (Goff, 1983). The value of Pr/Ph ranges within 1 to 1.5 for the oil generated in the Draupne Formation (Gormly et al., 1994).

2.4.1.2 Heather Formation

The second most significant source rock in the northern North Sea is Heather Formation that comprises TOC of 1 to 2%. The formation is known as gas-prone and produced dry gas in a substantial amount. Moreover, it is a thick formation, comprises thickness of 1 to 2 km (Goff, 1983). The general Pr/Ph values of oil and gas generating in the Heather Formation ranging within 2.15 and 4 (Gormly et al., 1994).

2.4.2 Reservoirs

The reservoir qualities related to the Brent Group, which comprises the foremost and significant hydrocarbon-bearing reservoir rocks, are discussed in the following subchapter. In the northern North Sea, this group deposited during an uplifting of the North Sea dome (Folkestad et al., 2014). Moreover, in the northern Viking Graben, the group deposited prior to start of rifting event related to Late-Jurassic (Yielding et al., 1992). The progression of the Brent delta in the north direction results from the upliftment and erosion of the North Sea dome (Folkestad et al., 2014).

2.4.2.1 Brent Group

The Brent Group comprises five formations that are Tarbert, Ness, Etive, Rannoch, and Broom Formations (displayed as younger to older). The formations in the Brent Group deposited in the coastal, deltaic, and fluvial environments and are laterally high in thickness. It exhibits high porosity values of about 20 to 30% at shallow depths. Additionally, in some areas, the group displays highly permeable sands of values as far as 500mD (Giles et al., 1992; Vollset et al., 1984).

2.4.2 Traps

In the northern North Sea, the generated traps are majorly seen as rotated fault blocks. The post-rift generated fine-grained sediments deposited or covered the top of tilted fault blocks and reservoirs. The Brent Group reservoirs are vertically sealed in a few cases by the shales of the Cretaceous and Jurassic age. Moreover, they are laterally capped from a combination of sealing fault boundaries and shales (Gautier, 2005).

2.4.3 Migration

The migration of oil and gas from its source rocks into an aquifer or carrier bed is known as primary migration. This happens in the northern North Sea where a sufficient quantity of petroleum been produced through pressure-influenced movement from the source rocks (Mackenzie et al., 1988). The migration from the source rock to the reservoir due to the buoyant forces is known as secondary migration (Cornford, 1998). In the northern North Sea, secondary migration occurs in the rotated fault blocks. The remigration of hydrocarbon from the reservoir is known as tertiary migration, which is associated with the trapping and capping mechanism. Generally, mudstones are considered as the most efficient cap rocks related to oil-bearing reservoirs. Moreover, in the northern North Sea, the majority of the cap rocks are interpreted as mudstones. It is observed that a lack of major multiple pay reservoirs zones and the overlying sands in the well comprises low percentages of hydrocarbon in the presence of mudstone as a cap rock (Cornford, 1998).

Chapter 3: Research Methodologies and Theoretical Background

3.1 Workflow

In order to conduct this study, the following workflow has been employed (Figure 3.1). Initially, well log data quality was checked before loading well tops and well correlation. Beginning with petrophysical analysis, then rock physics diagnostics and in the end, AVO forward modelling, and quality control and correlations were applied between all three disciplines.

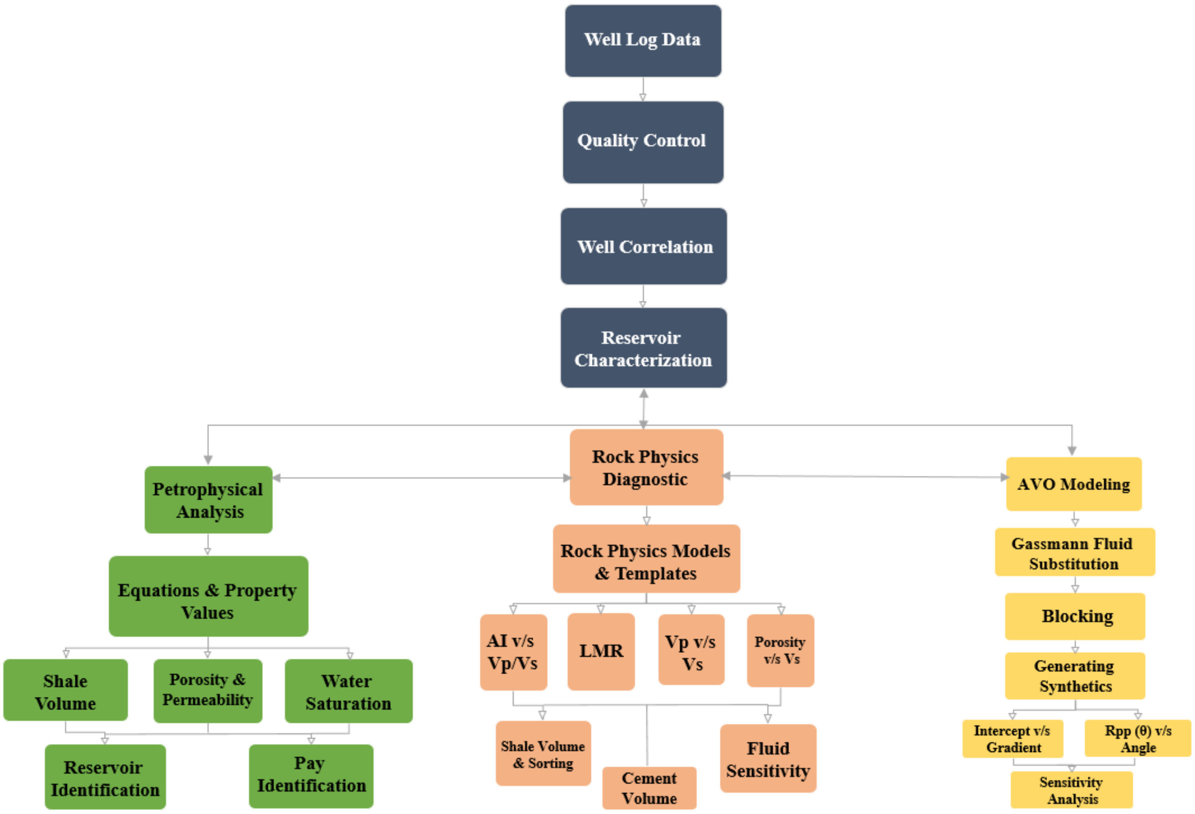

Figure 3. 1: The workflow chart of this study.

3.2 QC of Well Log Data

Quality of well log data is checked to make sure log data should be in proper conditions, and best quality for calculations and modelling should be provided. The procedure starts by recognizing the bad boreholes portions (damaged formations or washouts) are identified using caliper log and the density correction log, which is commonly caused by clumsy formations and interactions between clays and mud filtrate. In the presence of a bad borehole environment, the Density log becomes highly sensitive (Simm et al., 2014). For instance, the situation was seen in well 34/10-35 (Figure 3.2).

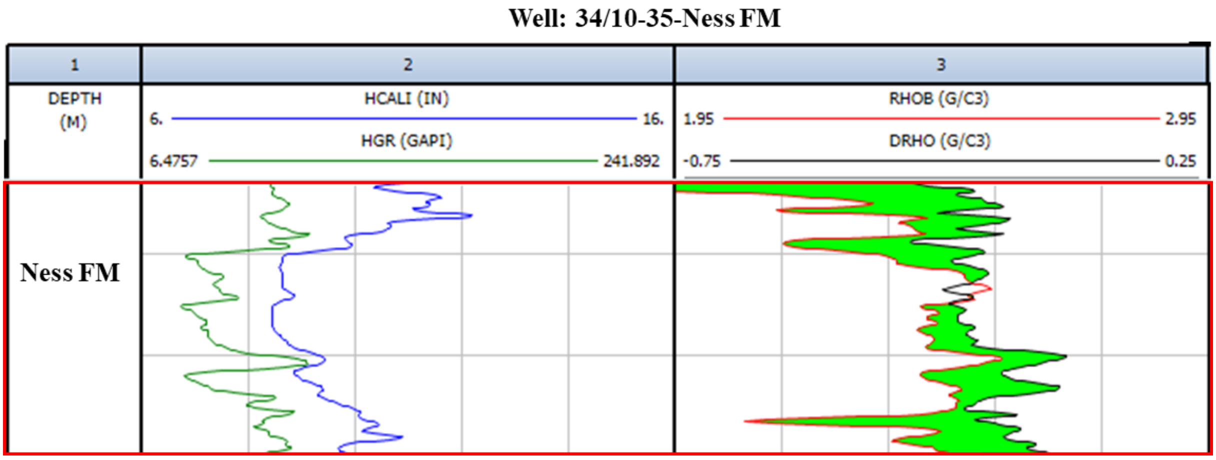

Figure 3. 2: The well 34/10-35, as an example, shows bad borehole data. The lime color shading displaying the shift for the density correction log (DRHO) at or below zero. Inconsistent high caliper (blue curve) values and DRHO (black curve) are identified within intervals in the Ness Formation.

3.3 Petrophysical Analysis

The petrophysical analysis is carried out for defining the rock properties. Additionally, for recognizing and estimating the quantity of hydrocarbons within the reservoir, calculating subsurface rock formation using well log data. Moreover, petrophysical analysis helps in the identification of reservoir, cap and source rocks, stratigraphy, depositional environment, lithology etc. For more information about well borehole effects, different well logs are combined and loggings tools help in calculating, such as for radioactivity the gamma ray, neutron and density logs utilized. Moreover, resistivity log for the electrical properties, caliper log for borehole environment and measurements, and sonic log for acoustic properties (Mondol, 2015). The steps followed for petrophysical analysis include; marking potential reservoirs with the help of lithology discrimination, clay volume estimation, and porosity calculations. The fluid content is then measured within the identified reservoir units, and in the end, several properties such as saturation and permeability are calculated and studied.

3.3.1 Lithology Discrimination and Depositional Conditions

From many of the available logs, different lithologies can be identified, for instance, gamma ray log and combination of neutron-density log. Moreover, sonic and caliper logs are utilized with the available logs for making the interpretation more accurate and reliable.

3.3.1.1 Gamma Ray log

The gamma ray log continuously records a formation’s overall natural gamma radiations that emit from the natural elements, such as, Potassium (K), isotopes of Radium (Ra), Thorium (Th), and Uranium (U). Moreover, when the value of gamma ray log is high, it specifies to shale because clay minerals comprise radioactive isotopes. Whereas the low value of gamma ray log refers to a suitable reservoir rock that contains minerals, such as quartz, dolomite, or calcite, and no radioactive isotopes are present (Asquith et al., 2004; Mondol, 2015; Schlumberger, 1991). Additionally, the tight carbonates, coal, and evaporates show low gamma ray values; therefore, low gamma ray value does not always indicate a reservoir. Whereas, if the reservoir contains radioactive minerals (mica or feldspar), perhaps exhibit high gamma ray values, even then it will count as a good reservoir. Furthermore, the gamma ray values would display as high in response to a reservoir rock due to the presence of potassium chlorite mud (KCL) that increases radioactivity in the presence of potassium. The gamma ray log unit is API (Asquith et al., 2004; Mondol, 2015; Schlumberger, 1991).

Two different kinds of gamma ray tools exist that are standard gamma ray log and spectral gamma ray log, which estimates the response of total gamma ray log and individual isotopes, respectively. To discriminate shale packages for being clean or comprising organic content, the spectral gamma ray log is utilized. Moreover, the presence of organic content in the shales can be confirmed from the high amount of uranium existing in the spectral gamma ray log (Gelius & Johansen, 2010).

It can also be utilized for predicting and studying the sedimentary depositional environments and, thus, mineral composition. Furthermore, it illuminates several gamma ray responses from the total gamma ray log that displays radiations emitting within non-clay rocks comprising constituents like micas, glauconite, organic matter, feldspar, heavy minerals, etc. (Glover, 2016; Klaja & Dudek, 2016). The presence of uranium, potassium, and thorium in formations increases the percentage of natural radioactivity. The Uranium influences gamma ray value due to the presence of organic matter. While thorium exits in the shales and influences the gamma ray due to the clay content. Moreover, potassium is also present in shale but indicates the presence of feldspar and mica. Furthermore, thorium is considered to be the best indicator of clay content. More often, clay content can also be determined from potassium but hardly uranium (Klaja & Dudek, 2016).

The identification regarding the type of mineral associated with several facies can be done utilizing Th/K ratio that also helps in defining the paleo-shoreline (Klaja & Dudek, 2016). The unit of uranium and thorium is ppm, whereas, the unit of potassium is the percentage (%). The ratio of Th/K is estimated in parts per million (ppm/%). The increasing trend of Th/K ratio starts as Glauconite, Muscovite, Illite, Mixed-layer minerals, Kaolinite, Chlorite, and Bauxite (Glover, 2016). According to (Klaja & Dudek, 2016), the range of Th/K ratio is as follows:

- Th/K less than 0.6 = Feldspars
- Th/K in the range of 0.6 and 1.5 = Glauconite
- Th/K in the range of 1.5 and 2.0 = Micas
- Th/K in the range of 2.0 and 3.5 = Illite
- Th/K more than 3.5 = mixed layered clay

The Th/K ratio and series of different minerals are shown in Figure 3.3. Due to the increase in Th/K ratio, weathering and chemical reactions also increase, progressing from K-Feldspar to micas and clays.

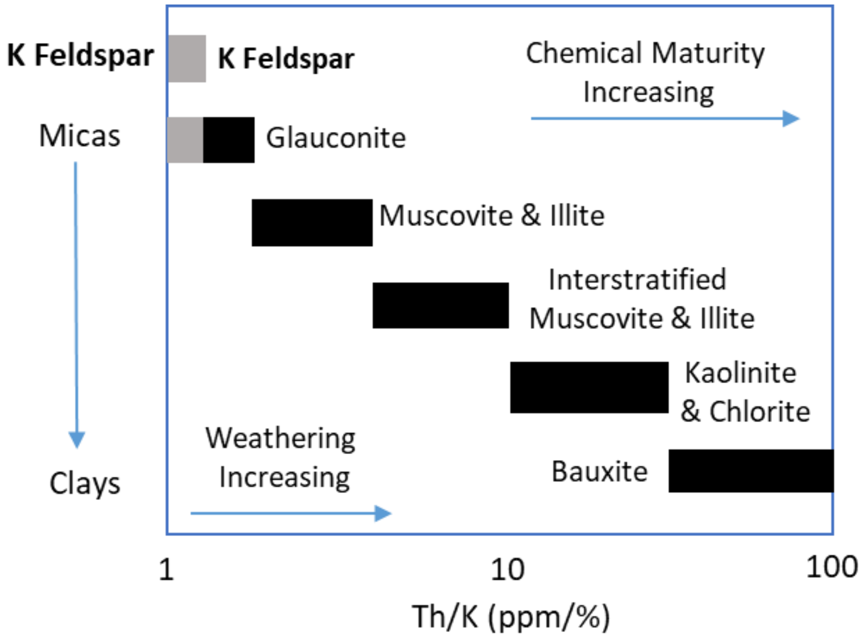

Figure 3. 3: The general range of various minerals concerning the Th/K ratio [ppm/%] chart (modified after Glover, 2016).

According to (Glover, 2016), the interpretations are as follows:

- Glauconite presence occurs in the marine environment, primarily continental shelf.
- Phosphatic deposit occurs in the marine environment and most continental shelf, comprising reducing and warm water conditions.
- Uranium presence occurs in low energy environment and reducing conditions.
- Bauxite presence occurs in the continental environment, warm and humid comprising efficient drainage.
- Feldspar occurring majorly in the areas near to the presence of igneous source.

3.3.1.2 Neutron Density Combination

Density log measures bulk density along borehole while Neutron log measures hydrogen ion concentration in formations. The neutron-density combination uses to porosity estimation in the hydrocarbon zone.

In the presence of mudcake, density log is used that have source and detectors, which are mounted on a plough-shaped pad which is pressed hard against the borehole wall so mudcake effect can be decreased and remaining effect is corrected by count rate of close and far receivers. Neutron log measures the amount of hydrogen present in the formation and estimates the porosity of the fluids (water or hydrocarbons) in pore spaces that contain hydrogen. The neutron log is calibrated in terms of a freshwater-bearing limestone model. Hence, exact porosity values can only be measured for this lithology, otherwise, regarding different rocks and fluids, it is essential to calibrate the data.

The correction is minor when there is clean oil-saturated or water-saturated sandstone present. Moreover, the estimated values are utilized. The response would be high when the formation comprises gas or shale. Furthermore, gas contains relatively low hydrogen quantity relative to oil and water; therefore, the apparent porosity gets low. While, the apparent porosity increases in the presence of shale, as the shale matrix comprises hydrogen. The estimation of apparent porosities would be significantly high in case of poor contact between tool and formation because the tool is susceptible to the wellbore wall conditions (Asquith et al., 2004; Mondol, 2015).

Neutron and density logs are combined for lithology identification. If neutron and density logs move apart, it indicates shale, if both the logs move towards each other, it indicates sand, and if a crossover is seen on the log, it indicates sand with hydrocarbons. The scale of the neutron log is displayed reversed relative to the density log. The range of values should be synchronized in such a manner that the density and the neutron log overlay each other for measurements in the calibrated lithology. A scheme is represented by (Ellis & Singer, 2007) that is:

- Limestone ranges: 1.95 to 2.95 (g/cm^3) - density and 0.45 to -0.15 (fraction) - neutron porosity.
- Sandstone ranges: 1.9 to 2.9 [g/cm^3] - density and 0.45 to -0.15 - neutron porosity.

3.3.2 Clay Volume Calculation

For the calculation of clay volume, the objective is to estimate clay proportion in formation to separate reservoir and non-reservoir rocks with respect to depth (Mondol, 2015). For this, the gamma ray and density-neutron combination logs are used. To define the volume of clay, two lines are specified, sand line (GRmin) and shale line (GRmax). The gamma ray index (IGR) can then be calculated using the equation below (Ellis & Singer, 2007; Mondol, 2015):

$$\boldsymbol{IGR = \frac{GRLog - GRmin}{GRmax - GRmin}} \qquad \textbf{\textit{Equation:} 3.1}$$

Where;
I_{GR} = gamma ray index,
GR_{Log} = gamma ray reading at a specific depth,
GR_{min} = sand line (minimum gamma ray value through a sandstone or carbonate formation),
GR_{max} = shale line (maximum gamma ray value through a shale or clay formation).

The clay/shale volume is over estimated by linear relationships, and gamma ray index shows high Vcl value, for this error, gamma ray index has to be calibrated with several proposed empirical non-linear trends for the actual result (Asquith et al., 2004; Crain, 2015; Mondol, 2015) (Figure. 3.4).

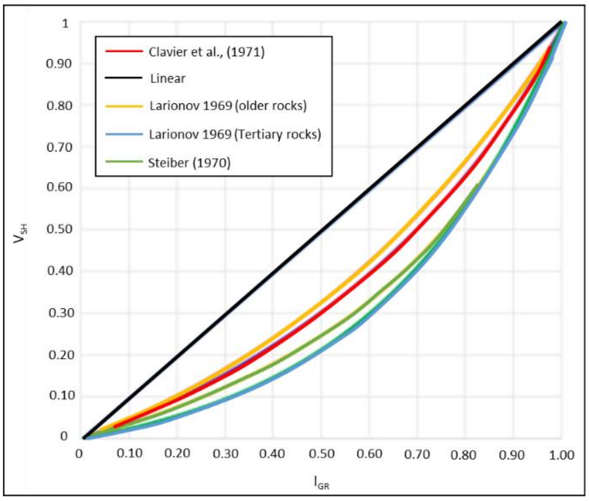

Figure 3. 4: Linear and non-linear trends generated from five different volume of shale (Vsh) equations.

The different equations for calculating volume of shale (or Vclay) are as follows:

(Larionov, 1969) (Older rocks): $\boldsymbol{V_{sh} = 0.33(22 \times I_{GR} - 1)}$ **Equation: 3.2**

(Clavier et al., 1971): $\boldsymbol{V_{sh} = 1.7 - [3.38 - (I_{GR} + 0.7)^2]}$½ **Equation: 3.3**

(Stieber, 1970): $\boldsymbol{V_{sh} = \frac{I_{GR}}{3-2} \times I_{GR}}$ **Equation: 3.4**

(Larionov, 1969) (Tertiary rocks): $\boldsymbol{Vsh = 0.083\ (2^{3.7} \times I_{GR} - 1)}$ **Equation: 3.5**

A shale and sand lines can vary in different wells and depths. Likewise, extreme high gamma ray values perhaps, exhibit the presence of organic-rich shales (Mondol, 2015). This response must be ignored while observing the shale line; thus along with gamma ray log, the neutron-density combination is also utilized in estimating shale volume (Vsh), mentioned in the Interactive Petrophysics (IP) help manual:

$$\boldsymbol{Vcl = \frac{[(D_{CL2}-D_{CL1}) \times (N-N_{CL1}) - (D-D_{CL1}) \times (N_{CL2}-N_{CL1})]}{(D_{CL2}-D_{CL1}) \times (N_{Clay}-N_{CL1}) - (D_{Clay}-D_{CL1}) \times (N_{CL2}-N_{CL1})}}$$ ***Equation:* 3.6**

Where;
D and N = estimated density and neutron values,
D_{CL1}, N_{CL1}, D_{CL2} and N_{CL2} = selected values at the two ends on the clean line,
D_{Clay} and N_{Clay} = values on the shale point of density and neutron.
Within the two clay volume calculations, the minimum value must be picked, due to the errors that commonly overestimates the apparent clay volume (Crain, 2015).

3.3.3 Porosity Estimation

The porosity is defined as the ratio of void spaces (pore spaces) to the total volume of the rock, whether pores are connected or not. The small amount of fluids present in the pore spaces has the ability to move within the rock. Thus, there are two different kinds of porosities, effective (interconnected porosity) and ineffective. The grain size and sorting mainly control the connectivity of pores. While studying the logs, reservoir rock consists of water, hydrocarbon, clay, and matrix, as shown in Figure 3.5 (Simm et al., 2014).

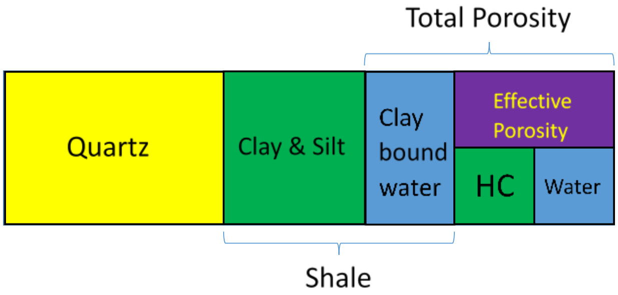

Figure 3. 5: A model constituting parts of a shaly sandstone (modified after Simm et al., 2014).

Three logs are used to calculate porosity that are density log, sonic log, and neutron log. Porosity is not measured directly from logs, but rather by mathematical relations in sufficient lithology information. The lithology effects present in all three porosity logs, i.e. density, sonic, and neutron, lead to the estimation error. The combined use of all three porosity logs minimized the lithology effects and resulted in precise measurement of porosity (Mondol, 2015; Schlumberger, 1991). The effective porosity is defined as the total number of pore spaces, which are sufficiently interconnected with each other to produce fluid (oil or gas) for recovery. Estimation of the porosity given by well logs are calculated by Hook, (2003) formula:

$$\varphi e = \frac{(V_{pt} - V_{cbw})}{V_b} \qquad \textbf{Equation}: 3.7$$

Where;
φ_e = effective porosity,
V_{pt} = total pore volume,
V_{cbw} = volume of clay bound water,
V_b = bulk volume of rock.

The total porosity is defined as, the ratio of total pore and the bulk volume of the formation, irrespective of the type of fluid present. Because of ambiguity in the dry clay density, the estimation of total porosity is more complex. According to Hook, (2003), total porosity is as follows:

$$\varphi t = \frac{V_{pt}}{V_b} \qquad \textbf{Equation}: 3.8$$

Where;
φ_t = total porosity,
V_{pt} = total pore volume,
V_b = bulk volume of rock.

3.3.3.1 Porosity from density log

The porosity from the density log is estimated by the given formula (Mondol, 2015):

$$\varphi D = \frac{\rho ma - \rho b}{\rho ma - \rho fl} \qquad \textbf{Equation}: 3.9$$

Where;
φ_D = density porosity,

ρ_{ma} = density of the matrix,
ρ_{fl} = density of the pore fluids,
ρ_b = bulk density reading at a specific depth.

The following Table 3.3 represents the general density values for fresh-water, salt-water, and sandstones.

Table 3. 1: According to Asquith et al., (2004), the general density values of water and sandstone (g/cm^3):

Lithology/Fluid	Density (g/cm^3)
Fresh Water	1
Salt Water	1.15
Sandstone	2.64

In the case of sand and shales, it does not influence the results because shale sometimes possesses the same density as quartz. The resolution of the density tool is limited i.e., about 6 inches, which does not allow deep insight into the formation. Thus, the primary pore fluids density (ρfl) is associated with the mud invaded zone, and salinity controls the density of the mud filtrate. When the invaded zone is hydrocarbon saturated, the invaded zone comprising fluid becomes a mixture of hydrocarbon, mud filtrate, and formation water. For this scenario, fluid density is supposed to be 1 g/cm3. When the invasion of filtrate is restricted, the density being recorded is greatly influenced by gas saturation, whereas the density of pore fluid gets lowered (Schlumberger, 1991). With respect to clay volume, the density of the matrix shows variations. As input for density of shale (ρsh), wet shale density is utilized. Whereas, if the density of dry shale is used, then total porosity will be estimated (Kennedy, 2015). Furthermore, the shale term is included into Equation 3.10 that shows a new equation:

$$\varphi D = \left[\frac{\rho ma - \rho b}{\rho ma - \rho fl}\right] - \left[Vsh \times \frac{(\rho ma - \rho sh)}{\rho ma - \rho fl}\right] \qquad \textbf{Equation: 3.10}$$

Where;
φ_D = density porosity,
ρ_{ma} = density of the matrix,
ρ_{fl} = density of the pore fluids,
ρ_b = bulk density reading at a specific depth,
V_{sh} = shale volume,
ρ_{sh} = shale density.

3.3.3.2 Porosity from Sonic Log

It is a porosity log, which records the travel time (Δt) of high-frequency sound waves, traveling within the formation and receiving to the tool. Two receivers are placed at some distance from the source. When sound waves coming from formation are received at different times on the receiver, the near receiver recorded transit time is subtracted from the distant receiver to produce the interval transit time (also the velocity) of the formation. The unit used for sonic log calculations is µs/ft (Asquith et al., 2004; Mondol, 2015). To calculate porosity from sonic log, Wyllie Time Average equation can be utilized (Wyllie et al., 1958), which is as follows:

$$\boldsymbol{\varphi S} = \frac{[\Delta t\ Log - \Delta t_{matrix}]}{[\Delta t_{fluid} - \Delta t_{matrix}]} \qquad \textbf{Equation: 3.11}$$

Where;
φ_S = sonic porosity,
Δt_{Log} = interval transit time from the log at a specific depth,
Δt_{matrix} = interval transit time of the matrix,
Δt_{fluid} = interval transit time of the fluid.

General values for interval travel time of fluids and minerals existing in the formation are mentioned in Table 3.2.

Table 3. 2: According to Asquith et al., (2004), the general travel time values of sandstone and water (µs/ft) are as follows:

Lithology / Fluid	**Travel Time (µs/ft)**
Sandstone	51.5 to 55.5
Fresh-Water Mud Filtrate	189
Salt-Water Mud Filtrate	185

Moreover, the Raymer-Hunt-Gardener equation could be alternatively utilized (Raymer et al., 1980) to calculate porosity:

$$\boldsymbol{\varphi S} = \frac{5}{8} \times \frac{[\Delta tLog - \Delta t_{matrix}]}{\Delta tLog} \qquad \textbf{Equation: 3.12}$$

Where;
φ_S = sonic porosity,
Δt_{Log} = interval transit time at a specific depth,
Δt_{matrix} = interval transit time of the matrix.

The average transit time related to unconsolidated formations, display errors in the calculations. As a result of ineffective grain contacts in the unconsolidated formations, the measured transit time is overestimated. Moreover, to minimize this error, there is a need to utilize an empirical compaction factor (Asquith et al., 2004).

$$\boldsymbol{\varphi S} = \frac{[\Delta t\ Log - \Delta t_{matrix}]}{[\Delta t_{fluid} - \Delta t_{matrix}} \times \frac{1}{C_p} \qquad \textbf{Equation: 3.13}$$

Where;

Cp = estimated compaction factor.

The estimation of compaction factor can be done from following equation:

$$\boldsymbol{Cp = \frac{[\Delta tsh * C]}{100}} \qquad \boldsymbol{Equation: 3.14}$$

Where;
Cp = compaction factor,
Δt_{sh} = shale interval transit time,
C = constant (1)

When the rock is hydrocarbon bearing, it increases transit time, which results in the overestimation of porosity calculated from sonic log (Asquith et al., 2004). Therefore, a relation for correction is recommended by (Hilchie, 1978), which is as follows:

For gas: $\boldsymbol{\varphi = \varphi S \times 0.7}$ $\qquad \boldsymbol{Equation: 3.15}$

For oil: $\boldsymbol{\varphi = \varphi S \times 0.9}$ $\qquad \boldsymbol{Equation: 3.16}$

3.3.3.3 Porosity from Neutron-Density porosity combination

Neutron and density logs are combined to measure average porosity for different formations. To overcome the gas effect in flushed zone, the following relation is utilized (Mondol, 2015):

$$\boldsymbol{\varphi ND = \sqrt{(\varphi N)^2 + \frac{(\varphi D)^2}{2}}} \qquad \boldsymbol{Equation: 3.17}$$

Where;
φ_{ND} = neutron-density porosity,
φ_N = neutron porosity,
φ_D = density porosity.

In the Interactive Petrophysics (IP) software, several equations for estimating porosity from neutron and density models can be utilized and comprise several new elements therefore, if understanding the new elements is not clear, which might lead to limitations. Moreover, some new equations were used in order to avoid the effects of hydrocarbon and shale. The correct usage of these equations might estimate porosities even more precisely. In the help manual of the Interactive Petrophysics software (IP), the following equations are present:

$$\boldsymbol{\varphi D = \frac{[\rho ma - \rho b - Vcl \times (\rho ma - \rho cl)]}{[(\rho ma - \rho fl \times Sxo - \rho HCAp \times (1 - Sxo)]}} \qquad \boldsymbol{Equation: 3.18}$$

$$\boldsymbol{\varphi N} = \frac{[(\varphi Neu - Vcl \times NeuCl + NeuMatrix + Exfact + NeuSal)]}{[Sxo+(1-Sxo) \times NeuHCHI)} \qquad \textit{Equation}\text{: 3.19}$$

Where;
φ_N = estimating neutron porosity,
φ_D = estimating density porosity,
φ_{Neu} = value of neutron log,
V_{cl} = clay volume - wet,
NeuCl = value of neutron log wet clay,
NeuMatrix = value of neutron log related to matrix correction,
Exfact = value of neutron log excavation factor,
NeuSal = value of neutron log related to formation salinity correction,
Sxo = water saturation value of the flushed zone,
NeuHCHI = value of neutron log related to hydrocarbon hydrogen index,
ρ_{ma} = value of matrix density,
ρ_b = value from density log,
ρ_{cl} = value of clay density - wet,
ρ_{fl} = fluid density,
ρ_{HCAp} = apparent value of hydrocarbon density.

3.3.4 Water Saturation and Pay Zone Identification

Saturation is defined as the ratio of fluid and pore volume. Moreover, water saturation is defined as the percentage of water filled in pore volumes of the formation. The pores in the rock should comprise some fluid, and the total of all the fluids should be making 100% fluid content. The three common types of fluids are oil, gas, and water, but in rare conditions, pores can be filled with air or carbon dioxide. Furthermore, if the water saturation is measured as less than 100%, it reflects the presence of hydrocarbon saturation because the formula for hydrocarbon saturation is taken as 1-Sw (Schlumberger, 1991). In order to estimate the water saturation, a resistivity log can be utilized. In the resistivity tool, electrodes are present that are arranged to transmit electric current to formations (Asquith et al., 2004; Mondol, 2015). The resistivity tool comprises deep penetration and records the fluid saturation in the uninvaded zone, which is true resistivity (Rt). The unit of resistivity is ohm-meter (ohm-m). Archie's law (Equation 3.20) is utilized to determine water saturation, and the equation is derived for a consolidated, clean sandstone having different intergranular porosity (Mondol, 2015):

$$\boldsymbol{Sw} = \left[\left(\frac{a}{R_t}\right) \times \left(\frac{Rw}{\varphi_m}\right)\right]^{\frac{1}{n}} \qquad \boldsymbol{Equation: 3.20}$$

Where;
Sw = water saturation,
Rw = formation water resistivity,
a = tortuosity factor,
m = value of cementation exponent,
n = value of saturation exponent,
φ = porosity,
R_t = true formation resistivity.

In the range of 1 to 3, the cementation exponent (m) is calculated that reflect 1 as a porous rock and 3 as greatly cemented rock. For the unconsolidated sands, the general value is 1.3, whereas, for consolidated sands, the range is 1.8 to 2.0 and carbonates 1.7 to 4.1 (Mondol, 2015).

Moreover, tortuosity factor (a) is defined as the variation present within the flowing area of the pore body and pore throat. For the carbonates, its value is about 1. Furthermore, the saturation exponent (n) represents the rock wettability and hydrocarbon occurrence within the pore space. In the hydrocarbon saturated situation, the water-wet rocks are relatively more conductive than an oil-wet rock. According to (Varhaug, 2016), the adjacent water-saturated rock is utilized for estimating the formation water resistivity (Rw), as present in Equation 3.21:

$$\boldsymbol{Rw = \frac{Rt}{F}} \qquad \boldsymbol{Equation: 3.21}$$

Where;
Rw = estimated formation water resistivity,
F = resistivity factor of formation,
R_t = value of true formation resistivity.

The quantity of rock matrix is defined from the resistivity factor of formation, as it is related to the permeability and porosity of rock. Moreover, it is ineffective to the conductivity of pore water (Mondol, 2015). To estimate the formation resistivity factor, the following relation is utilized:

$$\boldsymbol{F = \frac{a}{\varphi m}} \qquad \boldsymbol{Equation: 3.22}$$

Where
F = resistivity factor of formation,
a = value of tortuosity factor,
m = the cementation exponent,
φ = porosity value.

Several limitations related to water saturation are discussed as follow:

It is impossible to contain no water saturation (0%) in a rock as capillary water always exists. The oil and gas are not able to eliminate the capillary water present in the rock; this water is also known as connate water. Similarly, in a rock comprising oil and gas saturation, some amount of hydrocarbon always remains accumulated in rock pore spaces after migrating or producing. This remaining oil or gas is known as residual oil or residual gas (Schlumberger, 1991). Moreover, the resistivity of drilling muds and formation fluids is affected by the temperature. Furthermore, several limitations exist regarding calculations of Rt and Rw, the preferred value of cementation and saturation exponents, and the drilling mud infiltration (Mondol, 2015).

3.3.5 Permeability Prediction

The permeability of a rock is defined as allowing fluids to flow through the rock without bringing any alterations within the rock. A rock is called permeable if it has interconnected pores or fractures. Sometimes porosity and permeability make a direct relationship. That is, high porosity reflects high permeability, but it is not seen frequently. Moreover, the shales have higher porosity; however, they do not possess the ability to pass fluid easily because shale comprises small pores in it. The unit of permeability is millidarcy (mD) (Schlumberger, 1991). Estimation of permeability is achieved while utilizing empirical relations from well logs related to water saturation and porosity, recommended by

Timur Equation: $k = \frac{[10^4\ \varphi e^{4.5}]}{Sw^2}$ *Equation:* **3.23**

Logarithmic – linear for sandstones: $log_{10}k = Clog_{10}\ \varphi_e + D$ *Equation:* **3.24**

Wylie – Rose formula (Morris – Biggs parameters): k = $\frac{62500*\varphi e^{4.4}}{Sw^2}$ *Equation:* **3.25**

Where;
k = estimated permeability,
φ_e = value of effective porosity,
S_w = irreducible water saturation present in the hydrocarbon-bearing rock,
C/D = estimated constants.

Several limitations related to permeability prediction are observed. All permeability equations stated shows that if permeability increase, porosity also increases, whereas the irreducible water saturation decreases. Moreover, when porosity is calculated like in Equation. 3.24, it shows many errors, specifically in the carbonate reservoir. Moreover, in the Timur equation and Wylie-Rose formula, the existing constants of permeability are only utilized for oil reservoirs. Whereas, different permeability constants must be utilized for the gas-bearing reservoirs, which can be seen in Crain, (2015). Additionally, the utilized permeability constants were not adjusted to the related cores and with respect to the study area.

For explaining the effective permeability limit, cutoff values of gamma ray can be utilized. Moreover, an inverse relationship is seen between permeability and clay volume. The permeability gets low as the clay volume increases because the paths and pore spaces get blocked. Furthermore, the pore spaces are filled, leading to low porosity (Klaja & Dudek, 2016). Identification of mudcake from the caliper log can also indicate permeable intervals (caliper < bit size indicating a permeable rock) (Mondol, 2015).

3.3.6 Net to Gross ratio and Petrophysical Cut-offs

The ability of a rock to accumulate and move fluids depending on the basis of thickness or thickness ratio are explained through several descriptive terms (Worthington & Cosentino, 2005), which are described and demonstrated in Figure 3.6.

- Gross rock is defined as the whole rock volume.
- Net sand represents the rocks, perhaps comprising good reservoir properties. Here sand reflects to clean (no lithology variation) sedimentary rock. The net sand is

referred by combining all the intervals that comprise sand equal to or greater than the mentioned cutoff value.

- Net reservoir refers to those identified net sand formations comprising good reservoir properties. The net reservoir is measured by adding the net sand intervals that exhibits a porosity value equal or more than the mentioned cutoff value. Moreover, this rock possesses effective permeability that reflects the rock's ability to accumulate and flow hydrocarbons.
- Net pay corresponds to the net reservoir intervals, which contain a significant amount of hydrocarbons. The cutoff value defines it for water saturation. The net pay should be equal or less than the water saturation cutoff. Nowadays, net pay not only describes the rock type but also has an economic aspect. It defines those hydrocarbon reservoirs that can be produced economically using a particular production procedure.
- Net-to-Gross is defined as thickness ratio divided by the gross thickness related to any of the three above-mentioned net-properties, such as net-to-gross pay, net-to-gross reservoir, and net-to-gross sand.

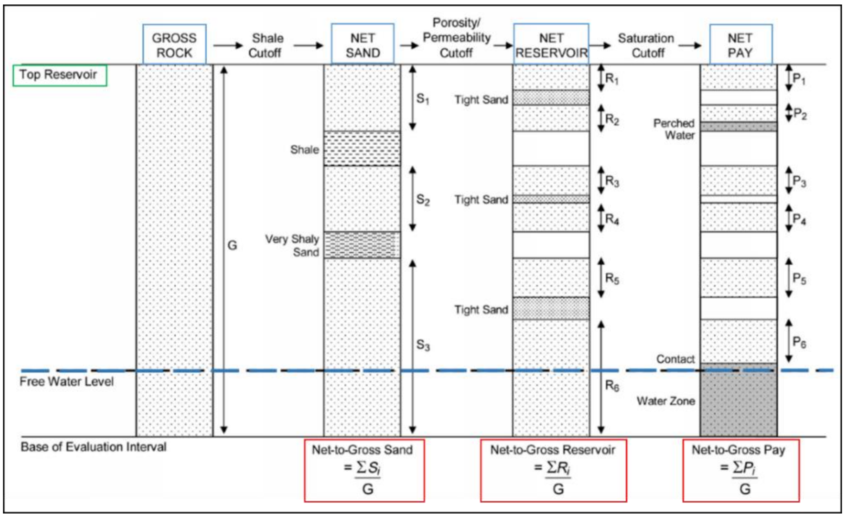

Figure 3. 6: On the basis of cutoff values, the net parameters to gross rock calculation is displayed (modified after Worthington & Cosentino, (2005).

The permeability is estimated from measured porosity or several well logs, thus, the cutoff related to permeability is defined as pseudopermeability cutoff. Moreover, the values of permeability cutoff for oil and gas are 1.0 and 0.1 mD, respectively (Worthington & Cosentino, 2005). According to (Worthington & Cosentino, 2005), the cutoff value related to the producible sandstone reservoir is mentioned in Table 3.5. Moreover, some limitations such as fractured reservoir possess relatively low porosity values compared to the respective cutoff values. However, the fractured reservoir rocks still the ability to produce hydrocarbons (Bjørlykke & Jahren, 2015).

Table 3. 3: The cutoff values recommended related to producible sandstone reservoir by Worthington & Cosentino, (2005) is as follows:

Cutoff Parameters	Values
Vsh	<= 0.3 to 0.5
ϕ	>= 0.06 to 0.08
Sw	<= 0.5 to 0.6

3.4 Rock Physics Diagnostics

A connection between reservoir properties (saturation, sorting, porosity, clay volume, etc.) and seismic parameters (Vp/Vs ratio, acoustic impedance, density, etc.) inside a reservoir is formed by rock physics. Seismic properties can be forecast through the rock physics models by observing reservoir properties. This approach can also be utilized in revealing the impacts of different lithologies and fluids applied to the existing data (Avseth et al., 2009). Moreover, rock physics is utilized to highlight errors present in the log data and data quality control.

Usually, to define several relationships (e.g., Lambda-Rho versus Mu-Rho), rock physics crossplots are utilized. Moreover, various models occur comprising the existing merits and demerits (Avseth, 2015). In crossplots, two properties are used for plotting, and in order to find out the rock properties, data is plotted according to theoretical trends. Additionally, plotted data is color-coded with different rock properties for identifying and highlighting the interesting zones. The upcoming subchapters discuss the descriptive explaination of rock physics models, consisting of empirical models, theoretical bounds, Gassmann’s equation and contact models, and generation of rock physics templates (RPTs).

3.4.1 Calculation of Elastic parameters

The response of rocks as a function of stress (force per area) is explained by the elastic moduli. The alteration in the medium shape as a result of shear stress is known as shear modulus (μ). Moreover, it demonstrates the rigidity present in a rock as the stresses to a rock are applied in the direction of the deposited bed. The shear modulus does not apply to fluids because they do not have the ability to transform their shape according to the hosting medium (Simm et al., 2014) (Figure 3.7, A). The ratio of change in volume to the original volume (ΔV/V) is defined as bulk modulus (K). It is because of the uniform pressure experienced by the rock from all directions (Figure 3.7, B). Through the following equations, bulk and shear moduli are associated with P-wave and S-wave velocities (Avseth, 2015; Gelius & Johansen, 2010).

$$\boldsymbol{Vp} = \sqrt{\frac{\boldsymbol{K} + \left(\frac{\boldsymbol{4\mu}}{\boldsymbol{3}}\right)}{\rho}} \qquad \boldsymbol{Equation: 3.27}$$

$$\boldsymbol{Vs} = \sqrt{\left(\frac{\boldsymbol{\mu}}{\boldsymbol{\rho}}\right)} \qquad \boldsymbol{Equation: 3.28}$$

Where;
Vp = velocity of P-wave,
Vs = velocity of S-wave,
K = value of effective bulk modulus,
µ = value of effective shear modulus,
ρ = value of effective density.

In order to estimate K and µ directly, the Vp and Vs formula is altered (Gelius & Johansen, 2010), which is as follows:

$$\boldsymbol{K} = \boldsymbol{\rho}\left[\boldsymbol{V}_{\mathrm{p}}^{\mathbf{2}} - \left(\frac{\mathbf{4}}{\mathbf{3}}\right)\boldsymbol{V}_{\mathrm{s}}^{\mathbf{2}}\right] \qquad \boldsymbol{Equation}: \mathbf{3.29}$$

$$\boldsymbol{\mu} = \boldsymbol{\rho} \times \boldsymbol{V}_{\mathrm{s}} \qquad \boldsymbol{Equation}: \mathbf{3.30}$$

The Poisson´s ratio (PR) is the ratio between transverse strain and longitudinal strain (difference in width and length, respect to the original), when a uni-axial stress is applied on a medium (Figure. 3.7, C). The relation of Poisson’s ratio is as follows:

$$\boldsymbol{\nu} = \frac{\left[\frac{\mathbf{1}}{\mathbf{2}} \times \left(\frac{\boldsymbol{Vp}}{\boldsymbol{Vs}}\right)^{\mathbf{2}} - \mathbf{1}\right]}{\left[\left(\frac{\boldsymbol{Vp}}{\boldsymbol{Vs}}\right)^{\mathbf{2}} - \mathbf{1}\right]} \qquad \boldsymbol{Equation}: \mathbf{3.31}$$

The Vp/Vs ratio of quartz is relatively less than to rest of the minerals. Thus Poisson´s ratio of sands is relatively less than the shales. Additionally, the gas-bearing sands comprise relatively less Poisson´s ratio than water-bearing sands. In the hydrocarbon zone, the Vp exhibits relatively much lower values, while Vs shows relatively higher values (Simm et al., 2014). Moreover, the velocity, when replaced with the bulk and shear moduli, results in the following relation:

$$\boldsymbol{\nu} = \frac{[\mathbf{2}\boldsymbol{K} - \mathbf{2}\,\mu]}{[\mathbf{2}(\mathbf{3}\boldsymbol{K} + \mu)]} \qquad \boldsymbol{Equation}: \mathbf{3.32}$$

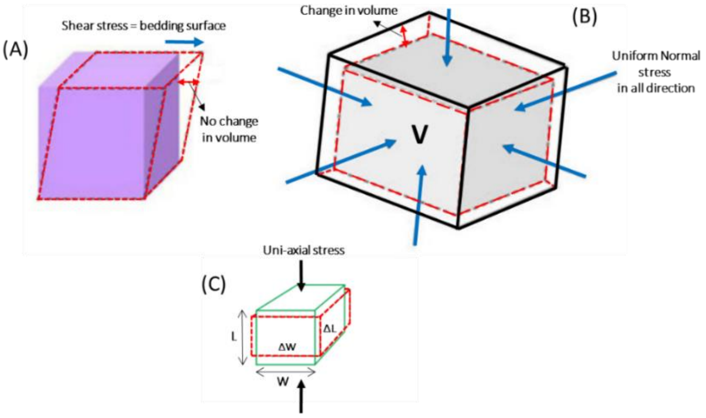

Figure 3. 7: The illustrations of (A): Shear modulus comprises shear stress in the direction of bedding surface with no volume change, (B): Bulk modulus comprises uniform stress in all directions with change in volume, and (C): Poisson´s ratio, which comprises the ratio of transverse strain to the longitudinal strain (modified after Simm et al., 2014).

While studying rock physics, a detailed explanation of the rock is achieved as the nature of scale changes (Figure. 3.8). The nature of rocks is considered as homogenous at the macroscopic scale, whereas considered heterogeneous at the microscopic scale. The medium considered as effective with respect to the rock physics approach comprises elastic property that is the average elastic property of all the individual constituents (Gelius & Johansen, 2010). Moreover, to measure the average of elastic properties, parameters of individual constituents, such as volume, elastic moduli, and framework arrangement (structural arrangement) details, are required. Furthermore, upper and lower bounds can be calculated in the absence of structural arrangement information because usually, it is not known. One thing to remember is that when the calculations of constituents plot over the bounds limit, it represents the errors in calculations (Mavko, 2005).

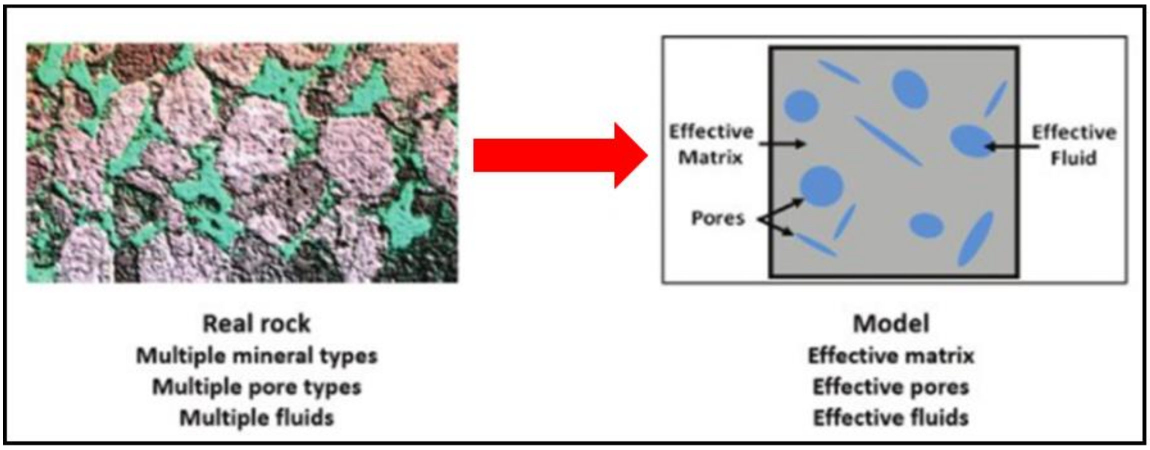

Figure 3. 8: Models of real rock (consisting of multiple mineral types, fluids, and complex structure) vs. general model (consists of effective grain, fluid, and simple texture) (modified after Babasafari et al., 2020).

The Density log is utilized for measuring effective density (ρ), which is the average taken for the entire density parameters:

$$\rho = \varphi \times \rho_{fluid} + (1 - \varphi)\, \rho_{grain} \qquad Equation: 3.33$$

Where
ρ = value of effective density,
φ = estimated value of porosity,
ρ_{fluid} = value of fluid density,
ρ_{grain} = value of grain density.

Whereas, in the presence of two fluids, the density of the fluid will be the combination of both fluid densities, which represents the following relation:

$$\rho_{fluid} = Sw \times \rho_{w} + (1 - S_w)\rho_{HC} \qquad Equation: 3.34$$

Where
ρ_{fluid} = value of two fluid densities,
S_w = value of water saturation,
ρ_w = value of brine density,
ρ_{HC} = value of hydrocarbon density.

3.4.2 Empirical models and Vs prediction

The Empirical models are developed after experiments and generate resultant trends. The generated trends comprise linear regression with real complexities. However, these generated trends were utilized in identifying and estimating several properties; for instance, the Greenberg & Castagna (1992) model generated equations for estimating P-wave and S-wave velocity.

In the rock physics diagnostics, several cross plot templates, such as LMR and Vp/VsRatio, require shear wave velocity (Vs) as a key element in generating the cross plots. Moreover, Gassmann´s fluid substitution process requires Vs as one of the main parameters. None of the available well comprises shear wave velocity; therefore, Vs estimated from HampsonRussell software by fluid substitution process. Moreover, it can also be generated by Vp, and other equations that are proposed for various lithologies and fluids (Dvorkin, 2008). Table 3.6 displays equations for estimating Vs from Vp. The equations for estimating Vp and Vs generated by Greenberg-Castagna, associated with various lithologies, are displayed in the Figure. 3.9 - Left.

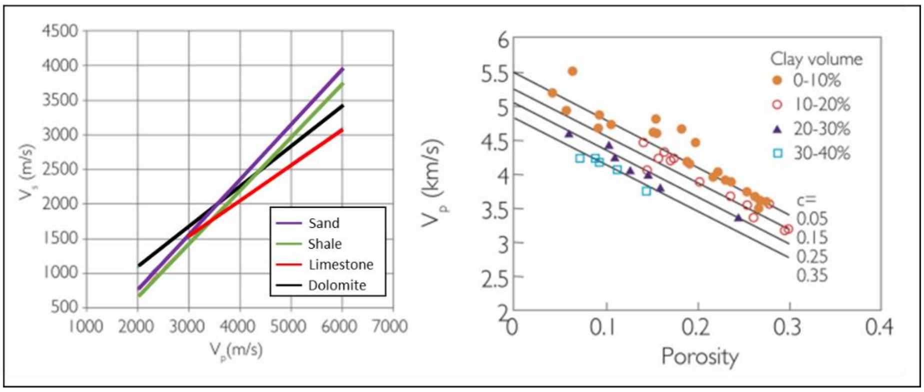

Figure 3. 9: (Left) Vp-Vs relation crossplot by Greenberg-Castagna. (Right) Crossplot of Vp vs Porosity relation generated by Hans, comprising constant clay lines along with different clay volumes (modified after Simm et al., 2014).

In the Table 3.4, mudrock relation is applicable only for slightly compacted and highly porous mudrocks. The Krief et al., (1990) relation proposed for gas sand, whereas rest of the relations estimated only for water saturated formations. According to Simm et al., (2014), the general Vp/Vs ratio value related to gas sand ranges between 1.4-1.8, and as an average, it is 1.6. The relations of Han et al., (1986) are proposed after lab tests applied to compacted brine saturated sandstones, which defines the medium's porosity, amount of clay, and P-wave velocity. Moreover, Han et al., (1986) generated the relations concerning amounts of pressures are explained in Table 3.7. In the cross plot of porosity versus Vp, the Han et al., (1986) equations are utilized to plot various amount of clay lines (Simm et al., 2014) (Figure 3.9 - Right).

Table 3. 4: Various Vp-Vs relations.

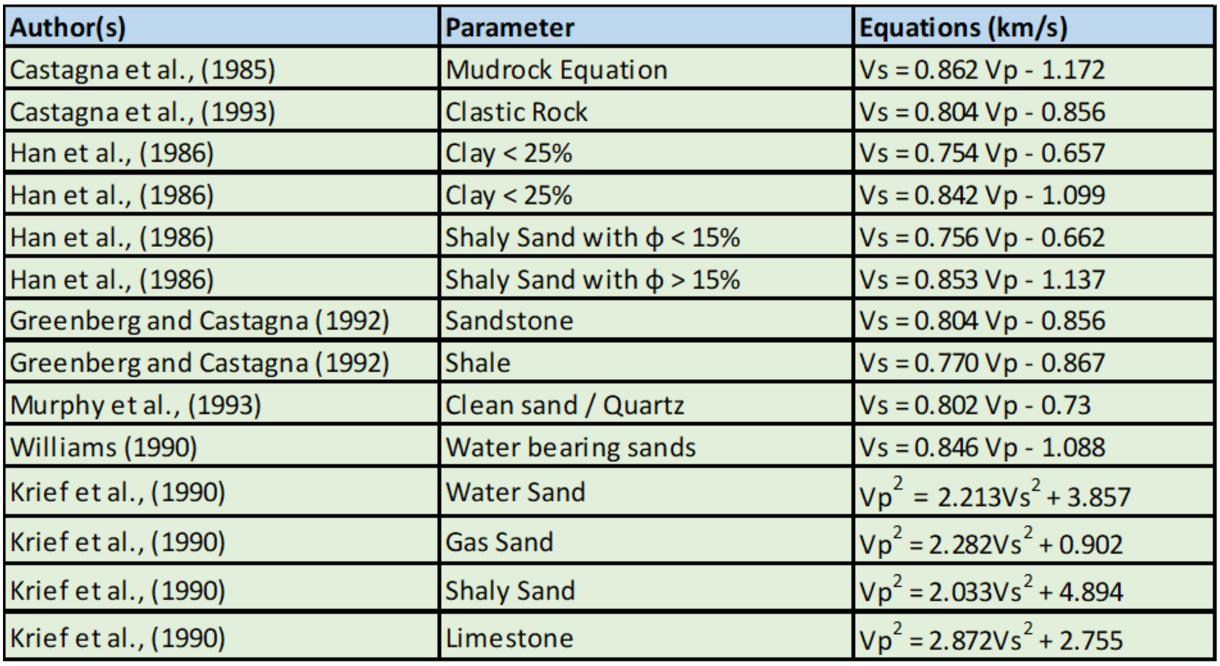

Author(s)	Parameter	Equations (km/s)
Castagna et al., (1985)	Mudrock Equation	Vs = 0.862 Vp - 1.172
Castagna et al., (1993)	Clastic Rock	Vs = 0.804 Vp - 0.856
Han et al., (1986)	Clay < 25%	Vs = 0.754 Vp - 0.657
Han et al., (1986)	Clay < 25%	Vs = 0.842 Vp - 1.099
Han et al., (1986)	Shaly Sand with $\phi < 15\%$	Vs = 0.756 Vp - 0.662
Han et al., (1986)	Shaly Sand with $\phi > 15\%$	Vs = 0.853 Vp - 1.137
Greenberg and Castagna (1992)	Sandstone	Vs = 0.804 Vp - 0.856
Greenberg and Castagna (1992)	Shale	Vs = 0.770 Vp - 0.867
Murphy et al., (1993)	Clean sand / Quartz	Vs = 0.802 Vp - 0.73
Williams (1990)	Water bearing sands	Vs = 0.846 Vp - 1.088
Krief et al., (1990)	Water Sand	$Vp^2 = 2.213Vs^2 + 3.857$
Krief et al., (1990)	Gas Sand	$Vp^2 = 2.282Vs^2 + 0.902$
Krief et al., (1990)	Shaly Sand	$Vp^2 = 2.033Vs^2 + 4.894$
Krief et al., (1990)	Limestone	$Vp^2 = 2.872Vs^2 + 2.755$

Table 3. 5: This table explains the Han et al., (1986) equations, in which Vp is P-wave velocity (km/s), Vs is S-wave velocity (km/s), φ is porosity (%) and C is the clay content (%).

Pressure	Equation (km/s)
40 MPa	$Vp = 5.59 - 6.93\phi - 2.18C$
30 MPa	$Vp = 5.55 - 6.96\phi - 2.18C$
20 MPa	$Vp = 5.49 - 6.94\phi - 2.17C$
10 MPa	$Vp = 5.39 - 7.08\phi - 2.13C$

3.4.3 Theoretical bounds

The limitations of physical properties are described utilizing theoretical bounds related to various kinds of rock and fluid mixtures, depending upon upper (Voigt) or lower (Reuss) bounds. The upper bound Voigt average explains that the strain is uniform from all over the sides, whereas the lower bound Reuss average explains that the stress is uniform from all over the sides (Mavko, 2005) (Figure 3.10). The suspension particles comprise more than 40% porosity, plotting adjacent to Reuss bound and the rest of the particles data plotting between the Voigt and Reuss bound trends (Figure 3.11).

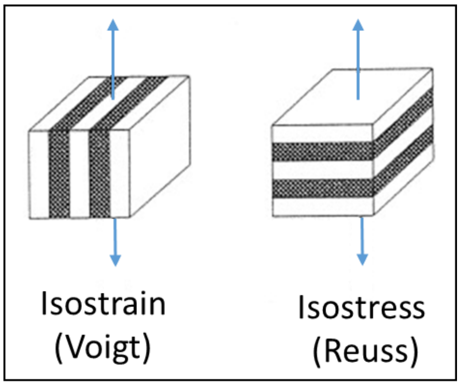

Figure 3. 10: (Left) Representation of Voigt Bound (Iso-strain) and (Right) Reuss Bound (Iso-stress) (modified after Verbeek & Focke, 2002).

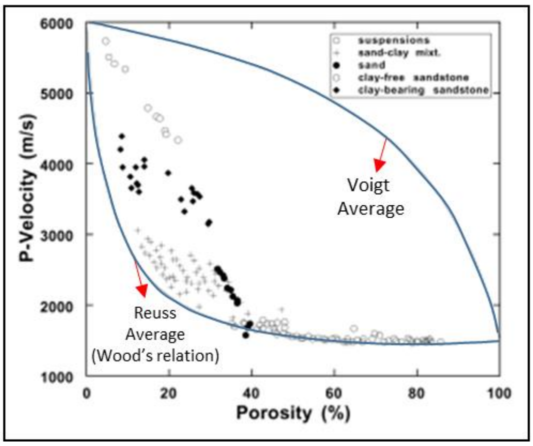

Figure 3. 11: Crossplot template of Porosity vs P-wave velocity along with Voigt and Reuss bounds (modified after Mavko, 2005).

Moreover, Hashin & Shtrikman, (1963) is a different bound. Relatively this bound is efficient and advanced than others. This method reflects a combination of two materials (Figure 3.12). The moduli relations related to Hashin & Shtrikman, (1963).

$$K^{HS\pm} = K_1 + \frac{f_2}{(K_2 K_1)^{-1} + f_1 \left(K_1 + \frac{4}{3}\mu_1\right)^{-1}} \qquad \boldsymbol{Equation: 3.35}$$

$$\mu^{HS\pm} = \mu_1 + \frac{f_2}{(\mu_2 \mu_1)^{-1} + \frac{2 f_1 (K_1 + 2\mu_1)}{5\mu_1 (K_1 + \frac{4}{3}\mu_1)}} \qquad \boldsymbol{Equation: 3.36}$$

Where
K = value of bulk modulus,
μ = value of shear modulus,
f_1 = phase 1 related volume fraction,
f_2 = phase 2 related volume fraction.

The equation explains that when the stiffest material value is 1, whereas the softest value is 2, thus it determines as upper bound. While considering the softest material value as 1 and stiffest material value as 2, thus it defines as the lower bound (Simm et al., 2014).

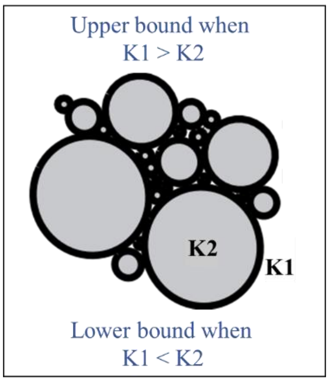

Figure 3. 12: The bulk modulus of two-phase material illustrated by Hashin-Shtrikman (modified after SubSurfWiki, 2021).

To estimate the effective modulus of fluids and rock combinations, the bounds are utilized that are further applied as the input properties in the Gassmann´s equation (Simm et al., 2014). The lower bound of Hashin-Shtrikman and Reuss bound are similar in the presence of water-bearing quartz medium due to the insensitivity of shear modulus in the brine system (Simm et al., 2014). Figure 3.13 exhibits several bounds related to quartz and clay.

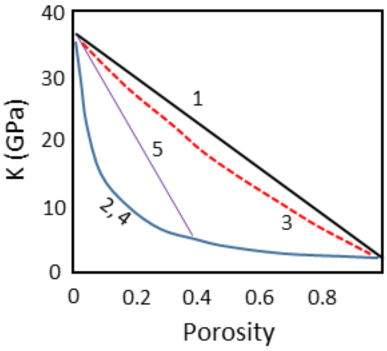

Figure 3. 13: The crossplot template of Bulk Modulus and Porosity shows trend lines of 1: Voigt Average, 2: Reuss Average, 3: Upper Hashin-Shtrikman Line, 4: Lower Hashin-Shtrikman Line, and 5: a modified form of Voigt Bound Line for quartz and clay bounds (brine saturated sandstone) (modified after Simm et al., 2014).

3.4.4 Contact models

The contact models generated depending upon mathematical equations associated with sandstones grain contacts, as they are applicable to sandstones. The bounds generated by Hashin & Shtrikman, (1963) explain low and high porosity end members of the dry rock (no fluid saturation). The influence of effective pressure and cement generated on the porous sediments that result in increased rigidity of the rock is explained through this model. Moreover, the model can exhibit the presence of cement and porosity levels in the sand (compacted or porous sand) (Simm et al., 2014). Generally, two contact models are utilized, contact cement sand and friable sand models developed by Dvorkin & Nur, (1996). The non-cemented sand model or friable sand model explains a relation between porosity and velocity associated with a decrease in grains sorting, related to a certain effective pressure. Moreover, the model describes the decrease in sorting results in filling the pore spaces by small size grains (Avseth et al., 2010). The model measures elastic moduli from Hertz-Mindlin Theory (Equations 3.37-3.38), for the high porosity dry rock end members at the point of critical porosity (Mindlin, 1949).

$$K_{HM} = \left(\frac{n^2\,(1-\emptyset_c)^2\mu^2}{18\pi^2\,(1-v)^2}\,P\right)^{\frac{1}{3}} \qquad \boldsymbol{Equation: 3.37}$$

$$\mu_{HM} = \frac{5-4v}{5(2-v)}\left(\frac{3n^2\,(1-\emptyset_c)^2\mu^2}{18\pi^2\,(1-v)^2}\,P\right)^{\frac{1}{3}} \qquad \boldsymbol{Equation: 3.38}$$

Where
φ_c = value of critical porosity,
K = value of bulk modulus,
μ = value of shear modulus,
v = value of the Poisson´s ratio related to solid phase,
P = value of effective pressure,
n = value of coordinate number.

According to Avseth et al., (2010), the cement layer comprising contact radius is exhibited by coordinate number (n), which is empirically associated with the porosity. The relation is as follows:

$$n = 20 - 34\varphi + 14\varphi^2 \qquad \textbf{Equation: 3.39}$$

Where
n = value of coordination number,
φ = value of estimated porosity.

Applying the Hashin-Shtrikman lower bound for estimating moduli with respect to the end members, the relation is as follows:

$$K_{dry} = \left(\frac{\frac{\varphi}{\varphi_c}}{K_{HM} + \frac{4\mu_{HM}}{3}} + \frac{1 - \frac{\varphi}{\varphi_c}}{K + \frac{4\mu_{HM}}{3}} \right)^{-1} - \frac{4}{3}\mu_{HM} \qquad \textbf{Equation: 3.40}$$

$$\mu_{dry} = \left(\frac{\frac{\varphi}{\varphi_c}}{\mu_{HM} + z} + \frac{1 - \frac{\varphi}{\varphi_c}}{\mu + z} \right)^{-1} - z \qquad \textbf{Equation: 3.41}$$

$$z = \frac{\mu_{HM}}{6} \left(\frac{9K_{HM} + 8\mu_{HM}}{K_{HM} + 2\mu_{HM}} \right) \qquad \textbf{Equation: 3.42}$$

Where
K_{dry} = value of the dry rock bulk modulus for friable sand mix,
μ_{dry} = value of the dry rock shear modulus for friable sand mix,
φ = estimated value of porosity,
φ_c = value of critical porosity,
K_{HM} = value of bulk modulus related to mineral,
μ_{HM} = value of shear modulus related to mineral.

The porosity reduction is illustrated in the contact cement model. As the sand grains during deposition allow cementation process on the grains surface in a uniform manner (Simm et al., 2014). Moreover, the rock displays an increase in the stiffness due to the presence of s an increase in the stiffness due to the minimal percentage of cement deposited in the space between grains contacts (Avseth et al., 2010). The equation related to the contact cement model is explained by Dvorkin et al., (1994).

Moreover, a blend of two models developed the constant cement model. In this model trend of porosity reduction is associated with the grains sorting, and whereas, sorting trend comprises uniform cement value. The contact and constant cement models display the same mathematical relations, however the contact cement model is associated with lower bound (Avseth et al., 2010) In the Figure 3.14, the mentioned three models are displaying with porosity and elastic modulus cross plot template.

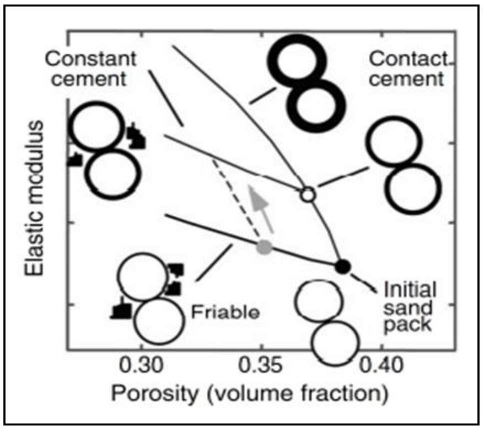

Figure 3. 14: The constant cement model displaying Contact Cement and Friable trend lines for high porous sands on Elastic modulus vs Porosity crossplot (modified after Avseth et al., 2010).

3.4.5 Gassmann Equation

The Gassmann's equation is utilized in order to estimate the bulk moduli and analyze fluid substitution Modelling related to a fluid-saturated rock based on porosity, dry rock frame, fluid, and mineral. The equations are as follows (Gassmann, 1951):

$$\frac{K_{sat}}{K_0 - K_{sat}} = \frac{K_d}{K_0 - K_d} - \frac{K_{fl}}{\varphi(K_0 - K_{fl})} \qquad \boldsymbol{Equation: 3.43}$$

$$\mu_{sat} = \mu_d \qquad \boldsymbol{Equation: 3.44}$$

Where
K_{sat} = value of bulk modulus for fluid saturated rock,
K_0 = value of bulk modulus for matrix,
K_d = value of bulk modulus for dry rock frame,
K_{fl} = pore fluid bulk modulus value,
φ = estimated porosity value,
μ_{sat} = value of shear modulus for fluid saturated rock,
μ_d = value of shear modulus for dry rock frame.

The entire rock is considered a dry rock frame but excludes fluids in the pores. Whereas applying the Gassmann equation with considering pore space filled with fluid. When the pores are filled with liquids, then the shear modulus becomes insensitive to it.

In Figure 3.15 exhibit the several inputs for the Gassmann equation. Table 3.8 displays general input values related to the Gassmann equation with respect to quartz and clay. Clay has various chemical compositions and related properties; therefore, it is challenging to assign a precise value for it (Avseth et al., 2010).

There are several uncertainties for Gassmann's model that can be particularly applied for a medium to higher porosity, clean sandstone comprising low seismic waves frequency (Simm et al., 2014). Whereas this model is applicable for any kind of pore shape (Mavko, 2005). The well log data represents frequencies ranging from lower to higher, perhaps basically lower frequency (Biot, 1956). Therefore, normally Gassmann's equation is utilized on the well log related frequencies. Furthermore, this model has limitations regarding rocks comprising two kinds of porosities (primary and secondary) and also in the presence of tight sand or shales because it might overestimate the effect of fluid substitution (Simm et al., 2014).

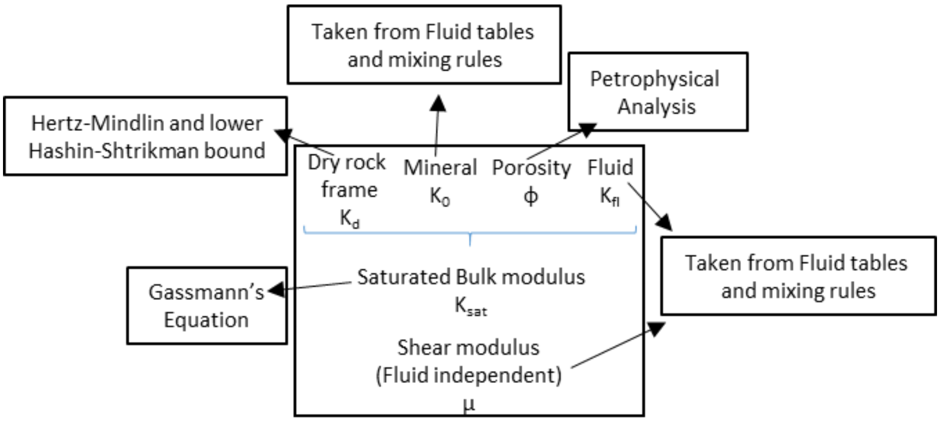

Figure 3. 15: Details of the Gassmann´s equation parameters (Simm et al., 2014).

Table 3. 6: The general clay and quartz values are as follows. Modified after Simm et al., (2014).

Mineral	**Density (g/cm^3)**	**Poisson's Ratio**	**Vp (km/s)**	**Vs (km/s)**	**K (GPa)**	**μ (GPa)**
Clay	2.680	0.324	4.900	2.500	41	17
Quartz	2.650	0.064	6.038	4.121	36.6	45

Moreover, the Reuss (or Wood´s) law represents a relation for bulk modulus related to two-fluid mix, which is as follows:

$$\frac{1}{K_{fl}} = \frac{S_w}{K_w} + \frac{1 - S_w}{K_h} \qquad \boldsymbol{Equation: 3.45}$$

Where
K_{fl} = value of bulk modulus for fluid mixture,
K_w = value of bulk modulus for water,
K_h = value of bulk modulus for hydrocarbon,
S_w = value of water saturation.

When there is a replacement of fluid against a different type of fluid within the fluid-saturated medium, thus, in order to calculate the effective bulk modulus of the medium, the following relation can be utilized (Gelius & Johansen, 2010):

$$\frac{K_1}{K_s - K_1} - \frac{K_{f1}}{\varphi(K_s - K_{f1})} = \frac{K_2}{K_s - K_2} - \frac{K_{f2}}{\varphi(K_s - K_{f2})} \qquad \boldsymbol{Equation: 3.46}$$

Where
K_1 = value of effective bulk modulus for medium - fluid type 1,

K_2 = value of effective bulk modulus for medium - fluid type 2,
K_s = value of bulk modulus related to rock frame/solid component,
K_{f1} = value of fluid 1 bulk modulus,
K_{f2} = value of fluid 2 bulk modulus.
φ = porosity

Therefore, a new bulk density relation related to the fluid-saturated rock is as follows (Simm et al., 2014):

$$\rho_{b2} = \rho_{b1} - [(\varphi\rho_{fl1})] - [(\varphi\rho_{fl2})] \qquad \boldsymbol{Equation}: \mathbf{3.47}$$

Where
ρ_{fl1} = value of fluid type-1 density,
ρ_{fl2} = value of fluid type-2 density,
ρ_{b1} = value of bulk density for medium comprising fluid type-1,
ρ_{b2} = value of bulk density for medium comprising fluid type-2.

3.4.6 Formation of Rock Physics Templates (RPTs)

For defining reservoir characteristics (lithology and fluid type), the rock physics templates (RPTs) approach was presented by Ødegaard & Avseth, (2003). The RPTs crossplots are utilized to get in-sight knowledge related to the effects of fluid presence, cement volume, varying porosity, etc. While focusing on a particular area to produce RPT cross plots, several geological parameters (for example mineralogical composition, depth of burial, and lithology) must be known (Avseth, 2015). The procedure to produce a rock physics template is explained in the Figure 3.16.

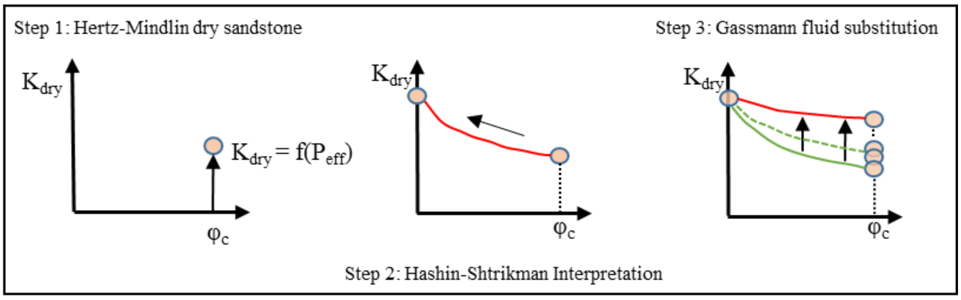

Figure 3. 16: The three steps explained for the development of Rock Physics Template (RPT) (modified after Avseth et al., 2009).

Step 1: Utilizing the Hertz-Mindlin theory, the dry rock frame modulus is calculated with respect to a specific pressure level and particular porosity.

Step 2: The dry rock modulus is then calculated while considering the porosity range between critical to zero porosity. The usage of Hashin-Shtrikman lower bound is recommended when the sorting and compaction influence the decrease in porosity. Whereas, in the presence of cemented rocks, the Hashin-Shtrikman upper bound can be used.

Step 3: To estimate the bulk modulus for a fluid-saturated rock, Gassmann´s equation is then utilized to fill pores with fluids. This is done with a fluid substitution process in the presence of several fluid saturations. Therefore, at this stage, the bulk and shear moduli of the rock are measured with several fluid saturations and porosities.

3.4.6.1 AI versus Vp/Vs

The cross plot of Acoustic Impedance (AI) versus P- and S-wave velocity ratio (Vp/Vs) is utilized for the analysis regarding porosity, fluid saturation, and lithology when the hydrocarbons exist. To differentiate the fluids, normally Vp/Vs ratio is recommended, as the low ratio values reflect hydrocarbon-bearing rock. Considering an unconsolidated homogeneous rock in which hydrocarbon-bearing sandstone can be feasibly discriminated against brine-saturated sandstone. The fluid sensitivity experiences changes in the presence of shale and cement. When the cement volume is increased, it plots the brine-bearing sandstone data on the lower Vp/Vs ratio values. This makes it challenging to distinguish brine-filled sandstone with respect to hydrocarbon-bearing sandstone. Whereas the values of Vp/Vs ratios increase in shale's existence (Avseth, 2015). Figure 3.17 illustrates AI versus Vp/Vs crossplot.

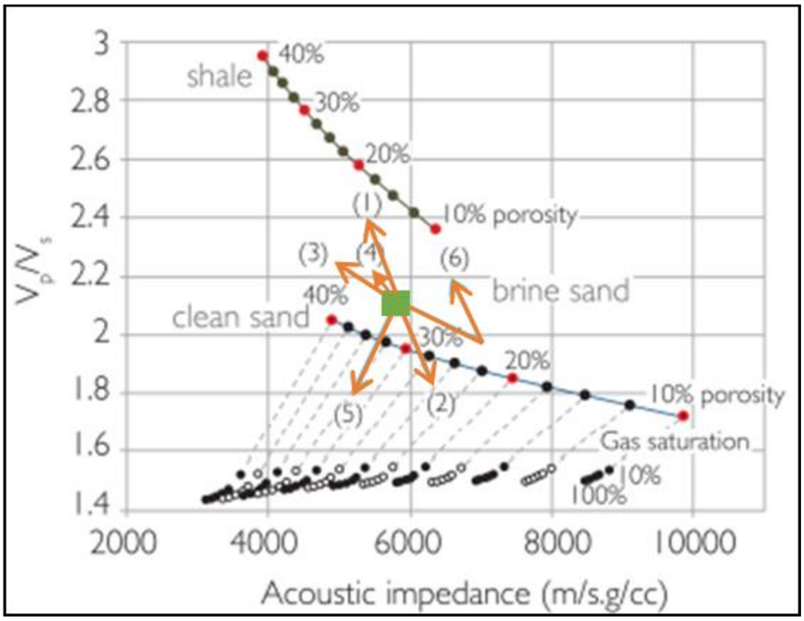

Figure 3. 17: The general template of Vp/Vs versus AI crossplot, which shows different trends, for instance, 1: Shale content increasing, 2: Volume of Cement increasing, 3: Percentage of Porosity increasing, (4) Effective pressure decreasing, 5: Saturation of Hydrocarbon increasing and 6: Disperse content of shale increasing (modified after Simm et al., 2014).

3.4.6.2 LMR

The crossplot of Lambda-Rho versus Mu-Rho identifies and discriminates fluid and lithology. Moreover, this cross plot exhibits incompressibility and rigidity properties. In the presence of gas saturation, the incompressibility of sandstone decreases because the gas can be compressed feasibly relative to other fluids and rocks. Furthermore, the rigidity is insensitive towards gas saturation. The shales comprise relatively low rigidity, as they have a laminated depositional structure (fissile) and can simply move above each other. Whereas the carbonates are hard, comprise high rigidity and incompressibility. The sponge is easily compressible, and uncompacted sand behaves similar to a sponge. Therefore, uncompacted sands can be easily compressed, as they comprise lower incompressibility (Gelius & Johansen, 2010). A model is developed as the above-mentioned properties exhibit variation. Therefore, Goodway et al., (1997) proposed this model comprising threshold cutoff for porous gas sand and clastic carbonates, at 20 and 100 Lambda-Rho values, respectively (Figure 3.18).

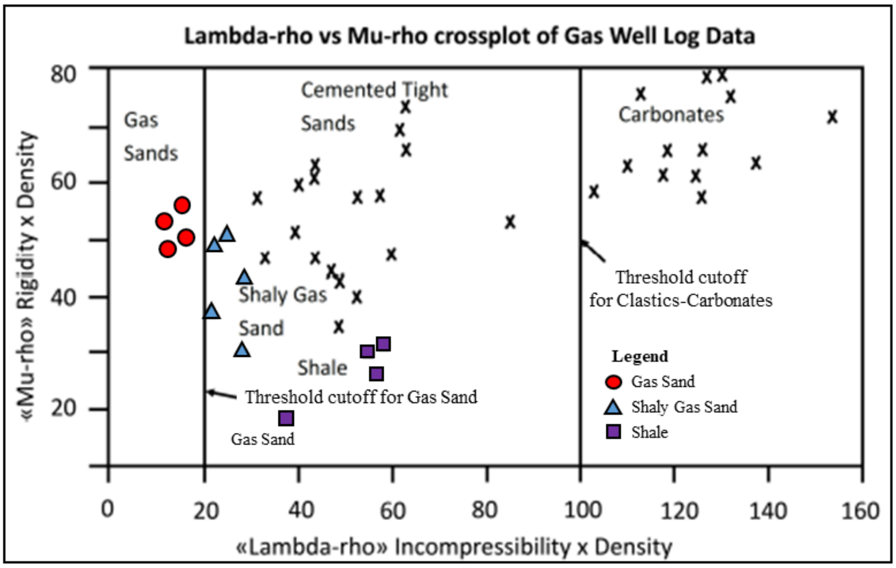

Figure 3. 18: Generalized crossplot template of Lambda-rho versus Mu-rho, comprising threshold cutoff for gas sand and clastic carbonate (modified after Goodway et al., 1997).

3.4.6.3 Porosity versus Vp

Rock velocity and rigidity are controlled by the rock material and pore shape, such as volume and kind of shale and cement available and the number of grain contacts present in the rock frame. The soft rocks comprise lower values of acoustic impedance that means having low velocity and density. In contrast, the hard rocks comprise higher acoustic impedance values that show it has high velocity and density values (Simm et al., 2014). As we have seen in the previous subchapters, a sandstone is plotting along a lower bound such as Reuss and Hashin-Shtrikman lower bound, when the decrease in porosity is linked with sorting. Whereas, it is plotting with Hashin-Shtrikman upper bound shows that it is associated with cementation (diagenesis). It is illustrated in Figure 3.19.

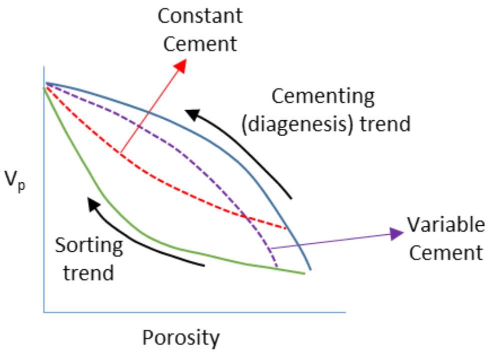

Figure 3. 19: General Porosity vs Vp crossplot template displaying trends of cementation and sorting for a clean sandstone (modified after Simm et al., 2014).

In defining the acoustic properties with respect to sandstone, the most effective parameter is the amount of shale. The two general sand and shale conditions can be a combination of sand and shale with grain or matrix framework and intercalations of sand and shale. The presence of clay is seen as either structural or filling pore spaces or even existing in both conditions (Simm et al., 2014).

The impacts generated from a combination of clay and sand are illustrated in Figure 3.20, an experiment by Marion et al., (1992). A minor quantity of clay filling the pore spaces demonstrates a rise in acoustic impedance is experienced until the pores are fully filled. When sand porosity becomes lower than the amount of clay, thus sand grains are disconnected, and the entire rock changes from being grain-supported framework to clay-supported. This transition basically exhibits the rock being shaly sand and progressing towards sandy shale (Avseth, 2015). Moreover, the addition of more clay in the rock even after filling the entire pore space. This leads the rock to become softer, which decreases the acoustic impedance property of the rock. As a result, an opposite V trend is seen in the cross plot (Simm et al., 2014).

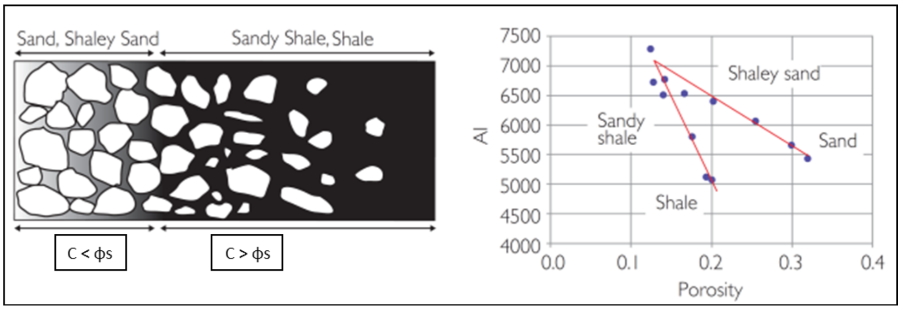

Figure 3. 20: Displaying rock framework with the transition of sand, shaly sand to sandy shale and shale. The parameter φs displays the porosity of Sand, and C is the amount of Clay. (Right) The Porosity vs. AI crossplot displays dispersed shale impact with respect to sandstone (modified after Marion et al., 1992; Simm et al., 2014).

In the places, exhibiting the amount of clay is similar with respect to sand's porosity, displaying lowest porosity and highest velocity values (Avseth, 2015). In the crossplots, a straight line trend is seen with sand and clay framework. Moreover, the rock becomes softer in the presence of clay framework, which drops acoustic impedance values (Simm et al., 2014).

3.5 AVO Modelling

In order to minimize the exploration risk, enhance reservoir characterization, and verify hydrocarbons, AVO (amplitude variation with offset) is one of the dominant tools. This method illustrates rock properties in terms of seismic amplitudes and pore fluids by reviewing variations in the amplitude occurring with the offset increase in a pre-stack seismic data at an interface (acoustic impedance boundary) in the subsurface (Avseth, 2015).

Moreover, the Amplitude versus offset (AVO) or angle (AVA) is associated with the dissimilarity in the velocities of P-wave and S-wave at the impedance boundary. Verifying the presence of hydrocarbons is the foremost objective. This hydrocarbon presence is then substantiated from the variations in amplitude resulting from the fluid transition from water to hydrocarbon; therefore, it is one of the direct hydrocarbon indicators (DHI). The amplitude changes with the offset mainly because of dissimilarities in the Poisson's ratio (Simm et al., 2014). Furthermore, this tool has some limitations; for instance, inaccurate anomalies can be seen because of the tuning effect, overburden, and lithology (Avseth, 2015). In the case of poorly compacted and young lithologies or beds, this tool works effectively.

3.5.1 Generation of Synthetic Seismogram

A seismic trace is generated from the convolution process of a seismic pulse and reflectivity coefficients related to the variations occurring in the rock properties at the bed interface in the subsurface. The acoustic impedance (AI) exhibits the rock properties as a product of bulk density (ρ) and velocity (Vp).

The formula of reflectivity is as follows:

$$\mathbf{R\ (0)} = \frac{\boldsymbol{AI_2 - AI_1}}{\boldsymbol{AI_2 + AI_1}} = \frac{\boldsymbol{V_{\rho 2}\rho_2 - V_{\rho 1}\rho_1}}{\boldsymbol{V_{\rho 2}\rho_2 + V_{\rho 1}\rho_2}} \qquad \textit{\textbf{Equation}}\textbf{: 3.49}$$

Where;
R (0) = reflectivity at zero offset,
AI_1 = acoustic impedance above the boundary where the incident wave hits,
AI_2 = acoustic impedance below the boundary where the wave is transmitted,
V_{p1} = P-wave velocity in the layer 1,
V_{p2} = P-wave velocity in the layer 2,
ρ_1 = density in the layer 1,
ρ_2 = density in the layer 2

The well data is used to extract AVO responses, which are then utilized for the synthetic seismic creation (Figure 3.21). The reflectivity series and form of the seismic pulse are the information required for the synthetic generation. The sonic (P-wave) log and density log are utilized to determine the reflectivity series. These logs are first multiplied and then convolved to produce the acoustic impedance log (AI = Vp×ρ), which helps generate reflectivity series by applying Eq. 3.49. Synthetic seismic is then generated by the convolution of the reflectivity series with the Ricker wavelet (chosen for this thesis).

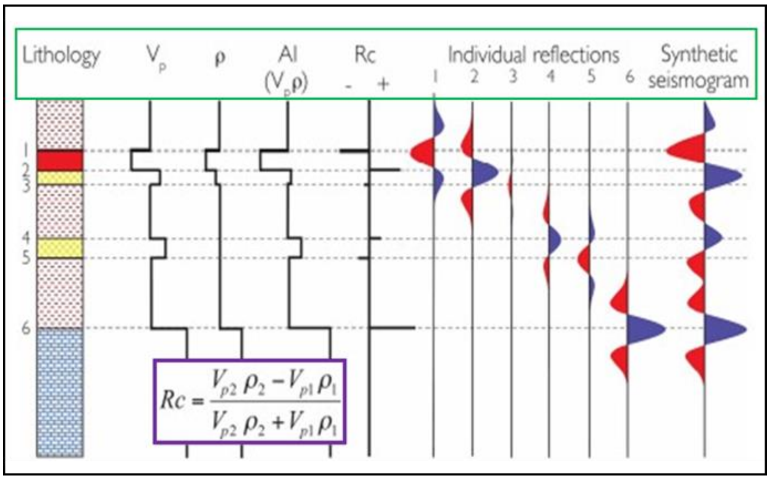

Figure 3. 21: Process explaining the generation of synthetic seismic, starting from well log data (Sonic and Density logs) that are multiplied and generates AI series, which helps in creating reflectivity series (RC), then it leads to convolution step between reflectivity series and input symmetrical zero-phase wavelet, which is of positive polarity (Simm et al., 2014).

According to (Mondol, 2015), a wavelet is considered a mathematical function that spreads an input function into several frequency constituents in a corresponding scale. Moreover, in general, a recorded seismic pulse comprises three primary amplitudes. The shape of the wave changes according to the source type and geology etc. If the wavelet is recording and no variation is seen in its shape and time, that means it is at zero time, which displays as a causal wavelet (Figure 3.22).

The drawback in the utilization of causal wavelets is the time lag among the reflector boundary and the reflection energy at an interface. Moreover, it becomes complex while correlating seismic with geology. Further steps include processing the seismic wavelet, converting its shape into a solid symmetrical shape (Figure 3.22). During processing, the energy is repositioned at the boundary eliminating the time lag effect. Thus, it creates a processed seismic wavelet, which contributes to interpreting the data because the correlation between processed wavelet and geology becomes more accurate (Simm et al., 2014).

Furthermore, the selection of polarity convention is required; conventionally, t two polarity conventions are shown for the processed wavelet. For this study, standard positive polarity is utilized as referred by (Sheriff & Geldart, 1995), in which troughs are represented by negative reflection coefficient and peaks by positive reflection coefficient. Both of the processed and causal wavelets are demonstrated in Figure 3.22.

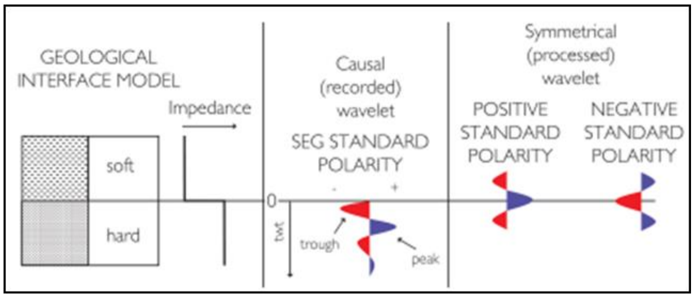

Figure 3. 22: The Geological model with its Impedance response and representation of both the Causal and symmetrical wavelets along with polarity standards (modified after Simm et al., 2014).

A statistical wavelet is obtained from the actual seismic data for the generation of synthetic seismic, whereas, if this information is missing, the ideal symmetric wavelet is utilized. There are various standard wavelets, but in this study, the Ricker wavelet is used. The Ricker wavelet comprises two side lobes and a single central frequency. According to Hosken, (1988), it is not recommended to use Ricker wavelet because of the variation in the peaked amplitude spectrum of the wavelet compared to the flat-topped amplitude spectrum of the actual seismic data. Despite this fact, the Ricker wavelet is being utilized because of its simplicity while lack of seismic data to accomplish well to seismic tie.

Synthetic seismic generation requires upscaling of the well logs, in which the well logs values are averaged and transformed into sample intervals for adjustment of seismic frequency. The upscaling process is further discussed in chapter 6. In the case of zero offsets, when the synthetic data is generated, it is necessary to know that if the seismic wavelet is larger than reflector intervals, the wavelet of the reflectors will combine. Another term, Tuning, defined as the interaction of amplitudes with each other (resulting in constructive or destructive amplitudes) because of the closed spacing between reflections (SEG Wiki, 2021). The tuning thickness is described as the vertical resolution (Equation: 3.50) that depends on the wavelength and P-wave velocity.

$$\boldsymbol{Tuning\ thickness = \frac{\lambda}{4}} \qquad \boldsymbol{Equation: 3.50}$$

$$\boldsymbol{\lambda = \frac{V_{\mathrm{p}}}{F_d}} \qquad \boldsymbol{Equation: 3.51}$$

$$\boldsymbol{F_d = \frac{1}{T}} \qquad \boldsymbol{Equation: 3.52}$$

Where;
λ = Wavelength (m),
F_d = Dominant Frequency (Hz),
V_p = P-wave Velocity (m/s),
T = Period (one complete cycle of the wave - peak to trough).

In Figure 3.23, the interference mechanism is described by a three-layered model, showing the impedance contrasts. Consider a three-layered model, in which a permeable sand layer (layer 2) is present in-between impermeable shales (layer 1 and 3). Moreover, a difference in polarity of the reflection coefficient exists on the top and base of this permeable sand layer. In Figure

3.23, a 30 Hz of zero offset Ricker wavelet is applied Figure 3.23 displays the complexity of differentiating the reflectors in terms of their top and base. If the wedge thickness is about 40 meters, it is considered a noticeable separation interval between the top and base of the reflector, whereas the amplitudes remain unchanged. Furthermore, in a case where the sand thickness is less than 40 meters, amplitudes of peak and trough overlap constructively resulting in an overestimation. The tuning curve displays the relationship between amplitude and sand thickness. In Figure 3.23, the tuning thickness is at 17 meters, where the amplitude is maximum; therefore, the separation of the top and base of the reflector here begins to be inseparable from each other. Conversely, the amplitudes start reducing when the tuning thickness is less than 17 meters (thin sand layer); therefore, destructive interference occurs (SEG Wiki, 2021).

Consider another case, when there is the same polarity of top and base layer; for instance, in an angular unconformity, reflection is being displayed as one peak or trough with constructive interference at the tuning thickness, whereas amplitude starts growing beneath the tuning thickness (Simm et al., 2014).

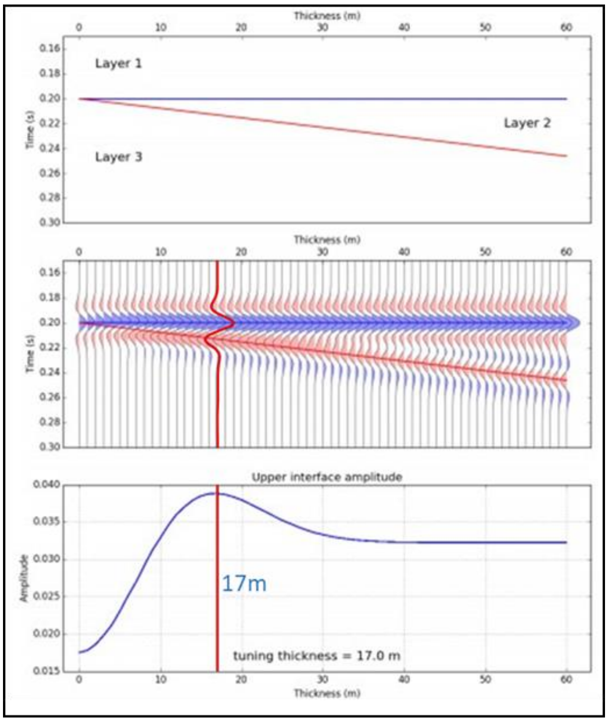

Figure 3. 23: Three-layered model exhibiting vertical seismic resolution limit and tuning thickness being at 17m (red curve and line), along with the constructive and destructive interference (modified after SEG Wiki, 2021a).

3.5.2 Angle dependent reflection coefficient

In this section, the introduction of S-wave and incident angles is being discussed, and it majorly emphasizes real seismic to have a knowledge of the synthetic seismic principle. When seismic waves are generated from a source, waves penetrate the subsurface and strike an interface. The waves split into reflection and refraction components due to acoustic impedance contrast (Figure 3.24).

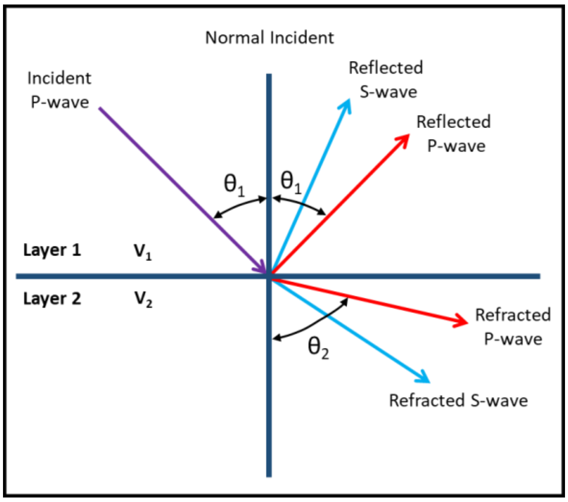

Figure 3. 24: One incident P-wave splitting at the boundary into two Reflected and two Refracted P and S-waves (modified after Mondol, 2015).

In total, four waves are produced at the acoustic impedance boundary, comprising two reflected P-wave and S-wave, and two refracted P-wave and S-wave. Therefore, according to Snell's law:

$$\boldsymbol{\frac{Sin\ \theta_1}{V_1} = \frac{Sin\ \theta_2}{V_2}} \qquad \textit{Equation}\textbf{: 3.53}$$

Where;
V_1 = velocity of medium 1
V_2 = velocity of medium 2
θ_1 = angle of incident ray
θ_2 = angle of refracted ray

Snell's law describes the change in wavefront when a wave travels in a different medium with different velocities. Moreover, S-wave does not travel through liquids in case of a fluid-solid interface, for instance, seafloor. In equation 3.49, the formula for calculating the reflection coefficient for a rock boundary at zero offsets. The Zoeppritz, (1919) equation expresses the P-wave reflection coefficient for any incident ray with an angle (θ). Several estimations were applied to the Zoeppritz equation in order to make it intuitive. Aki & Richards, (1980) generated an estimation with three terms. Furthermore, Wiggins et al., (1983) redesigned the equation. The equation is as follows:

$$\boldsymbol{R\ (\theta) = A + B\ sin^2\ \theta + C\ sin^2\ \theta\ tan^2\ \theta} \qquad \textit{Equation}\textbf{: 3.54}$$

Where;

$$\boldsymbol{A = \frac{1}{2}\left(\frac{\Delta V_{\mathrm{p}}}{V_{\mathrm{p}}} + \frac{\Delta \rho}{\rho}\right) \qquad B = \frac{\Delta V_{\mathrm{p}}}{2V_{\mathrm{p}}} - 4\left(\frac{V_{\mathrm{s}}}{V_{\mathrm{p}}}\right)^2 \left(\frac{\Delta V_{\mathrm{s}}}{V_{\mathrm{s}}}\right) - 2\left(\frac{V_{\mathrm{s}}}{V_{\mathrm{p}}}\right)^2 \left(\frac{\Delta \rho}{\rho}\right) \qquad C = \frac{1}{2}\,\frac{\Delta V_{\mathrm{p}}{}^2}{V_{\mathrm{p}}}}$$

Whereas,

$$\boldsymbol{V}_{\mathrm{p}} = \frac{\boldsymbol{V}_{\mathrm{p1}} + \boldsymbol{V}_{\mathrm{p2}}}{\mathbf{2}} \qquad \boldsymbol{V}_{\mathrm{s}} = \frac{\boldsymbol{V}_{\mathrm{s1}} + \boldsymbol{V}_{\mathrm{s2}}}{\mathbf{2}} \qquad \boldsymbol{\rho} = \frac{\boldsymbol{\rho}_1 + \boldsymbol{\rho}_2}{\mathbf{2}} \qquad \left(\frac{\boldsymbol{V}_{\mathrm{s}}}{\boldsymbol{V}_{\mathrm{p}}}\right)^{\mathbf{2}} = \frac{\left(\frac{\boldsymbol{V}_{\mathrm{s1}}}{\boldsymbol{V}_{\mathrm{p1}}}\right)^{\mathbf{2}} + \left(\frac{\boldsymbol{V}_{\mathrm{s2}}}{\boldsymbol{V}_{\mathrm{p2}}}\right)^{\mathbf{2}}}{\mathbf{2}}$$

And

$$\Delta\boldsymbol{V}_{\mathrm{p}} = \boldsymbol{V}_{\mathrm{p2}} - \boldsymbol{V}_{\mathrm{p1}} \qquad \Delta\boldsymbol{V}_{\mathrm{s}} = \boldsymbol{V}_{\mathrm{s2}} - \boldsymbol{V}_{\mathrm{s1}} \qquad \Delta\boldsymbol{\rho} = \boldsymbol{\rho}_2 - \boldsymbol{\rho}_1$$

The explaination of the parameters A, B and C are as follows:

A= zero angle reflection coefficient (AVO intercept).
B= shear velocity effect on the angle of incidence (AVO gradient).
C= amplitude response curve adjacent to the critical angle.

In order to provide the simple linear regression Shuey (1985) equation, the third term can be ignored, and it has validation to a range of angles, mostly limited to the incidence angle of 30° (Simm et al., 2014). Therefore, Equation 3.54 becomes as following:

$$R\,(\theta) = A + B \sin^2 \theta \qquad \textit{Equation}\textbf{: 3.55}$$

3.5.3 AVO Classification of Reservoir Sands

The amplitude interpretations have a number of models generated, but the AVO plots of a single interface are utilized in this research. The Zoeppritz equation algorithm contains ρ, Vp, and Vs as the input values in the Hampson Russell software, representing the impedance boundary between upper and lower layers that generates a graph with the parameters of incidence angle and the amplitude (reflection coefficient).

The slope ‘B’ is the AVO gradient in the I-G crossplot. If a constant positive amplitude and negative amplitude with offset are seen, it is positive AVO gradient and negative AVO gradient, respectively. Negative gradients linked to S-wave positive velocity difference that explains, S-wave is low in the upper layer, whereas positive gradients linked to S-wave negative velocity difference that describes, S-wave is high in the upper layer (Simm et al., 2014). Figure 3.25 shows, the AVO response is allocated into four classes that displays a shale boundary to gas sand.

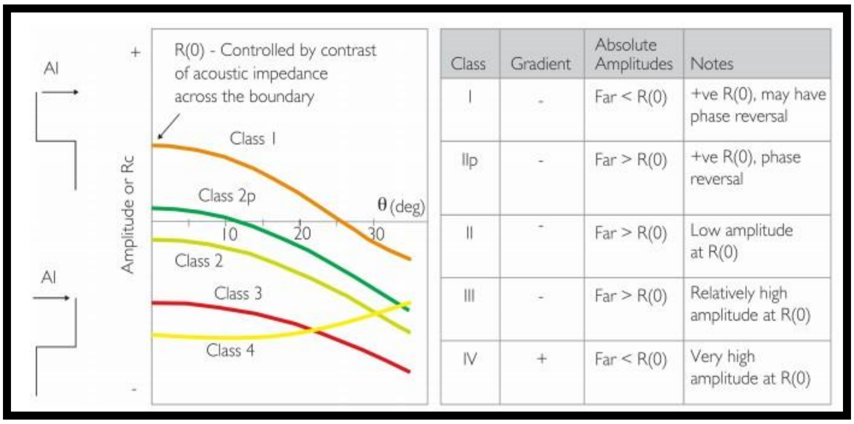

Class	Gradient	Absolute Amplitudes	Notes
I	-	Far < R(0)	+ve R(0), may have phase reversal
IIp	-	Far > R(0)	+ve R(0), phase reversal
II	-	Far > R(0)	Low amplitude at R(0)
III	-	Far > R(0)	Relatively high amplitude at R(0)
IV	+	Far < R(0)	Very high amplitude at R(0)

Figure 3. 25: (Left) Graph of amplitude and incidence angle with differentiation of four classes of gas sand. (Right) Chart of four gas sand classes along with Gradient, Amplitude, and keynotes (modified after Simm et al., 2014).

3.5.3.1 Class 1 Anomalies

The AVO having a Class 1 defined as a negative gradient and a positive impedance contrast; therefore, the reflection coefficient decreases with offset. Moreover, the impedance of shale is smaller than the impedance of sand. The AVO Class 1 is mostly linked with mature onshore sands, which are moderate to highly compacted (Gelius & Johansen, 2010).

3.5.3.2 Class 2 Anomalies

The AVO Class 2 has a negative impedance contrast, whereas the AVO Class 2p comprises a positive impedance contrast. The gradient displayed as being negative. Additionally, the reflection coefficient becomes negative and large at a greater offset. Both of these classes are linked with onshore and offshore sediments, which are comparatively consolidated and compacted (Gelius & Johansen, 2010).

3.5.3.3 Class 3 Anomalies

The AVO Class 3 demonstrates negative gradient, as well as negatively high impedance contrast. Class 3 is generally linked with unconsolidated sands and the marine environment. Moreover, Class 3 exhibits a bright spot in the stacked seismic data. To delineate the AVO response of Class 2 from Class 3, no general rule exits but relies on “close to zero intercept” rule that basically displays no amplitude (Gelius & Johansen, 2010).

3.5.3.4 Class 4 Anomalies

The AVO Class 4 exhibits a positive gradient, as well as negatively high impedance contrast. Similar to the AVO Class 3, it relates to unconsolidated sands and the marine environment (Gelius & Johansen, 2010).

In order to explain and illustrate the AVO response, the amplitude and angle related plot, shown in Figure 3.30, is suitable. Whereas, when a greater part of data is observed, Intercept versus Gradient or I-G crossplot is utilized. The I-G crossplot demonstrates values of intercept and gradient being a single point, whereas AVO classes gather data to certain areas in the plot (Figure 3.26).

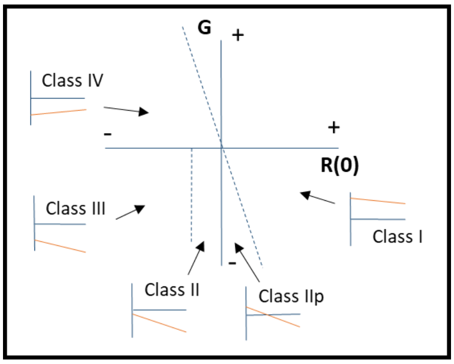

Figure 3. 26: Crossplot of the AVO Intercept versus AVO Gradient (I-G) with four different classes of gas sand (modified after Simm et al., 2014).

An increasing AVO does not always indicate a pay zone; brine sand also displays the same response. The geological setting holds a dominant significance; thus, the response should be validated according to the generated models under several scenarios, for instance, different shale content, fluids, porosities, and saturations (Simm et al., 2014).

The case of shale and hydrocarbon-bearing sand setting, displayed in Figure 3.27 left, shows the response of hydrocarbon contact, which exhibits positive AVO intercept and gradient, while on the right side of Figure 3.27, dissimilar responses are observed, which display the base of the brine bearing sand. In hydrocarbon contact, positive amplitude gradually moves up with increasing offset, therefore, mainly low gradients are seen. The impact of variation in lithology consists of positive intercept and also negative gradient; therefore, with the help of a base reflector, the hydrocarbon contact is interpreted. Moreover, considering with real seismic data, AVO response produced from the fluid contacts can be disturbed with decreasing amplitude (Simm et al., 2014).

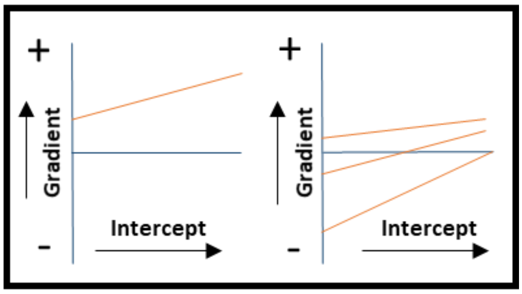

Figure 3. 27: (Left) General AVO response of GWC (Gas-Water-Contact). (Right) Responses of base sand (modified after Simm et al., 2014).

Chapter 4: Petrophysical Analysis

4.1 Results

In this subchapter, the results that are obtained from the petrophysical analysis will be presented. This chapter will consist of tables that summarize the pay zone or reservoir potential for sequences of Early and Middle-Jurassic sequences that are Cook (Early-Jurassic), Rannoch, Etive, Ness, and Tarbert Formations (Middle-Jurassic). The potential for each chosen reservoir sequence will discuss individually in this chapter. Though there are some limitations as well i.e. Cook Formation is not present in 34/11-5S and 34/11-6S. Moreover, the Density and Neutron log responses are not available in the whole Rannoch Formation. For general overview of the wells include in the current study consult Figure 2.9 and Table 1.1. The remaining well logs are displayed in the appendix section (A1-A6). Figure 4.1 illustrates the thickness maps that are extracted with the help of Petrel for all units of target reservoir. A general regional overview regarding the thickness variations is provided by thickness maps of target reservoir units.

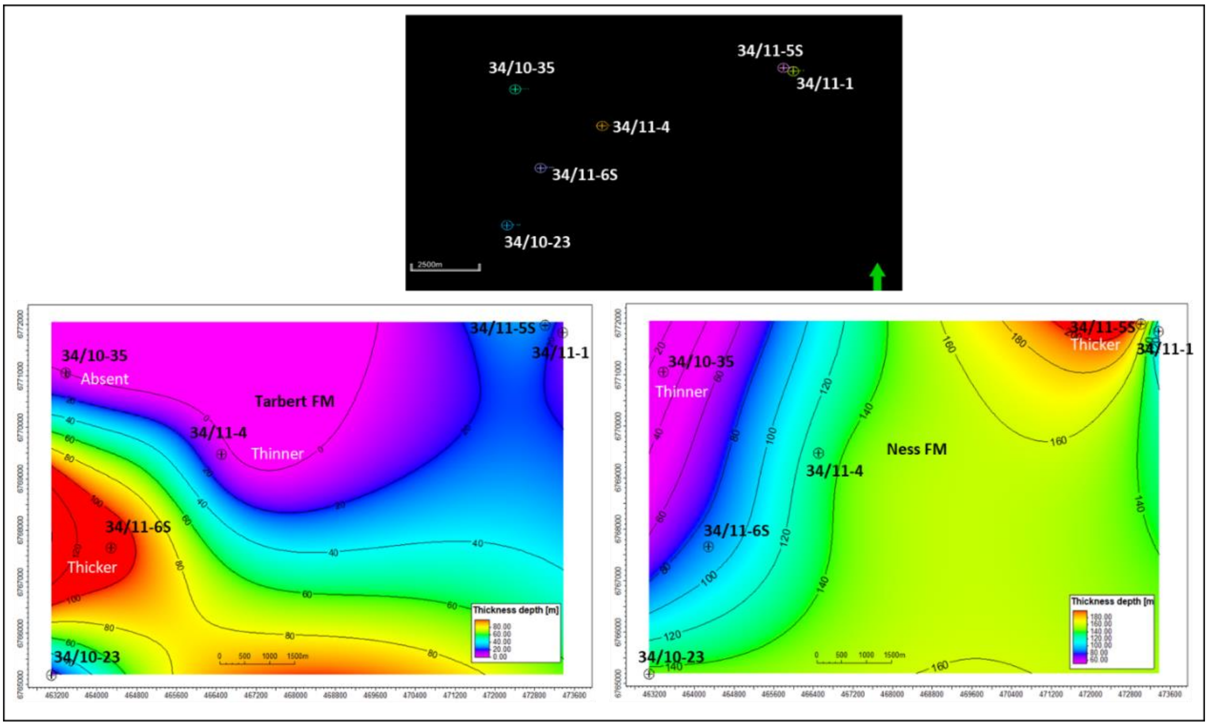

Figure 4. 1: Thickness maps of the gas-bearing reservoirs in the studied wells. (Left) The thickness map of Tarbert Formation along with the studied well locations. (Right) The thickness map of Ness Formation along with the studied well locations.

(Note: The color scale bar in thickness maps is dissimilar because Tarbert Formation is relatively low in thickness than Ness Formation).

Gamma ray log helps in estimating the Volume of Clay, whereas, the neutron-density combination helps in estimating the porosity (φ) of the zone. Archie's equation helps in computing the water saturation. For net reservoirs, the cut-off values for porosity and volume of clay are set to 0.1 and 0.4 respectively. For water saturation, value of 0.4 is set as cutoff for net pay. Net pay intervals and net reservoirs, which are below 2 m are not taken into consideration for the current study. In Table 4.1, the reservoir zones and potential pays are identified and presented based on the above-mentioned criteria. In all encountered formation, reservoir zones are identified from all wells. However, the amount of pay zones as compared to reservoir zones are encountered less and found in Ness and Tarbert Formations. The Etive, Rannoch and Cook Formations have no pay zones in all the wells.

Table 4. 1: Wells, Reservoir Zones, Pay Zone, Hydrocarbon content and Formations of the study area.

Well	Formation	Reservoir Zone	Pay Zone	Hydrocarbon
34/10-23	Tarbert	✓	✓	Gas
	Ness	✓	✗	-
	Etive	✗	✗	-
	Rannoch	✗	✗	-
	Cook	✗	✗	-
34/10-42S	Tarbert	✓	✗	-
	Ness	✓	✗	-
	Etive	✓	✗	-
	Rannoch	✓	✗	-
	Cook	✓	✗	-
34/11-1	Tarbert	✓	✓	Gas/Condensate
	Ness	✓	✓	Gas/Condensate
	Etive	✓	✗	-
	Rannoch	✓	✗	-
	Cook	✓	✗	-
34/11-4	Tarbert	✓	✓	Gas/Condensate
	Ness	✓	✓	Gas/Condensate
	Etive	✓	✗	-
	Rannoch	✓	✗	-
	Cook	✗	✗	-
34/11-5S	Tarbert	✓	✓	Gas/Condensate
	Ness	✓	✗	-
	Etive	✓	✗	-
	Rannoch	✓	✗	-
34/11-6S	Tarbert	✓	✓	Gas
	Ness	✓	✓	Gas
	Etive	✓	✗	-
	Rannoch	✓	✗	-

Terminologies of Clay Volume (assuming the presence of shale and sand content only):

- Sand: 0 to 25%
- Shaly Sand: 25 to 50%
- Sandy Shale: 50 to 75%
- Shale: 75 to 100%

Terminologies of porosity related to a hydrocarbon-bearing reservoir.

- Very poor: 0 to 5%
- Poor: 5 to 10%
- Fair: 10 to 15%
- Good: 15 to 20%
- Excellent: 20 to 25%

Terminologies of Permeability related to hydrocarbon-bearing reservoir.

- Poor: 10 to 10 mD
- Good: 10 to 100 mD
- Excellent: 100 to 1000 mD

In this current chapter and the following chapters, the wells are highlighted by their name such as 34/10-42S, 34/10-23, and 34/11-1. Depth reflects the measured depth regarding Kelly Bushing (m MDKB), until other is mentioned.

4.1.1 Tarbert Formation

In Table 4.2, the results generated from petrophysical analysis of the Tarbert Formation are presented. In Figure 4.2, the well log interval of well 34/10-23 is indicated the reservoir and pay zones. The thickest Tarbert Formation is located in the north-west (34/11-6S) where the thickness ranges from 107 m to 6 m. On the other hand, the thickness of Tarbert Formation reduces to 6 m in the well 34/11-4, which is located alongside the north-east of the well 34/11-6S as illustrated in Figure 4.1. For Tarbert reservoirs, the average volume of clay varies from 5.9% to 15%. In the well 34/11-1, the lowest volume of clay is identified and in well 34/11-5S, the highest volume of clay is identified.

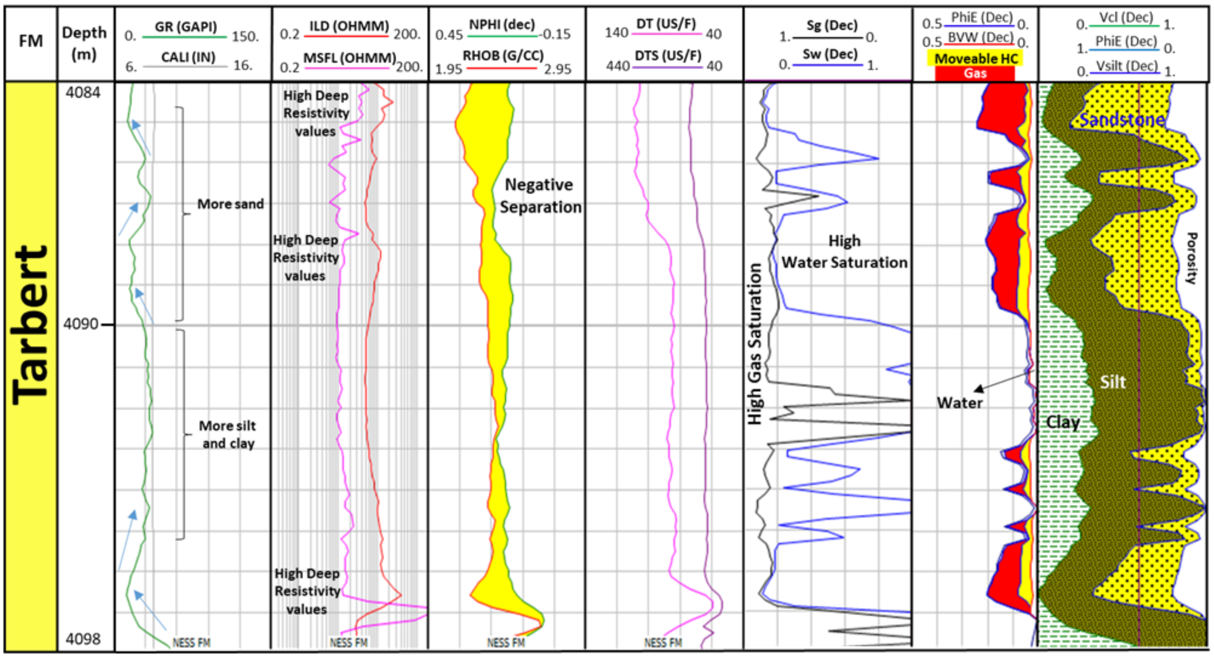

Figure 4. 2: The well log display of Tarbert Formation in well 34/10-23. The Heather Formation is above and the Ness Formation is below the Tarbert Formation.

Additionally, well 34/11-1 possess a high net to gross ratio of about 92%. Whereas, there is lower net to gross ratio in well 34/11-6S averaging for about 5%. The value of average porosity was ranging from 9% to 33%. The lowest value has been recorded in the well 34/11-5S and the highest recorded in the well 34/11-4. Moreover, in all the studied wells, the pay zones are identified except 34/10-42S because it possess 6 m value of gross reservoir and comprising net pay value and net reservoir as zero.

Table 4. 2: Reservoir properties of Tarbert Formation in all wells. Where Depth is in meters (MD), Res. = Reservoir. P = Pay. frac. = Fraction. Vsh = Volume of shale. φe = Effective Porosity. Sw = Water Saturation.

Well	FM depth (MD) (m)	Gross (m)	Net (Res.) (m)	N/G (Res.) (fract.)	ϕ_e (Res.) (fract.)	Vclay (Res.) (fract.)	Net (Pay) (m)	S_w (Pay) (m)
34/10-23	4084-4098	14	6.69	0.478	0.174	0.108	6.69	0.206
34/10-42S	4211-4217	6	-	-	-	0.06	-	0.8
34/11-1	4045-4060	15	13.86	0.924	0.225	0.059	13.86	0.213
34/11-4	4142-4148	6	4.93	0.822	0.33	0.097	4.93	0.114
34/11-5S	7086-7110	24	11.2	0.46	0.09	0.15	11.2	0.2
34/11-6S	6837-6944	107	5.33	0.05	0.161	0.113	5.33	0.22

4.1.2 Ness Formation

The results of the petrophysical analysis related to the Ness Formation are reflected in Table 4.3. In Figure 4.3, the well log interval is illustrated with reservoir and indicated pay zones of well 34/11-1. The thickness of the formation ranges from 112 to 163 m. In the Ness Formation, approximately a double amount of shale is observed as compared to Tarbert Formation in reservoir zones. The lowest volume of clay has recorded in the well 34/11-1, whereas, the highest volume of clay was recorded in the well 34/11-5S. The average volume of clay in the formation ranged from 13% to 26%. The well 34/10-23 in Ness Formation recorded a poor net to gross ratio i.e., only about 1.3%, perhaps, due to high water saturation. The volume of average clay in well 34/10-23 is highest for about 26%. The average water saturation in Ness Formation is ranging from 12% to 30%, being lowest in the well 34/11-6S and highest in the well 34/10-23.

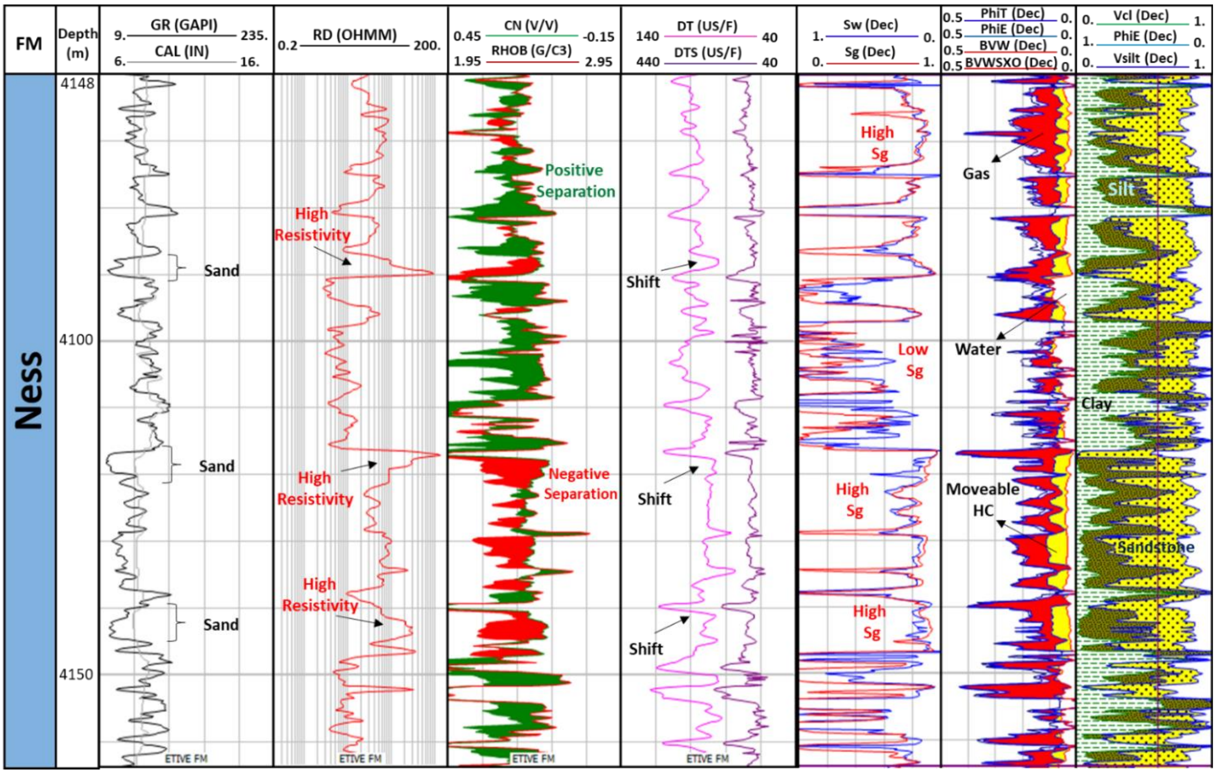

Figure 4. 3: The Ness Formation in well 34/11-1. The Tarbert Formation is above, and Etive Formation is below the Ness Formation.

Table 4. 3: Reservoir properties of Ness Formation in all wells. Where Depth is in meters (MD), Res. = Reservoir. P = Pay. frac. = Fraction. Vsh = Volume of shale. φe = Effective Porosity and Sw = Water Saturation.

Well	FM depth (MD) (m)	Gross (m)	Net (Res.) (m)	N/G (Res.) (fract.)	ϕ_e (Res.) (fract.)	Vclay (Res.) (fract.)	Net (Pay) (m)	S_w (Pay) (m)
34/10-23	4098-4243	145	1.83	0.013	0.229	0.241	1.83	0.302
34/10-42S	4217-4355	138	8.32	0.06	0.373	0.15	8.32	0.29
34/11-1	4060-4164	104	56.6	0.544	0.204	0.13	56.6	0.215
34/11-4	4148-4277	129	78.03	0.605	0.264	0.137	78.03	0.26
34/11-5S	7110-7291	181	4.57	0.025	0.31	0.26	4.57	0.29
34/11-6S	6944-7033	89	3.66	0.041	0.28	0.18	3.66	0.129

In all wells, pay zones are identified except well 34/10-42S, well 34/10-23 and well 34/11-5S and reflected below:

- Well 34/10-23: Gross 145m with 1.83m Net and 30% average water saturation.
- Well 34/10-42S: This well considered dry.
- Well 34/11-5S: Gross 181m with Net 4.57m and 29% average water saturation.

4.1.3 Etive Formation

In Table 4.4, the petrophysical analysis of the Etive Formation is presented. Figure 4.4 represents the well log interval with indicated reservoir zones. The thickness is uniform in overall region and yet poorly illustrated in Figure 4.1. For reservoirs, the average volume of clay varies between 5.2% and 25%, whereas the highest volume of clay was recorded in the well 34/11-5S and the lowest volume of clay is detected in the well 34/11-1. The highest net-to-gross ratio was about 83% in well 34/11-4. The average porosity values for Etive varies between 10% and 39%. The highest values are identified in well 34/10-42S (dry) and lowest in the well 34/11-6S. No pay zone in Etive Formation was identified in all the wells.

Table 4. 4: Reservoir properties of Etive Formation in all wells. Where Depth is in meters (MD), Res. = Reservoir. P = Pay. frac. = Fraction. Vsh = Volume of shale. φe = Effective Porosity. Sw = Water Saturation.

Well	FM depth (MD) (m)	Gross (m)	Net (Res.) (m)	N/G (Res.) (fract.)	ϕ_e (Res.) (fract.)	Vclay (Res.) (fract.)	Net (Pay) (m)	S_w (Pay) (m)
34/10-23	4243-4287	44	0	0	0.102	0.22	-	0.9
34/10-42S	4355-4369	14	0.52	0.037	0.392	0.074	0.52	0.247
34/11-1	4164-4177	13	0.55	0.043	0.209	0.052	0.55	0.391
34/11-4	4277-4292	15	12.5	0.83	0.314	0.064	12.5	0.315
34/11-5S	7291-7307	16	0.15	0.01	0.275	0.259	0.15	0.278
34/11-6S	7033-7057	24	0	0	0.1	0.23	-	0.82

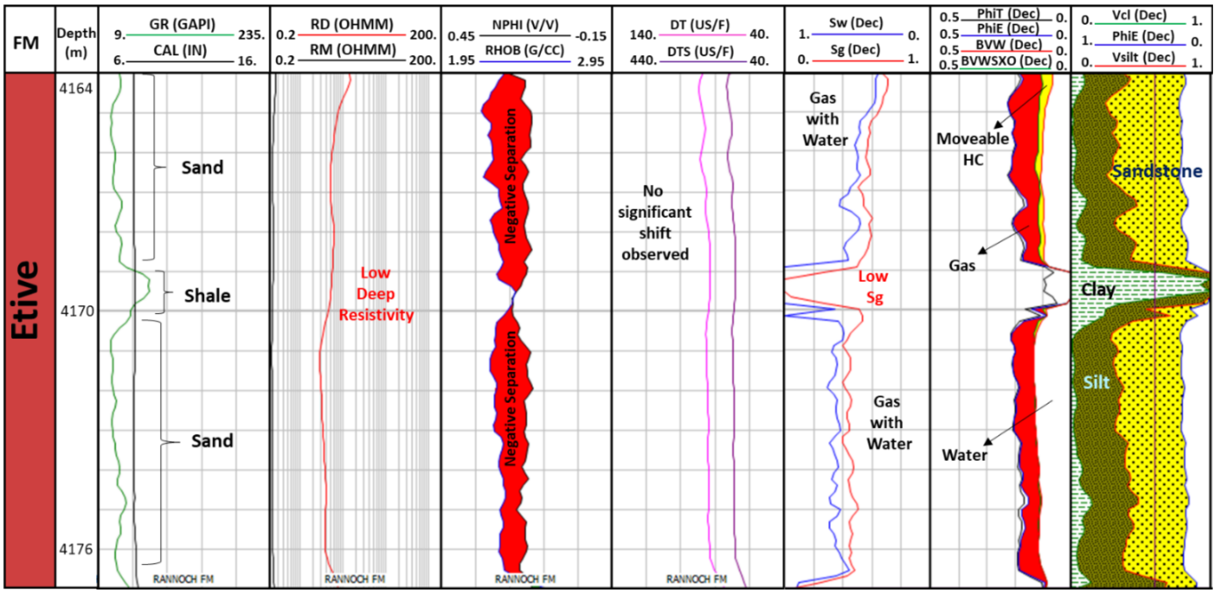

Figure 4. 4: The Etive Formation in well 34/11-1. The Ness Formation is above and the Rannoch Formation is below the Etive Formation.

4.1.4 Rannoch Formation

In Table 4.5, the petrophysical analysis of the Rannoch Formation are presented. The Figure 4.5 represents the well log interval with indicated possible reservoir zones in the well 34/10-23. The thickness varies from 34m to 63m as the lowest thickness encountered in the well 34/10-42S and the thickest succession encountered in well 34/11-5S. The thicknesses are overall very similar, such as, in four out of the six available wells (34/10-23, 34/11-1, 34/11-4 and 34/11-6S), the thickness of Rannoch ranges between 44m to 48m. For Rannoch Formation, the average volume of clay differs from 6% and 32%, where the highest volume of clay is recorded in the well 34/11-6S and lowest volume of clay is recorded in the well 34/10-42S. The Density and Neutron logs didn't run through whole Rannoch Formation but a smaller portion in the wells 34/11-5S, due to which they didn't calculate water saturation and porosity. In only three wells (34/10-23, 34/11-1 and 34/11-6S), the net reservoir is zero, therefore, N/G ratios are available only for the rest two wells 34/10-42S and 34/11-4. The lowest values of N/G is 0.4% in the well 34/10-42S, whereas, the highest is in the well 34/11-4, about 44.7%. For Rannoch Formation, the average value of porosity ranges from 10.3% to 25%. The highest value of porosity recorded in the 34/10-42S and the lowest recorded in the well 34/10-23.

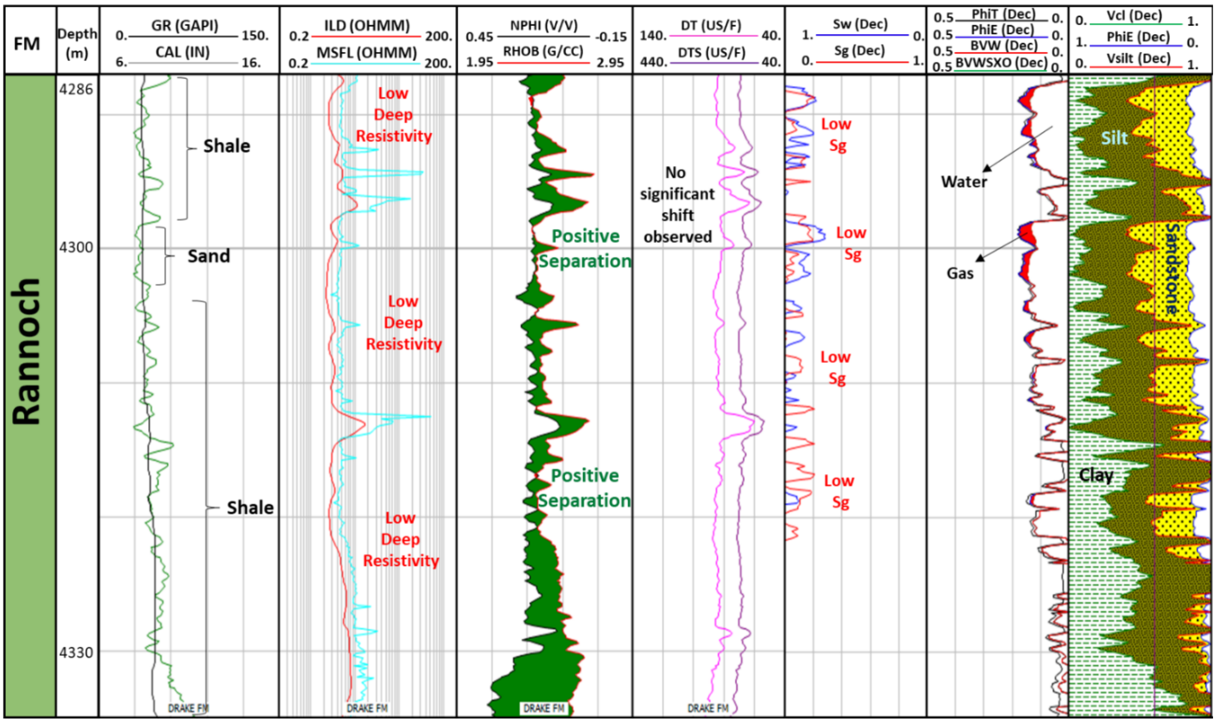

Figure 4. 5: Rannoch Formation in well 34/10-23. The Etive Formation is above and the Drake Formation is below the Rannoch Formation.

Table 4. 5: Reservoir properties of Rannoch formation in all wells. Where Depth is in meters (MD), Res. = Reservoir. P = Pay. fract. = Fraction. Vsh = Volume of shale. φe = Effective Porosity. Sw = Water Saturation.

Well	FM depth (MD) (m)	Gross (m)	Net (Res.) (m)	N/G (Res.) (fract.)	ϕ_e (Res.) (fract.)	Vclay (Res.) (fract.)	Net (Pay) (m)	S_w (Pay) (m)
34/10-23	4287-4335	48	0	0	0.103	0.22	-	0.87
34/10-42S	4369-4403	34	0.15	0.004	0.25	0.066	0.15	0.373
34/11-1	4177-4221	44	0	0	0.18	0.13	-	0.6
34/11-4	4292-4339	47	21.03	0.447	0.223	0.144	12.5	0.307
34/11-6S	7057-7105	48	0	0	0.11	0.32	-	0.48

4.1.5 Cook Formation

In Table 4.6, the petrophysical analysis of the Cook Formation are presented. Figure 4.6 represents the log interval of well 34/10-23 with indicated possible reservoir zones. The thickness of the formation is varying in all the wells, the high thickness of Cook Formation (102

m) is found in the well 34/10-23, whereas the low thickness (28 m) is present in well 34/11-4. The Cook Formation was not encountered in wells 34/11-5S and 34-11/6S.

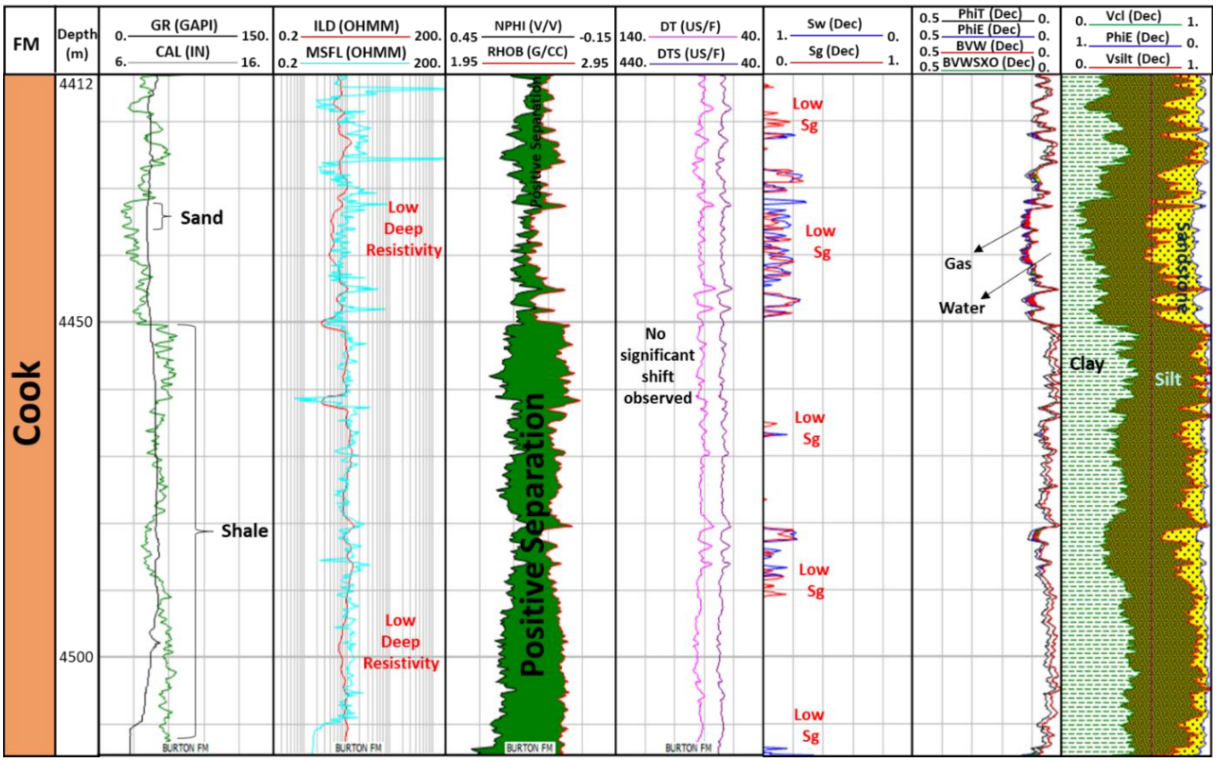

Figure 4. 6: Cook Formation in well 34/10-23. The Drake Formation is above and Burton is below the Cook Formation.

In the well 34/11-4, the Density and Neutron logs did not run throughout the whole formation. Therefore, log data is limited and estimation for porosity and water saturation was unavailable. Hence, reservoir properties of these mentioned wells are not discussed here. The average clay volume for Cook Formation varies between 6% and 39%. The lowest average clay volume is identified in the well 34/11-1 and this well does not have a net reservoir. Moreover, the highest average clay volume recognized in well 34/10-23, which also possesses no net reservoir. The porosity values for Cook is ranging between 6% and 23.2%. The Cook Formation comprises high water saturation in all the available wells, ranging from 35.9% to 88%.

Table 4. 6: Reservoir properties of Cook formation in all wells. Where Depth is in meters (MD), Res. = Reservoir. P = Pay. fract. = Fraction. Vsh = Volume of shale. φe = Effective Porosity. Sw = Water Saturation.

Well	FM depth (MD) (m)	Gross (m)	Net (Res.) (m)	N/G (Res.) (fract.)	ϕ_e (Res.) (fract.)	Vclay (Res.) (fract.)	Net (Pay) (m)	S_w (Pay) (m)
34/10-23	4413-4515	102	0	0	0.06	0.39	-	0.88
34/10-42S	4485-4520	35	0.91	0.026	0.232	0.067	0.91	0.359
34/11-1	4289-4338	49	0	0	0.14	0.06	-	0.65

4.1.6 Estimates of Permeability

Permeable zones are identified by qualitative approach with the help of interpreting mud-cake in the caliper log (if bit size > caliper log response, displaying a permeable zone) or by looking at the separation between the type of resistivity curves that illustrate the infiltration of mud-filtrate in permeable zones, thus permeability. Permeability can also be estimated indirectly with the help of multiple relationships i.e., Timur, Schlumberger and Morris Gas. The example of permeability of Tarbert Formation in the well 34/11-1 is shown in Figure 4.7. All the permeability data follows the general trend with porosity that is permeability increases with the effective porosity increase. Continuous and excellent to good permeable zones are identified in the lower hydrocarbons filled reservoir parts. In case of gas, the Morris Biggs gas equation and the Timur equations are used to calculate permeability. When the porosity is high, a good correlation is seen between Schlumberger and Timur (Figure. 4.7).

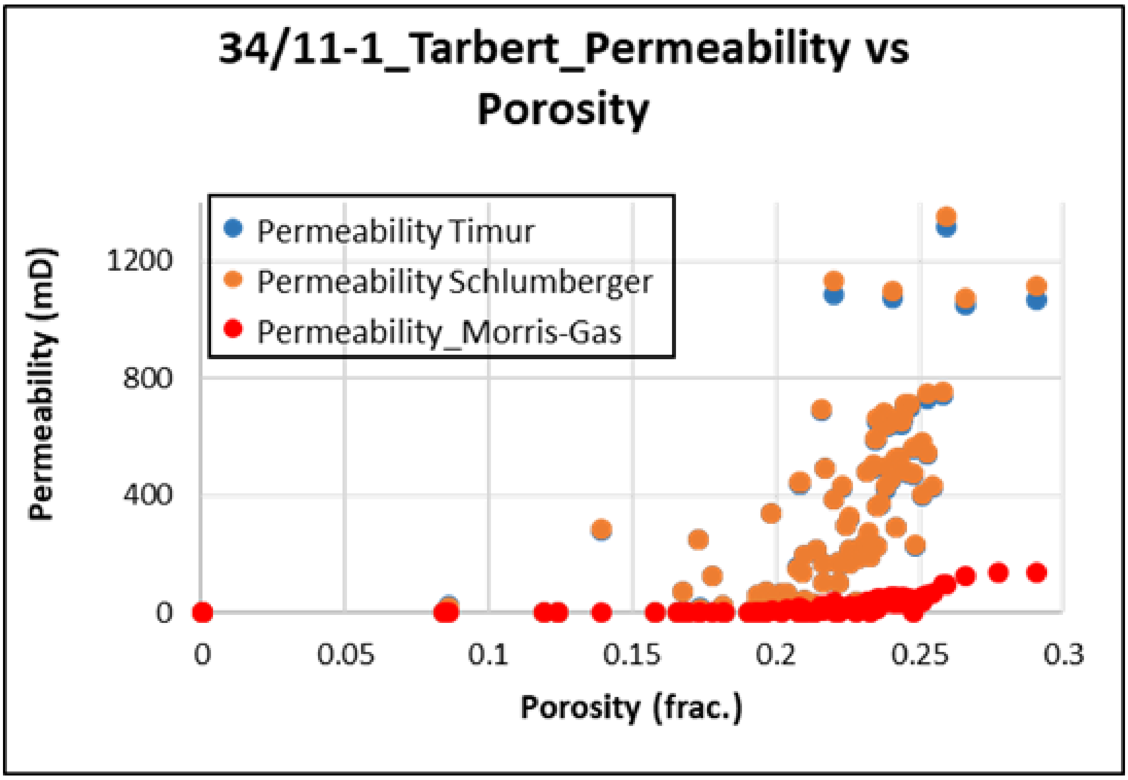

Figure 4. 7: Crossplot of Porosity vs Permeability of Tarbert in the wells 34/10-23 and 34/11-1, where Permeability_Timur = blue, Permeability _Schlumberger = orange and Permeability_Morris-Gas = red.

4.1.7 Deposition Environment of Brent Group

In the North Viking Graben area, the Brent Group deposited before the beginning of the Late Jurassic rifting. Thermal subsidence was the main reason for controlling the deposition of these sediments resulting from the rifting episode of Permian-Triassic (Yielding et al., 1992). The rifting mechanism from the Late-Jurassic to Early-Cretaceous has led the sediments to deposit in the wedge-shaped, which is filled in the topography of the tilted fault block. Moreover, in the Brent province, these tilted fault blocks are the major hydrocarbon-bearing reservoirs. The sediments from the Brent Group were deposited to significantly dissimilar depths because of the last rifting event (Marcussen, et al., 2010). According to Brown et al., (1987) and Graue et al., (1987), in the northern North Sea area, the sediments of Brent Groups are found about 60°N and comprised of five formations (Figure 4.8), which are Broom, Rannoch, Etive, Ness, and Tarbert; these formations are a part of the foremost river-dominated delta system. The quartz cementation in the Brent Group increases significantly at the thickness exceeding more than 3 km (Bjørlykke et al., 1992). Studies related to quartz cementation explain that it is temperature dominant (Bjørlykke & Jahren, 2015). Furthermore, the quartz cementation fundamentally determines the presence of enough porosity for production of petroleum, thus predicts reservoir quality (Faleide et al., 2010). Moreover, cementation is ineffective to the changes produced by vertical stress or overburden (Bjørlykke & Jahren, 2015).

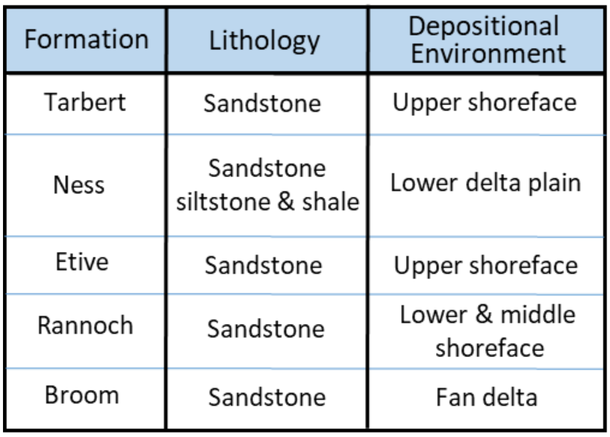

Formation	Lithology	Depositional Environment
Tarbert	Sandstone	Upper shoreface
Ness	Sandstone siltstone & shale	Lower delta plain
Etive	Sandstone	Upper shoreface
Rannoch	Sandstone	Lower & middle shoreface
Broom	Sandstone	Fan delta

Figure 4. 8: Lithostratigraphy observed in the Brent Group (modified after Marcussen, et al., 2010).

According to, Johnson & Stewart (1985), Brown et al. (1987) and Graue et al. (1987) the Etive and Rannoch formations deposited as the Brent delta was in prograding phase. According to Richards & Brown (1986), Brown et al. (1987), and Graue et al. (1987) the Rannoch Formation is shoreface sediments under the influence of storm wave. Whereas, according to Budding & Inglin (1981), Johnson & Stewart (1985), Brown et al. (1987) and Graue et al. (1987) the Etive formation is the deposition of barrier/beach environment. Moreover, the Etive formations is also interpreted as channel deposits in few locations (Brown et al., 1987).

In the Ness Formation, variation in lithology is present, and the depositional environment is said to be the mixture of coastal plain and deltaic sediments (Livera, 1989). The Tarbert Formation was considered to be deposited during the time when the Brent Delta experienced the last retreat (Fält et al., 1989; Graue et al., 1987). All the formations in the Brent Group are believed to have the same diagenetic mechanism, even though, comprising dissimilar facies and the main composition of the Brent Group Sandstones (Bjørlykke et al., 1992).

4.2 Discussion

This subsection will elaborate quality of HTHP reservoir, depositional features, and hydrocarbon potential of the individual formations. A general overview of the average values of the five studied reservoir units that include clay volume, porosity and net-to-gas ratio are displayed in Figure 4.9.

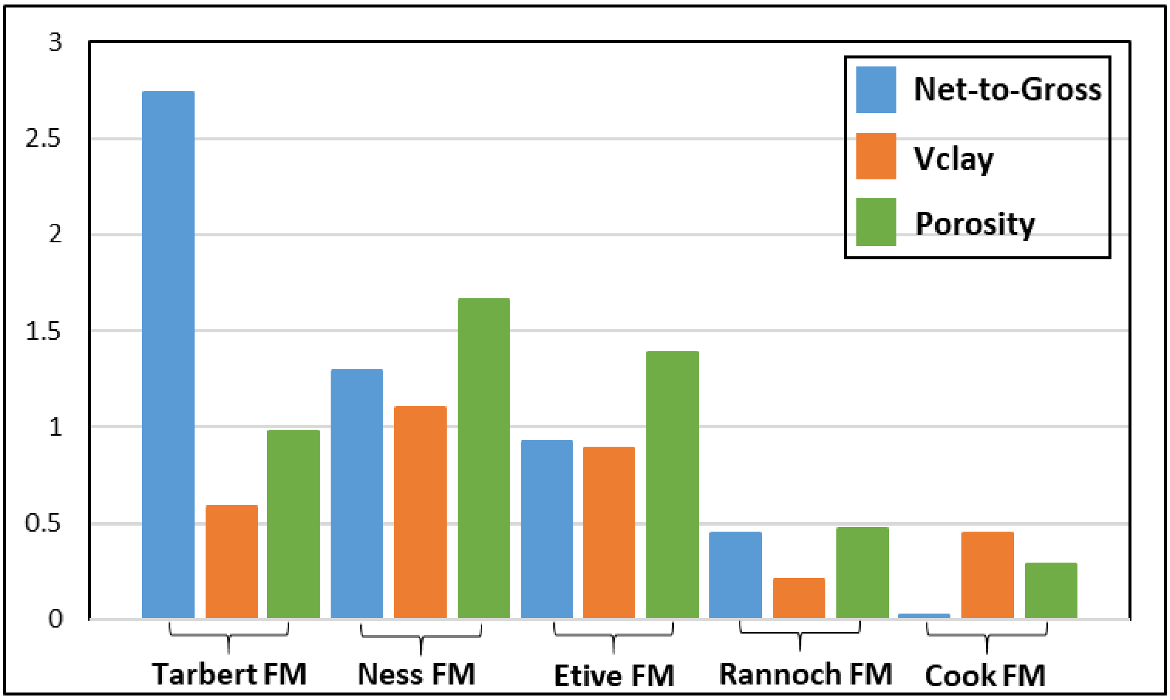

Figure 4. 9: The five studied reservoir units (Tarbert, Ness, Etive, Rannoch and Cook FMs) along with the average reservoir properties, such as, Net-to-Gross, Clay Volume and Porosity.

All gas bearing reservoirs in this study are known as High-Temperature High-Pressure (HTHP) reservoirs in the Valemon and Kvitebjørn fields in the area of northern Viking Graben, northern North Sea. There are three mechanisms creating HTHP reservoirs. In this study, HTHP reservoirs could be due to formation stress, which includes; disequilibrium compaction and tectonic movement mechanisms. In order to display and estimate the high pressure, the normal hydrostatic curve was generated with the formation pressure data acquired from NPD and formation depth. A general rule of thumb is, with 1km depth, formation pressure is 10MPa.The normal hydrostatic curve produced for the two reservoirs, Tarbert and Ness Formations, for all the wells (Figure 4.10). The formation depths are referenced from mean sea level. The Tarbert Formation in different wells with different depths exhibiting more or less similar formation pressure values. In the well 34/10-23, Tarbert is at 4084m depth and comprising formation pressure in the range of 79 to 82 MPa. Tarbert and Ness in the wells 34/10-23, 34/11-1, 34/11-4 and 34/10-42S is available in the range of 3.8 to 4.1km depths, whereas, in well 34/11-5S, at deeper depths of about 6.8km. The depth. In all the wells, it is seen that Tarbert (gas reservoir) and Ness (gas reservoir) comprising higher formation pressure relative to the hydrostatic curve, therefore, both the formation pressures are opposing the general rule of thumb. It can be concluded that Tarbert and Ness gas reservoirs in the wells comprising formation pressure, ranging between 77 MPa to 82 MPa. Hence, they are named as Overpressure or High Pressure Reservoirs. Moreover, all the discoveries of Middle-Jurassic succession in this study is mainly in the Tarbert Formation. In addition, the hydrocarbon column in few wells extend up to the Ness Formation, which is underneath Tarbert Formation and it is relatively more in thickness. The Ness Formation is less clean as compared to the Tarbert Formation.

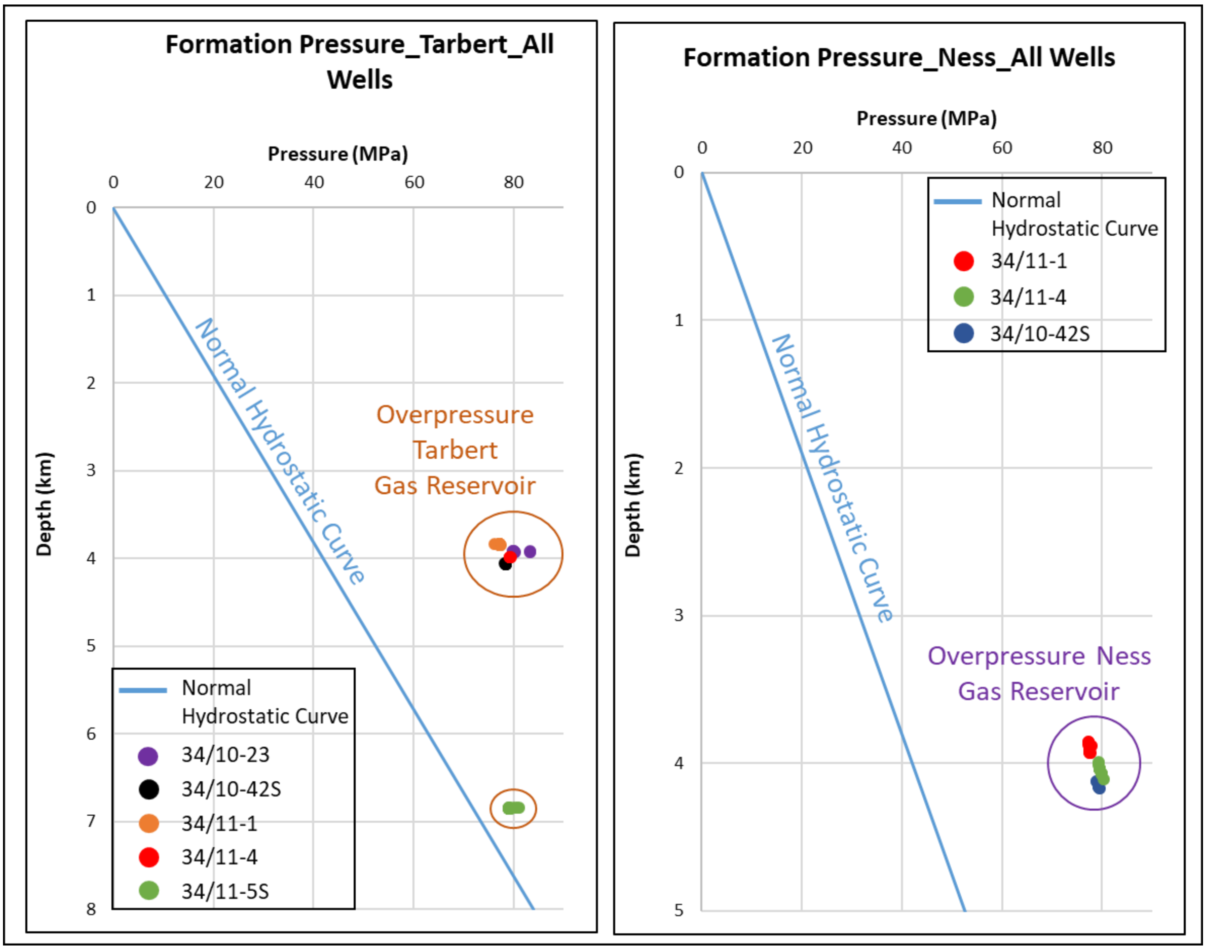

Figure 4. 10: Normal Hydrostatic curve generated for (left) Tarbert Formation and (Right) Ness Formation in wells 34/10-23, 34/10-42S, 34/11-1, 34/11-4, 34/11-5S, 34/11-6S, showing the presence of High Pressure reservoirs (orange and purple circles) in the studied wells. The depth is measured as [m RKB], thus highly deviated well (34/11-5S) plotting at about 7.1 km depth. If depth measured as [m TVD], data points of well 34/11-5S would have plotted similar to the other data points at about 4 km depth.

In Table 4.1, it can be observed that the Tarbert and Ness Formations have the best reservoir properties. Moreover, the Ness Formation relatively has the highest net-to-gross ratio, whereas the Tarbert Formation has the lowest clay volume. As compared to Tarbert Formation, reservoir quality in the Ness Formation is poor. It is primarily due to the variation in lithology and the presence of shale content in the reservoir.

4.2.1 Tarbert Formation

A transgressive/regressive system is observed in the entire Brent delta. In the upper part of the Brent Group, the Tarbert Formation is identified by the shoreline sediments (shore face or delta front) over the Ness Formation, which comprises continental deposits. The Tarbert Formation mainly consists of shoreline sediments related to the entire retreat process of Brent delta. Moreover, it comprises continental deposits with thinner units, which is deposited behind the shoreline over the existing prograding huge shoreline prisms (Helland-Hansen et al., 1992).

In Tarbert Formation, the response of gamma ray is blocky and generally low i.e., cylindrical-shaped, across the formation, but the formation reflects high gamma ray values in well 34/11-6S, where Tarbert Formation has relatively high thickness. It shows a minor rise and uneven behavior, mostly upwards coarsening, in the upper part. Similarly, in the lower parts, the formation comprises shale content, whereas, in the upper parts, clean sandstone with intercalations of shale. The impermeable shale capped the top of the Tarbert Formation that is similar in all the wells:

- 34/10-23: Heather Formation.
- 34/10-42S: Heather Formation.
- 34/11-1: Heather Formation.
- 34/11-4: Heather Formation.
- 34/11-5S: Heather Formation.
- 34/11-6S: Heather Formation.

It is concluded that in all wells Tarbert Formation comprises good reservoir properties. It is mostly thin in thickness relative to other Brent Group formations in all the wells. Whereas, in well 34/11-6S, Tarbert is thicker (107 m) than Ness Formation (89 m). The neutron density separation and the resistivity log are used for the identification of hydrocarbon saturation. A lower neutron and density value is estimated for gas as compared to oil and generates a larger negative separation. Moreover, waves travel slower through a gas-saturated reservoir than an oil-saturated reservoir, supposing similar lithology. A small rise in the transit time is estimated when moving from oil to gas. A significant amount of hydrocarbon is also recorded in 5 out of 6 wells in the Tarbert Formation (well 34/10-42S contains relatively high water saturation, therefore, non-economical).

4.2.2 Ness Formation

The Middle-Jurassic Ness Formation is a member of Brent Group. It includes a heterolithic and irregularly thick interval of delta-plain buried sediments. The coal sequence, mud rock, and mixed sandstone represent the sub-environments of delta plain, such as overbank, fluvial channel/mouth-bar, interdistributary bay, and lagoonal (Graue et al., 1987; Helland-Hansen et al., 1992). However, it is significant to consider that Ness Formation comprises notable heterogeneity in lithology, but here the discussion is regarding the progradational section that shows the dominance of fining-up fluvial sand bodies. In addition, to the facies generated by the associated flood. According to Helland-Hansen et al. (1992), gamma ray profiles demonstrates the Ness Formation's general heterogeneity that are both characteristically displayed by upwards decreasing responses and complex above the main sand bodies.

The Ness Formation possesses uneven gamma ray responses normally higher values relative to Tarbert Formation. In most of the wells, the top of Ness Formation displaying sequence is seen as fining upward. It comprises a high number of shale intercalation as compared to Tarbert Formation. The Ness Formation is relatively thickness thicker than Tarbert Formation in most wells. In contrast, it is less in thickness than Tarbert Formation only in the well 34/11-6S. The Ness Formation comprises good reservoir properties in all wells. Whereas it has no pay zone in three wells 34/10-23, 34/10-42S, and 34/11-5S.

4.2.3 Etive Formation

The Middle-Jurassic Etive formation comprises fine to coarse, massive gray-brown to clear and often cross-bedded and pebbly sandstones. In Etive formation, the mica content is normally found low (NPD.no/Etive Formation, 2021). Rannoch and Etive formations constitutes a storm-wave dominated, irregularly thick, barrier/shoreface or delta-front, which displays gamma ray profile by coarsening-up sequence and upward diminishing pattern. In the Etive Formation, generally lower gamma ray values are seen (Helland-Hansen et al., 1992).

The Etive Formation is differentiated because of the low mica content and gamma ray values from the underneath Rannoch Formation. However, the lower boundary is transitional in some places. Often, the formation is found to be amalgamated into underlying formation. It leads the formation to give blocky gamma ray log character. The upper boundary of Etive Formation with the overlying Ness Formation, is marked at the first major coal or shale (NPD.no/Etive Formation, 2021). The Etive formation in all the wells is not considered a pay zone, whereas, it has reservoir properties that makes it a reservoir zone in the studied wells, other than well 34/10-23. The thickness of Etive formation in most of the wells is relatively less. The minimum thickness is of 13m in 34/11-1 well, whereas, maximum thickness is of 44m in the well 34/10-23.

4.2.4 Rannoch Formation

The Middle Jurassic Rannoch Formation is the lower part in the Brent field area, which is relatively more argillaceous and consists of thin shales and siltstones. The formation tends to be less micaceous and coarser-grained towards the top. Therefore, it leads the formation to generate a unique pattern of the gamma ray that reflects the coarsening upward sequence. Generally, the formation is considered as prograding sands of shoreface and/or delta front sheet. The greater mica content produces a high gamma ray log in the sandstones and it generally separates the Rannoch formation from underlying and overlying sandstones. The Broom Formation is absent in the lower boundary; therefore, it is marking the lower boundary with the silty shales of the Dunlin Group. The blocky gamma ray log of the overlying Etive Formation defines the upper boundary of the Rannoch Formation (NPD.no/Rannoch Formation, 2021).

The Rannoch Formation is not reflected as a pay zone in this study (Table 4.1 and 4.5). It is considered a reservoir zone as it consists reservoir properties in the available wells but not in well 34/10-23. Generally, it comprises relatively high thickness in the wells. The Rannoch Formation is thinner in well 34/10-42S (34 m), whereas thickest in well 34/11-5S (63 m).

4.2.5 Cook Formation

In Early Jurassic time, the Cook Formation was deposited in the north-eastern region of the North Sea. According to Vollset et al (1984), the Cook Formation is spread across the eastern region of the East Shetland Basin, northern Viking Graben, Sogn Graben, Tampen Spur on the northern region of the Horda Platform. In the Valemon area and Kvitebjørn field, (Folkestad et al., 2012) interpret that the Cook Formation deposited as tidal-fluvial delta during regression and wave-dominated estuary during transgression.

The Cook formation is not available in wells 34/11-5S and 34/11-6S. It exhibits reservoir properties in the wells 34/10-23, 34/10-42S, 34/11-4, and 34/11-4. In contrast, it is not reflected as a pay zone in any of the studied wells. In the wells where Cook formation is present, displaying considerable thickness. The Cook Formation consists relatively less thickness that is 28 m in well 34/11-4. Whereas it has a highest thickness of 102 m in well 34/10-23.

4.2.6 Individual Well Analysis

The petrophysical analysis in each well is briefly explained as follows:

Well 34/10-23: In the Tarbert Formation, the top of gas (TG) is recognized at 4085 m in well 34/10-23 (NPD.no/34-10-23, 2021). According to NPD.no/34-10-23, (2021), the GWC (Gas Water Contact) was found at 4120m. Throughout the Tarbert Formation, the neutron-density separation is observed. Moreover, the deep resistivity log also exhibits high resistivity values from the top of Tarbert 4084 to 4095m. The formation temperature of Tarbert is 138°C, and formation pressure is 79 to 82 MPa (NPD.no/34-10-23, 2021).

Well 34/10-42S: In this well, Tarbert is studied because it is considered as a dry well. Therefore, Brent Group (Tarbert Formation only) and Cook formation are taken into consideration. The crossover of Neutron-Density logs displays Brent Group and Cook Formation with negative separation. Whereas the resistivity log showed lower resistivity values throughout the Brent Group and Cook Formation. Moreover, the water saturation curve within the Brent Group and Cook Formation was relatively higher. The tops of the reservoir came in deeper than the indications made by the geological forecast. The Tarbert and Cook Formation tops were found with deeper depths of 174m and 112m, respectively (NPD.no/34-10-42S, 2021). The Cook Formation and Brent Group are found to be water wet, showing a sealing fault in between the wells 34/10-23 and 34/10-42S. The Tarbert Formation and the upper part of Ness Formation comprise sandstone that shows no direct fluorescence. The gas readings in the Brent reservoir were generally showing levels slightly above and below 2 %, with the 7.2 % maximum in the arkosic and relatively tight Rannoch formation. In an impermeable, very tight arkosic sand near the total depth of the well within the sandstone unit of the Cook Formation, the gas level was recorded as 14.4%. The formation temperature in the Tarbert is 144°C, Ness is 147°C, Etive is 149°C, Rannoch is 150°C and Cook is 154°C. The formation pressure of Tarbert Formation in this well is 77 to 79 MPa (NPD.no/34-10-42S, 2021).

Well 34/11-1: In this well, the top of the Brent Group was found at 4045m that is 18m lower than the predetermined depth, and confirmed to be a gas/condensate bearing reservoir. This well has two gas-bearing reservoir units, Tarbert and Ness Formations. In the Tarbert Formations, the top of gas (TG) was recognized at 4047 m. Ness Formation has several intervals where neutron-density logs crossover shows high negative separations with the increase of resistivity log values at the same location. At the base of the Ness Formation, a true gas-water contact was found at 4163 m. The formation temperature in Tarbert is 144°C, and Ness is

145°C. In this well, the formation pressure of Tarbert is 77 to 78 MPa, and Ness comprises 78 to 79 MPa (NPD.no/34-11-1, 2021).

Well 34/11-4: In this well, the top of the Brent Group was found at 4124 m and confirmed to be gas-bearing reservoir. The well comprises two gas/condensate reservoirs at different depths. In this well, the formation temperature of Tarbert is 148°C, and Ness is 152°C. The Tarbert and Ness in this well comprise formation pressures of 79 MPa and 80 MPa, respectively (NPD.no/34-11-4, 2021).

Well 34/11-5S: The quality of the reservoir was identical compared to the exploration well 34/11-4 in the Valemon field. In this well, the Tarbert Formation is marked as the hydrocarbon-bearing reservoir and has a Gas-Water-Contact (GWC) at a depth of 7010 m (MD RKB). The formation pressure of Tarbert is 79 to 81 MPa, whereas formation temperature is 156°C (NPD.no/34-11-5S, 2021).

Well 34/11-6S: In this well, the top of the Brent Group (top of the Tarbert Formation) found at 6873m, whereas Ness Formation is at 6944 m. This well has two gas-bearing reservoirs, Tarbert and Ness Formations. The Tarbert Formation is the thickest in this well compared to all other wells. The thickness of the Tarbert Formation is 107 m, and relatively thick than the Ness Formation (89 m). In the entire Tarbert and Ness Formations, negative and positive separations were observed in the neutron-density combination log. Moreover, the formations contain sand with intercalations of shale. The deep resistivity log exhibits high resistivity values from the top of Tarbert 6873 m to 4095 m. The formation temperature of Tarbert is 154°C, and Ness is 156°C. The formation pressure data is not available in this well (NPD.no/34-11-6S, 2021).

4.3 Uncertainties

The petrophysical analysis provides the input data for reservoir characterization. Geological parameters are not measured directly but rely on various relations, carrying numerous uncertainties. Possible sources of error are summarized below:

- Several uncertainties could be present in the borehole environments. Some damages may experience by the walls of borehole, such as generation of fractures and disintegration of material in the rock while the drilling of borehole was carried out. Moreover, the destruction might be chemically influenced to the rocks, for instance, the contact between the formation and fluid might have altered. For example, clay mineral smectite gets swell while interacting with and absorbing water.
- The non-uniform walls of the borehole would generate errors in the measurements of the tools, if the contact of the tool with the formation is not sufficient. Additionally, errors can also be generated because of the utilization of a particular types of drilling mud, and the resultant corrections applied considering the nature of the drilling mud (Mondol, 2015). In a few wells, data might have some tool errors as they are displaying effects in the rock physics results.
- For sand and shale, the interpreted baselines depend on the interpreter’s understanding. Thus, the presence of organic-rich shales would reflect high response peaks in the gamma ray log that might create an impact while picking baselines. Inconsistency might

generate from the usage of linear/non-linear equations related to corrections of the clay volume.

- If the sandstone is not comprising radioactivity, then the response obtained from the gamma ray log might be accurate for estimating clay volume. In the case of density-neutron logs, it is reliable when the borehole environment is good, and there is no presence of heavy minerals and gas-crossover (negative separation). An overestimation is measured in the presence of heavy minerals. Thus, the errors influence and decreases accuracy in estimated clay volume.
- For porosity estimation, the best method available is to utilize the combination of neutron-density logs (if a gas-bearing reservoir is present). The uncertainty in the calculation might be due to the density and neutron values of shales and sands. The accuracy in measuring clay volume would determine the level of error in calculating porosity.
- The accurate and precise estimation for water saturation depends on different factors; for instance, the estimation of water resistivity is achieved with the help of brine-bearing interval. Therefore, it is challenging to differentiate it because the existing of a minimum amount of hydrocarbon might influence resistivity and raise the resistivity value. Moreover, the selection regarding exponents of saturation and cementation might initiate uncertainties. Furthermore, the formations comprising a relatively higher amount of shale need the correction process regarding the clay bound water (Ellis & Singer, 2007).
- The measure of permeability through different equations is complex. Several factors influence the permeability of the formation, such as grain size, pore size, shape, and surface area.

Chapter 5: Rock Physics Diagnostics

5.1 Results

The results generated from the rock physics diagnostics are presented in this chapter. The object is to connect the elastic properties (e.g., IP, VP/Vs, LMR) of the target reservoirs along with the reservoir properties, for instance, clay volume, porosity, cementation, hydrocarbon saturation, etc. in different crossplots. The rock physics diagnostic cross plots utilized in this study are Acoustic Impedance (AI) versus P-to S-wave velocity-ratio (Vp/Vs), Lambda-Rho ($\lambda\rho$) versus Mu-Rho ($\mu\rho$), Porosity (PhiT) versus Vp, and Vp versus Vs.

The properties such as water saturation, clay volume, and porosity are displayed and discussed in chapter 4, but the rock physics alternately explains the data, using dissimilar well log data. The rock physics results generated are compared with the petrophysical analysis generated results to look for the quality control and have insight into the reservoir properties. The cement volume calculation is an addition to this chapter, along with the previously discussed reservoir properties. The relevant interesting zones identified from the petrophysical analysis are only Tarbert Formation in the wells 34/10-23 and 34/11-5S, the Tarbert and Ness Formations in wells 34/11-1 34/11-4 and 34/11-6S. The main objective of these intervals is, nonetheless, interesting characteristics from other formations are also focused to a smaller ratio. The well 34/10-42S is considered dry; therefore, only Brent Group members and Cook Formation are studied. Moreover, for well 34/10-42S, only AI vs. Vp/Vs and LMR rock physics crossplots are generated.

5.1.1 Results of Well: 34/10-23

5.1.1.1 AI versus VpVsRatio cross plot

The AI versus Vp/Vs cross plots for all formations present in well 34/10-23 (Figure 5.1). The majority of the formations are plotting on either shale background Trend (black line) or brine sandstone trend (blue line) and only one formation plotting on the gas sandstone trend (orange line). The range of Acoustic Impedance (AI) is between 3100 and 14300 (g/cm3*m/s) and Vp/Vs ranging between 1.3 and 4.6 (Figure 5.1).

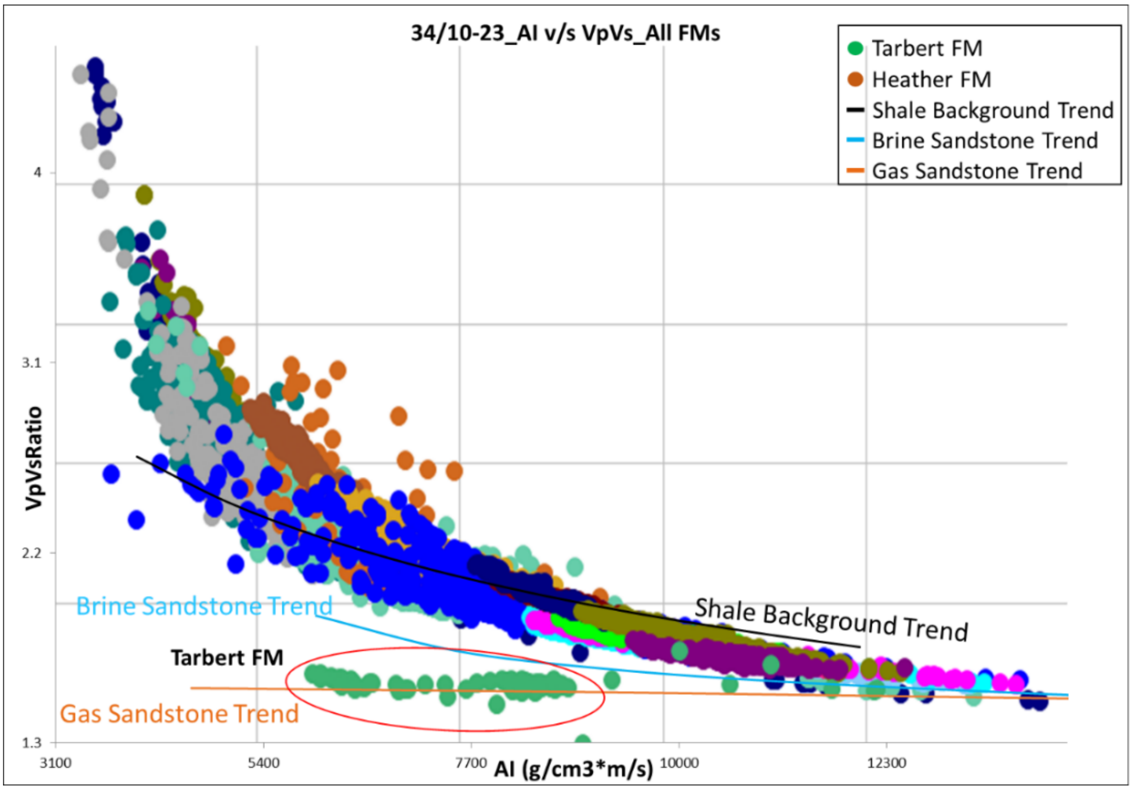

Figure 5. 1: The AI vs VpVsRatio cross plot template for all the formations present in the well 34/10-23. The template comprises Shale background trend, Brine Sandstone trend and Gas Sandstone trend. The color data points other than Heather and Tarbert Formations are representing different formations in well 34/10-23.

Moreover, the AI vs. Vp/Vs crossplots are color-coded with Gas Saturation (Sg), Clay Volume (Vclay), and Total Porosity (PhiT), in order to study the reservoir properties for well 34/10-23. The Heather Formation is plotting on Shale Background Trend, and the Tarbert Formation is plotting on Gas Sandstone Trend and few points on Brine Sandstone Trend (Figure 5.2-Top). The AI vs. Vp/Vs crossplot generated with color-coding of Gas Saturation (Sg) with a range between 20 to 70%. The cross plot shows the presence of high Sg (about 70%) in the Tarbert Formation plotting on the Gas-bearing Sand, whereas high water saturation or low Sg (about 20%) in the Heather Formation (cap rock) is plotted on the Shale background trend (Figure 5.2-Bottom).

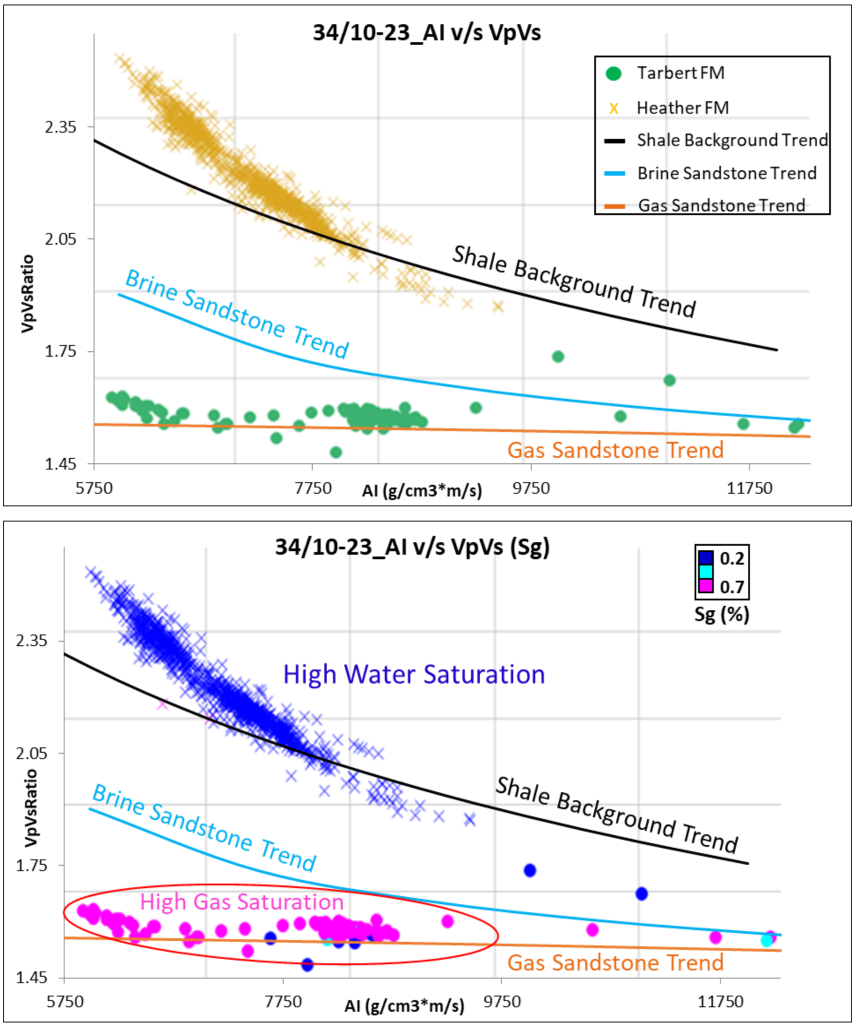

Figure 5. 2: The AI vs. VpVsRatio cross plot template for well 34/10-23. (Top) Displaying only Heather Formation (cap rock) and Tarbert Formation (reservoir rock). (Bottom) The AI vs. VpVsRatio cross plot template color-coded with the Gas saturation for well 34/10-23, exhibiting Heather Formation (cap rock) with low Sg along with the Shale background trend, whereas, Tarbert Formation (reservoir rock) with high Sg, along with the Gas Sandstone trend.

The AI vs. VpVsRatio cross plot color-coded with Total Porosity (PhiT) with a range between 0 to 25% shows porosity variation in both the formations. The Heather Formation (cap rock) mainly comprises porosity in the range of 8 to 16% and plotting on the Shale background trend. Moreover, the Tarbert Formation displays high porosity with the range of 16 to 25% and plotting on the Gas-bearing Sand (Figure 5.3-Top). The AI vs. VpVsRatio cross plot for well 34/10-23 color-coded with Clay Volume (Vclay) with a range between 0 to 100% demonstrates the presence of relatively high clay volume (more than 50%) in the Heather Formation (cap rock). Moreover, in Tarbert Formation, the clay volume is much lower (~30%) (Figure 5.3-Bottom).

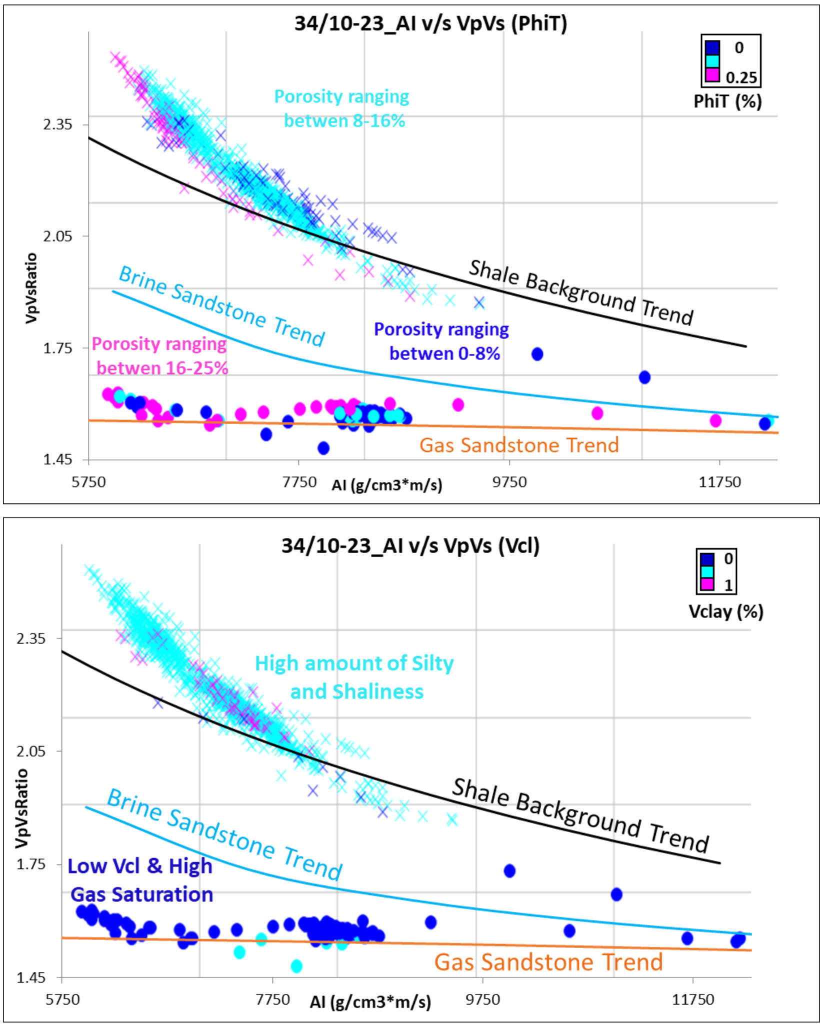

Figure 5. 3: The AI vs VpVsRatio cross plot template color-coded with the Clay Volume (Vclay) and Total Porosity (PhiT) for well 34/10-23. (Top) The cross plot color-coded with the Total Porosity (PhiT) - Heather Formation (cap rock) comprising moderate total porosity. On the other hand, the Tarbert Formation (reservoir rock) comprising high porosity. (Bottom) The cross plot color-coded with the Clay Volume (Vclay) - Heather Formation (cap rock) with high Vclay and Tarbert Formation (reservoir rock) with low Vclay.

5.1.1.2 Lambda-Rho versus Mu-Rho cross plot

The LMR crossplot adapted from Goodway et al., (1997), showing all formations present in the well 34/10-23 (Figure 5.4). All the formations follow the general trend in the LMR cross plot. The threshold cutoff porous Gas Sand line is at 20 LambdaRho value. This threshold line shows the presence of Gas Sand at the higher values of Mu-Rho and lower values of LambdaRho. Tarbert Formation can be seen plotting under the threshold cutoff porous Gas Sand and in the region of Gas Sand.

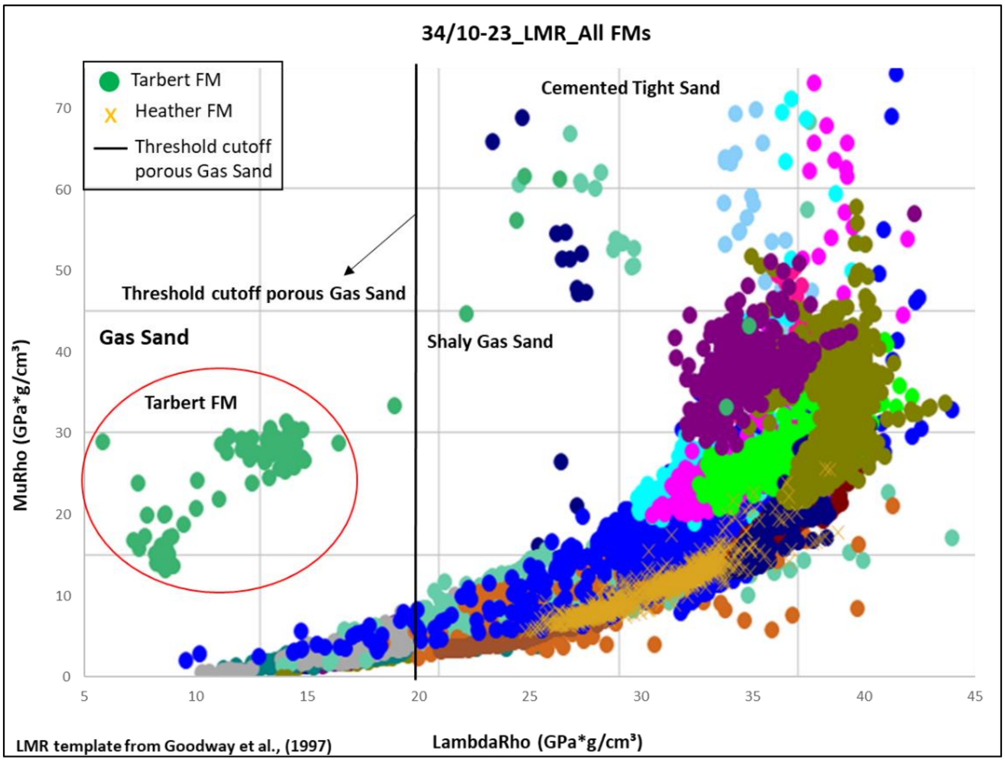

Figure 5. 4: The Lambda-Rho versus Mu-Rho (LMR) cross plot template, suggested by Goodway et al., (1997) for all the formations present in the well 34/10-23. The template comprises threshold cutoff porous Gas Sand at 20 GPa*g/cm3 of Lambda-Rho value. The color data points other than Heather and Tarbert Formations are representing different formations in well 34/10-23.

The LMR cross plot adapted from Goodway et al., (1997), color-coded with Gas Saturation (Sg), Clay Volume (Vcl), and Total Porosity (PhiT), in order to understand the reservoir properties for the target reservoir (Tarbert Formation) and the caprock (Heather Formation) in well 34/10-23. The Heather Formation is plotting in the LMR cross plot with relatively higher Lambda-Rho and lower Mu-Rho values. Whereas the Tarbert Formation is plotting with somewhat higher Mu-Rho and lower Lambda-Rho values. Moreover, the Tarbert Formation is plotting under the threshold cutoff for porous gas sand. According to the Goodway et al., (1997) the area under the threshold cutoff with higher Mu-Rho and lower Lambda-Rho values exhibits the area of Gas Sand data. (Figure 5.5-Top). The LMR cross plot color-coded with gas saturation (Sg) comprising a range between 20 to 70%. The color-coded cross plot shows the presence of high Sg (about 70%) in the Tarbert Formation.

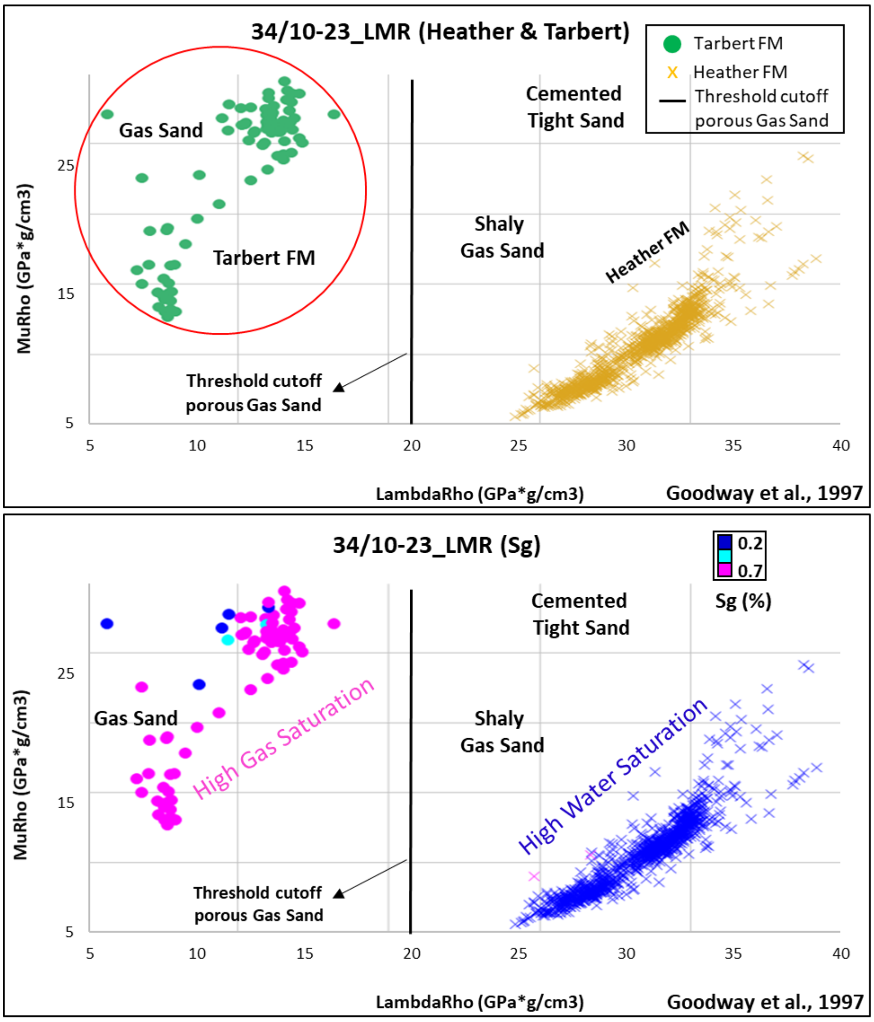

Figure 5. 5: The Lambda-Rho versus Mu-Rho (LMR) cross plot template, suggested by Goodway et al. (1997) for Heather (cap rock) and Tarbert (reservoir rock) Formations in well 34/10-23. (Top) The template display only Heather (cap rock) and Tarbert (reservoir rock) Formations. (Bottom) The LMR cross plot template color-coded with the gas saturation for both formations in well 34/10-23, exhibiting Heather Formation (cap rock) with high water saturation (dark blue color) and Tarbert Formation (reservoir rock) with high gas saturation (pink color) plotting under threshold cutoff for porous gas sand.

It is plotting with higher Mu-Rho and lower Lambda-Rho values under the threshold cutoff for porous gas sand. Whereas, presence of low Sg (about 20%) is prominent in the Heather Formation (cap rock) and plotting with relatively lower Mu-Rho and higher Lambda-Rho values (Figure 5.5-Bottom). The LMR cross plot color-coded with Clay Volume (Vclay) with a range between 0 to 100% shows the presence of relatively high clay volume (more than 50%, in light blue color) in the Heather Formation (cap rock) plotting on the higher and lower Mu-Rho and higher Lambda-Rho values. Moreover, the Tarbert Formation exhibiting clay volume relatively much lower (about 0 to 30%, in dark blue color) and plotting with higher Mu-Rho and lower Lambda-Rho values, plotting under the threshold cutoff for porous gas sand (Figure 5.6-top).

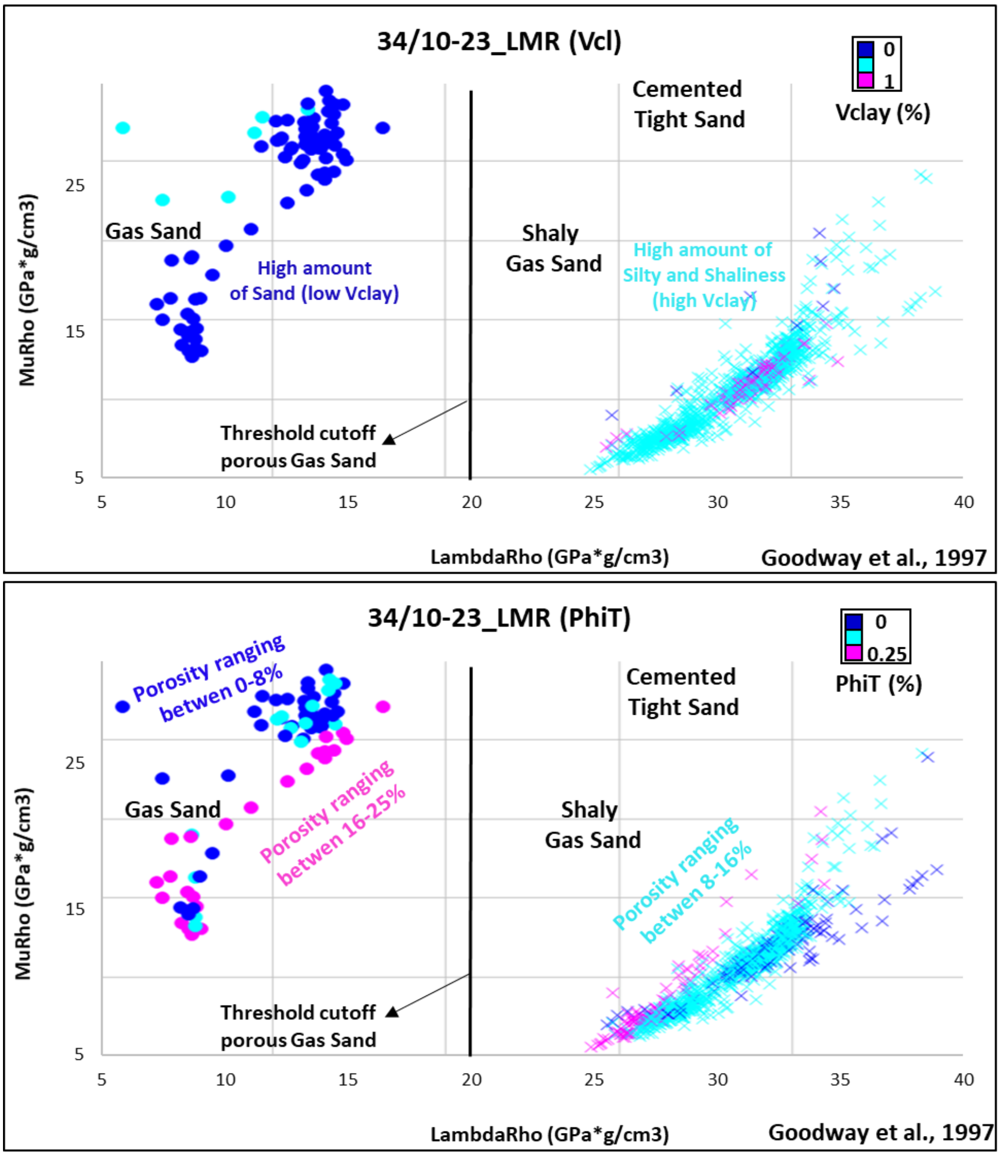

Figure 5. 6: The LMR cross plot template, suggested by (Goodway et al., 1997) color-coded with the Clay Volume (Vclay) and Total Porosity (PhiT) for the well 34/10-23. (Top) The cross plot color-coded with the Clay Volume (Vclay) - Heather Formation (cap rock) with high Vclay (light blue and pink color) and Tarbert Formation (reservoir rock) with low Vclay (dark blue color). (Bottom) The cross plot color-coded with the Total Porosity (PhiT) - Heather Formation (cap rock) majorly comprising moderate total porosity (light blue). The Tarbert Formation (reservoir rock) majorly comprising high porosity (pink color).

The LMR cross plot color-coded with Total Porosity (PhiT) with a range between 0 to 25%, display variation of porosity in the Heather and Tarbert Formations. The Heather Formation (cap rock) comprises porosity majorly in the range of 8 to 16% with higher Lambda-Rho values. Moreover, the Tarbert Formation comprises high porosity with the range of 16 to 25% and plotting with higher Mu-Rho values (Gas Sand area) (Figure 5.6-bottom).

5.1.1.3 PhiT versus Vp cross plot

The Porosity (PhiT) vs. Vp crossplot shows all formations present in well 34/10-23 (Figure 5.7). The template is known as Cement Model, and it consists of three curves, which are Contact Cement Model (gray curve), Constant Cement Model (blue curve), and Friable Clay-Quartz curve (red curve). In this well, most of the formations are plot under Friable Clay-Quartz curve, which shows no cementation, and under the Constant Cement Model trend, cementation is present with lower velocity and higher porosity values. Moreover, this template explains the trends of sorting and the increase of cement volume.

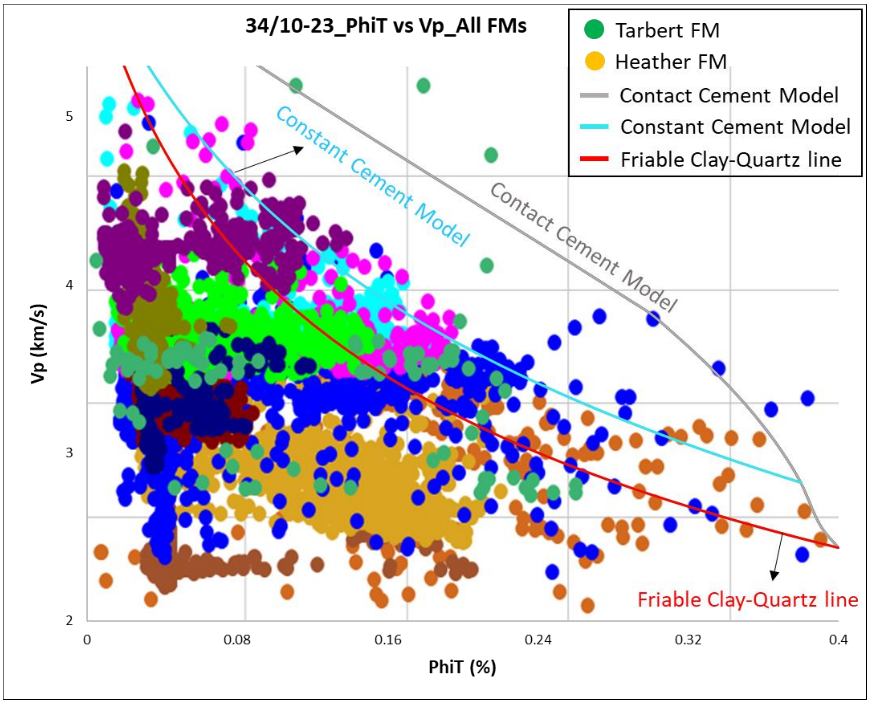

Figure 5. 7: The Porosity (PhiT) versus P-wave velocity (Vp) for all formations in the well 34/10-23. The cross plot consisting of cement models, such as, Friable Clay-Quartz curve (orange curve), Constant Cement Model (blue curve) and Contact Cement Model (gray curve). The color data points other than Heather and Tarbert Formations are representing different formations in well 34/10-23.

The Tarbert Formation can be seen plotting under the Friable Clay-Quartz curve, Constant Cement Model and few points near to Contact Cement Model trend, which shows Tarbert, comprises cementation and in between the grains, a cementation contact is present (Figure 5.8). Therefore, it is preserving the porosity that results in showing 2.8 to 3.6 km/s velocity. Moreover, the Tarbert Formation at depth 4084m has variations in porosity and showing low (about 1-9%) to high (14-24%) porosity. One interesting thing to note is that the Tarbert Formation is exhibiting relatively higher range of porosity compared to Heather Formation, even though the target reservoir formation is deeper than the cap rock formation. This characteristic of Tarbert Formation is due to the porosity preservation, as a result of cementation process.

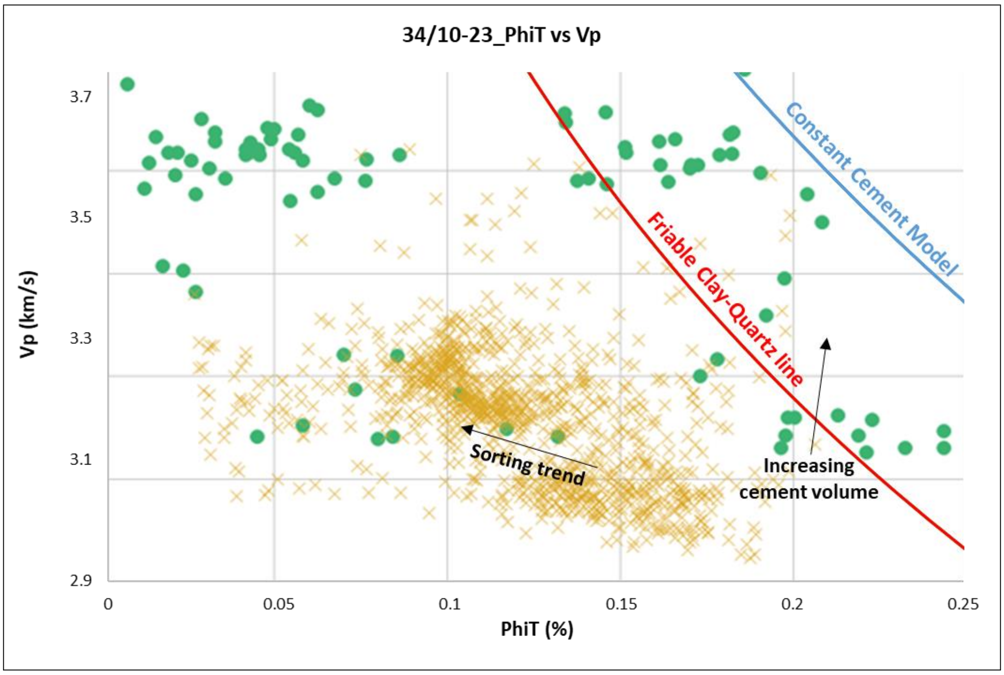

Figure 5. 8: The Porosity (PhiT) versus P-wave velocity (Vp) cross plot displaying only the Heather Formation (cap rock) and Tarbert Formation (reservoir rock) in the well 34/10-23. The cross plot also displaying the trend of sorting and increase of cement volume.

The PhiT vs Vp cross plot color-coded with the Gas Saturation (Sg) and Clay Volume (Vclay) are generated and discussed as follows. The cross plot color-coded with the gas saturation (Sg) for Tarbert Formation (target reservoir) and Heather Formation (cap rock), comprises high gas saturation (about 70%) in the Tarbert Formation at lower and higher porosity values. Whereas, the Heather Formation display high Water Saturation with relatively lower porosity values.

The cross plot color-coded with the clay volume (Vclay) for the Tarbert Formation display relatively low clay volume (about 30%) that means high sand percentage is present in the Tarbert Formation. Whereas, the Heather Formation shows variation in the clay volume but majorly display high percentage of clay volume (ranging between 60 to 100%).

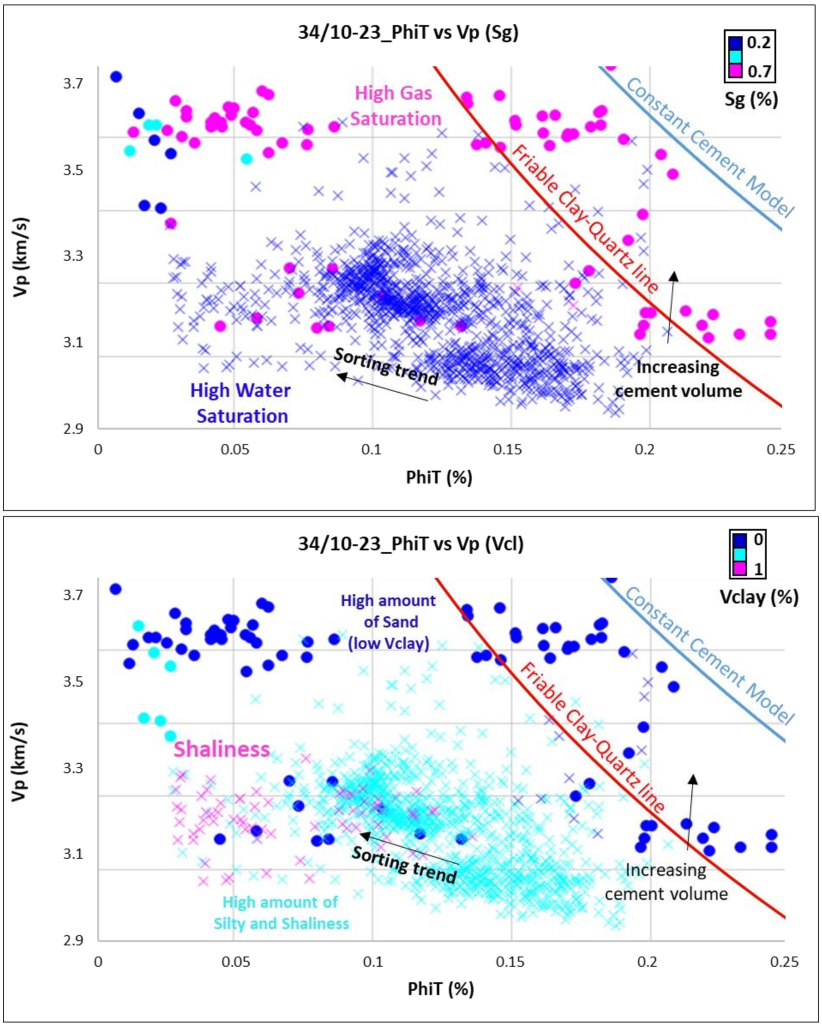

Figure 5. 9: The Porosity (PhiT) versus P-wave velocity (Vp) cross plot color-coded with gas saturation (Sg) and clay volume (Vclay) displaying only the Heather Formation (cap rock) and Tarbert Formation (reservoir rock) in the well 34/10-23. The cross plot also displaying the trend of sorting and increase of cement volume. (Top) The cross plot color-coded with gas saturation shows high gas saturation in the Tarbert Formation, whereas, low saturation in Heather Formation. (Bottom) The cross plot color-coded with clay volume display low clay volume in Tarbert Formation and high clay volume in Heather Formation.

5.1.1.4 Vp versus Vs cross plot

The Vp versus Vs crossplot template is generated from Interactive Petrophysics software (IP). The cross plot generated along with Sand and Shale trend lines for the Tarbert and Heather Formations present in the well 34/10-23 (Figure 5.10-Top). The Tarbert Formation is plotting over the Sand line; this might be due to the presence of gas saturation and the color-coding of Sg shows the Tarbert Formation comprises of about 70% gas saturation (Figure 5.10-Bottom). Whereas, the Heather Formation is plotting on the shale line (brine saturation) that displays the Heather Formation is high in water saturation and the color-coding of Sg displays the exact characteristic, Heather Formation comprising about 20% of gas saturation (Figure 5.10-bottom).

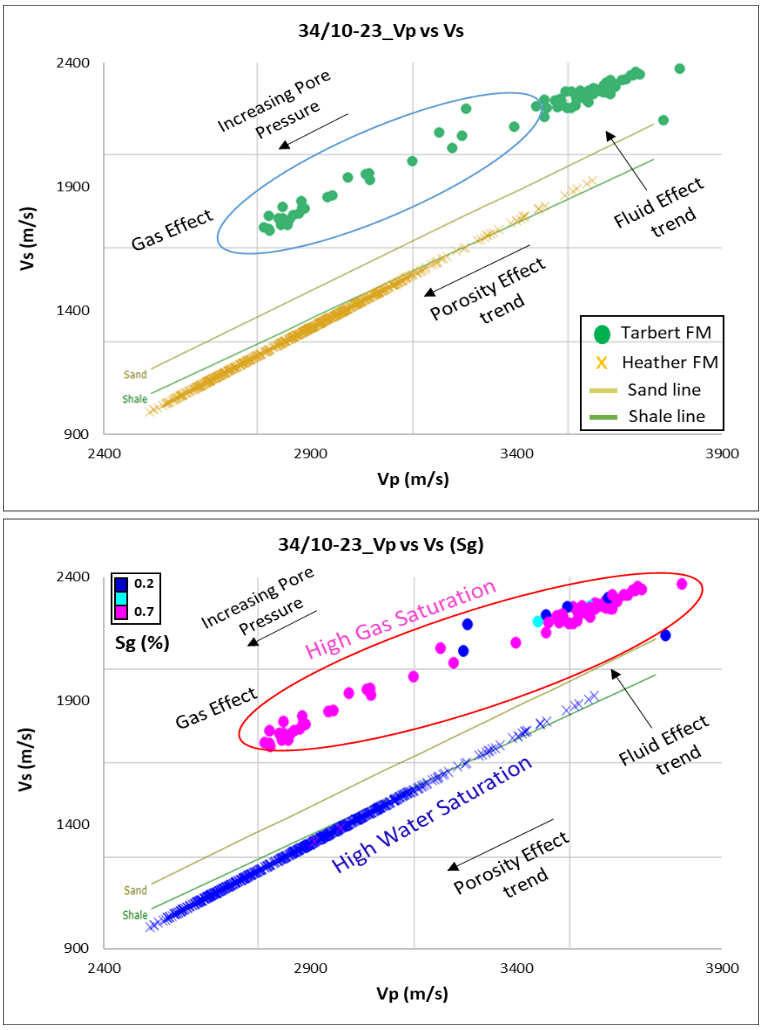

Figure 5. 10: (Top) The Vp versus Vs crossplot for Tarbert and Heather Formations in well 34/10-23, along with the Sand and Shale brine saturated trend lines. (Bottom) The Vp versus Vs crossplot color-coded with gas saturation (Sg), exhibiting relatively high gas saturation in the Tarbert Formation and relatively low gas saturation (high water saturation) in the Heather Formation. Additionally, displaying gas effect zone (blue oval), porosity effect, fluid effect and pore pressure increase trends.

The Vp versus Vs cross plot color-coded with Clay Volume (Vclay) with a range between 0 to 100%, shows presence of relatively high clay volume in the Heather Formation (cap rock). Moreover, the Tarbert Formation exhibiting clay volume relatively low, about 30% (Figure 5.11-Top). The Vp versus Vs cross plot color-coded with Total Porosity (PhiT) with a range between 0 to 25%, display variation of porosity in the Heather and Tarbert Formations. The Heather Formation (cap rock) comprises porosity in the range of 8 to 16% with linear trend on Shale line. Moreover, the Tarbert Formation comprises high porosity with the range of 16 to 25% and deviating from the Sand brine saturated line (Figure 5.11-Bottom).

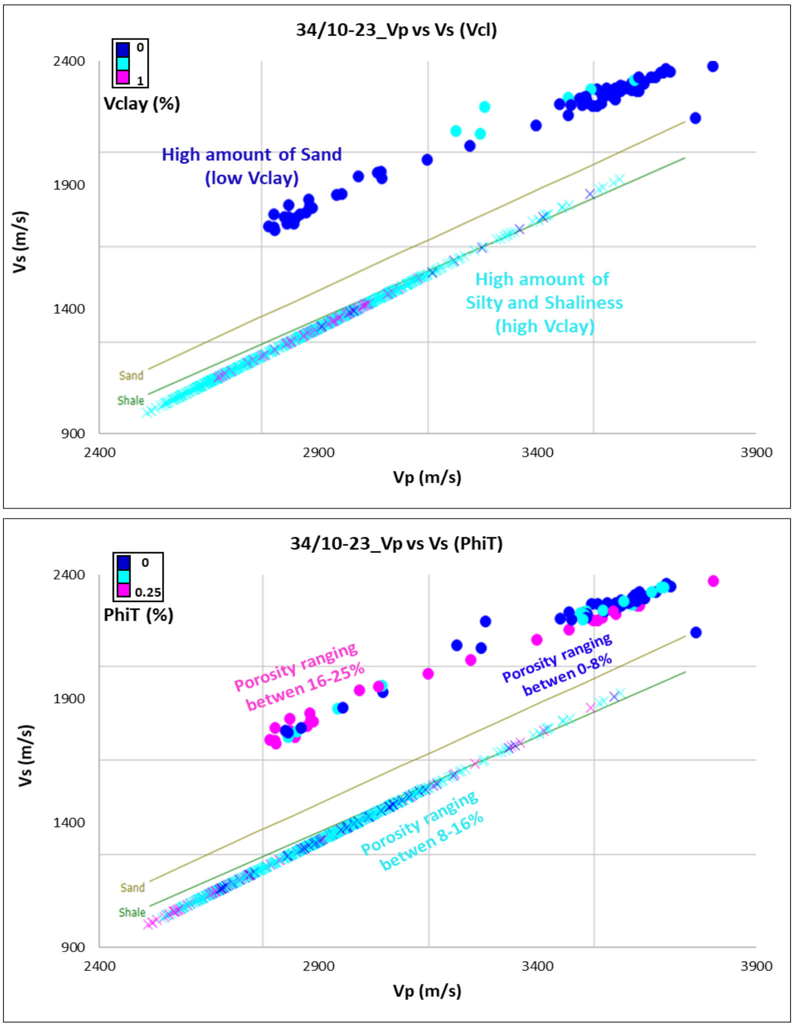

Figure 5. 11: (Top) The Vp versus Vs crossplot color-coded with clay volume (Vclay), exhibiting relatively low clay volume in the Tarbert Formation and relatively high clay volume (more silty and shaly) in the Heather Formation. (Bottom) The Vp versus Vs crossplot c color-coded with total porosity (PhiT) showing variations in the porosity but majorly comprising relatively high porosity (about 16-25%) in the Tarbert Formation. The Heather Formation display relatively low porosity (about 8-16%).

5.1.2 Results of Well: 34/10-42S

5.1.2.1 AI versus VpVsRatio cross plot

The AI versus VpVsRatio cross plot for the Heather Formation (cap rock) and the target reservoirs, which are Brent Group members (Tarbert, Ness, Etive, and Rannoch Formations) and Cook Formation present in the well 34/10-42S (Figure 5.12-Top). All the target formations are plotted between Shale Background Trend (black line) and Brine Sandstone Trend (blue line). Moreover, no formation can be seen plotting on Gas Sandstone Trend (orange line).

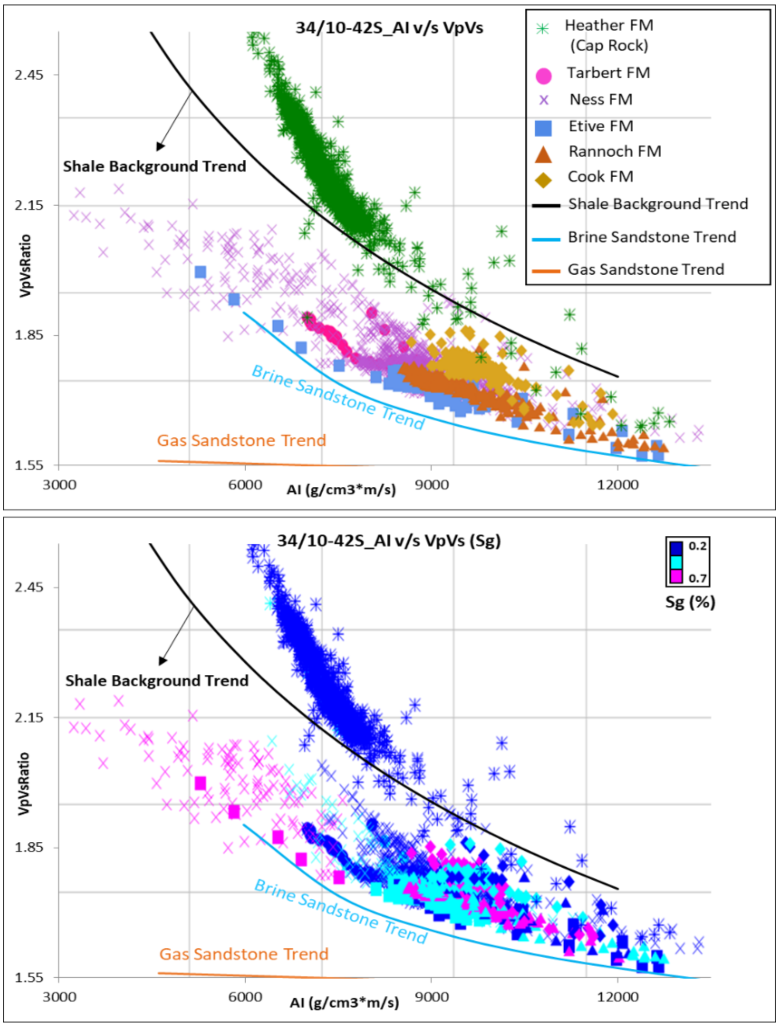

Figure 5. 12: (Top) The AI vs. VpVsRatio cross plot template comprises Shale background trend (black line), Brine Sandstone trend (blue line), and Gas Sandstone trend (orange line) for the Heather Formation and the target reservoirs Brent Group members (Tarbert, Ness, Etive, and Rannoch Formations) and Cook Formation present in the well 34/10-42S. (Bottom) The AI vs. VpVsRatio cross plot color-coded with gas saturation (Sg) exhibiting relatively high gas saturation in the target reservoirs, but all are plotting over the brine sandstone trend.

The AI vs. VpVsRatio crossplot color-coded with gas saturation (Sg) ranging between 20-70% shows the Brent Group (Tarbert, Ness, Etive, and Rannoch Formations) and Cook Formation comprising gas saturation, but the water saturation is relatively high in them. Moreover, the cross plot s that the high gas saturation points are plotted on the Brine Sandstone Trend and not on the Gas Sandstone Trend (Figure 5.12-Bottom). The AI vs. VpVsRatio crossplot color-coded with Clay Volume (Vclay) ranging in between 0-100% shows the Brent Group members and Cook Formation comprising low Vclay, shows the presence of Sand. This makes them a good reservoir quality rock (Figure 5.13-Top). The AI vs. VpVsRatio crossplot color-coded with Total Porosity (PhiT) ranging in between 0-40% shows the Brent Group members and Cook Formation comprising porosity majorly in the range of 13 to 40%. Therefore, characterizing a good quality reservoir rock (Figure 5.13-Bottom).

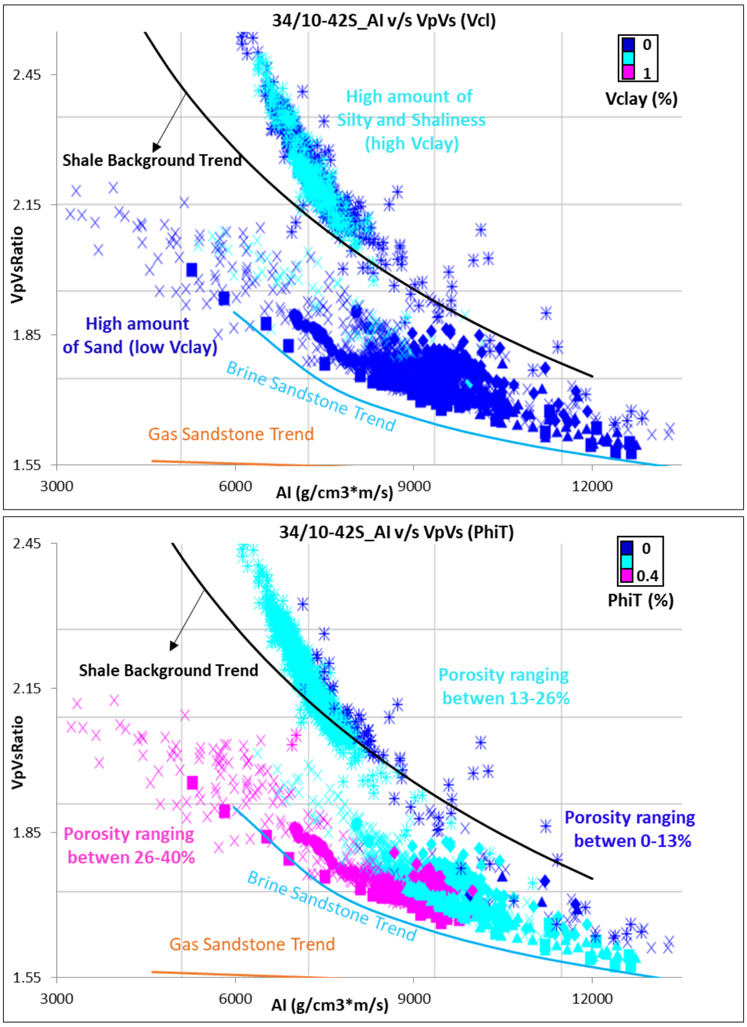

Figure 5. 13: (Top) The AI vs VpVsRatio cross plot color-coded with clay volume (Vclay) exhibiting relatively low Vclay in the target reservoirs, and all are plotting over the brine sandstone trend. Whereas, Heather Formation comprises a relatively high Vclay. (Bottom) The AI vs VpVsRatio cross plot color-coded with total porosity (PhiT) displaying relatively high porosity in the target reservoirs and relatively low in the Heather Formation.

5.1.2.2 Lambda-Rho versus Mu-Rho cross plot

The LMR crossplot adapted from Goodway et al., (1997), showing all formations present in the well 34/10-42S (Figure 5.14-Top). All the formations follow the general trend in the LMR cross plot. The Threshold cutoff porous Gas Sand line is at 20 Lambda-Rho value. This threshold line shows the presence of Gas Sand at the higher values of Mu-Rho and lower values of Lambda-Rho. Brent Group members and Cook Formation are plotting under the Threshold cutoff porous Gas Sand but with lower Mu-Rho and Lambda-Rho values, perhaps, displaying the presence of coal gas (Figure 5.14-Top). The LMR crossplot color-coded with Gas Saturation (Sg), Clay Volume (Vclay), and Total Porosity (PhiT) discussed as follows. The LMR crossplot color-coded with gas saturation (Sg) ranging 20-70%, shows the Brent Group members (Tarbert, Ness, Etive, and Rannoch Formations) and Cook Formation comprising relatively high gas saturation. Still, only the Ness and Etive Formations are plotting under the threshold cutoff porous Gas Sand with low Mu-Rho and Lambda-Rho values. Thus, it might be due to the presence of coal gas in both formations (Figure 5.14-Bottom).

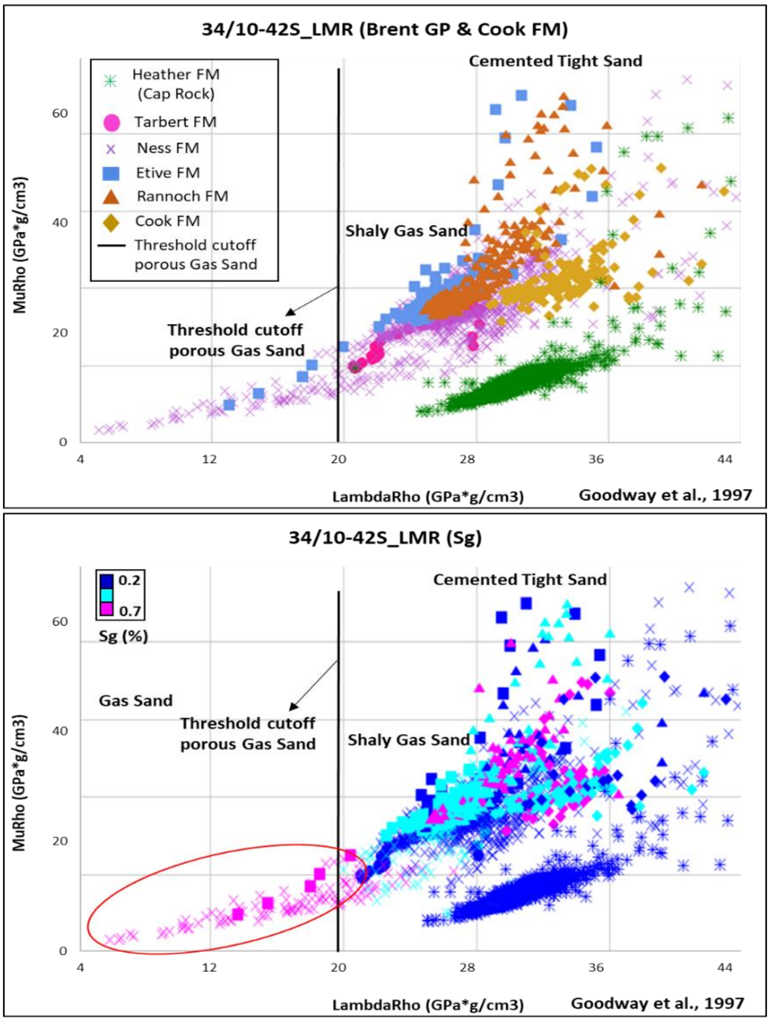

Figure 5. 14: (Top) The LMR cross plot for target reservoir Brent Group members and Cook Formation along with Heather Formation (cap rock). Only Ness and Etive Formations are plotting under the threshold cutoff for porous gas sand. (Bottom) The LMR cross plot color-coded with gas saturation (Sg) displaying relatively high gas saturation in Brent Group members and Cook Formation, but only Ness and Etive are seen under threshold cutoff for porous gas sand, perhaps exhibiting coal gas (red circle).

The LMR crossplot color-coded with Clay Volume (Vclay) shows the Brent Group members and Cook Formation comprising low Vclay. Whereas Heather Formation comprises a relatively high Vclay. (Figure 5.15-Top). The LMR crossplot is color-coded with Total Porosity (PhiT) displaying the Brent Group members and Cook Formation comprising relatively high porosity (ranging from 13 to 40%). Whereas, Heather Formation consists of relatively low porosity that is 13 to 26% (Figure 5.15-Bottom).

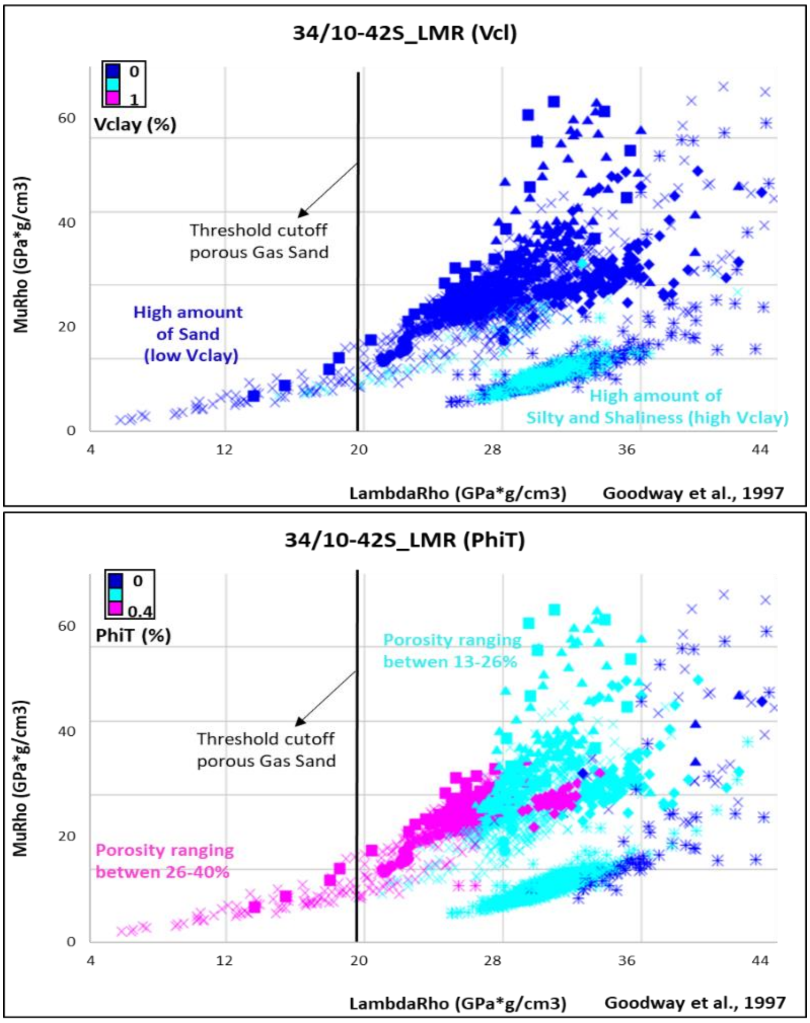

Figure 5. 15: (Top) The LMR cross plot template, suggested by Goodway et al., (1997) color-coded with Clay Volume (Vclay) for the target reservoir (Brent Group members and Cook Formation) and the cap rock (Heather Formation), exhibiting low Vclay in target reservoirs and relatively high Vclay in cap rock formation. (Bottom) The LMR cross plot color-coded with Total Porosity (PhiT) displaying relatively high porosity in the target reservoirs, whereas relatively low porosity in the cap rock formation.

5.1.3 Results of Well: 34/11-1

5.1.3.1 AI versus VpVsRatio cross plot

The AI versus VpVsRatio cross plot for all formations present in well 34/11-1. The formations are plotting on either Shale Background Trend (black line) or Brine Sandstone Trend (blue line), whereas only two formations are plotting on the Gas Sandstone Trend (orange line). Acoustic Impedance (AI) ranges between 2800 and 11500 (g/cm3*m/s) and VpVsRatio ranging between 1 and 2.7. The Heather Formation is plotting on Shale Background Trend, while the Tarbert and Ness Formations are plotting on and near to the Gas Sandstone Trend, shown with red circle (Figure 5.16). Moreover, the AI vs. Vp/Vs crossplots color-coded with Clay Volume

(Vclay), Gas Saturation (Sg), and Total Porosity (PhiT) in order to study the reservoir properties for well 34/11-1.

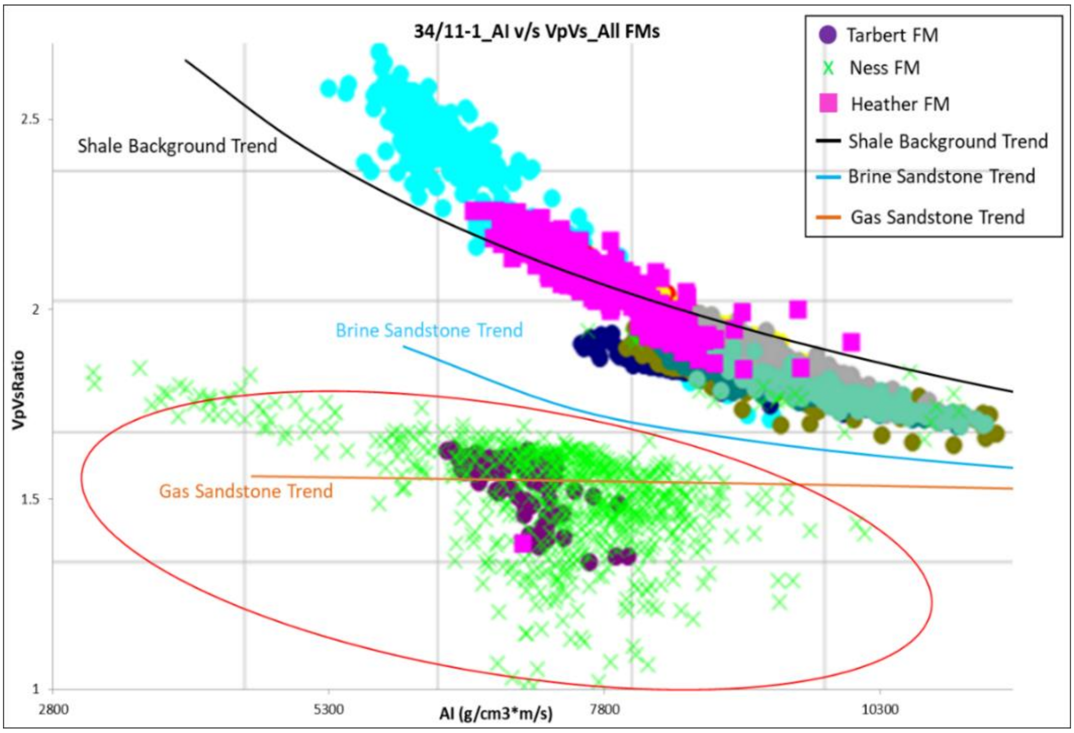

Figure 5. 16: The AI vs. VpVsRatio cross plot for the formations present in well 34/11-1, along with the Shale Background Trend (black line), Brine Sandstone Trend (blue line), and Gas Sandstone Trend (orange line). It is visible that the Tarbert and Ness Formations are plotting on the Gas Sandstone Trend line with relatively low VpVsRatio and AI values (red circle). The color data points other than Heather, Tarbert and Ness Formations are representing different formations in well 34/11-1.

The AI vs. VpVsRatio plot color-coded with Clay Volume (Vclay) shows relatively low Vclay in Tarbert Formation, whereas, in Ness Formation Vclay variation is present, but it can be considered relatively low Vclay. Here one thing to remember is that Tarbert Formation in this well comprises low thickness (15m) compared to Ness Formation (104m). The Heather Formation plots on Shale Background Trend and displays relatively high Vclay (silty and shaly) (Figure 5.17, A). The AI vs. VpVsRatio cross plot color-coded with Gas Saturation (Sg) shows the presence of high gas saturation in the Tarbert Formation (about 70%) and a portion of Ness Formation, both plotting on the Gas-bearing Sand Trend, whereas, low gas saturation (about 20%) exhibiting in the Heather Formation (cap rock), plotting on the Shale background trend (Figure 5.17, B).

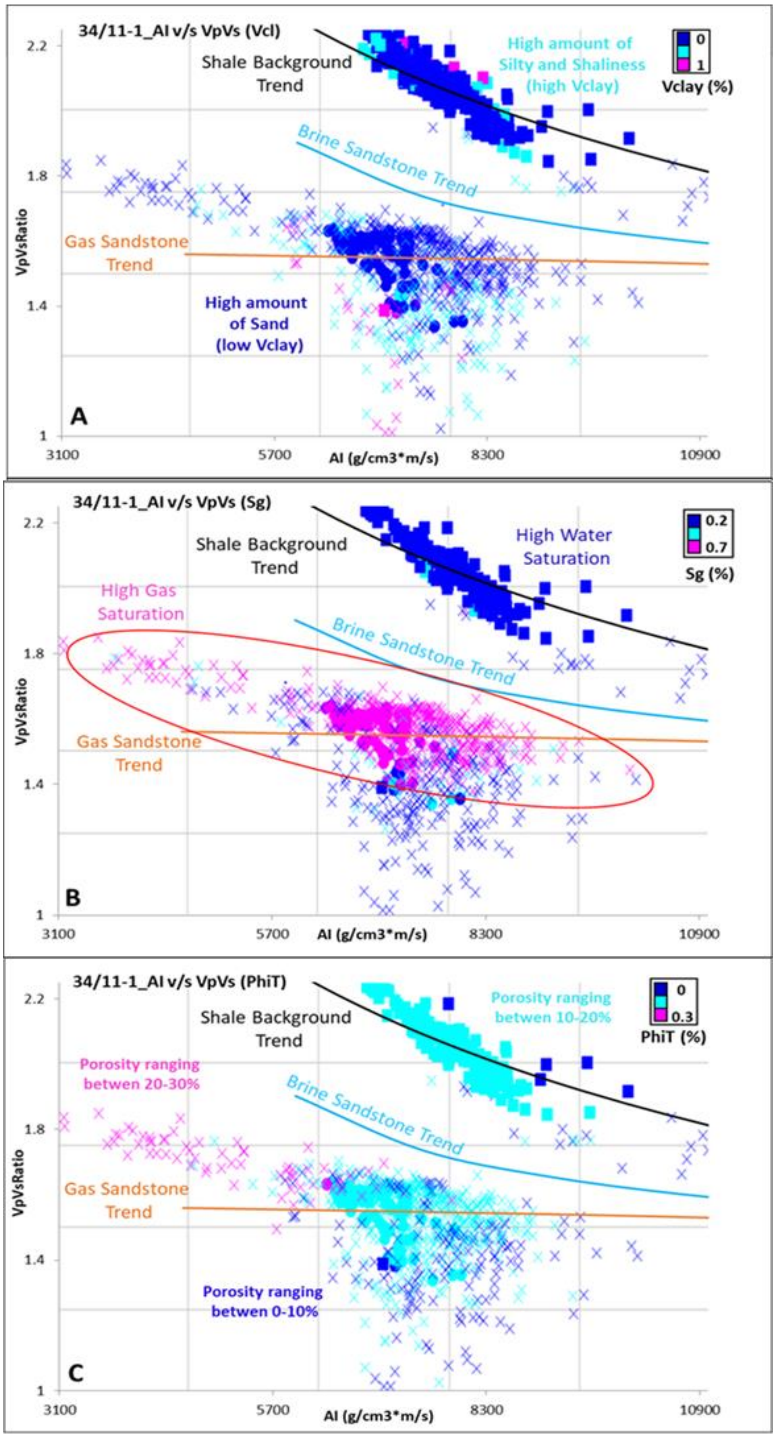

Figure 5. 17: (A) The AI vs VpVsRatio cross plot color-coded with Clay Volume (Vclay – range 0-100%), (B) Color-coded with Gas Saturation (Sg – range 20-70%) and (C) Color-coded with Total Porosity (PhiT – range 0-100%.

The AI vs. VpVsRatio plot color-coded with Total Porosity (PhiT) ranging between 0 to 30% explains that porosity ranges between 18 to 26% in Tarbert Formation. Whereas, the Ness Formation, being more thicker than Tarbert, porosity ranging between 10 to 30% but where high gas saturation in Ness Formation is present, at the same location porosity is high (Figure 5.17, C).

5.1.3.2 Lambda-Rho versus Mu-Rho cross plot

The LMR crossplot adapted from (Goodway et al., 1997) shows Tarbert and Ness Formations (target reservoirs) and Heather Formation (cap rock), present in the well 34/11-1 (Figure 5.18-top). All the formations follow the general trend in the LMR cross plot. The threshold cutoff porous Gas Sand line is at 20 Lambda-Rho value. This threshold line shows the presence of Gas Sand at the higher values of Mu-Rho and lower values of Lambda-Rho. The Heather Formation is plotting in the LMR cross plot with relatively higher Lambda-Rho and lower Mu-Rho values. Whereas the Tarbert and Ness Formations are plotting with relatively higher Mu-Rho and lower Lambda-Rho values, under the threshold cutoff for porous gas sand. Moreover, Ness Formation is 104m thick and exhibits lower to higher Mu-Rho values (Figure 5.18-Top).

The LMR crossplots are color-coded with Gas Saturation (Sg), Clay Volume (Vcl), and Total Porosity (PhiT) in order to understand the reservoir properties for target reservoir Tarbert and Ness Formations and the cap rock Heather Formation in well 34/11-1. The LMR cross plot color-coded with Gas Saturation (Sg) ranges between 20 to 70% (Figure 5.18-Bottom).

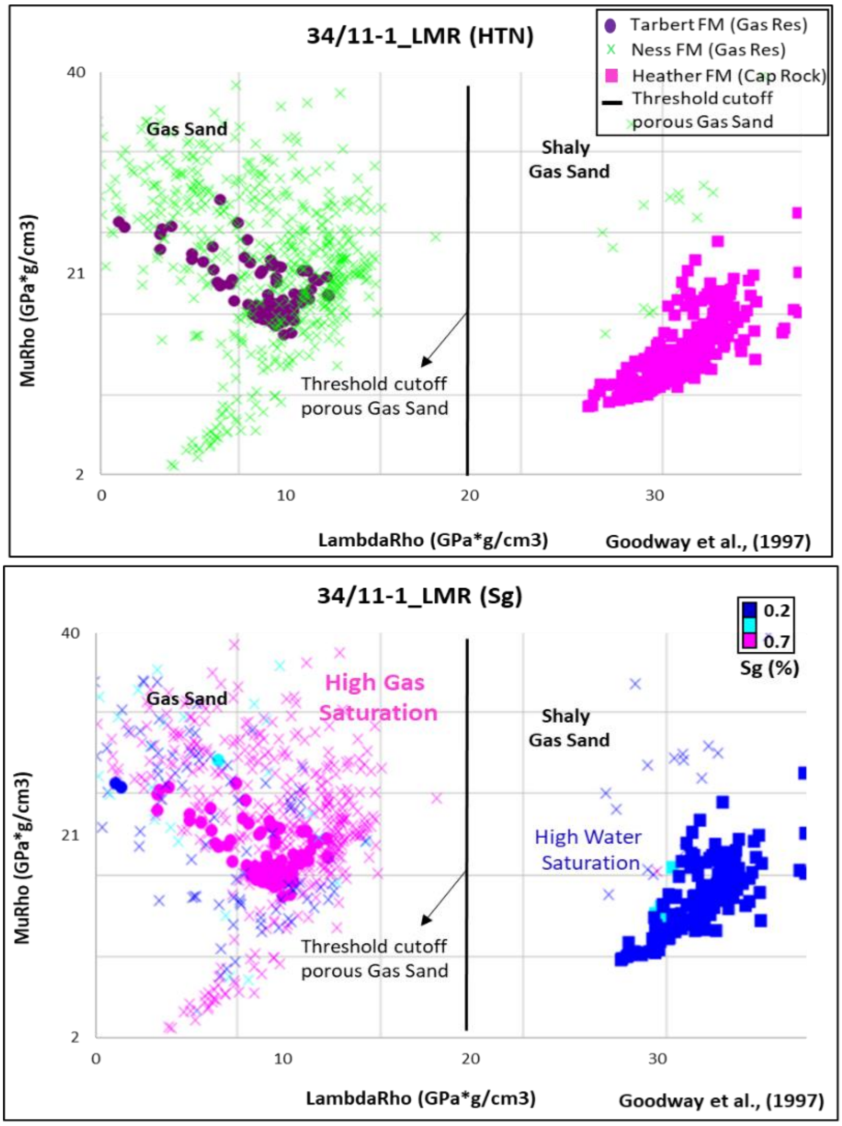

Figure 5. 18: The LMR cross plot suggested by (Goodway et al., 1997) presenting Tarbert and Ness Formations (reservoir rock) and Heather Formation (cap rock). (Top) The Tarbert and Ness Formations plot under the threshold cutoff porous Gas Sand with higher Mu-Rho and lower Lambda-Rho values. (Bottom) The LMR cross plot color-coded with Gas Saturation (Sg) exhibits relatively high gas saturation in the Tarbert and Ness Formations, whereas relatively low gas saturation in the Heather Formation.

The color-coded cross plot exhibit relatively high gas saturation in the Tarbert Formation (about 70%) and part of the Ness Formation. It plots with higher Mu-Rho and lower Lambda-Rho values under the threshold cutoff for porous gas sand. Whereas the Heather Formation (cap rock) shows relatively low gas saturation (about 20%) and plotting with relatively lower Mu-Rho and higher Lambda-Rho values (Figure 5.18-Bottom).

The LMR cross plot color-coded with Clay Volume (Vclay) displays the presence of relatively high clay volume (more than 50%) in the Heather Formation (cap rock) plotting on the higher and lower Mu-Rho and higher Lambda-Rho values. Moreover, the Tarbert and Ness Formations exhibit clay volume relatively much lower (about 30%) and plotting with higher Mu-Rho and lower Lambda-Rho values (Figure 5.19-Top).

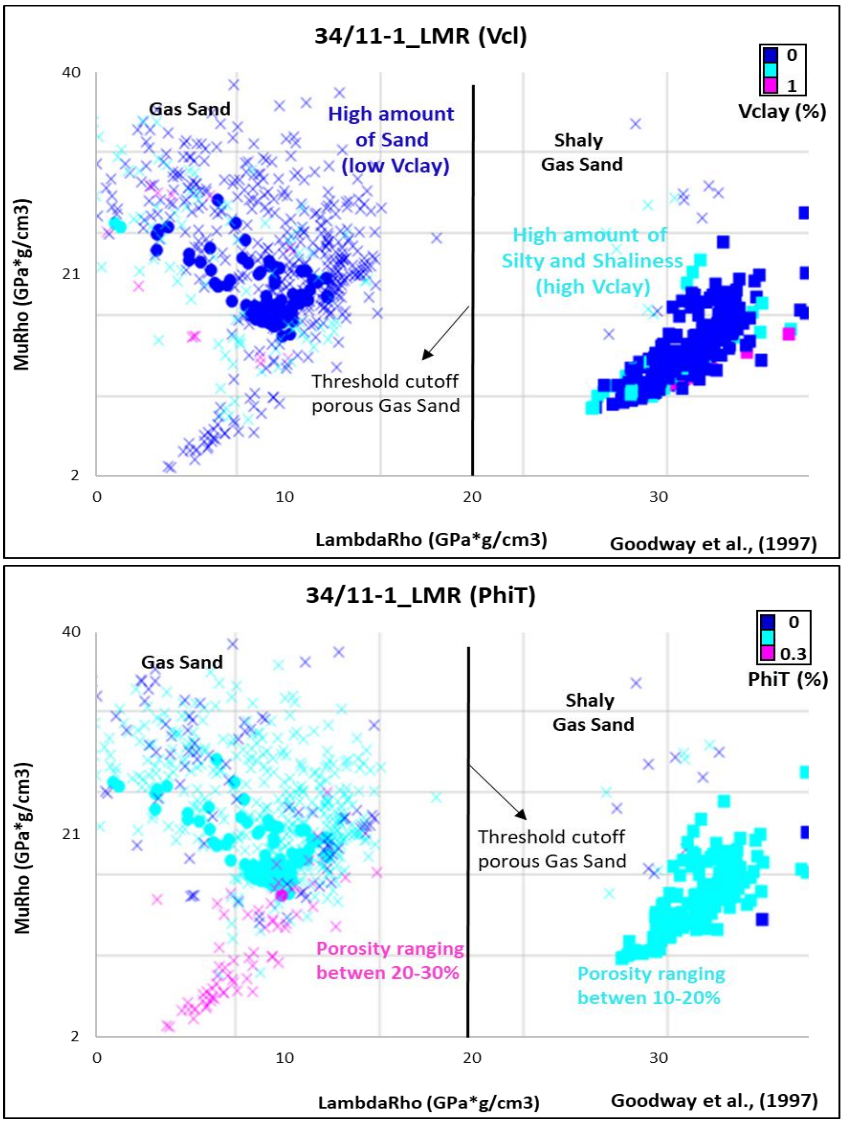

Figure 5. 19: (Top) The LMR cross plot color-coded with Clay Volume (Vclay), showing Tarbert and Ness Formations comprising relatively low Vclay, whereas Heather Formation consisting relatively more silt and shale that shows relatively high Vclay. (Bottom) The LMR cross plot color-coded with Total Porosity (PhiT) exhibits a relatively high porosity in the Tarbert and Ness Formations (12-30%), whereas a relatively low porosity (about 12-22%) in the Heather Formation.

The LMR cross plot color-coded with Total Porosity (PhiT) demonstrates variation of porosity in the Heather, Tarbert, and Ness Formations. The Heather Formation (cap rock) comprises porosity majorly in the range of 13 to 22% with higher Lambda-Rho values. Moreover, the Tarbert Formation comprises high porosity with the range of 18 to 29% and plotting with higher Mu-Rho values (Figure 5.6-Bottom). Whereas Ness Formation is relatively high in thickness displaying variation in porosity but, on average, showing relatively high porosity (about 12-30%).

5.1.3.3 PhiT versus Vp cross plot

The Porosity (PhiT) vs. Vp crossplot shows all formations present in the well 34/11-1 (Figure 5.20). The template is known as Cement Model, and it consists of three curves, which are Contact Cement Model (gray curve), Constant Cement Model (blue curve), and Friable Clay-Quartz curve (red curve). Moreover, this template explains the trends of sorting and the increase of cement volume. In this well, Tarbert Formation plotting under the Friable Clay-Quartz curve and Constant Cement Model, whereas Ness Formation spreading under all the three trends. The cross plot is displaying Tarbert and Ness Formations comprising relatively high porosity, about 20 to 28% and 10-35%, respectively. The possibility of cementation in the Tarbert Formation is present as the formation is plotting under the Constant Cement Model trend and proceeding towards it. Thus, not reaching the Contact Cement Model trend area. Even though Tarbert Formation is at a depth of 4045m, still displays high porosity. Perhaps, preserving the porosity because of the existence of cementation, additionally, the P-wave velocity (Vp) exhibiting higher values (2.9 to 3.3 km/s) (Figure 5.20, A). Whereas the Ness Formation distributed under the Friable Clay-Quartz curve, Constant Cement Model, and few points plotting near to the Contact Cement Model trend, which shows Ness Formation, comprises cementation contact in between the grains (Figure 5.20, A).

Therefore, it is preserving the porosity that results in showing 2.5 to 3.6 km/s P-wave velocity. Moreover, the Ness Formation at depth 4084m has variations in porosity and shows high porosity. One interesting thing to note is that Tarbert and Ness Formations are exhibiting a relatively higher porosity range than Heather Formation, even though the target reservoir formations are deeper than the cap rock formation. This characteristic of both formations is, perhaps, due to the cementation that led to porosity preservation. Moreover, the PhiT vs. Vp cross plot was generated with color-coding of Gas Saturation (Sg) and Clay Volume (Vclay) to understand the reservoir properties in the well. The cross plot color-coded with gas saturation (Sg) exhibits relatively high gas saturation in Tarbert and Ness Formations, at lower and higher porosity values (Figure 5.20, B). The cross plot color-coded with Clay Volume (Vclay) shows high sand percentage in Tarbert and Ness Formations, whereas, Ness Formation also consisting high silt and shale presence (Figure 5.20, C).

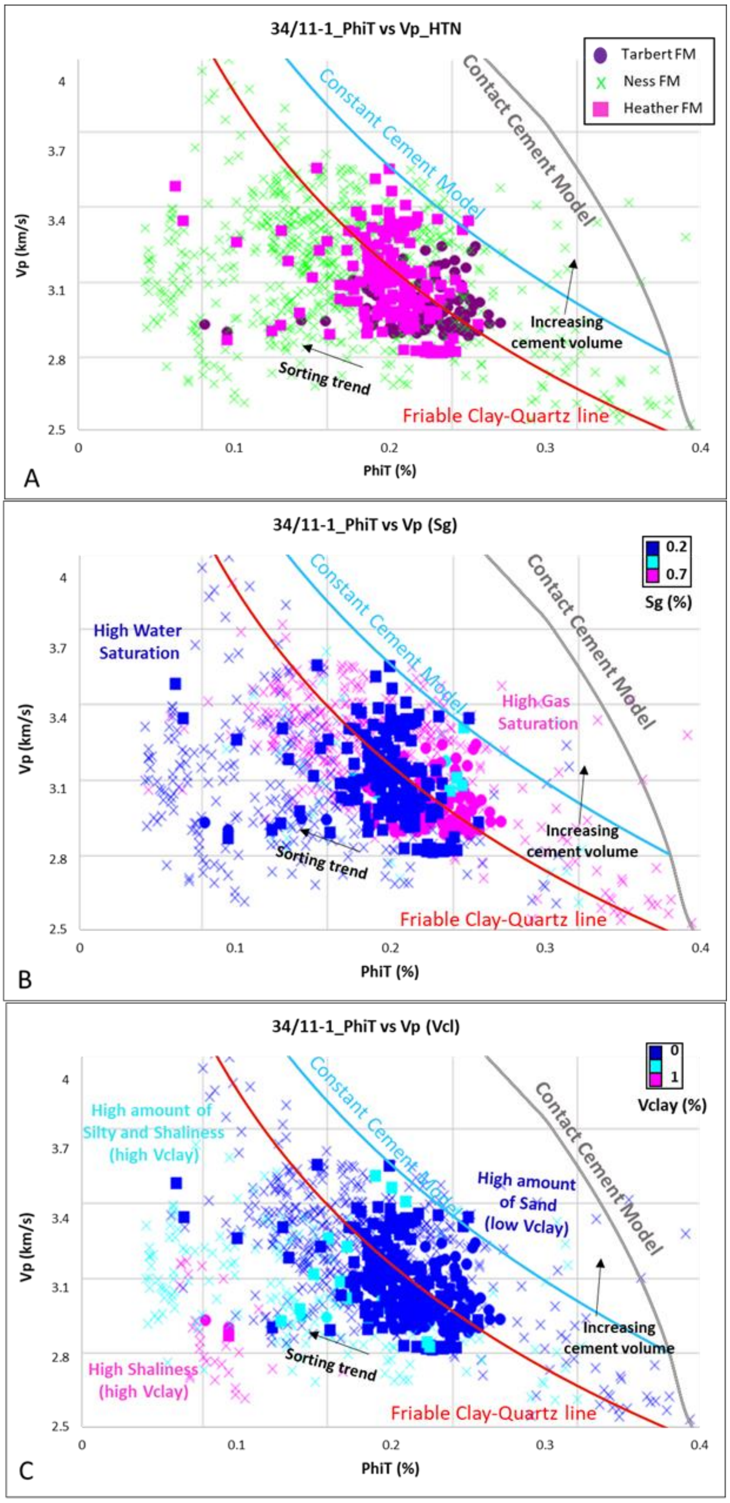

Figure 5. 20: (A) The PhiT vs. Vp cross plot exhibiting Heather, Tarbert, and Ness Formations in well 34/11-1. (B) The cross plot color-coded with Gas Saturation (Sg) shows relatively high Sg in the Tarbert and Ness Formations with somewhat higher PhiT and Vp values and Heather Formation comprising relatively low Sg. (C) The cross plot color-coded with Clay Volume (Vclay) shows relatively low Vclay in the Tarbert and Ness Formations. The Heather Formation relatively consists of silt and shale, therefore, displaying low Vclay.

5.1.3.4 Vp versus Vs cross plot

The Vp versus Vs crossplot template is generated from Interactive Petrophysics software (IP). The cross plot generated along with Brine Sand and Brine Shale trend lines for the Tarbert, Ness, and Heather Formations present in the well 34/11-1 (Figure 5.21-Top).

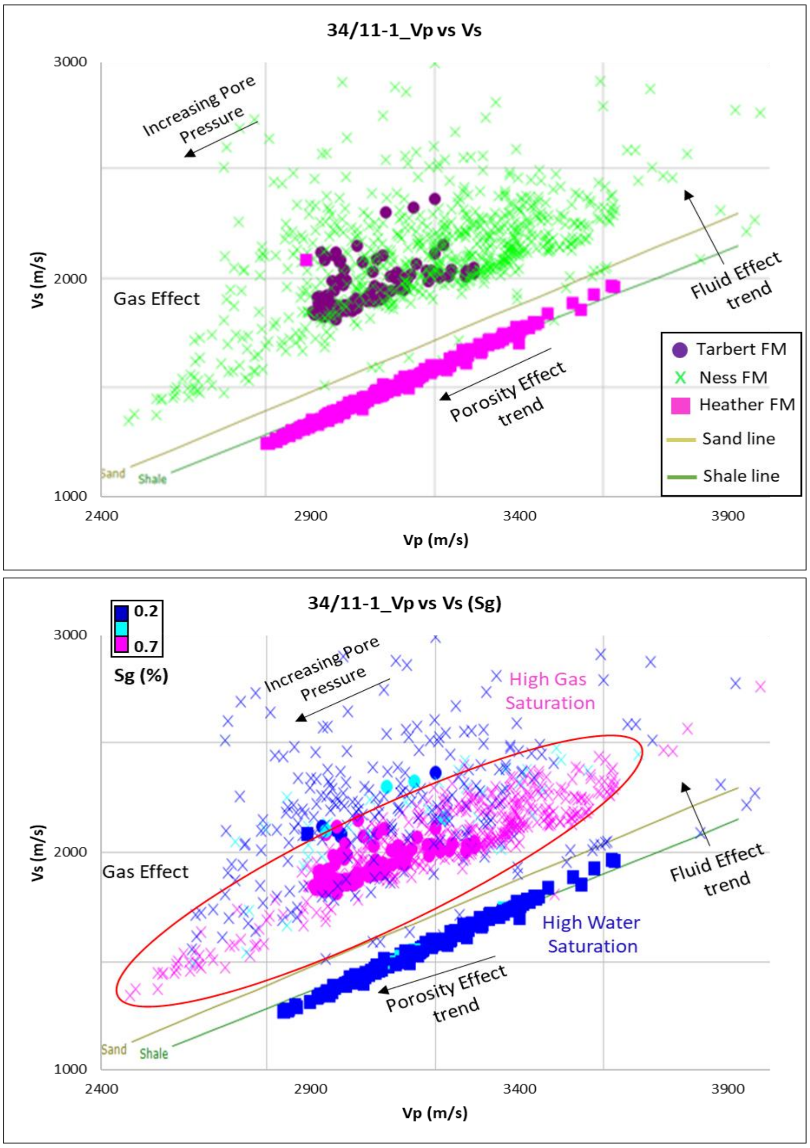

Figure 5. 21: (Top) The Vp versus Vs crossplot for Tarbert, Ness, and Heather Formations in the well 34/11-1 comprising Brine Sand and Brine Shale trends. Due to the fluid effect, the Tarbert and Ness Formations are shifting away from the Brine Sand trend. (Bottom) The cross plot color-coded with gas saturation (Sg) exhibits relatively high Sg in the Tarbert and Ness Formations.

The Tarbert and Ness Formations are plotting over the Sand line; this might be due to fluid saturation. Whereas Heather Formation (cap rock) plotting on the Shale line, comprising mainly shale. The cross plots generated with the color-coding of Gas Saturation (Sg), Clay Volume (Vclay), and Total Porosity (PhiT) for the well 34/11-1 are discussed as follows. The color-coding of Sg shows the Tarbert and Ness Formations comprised of relatively high gas saturation (about 70%) (Figure 5.21-Bottom).

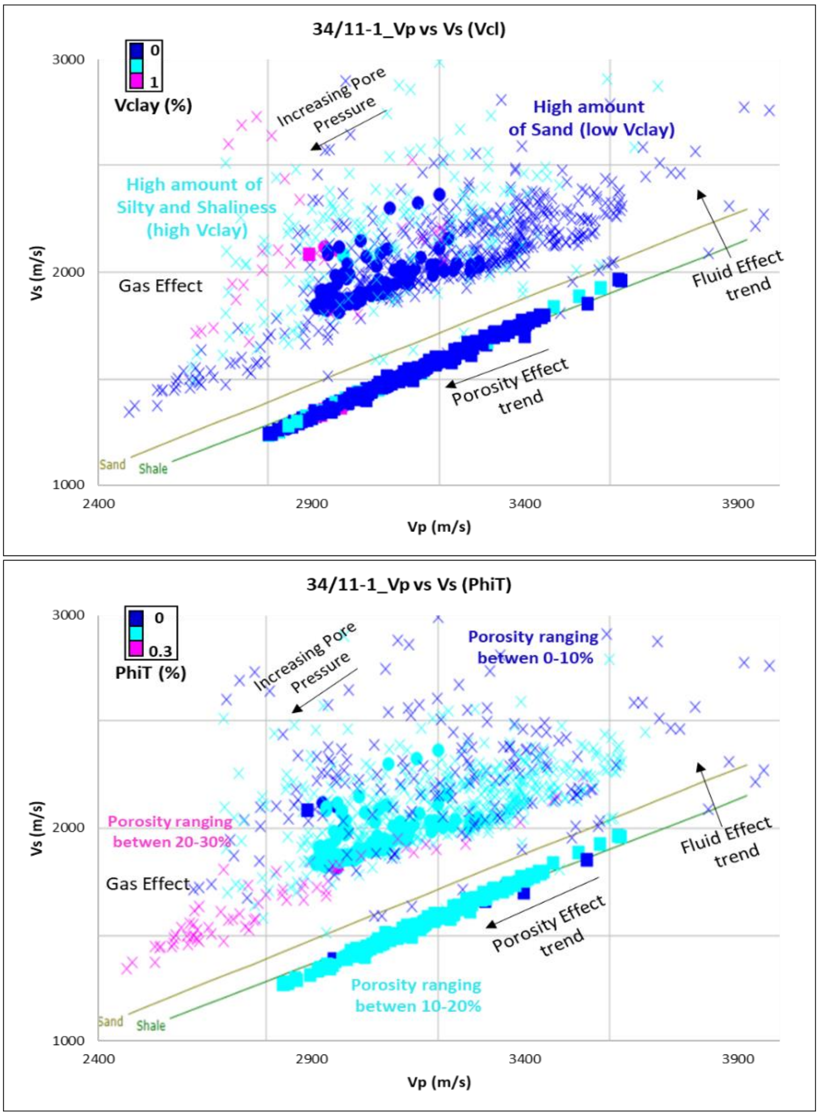

Figure 5. 22: (Top) The Vp versus Vs crossplot color-coded with clay volume (Vclay), exhibiting relatively low clay volume in the Tarbert and Ness Formations but Ness Formation also containing variation in Vclay. In the Heather Formation, relatively high clay volume is present (more silty and shaly). (Bottom) The Vp versus Vs crossplot color-coded with total porosity (PhiT) showing variations in the Tarbert and Ness Formations porosity but majorly comprising relatively high porosity. The Heather Formation displays relatively the same porosity trend as of Tarbert Formation as the Heather Formation consists of more silt than shale.

Whereas the Ness Formation being relatively more in thickness, shows variation in gas saturation. The Heather Formation plotting on the shale line (brine saturation) shows the Heather Formation is relatively low in Sg (Figure 5.21-Bottom).The Vp versus Vs cross plot color-coded with Clay Volume (Vclay) with a range between 0 to 100% shows relatively high clay volume in the Heather Formation (cap rock) plotting with the linear trend on shale line. Moreover, the Tarbert Formation exhibits clay volume relatively low and plotting with the non-linear trend with a deflection from the sand line (Figure 5.22-Top).

The Vp versus Vs cross plot color-coded with Total Porosity (PhiT) with a range between 0 to 100% display relatively high porosity in the Tarbert Formation. Whereas Ness Formation possesses variation in porosity but overall exhibits high porosity. The Heather Formation (cap rock) comprises porosity majorly in the range of 10 to 20% but comprising relatively low porosity. (Figure 5.22-Bottom).

5.1.4 Results of Well: 34/11-4

5.1.4.1 AI versus VpVsRatio cross plot

The AI versus VpVsRatio cross plot for all Tarbert, Ness, and Heather Formations present in the well 34/11-4. The Heather Formation is plotting on the Shale Background Trend (black line), whereas only Tarbert and Ness Formations are plotting on the Gas Sandstone Trend (orange line) highlighted with a red circle. Acoustic Impedance (AI) ranges between 3800 and 11550 (g/cm3*m/s) and VpVsRatio ranging between 1.2 and 2.3. (Figure 5.23-Top).

The AI vs. VpVsRatio cross plot color-coded with Gas Saturation (Sg) displaying the target reservoir formations Tarbert and Ness are relatively high in Sg and plotting on the template Gas Sandstone trend line with low VpVsRatio values. Several data points of the gas-bearing Ness Formation plotting are low in the cross plot (below 1.4 VpVsRatio value); therefore, this abnormality reflects the issues in data recording quality. Hence, we can ignore this error.

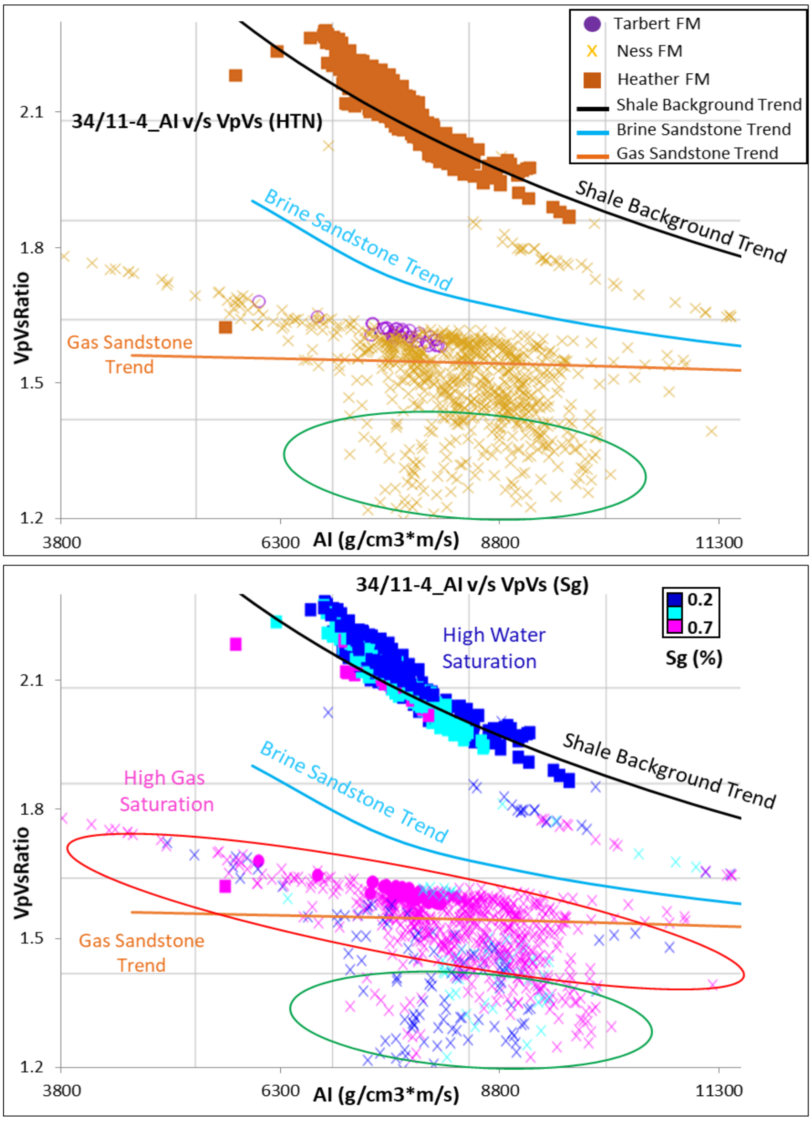

Figure 5. 23: (Top) The AI vs. VpVsRatio cross plot for the formations present in the well 34/11-4, along with the Shale Background Trend (black line), Brine Sandstone Trend (blue line), and Gas Sandstone Trend (orange line). It is visible that the Tarbert and Ness Formations are plotting on the Gas Sandstone Trend line with relatively low VpVsRatio (red circle). (Bottom) The cross plot color-coded with Gas Saturation (Sg) display Tarbert and Ness Formations comprises relatively high Sg and Heather Formation exhibiting relatively low Sg. The green circle displays the error in Ness Formation due to data recording quality.

The AI vs. VpVsRatio cross plot color-coded with Clay Volume (Vclay) displaying that Tarbert and Ness Formations comprises relatively low Vclay, whereas Ness Formation is thicker and thick contains lithology variation (Figure 5.24-Top). Therefore, Ness Formation is also exhibiting relatively high Vclay at some locations. The Heather Formation in this well comprises relatively low Vclay due to the presence of more silt in the formation, although it reflects as a good cap rock in this well (consult seal integrity LMR cross plot further in this chapter – Figure 5.54).

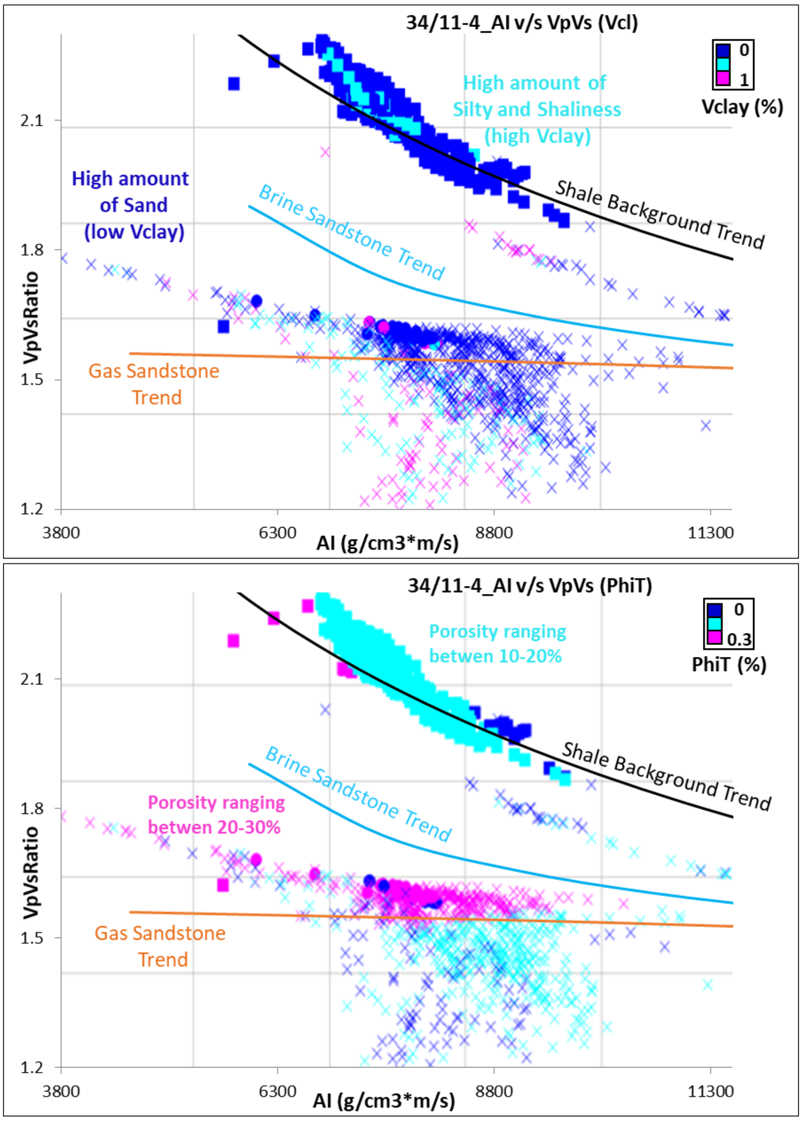

Figure 5. 24: (Top) The cross plot color-coded with Clay Volume (Vclay) display Tarbert and Ness Formations comprises relatively low Vclay. Additionally, Heather Formation exhibits relatively low Vclay to the presence of silt. (Bottom) The cross plot color-coded with Total Porosity (PhiT) display Tarbert and Ness Formations comprises relatively high PhiT, whereas Heather Formation exhibits relatively low PhiT.

5.1.4.2 Lambda-Rho versus Mu-Rho cross plot

The LMR crossplot adapted from Goodway et al., (1997) displaying the target reservoirs Tarbert and Ness Formations and cap rock Heather Formation, existing in the well 34/11-4 (Figure 5.25-Top). All three formations follow the general trend in the LMR cross plot. At 20 Lambda-Rho value, a threshold cutoff porous Gas Sand line is present. This threshold line shows the presence of Gas Sand at the higher values of Mu-Rho and lower values of Lambda-Rho.

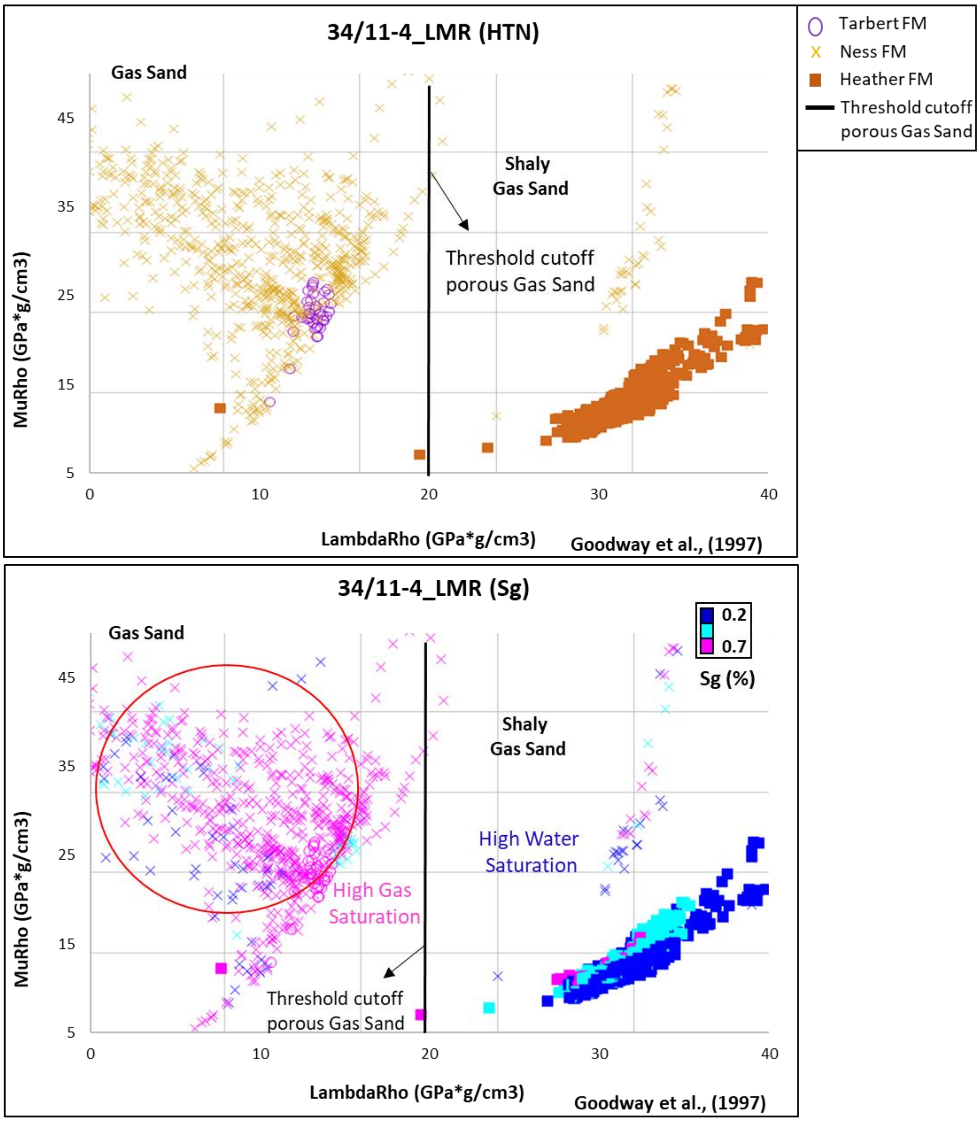

Figure 5. 25: The LMR cross plot suggested by Goodway et al., (1997) presenting Tarbert and Ness Formations (reservoir rock) and Heather Formation (cap rock) in the well 34/11-4. (Top) The Tarbert and Ness Formations are plotting under the threshold cutoff porous Ga Gas Sand with higher Mu-Rho and lower Lambda-Rho values, whereas Heather Formation plotting high Lambda-Rho values over the threshold cutoff. (Bottom) The LMR cross plot color-coded with Gas Saturation (Sg) exhibiting relatively high gas saturation in the Tarbert and Ness Formations, whereas, relatively low gas saturation in the Heather Formation.

The Heather Formation is plotting in the LMR cross plot with relatively higher Lambda-Rho and lower Mu-Rho values. Whereas the Tarbert and Ness Formations are plotting with somewhat higher Mu-Rho and lower Lambda-Rho values, under the threshold cutoff for porous gas sand. Moreover, Ness Formation is 129m thick and exhibits lower to higher Mu-Rho Lambda-Rho values (Figure 5.25-Top).

The LMR cross plot color-coded with Gas Saturation (Sg), Clay Volume (Vcl), and Total Porosity (PhiT) support in understanding reservoir properties for target reservoir Tarbert and Ness Formations and the cap rock Heather Formation in well 34/11-4. The LMR cross plot color-coded with Gas Saturation (Sg) ranges between 20 to 70% (Figure 5.25-bottom).

The Sg color-coded cross plot exhibits relatively high gas saturation in the Tarbert and Ness Formations. It plots with higher Mu-Rho and lower Lambda-Rho values under the threshold cutoff for porous gas sand, which displays the Gas Sand zone. Therefore, gas-bearing reservoirs plotting in the exact location and complement the template. Whereas the Heather Formation (cap rock) shows relatively low gas saturation (about 20%) and plotting with relatively lower Mu-Rho and higher Lambda-Rho values (Figure 5.25-Bottom).

The LMR cross plot color-coded with Clay Volume (Vclay) exhibiting Tarbert and Ness Formations comprising relatively low Vclay, moreover, displaying Vclay variations in the Ness Formation because of its lithology variations and high thickness (129m). The Heather Formation in this well comprises mainly silt, therefore, exhibiting low Vclay but also consisting more than 50% Vclay and at some places displaying high Vclay (Figure 5.26-Top).

The LMR cross plot color-coded with Total Porosity (PhiT) demonstrates a variation of porosity in the Heather, Tarbert, and Ness Formations. The Heather Formation (cap rock) comprises porosity majorly in the range of 13 to 26% with higher Lambda-Rho values. Moreover, the Tarbert Formation comprises high porosity with the range of 30 to 40% and plotting with higher Mu-Rho values (Figure 5.26-Bottom). Ness Formation is relatively high in thickness displaying variation in porosity but, on average, showing relatively high porosity (about 13-40%).

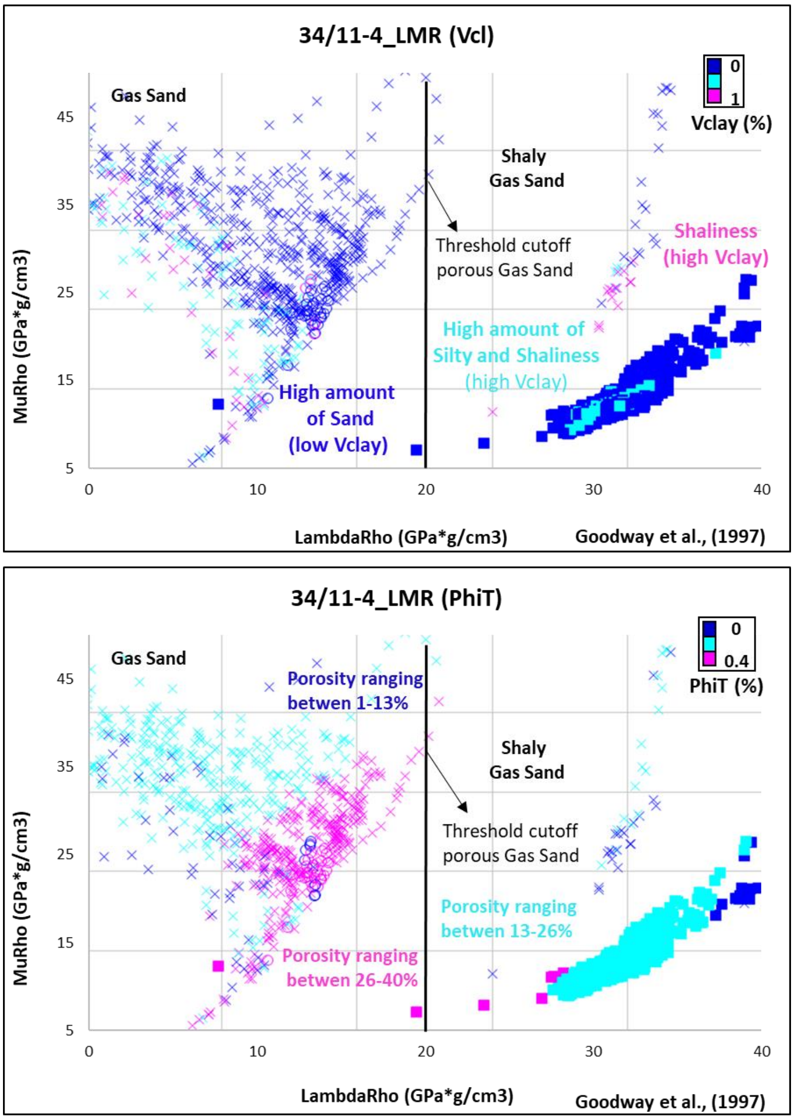

Figure 5. 26: (Top) The LMR cross plot color-coded with Clay Volume (Vclay) displaying Tarbert and Ness Formations comprising relatively low Vclay, whereas Ness Formation showing variation in Vclay due to lithology variation. The Heather Formation is exhibiting variation in Vclay but generally low due to silt in the formation. (Bottom) The LMR cross plot color-coded with Total Porosity (PhiT) unveiled relatively high porosity in the Tarbert and Ness Formations, whereas relatively low porosity in the Heather Formation.

5.1.4.3 PhiT versus Vp cross plot

The Porosity (PhiT) vs. Vp crossplot showing Tarbert, Ness, and Heather Formations present in the well 34/11-4 (Figure 5.27-top). The template is known as Cement Model, and it consists of three curves, which are Contact Cement Model (gray curve), Constant Cement Model (blue curve), and Friable Clay-Quartz curve (red curve). Moreover, this template explains the trends of sorting and the increase of cement volume. In this well, Tarbert Formation plotting under the Friable Clay-Quartz curve and Contact Cement Model, whereas Ness Formation spreading under all the three trends. The cross plot displays Tarbert and Ness Formations comprising relatively high porosity, about 30 to 40% and 13-40%, respectively.

The possibility of cementation in the Tarbert Formation is present as the formation is plotting on the Contact Cement Model trend. Even though Tarbert Formation is at a depth of 4045 m, still displaying high porosity, due to the porosity preserving as Tarbert Formation plotting on Contact Cementation Model trend. Additionally, the P-wave velocity (Vp) exhibited higher values (3.3 to 3.6km/s) (Figure 5.27-Top).

The Ness Formation distributed under the Friable Clay-Quartz curve, on the Constant Cement Model and on the Contact Cement Model, which shows Ness Formation, comprises cementation contact in between the grains (Figure 5.27-Top). Therefore, it preserves the porosity that results in showing 2.7 to 4km/s P-wave velocity. Moreover, the Ness Formation at depth 4084m has variations in porosity, and shows relatively high porosity. One interesting thing to note is that Tarbert and Ness Formations are exhibiting a relatively higher porosity than Heather Formation, even though the target reservoir formations are deeper than the cap rock formation. This characteristic of both formations is, perhaps, due to the cementation that led to porosity preservation.

Moreover, the PhiT vs. Vp cross plot was generated with color-coding of Gas Saturation (Sg) and Clay Volume (Vclay) to examine the reservoir properties in the target reservoirs (Tarbert and Ness). The cross plot color-coded with gas saturation (Sg) exhibits relatively high gas saturation in Tarbert and Ness Formations, at higher porosity values (Figure 5.27-Bottom).

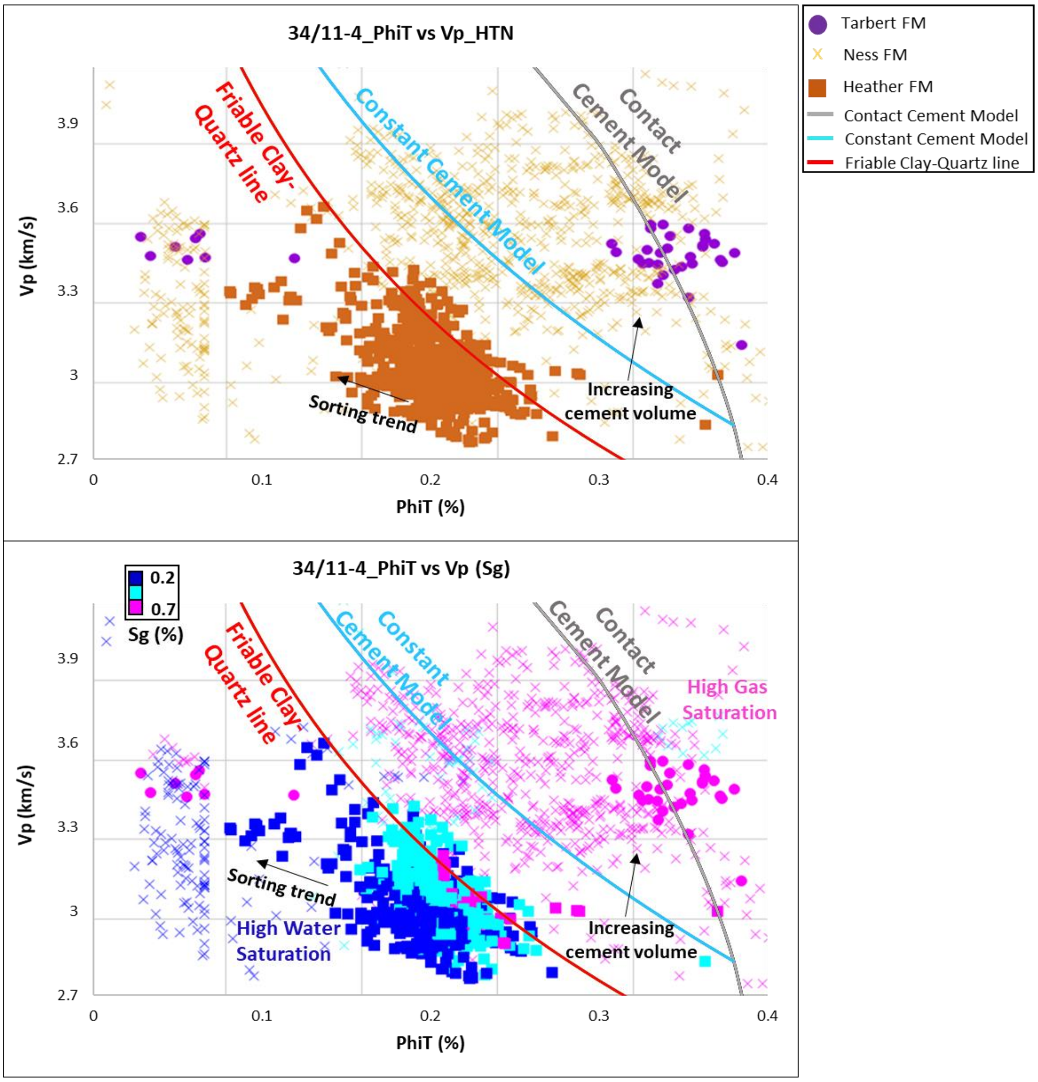

Figure 5. 27: (Top) The PhiT vs. Vp cross plot consists of Friable Clay-Quartz curve, Constant Cement Model trend and Constant Cement Model trend, exhibiting Heather, Tarbert, and Ness Formations in the well 34/11-4 displaying Tarbert and Ness Formation plotting with high porosity on Contact Cement Model that explains both the formations comprises cementation. The Heather Formation is seen plotting on the Friable Clay-Quartz curve with relatively low porosity values. (Bottom) The cross plot color-coded with Gas Saturation (Sg) shows relatively high Sg in the Tarbert and Ness Formations with somewhat higher PhiT and Vp values and Heather Formation comprising relatively low Sg.

The cross plot color-coded with Clay Volume (Vclay) shows high sand in Tarbert and Ness Formations, whereas, Ness Formation also has high silt and shale presence (Figure 5.28). Furthermore, the Heather Formation plotting on Friable Clay-Quartz curve shows a relatively low Vclay due to its silt presence (Figure 5.28).

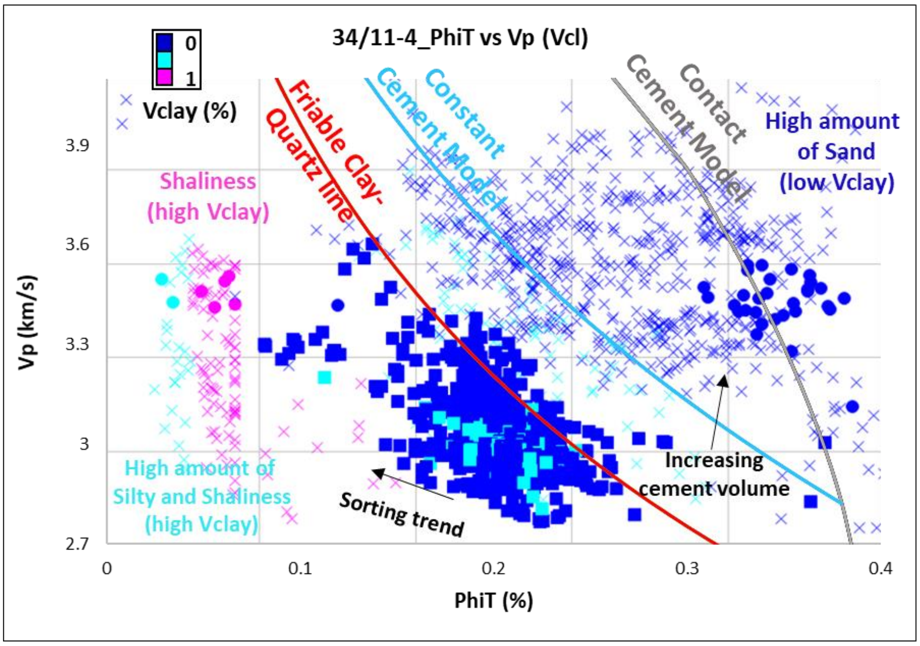

Figure 5. 28: The cross plot color-coded with Clay Volume (Vclay) shows relatively low Vclay in the Tarbert and Ness Formations. The Heather Formation is instead consisting of silt and shale, therefore, displaying low Vclay.

5.1.4.4 Vp versus Vs cross plot

The Vp versus Vs crossplot template is generated from the software Interactive Petrophysics (IP). The cross plot generated along with Brine Sand and Brine Shale trend lines can be picked in the setting manual before generating the cross plot. The cross plot displays target reservoir formations Tarbert and Ness, and cap rock Heather Formation present in the well 34/11-4 (Figure 5.21-Top). The Tarbert and Ness Formations are plotting over the Brine Sand line; this might be due to fluid saturation as the data deviates from brine sand trend when it encounters any fluid effect. Whereas Heather Formation (cap rock) plotting on the Brine Shale line shows the presence of shale or silt.

The cross plots generated with the color-coding of Gas Saturation (Sg), Clay Volume (Vclay), and Total Porosity (PhiT) for well 34/11-4 are discussed as follows. The color-coding of Sg shows the Tarbert and Ness Formations comprised of relatively high gas saturation (about 70%) (Figure 5.29-Bottom). Whereas the Ness Formation being relatively more in thickness, shows variation in gas saturation. The Heather Formation plotting on the shale line (brine saturation) displays the Heather Formation is relatively low in Sg (Figure 5.29-Bottom).

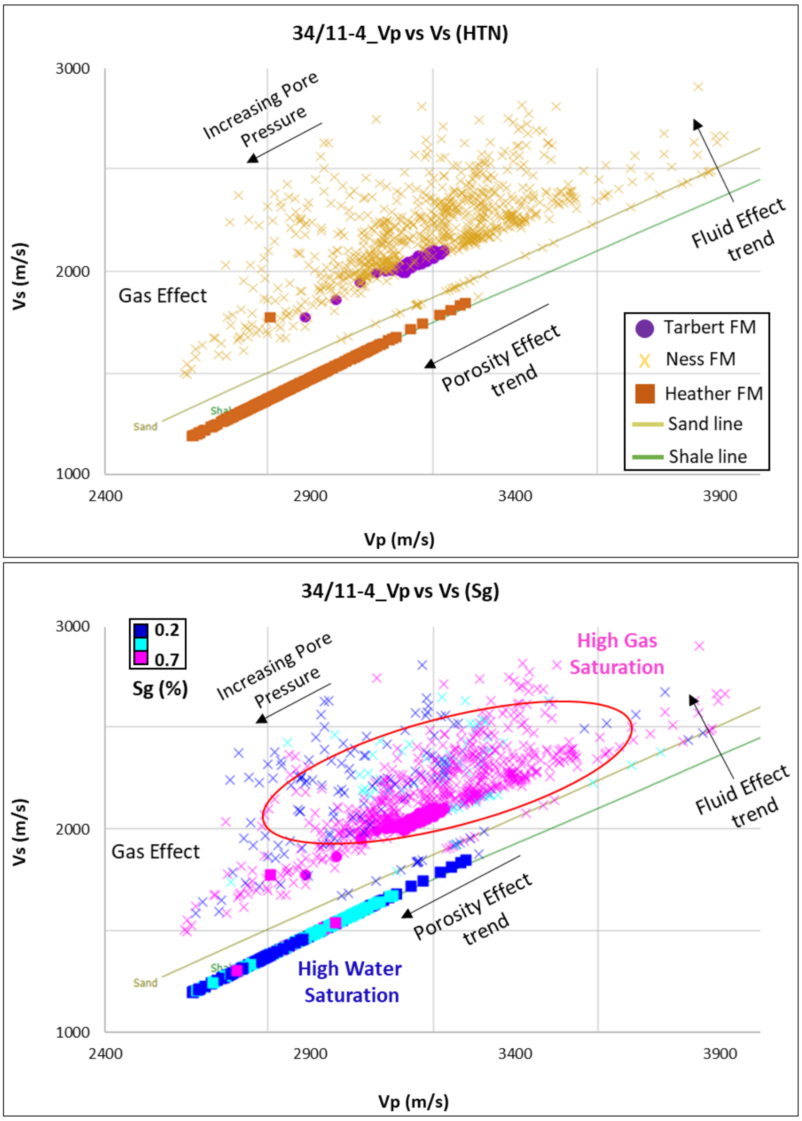

Figure 5. 29: (Top) The Vp versus Vs crossplot for Tarbert, Ness, and Heather Formations in the well 34/11-4 comprising Brine Sand and Brine Shale trends. The Tarbert and Ness Formations are shifting away from the Brine Sand trend due to the fluid effect. (Bottom) The cross plot color-coded with gas saturation (Sg) exhibits relatively high Sg in the Tarbert and Ness Formations and low in caprock Heather Formation.

The Vp versus Vs cross plot color-coded with Clay Volume (Vclay) shows the presence of relatively low clay volume in the Tarbert and Ness Formations, whereas Ness possesses Vclay variations in it as well (Figure 5.30-Top). Moreover, the Vp versus Vs cross plot color-coded with Total Porosity (PhiT) display relatively high porosity in the Tarbert and Ness Formations. Whereas, Ness being more in thickness than Tarbert, therefore, show porosity variations in it. The Heather Formation (cap rock) comprises porosity majorly in the range of 13 to 26%, with a linear trend exhibiting on the shale line (Figure 5.30-Bottom).

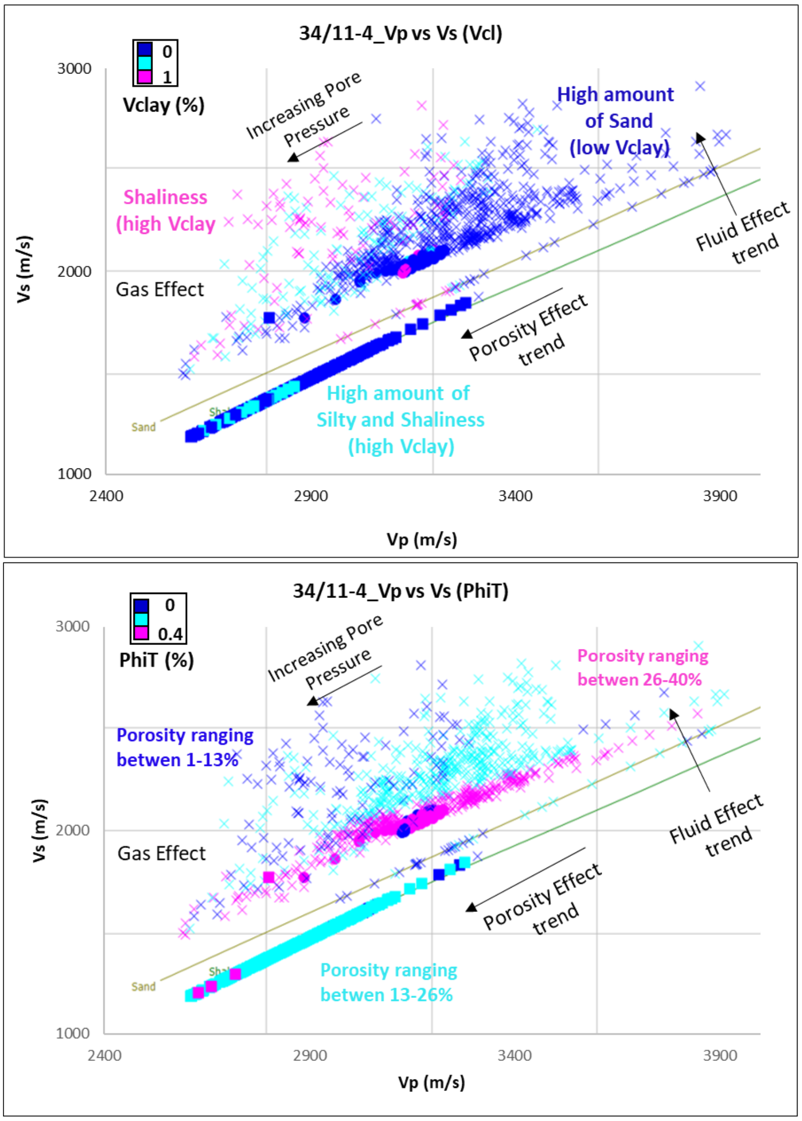

Figure 5. 30: (Top) The Vp versus Vs crossplot color-coded with clay volume (Vclay), exhibiting relatively low clay volume in the Tarbert and Ness Formations but Ness Formation also containing variation in Vclay. In the Heather Formation, relatively high clay volume is present (more silty and shaly). (Bottom) The Vp versus Vs crossplot color-coded with total porosity (PhiT) showing variations in the Tarbert and Ness Formations porosity but majorly comprising relatively high porosity. The Heather Formation displays relatively the same porosity trend as of Tarbert Formation as the Heather Formation consists of more silt than shale.

5.1.5 Results of Well: 34/11-5S

5.1.5.1 AI versus VpVsRatio cross plot

The AI versus VpVsRatio cross plot for all formations present in the well 34/11-5S (Figure 5.31). The majority of the formations are plotting on either Shale Background Trend (black line) or Brine Sandstone Trend (blue line), whereas only Tarbert Formation is plotting on the Gas Sandstone Trend (orange line).

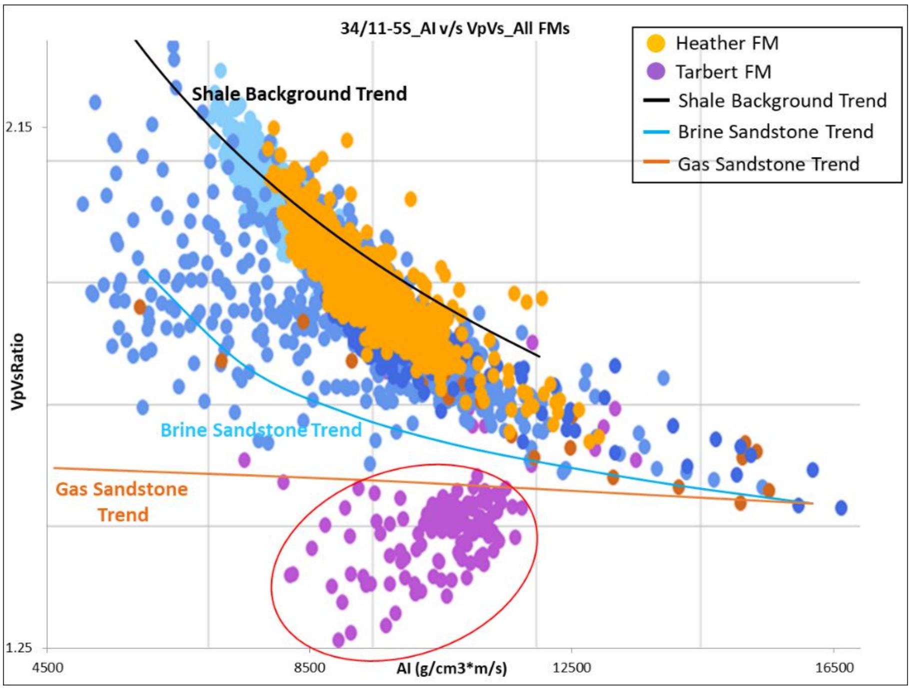

Figure 5. 31: The AI vs. VpVsRatio cross plot template for all the formations present in the well 34/11-5S. The template comprises Shale background trend, Brine Sandstone trend, and Gas Sandstone trend. The red circle display data points of the Tarbert Formation (target reservoir) plotting on the Gas sandstone trend. The color data points other than Heather and Tarbert Formations are representing different formations in well 34/11-5S.

Few data points of Tarbert are plotting on the Brine Sandstone and Shale Background trends, which explains a low percentage of lithology variation, as Tarbert is reflecting 24 m thickness. The Heather Formation (cap rock) plotting on Shale Background Trend. The range of Acoustic Impedance (AI) is between 4500 and 16900 (g/cm3*m/s) and VpVsRatio ranging between 1.25 and 2.3 (Figure 5.31). Interestingly, this well comprises the deepest gas-bearing reservoir (7086m), compared to all the available wells in this study. Moreover, the AI vs. Vp/Vs crossplots color-coded with Gas Saturation (Sg), Clay Volume (Vclay), and Total Porosity (PhiT) to evaluate the reservoir properties for the well 34/11-5S. For the color-coded cross plots, only the target reservoir (Tarbert Formation) is considered to focus only on the deepest target reservoir for better understanding and time-saving. The AI vs. VpVsRatio cross plot color-coded with Gas Saturation (Sg) with a range between 20 to 70% illustrates the presence of high Sg (about 70%) in the Tarbert Formation (Figure 5.32). The high Sg is displayed almost in the entire formation; even data points plotting on shale background also display high Sg (perhaps shaly gas sand).

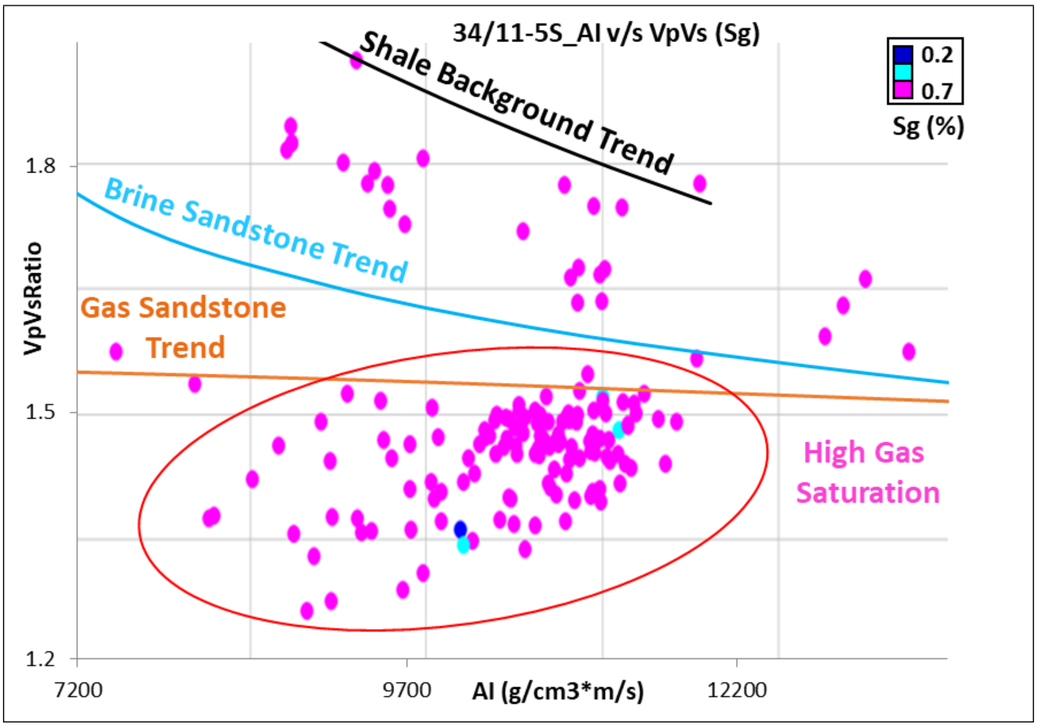

Figure 5. 32: The AI vs. VpVsRatio cross plot template color-coded with Gas Saturation (Sg) for Tarbert Formation illustrates that the target reservoir (Tarbert Formation) comprising high Sg (about 70%) and plotting majorly on the Gas Sandstone trend. A few points are also plotting between the Brine Sandstone and Shale Background trends. The template comprises Shale background trend, Brine Sandstone trend, and Gas Sandstone trend. The red circle shows data points of Tarbert Formation (target reservoir) plotting on the Gas sandstone trend, perhaps comprising shaly gas sand.

The AI vs. VpVsRatio cross plot color-coded with Total Porosity (PhiT) with a range between 0 to 18% generated that display variation of porosity in Tarbert Formation. Mostly, the porosity present in Tarbert Formation ranges between 6-12% at a depth of 7086 m. This range of porosity in Tarbert is mostly plotted on the Gas Sandstone trend, which is considered a gas-bearing zone on AI vs. VpVsRatio cross plot.

The AI vs. VpVsRatio cross plot for the well 34/11-5S color-coded with Clay Volume (Vclay) with a range between 0 to 100% shows the presence of relatively low clay volume (average 15%) in the Tarbert Formation (gas-bearing reservoir rock). Overall, the Tarbert data points plotting on the Gas Sandstone trend exhibit relatively low clay volume (Figure 5.34).

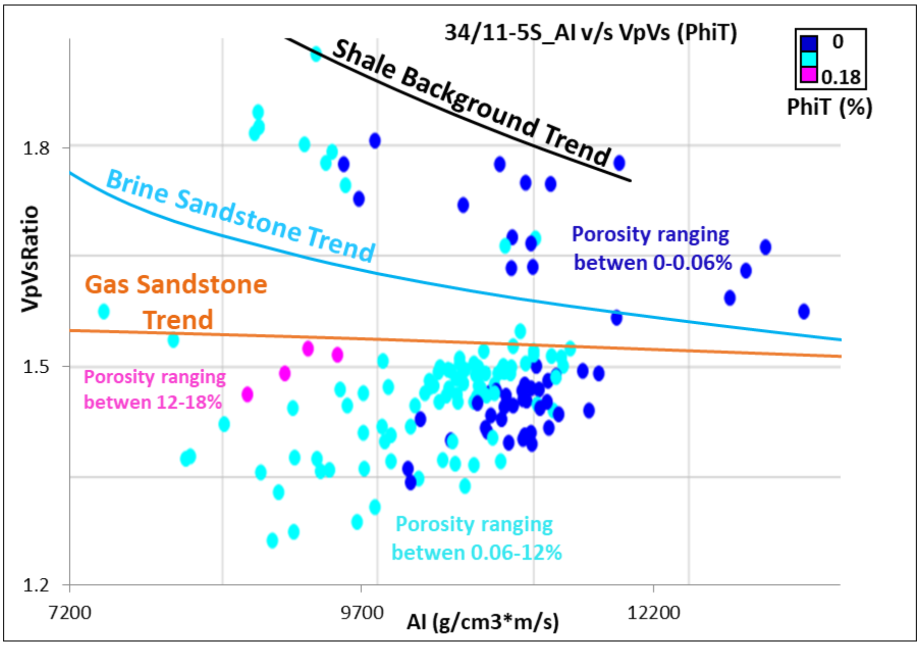

Figure 5. 33: The AI vs. VpVsRatio cross plot template color-coded with Total Porosity (PhiT) for Tarbert Formation, ranges between 0-18%, demonstrate that the target reservoir (Tarbert Formation) contain porosity variation but majorly comprises porosity in the range of 6-12% (low PhiT) and porosity ranging 0-6% displaying Tarbert data under the Shale Background trend.

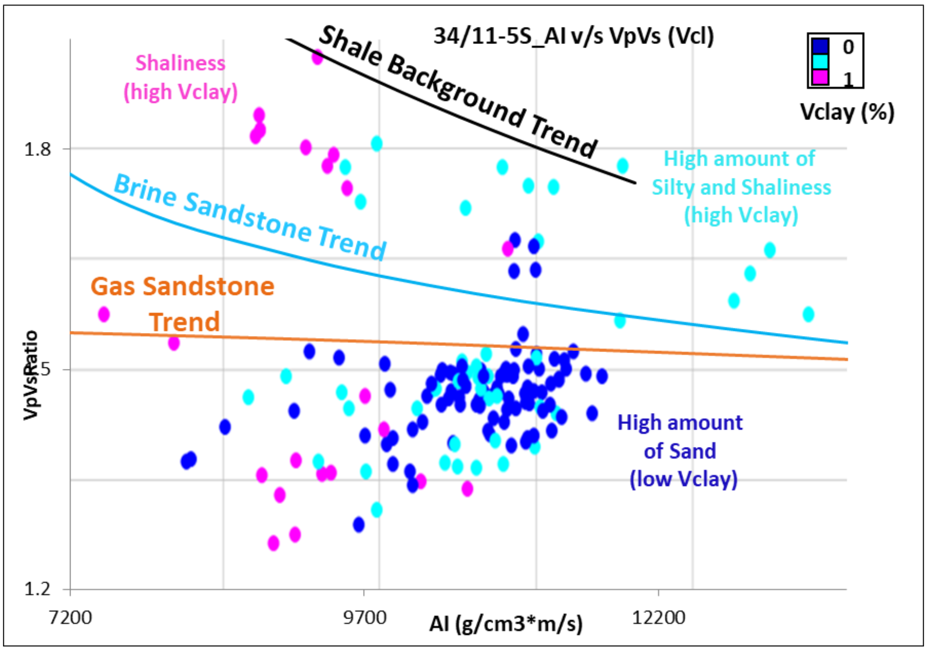

Figure 5. 34: The AI vs. VpVsRatio cross plot template color-coded with Clay Volume (Vclay) for the Tarbert Formation, ranges between 0-100%, reveal that the Tarbert Formation (target reservoir) hold Vclay variation but mainly includes relatively low Vclay (average 15%).

5.1.5.2 Lambda-Rho versus Mu-Rho cross plot

The LMR crossplot adapted from Goodway et al., (1997) showing all formations present in the well 34/11-5S (Figure 5.35). All the formations follow the general trend in the LMR cross plot. At 20 LambdaRho value, a threshold cutoff for porous Gas Sand is situated. This threshold line shows the presence of Gas Sand at the higher values of Mu-Rho and lower values of LambdaRho. Tarbert Formation can be seen plotting under the threshold cutoff porous Gas Sand and in the region of Gas Sand (Figure 5.35). The LMR cross plot color-coded with Gas Saturation (Sg), Clay Volume (Vcl), and Total Porosity (PhiT) to understand the reservoir properties for the target reservoir (Tarbert Formation) and the cap rock (Heather Formation) for well 34/11-5S. The Tarbert Formation is plotting with relatively higher Mu-Rho and lower Lambda-Rho values. Moreover, the Tarbert Formation is plotting under the threshold cutoff for porous gas sand. According to (Goodway et al., 1997), the area under the threshold cutoff with higher Mu-Rho and lower Lambda-Rho values exhibit the area of Gas Sand data. (Figure 5.35).

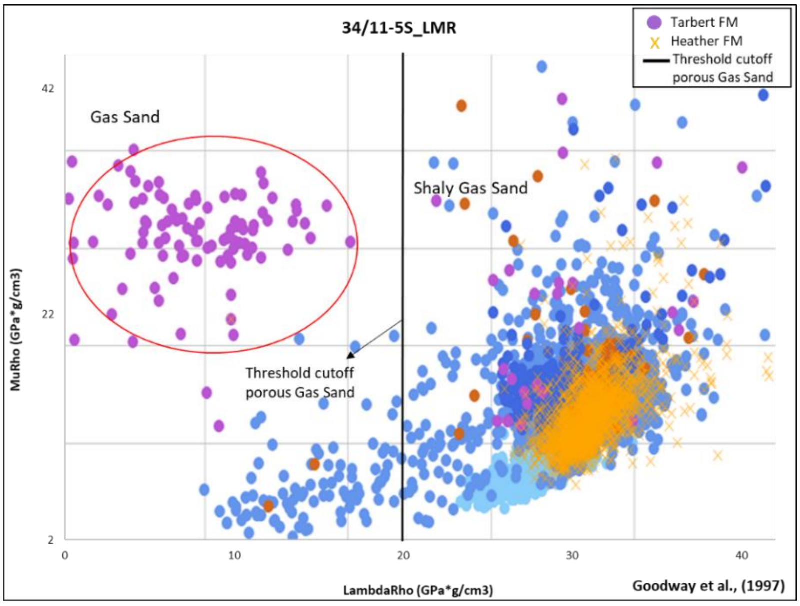

Figure 5. 35: The Lambda-Rho versus Mu-Rho (LMR) cross plot template, suggested by Goodway et al. (1997) for all the formations present in well 34/11-5. The template comprises threshold cutoff porous Gas Sand at 20 GPa*g/cm3 of Lambda-Rho value. The red circle displays the target reservoir (Tarbert Formation), which is the only formation plotting under the threshold cutoff for porous gas sand.

The LMR cross plot color-coded with gas saturation (Sg) comprising a range between 20 to 70%. The color-coded cross plot shows the presence of high Sg (about 70%) in the Tarbert Formation. It is plotting with higher Mu-Rho and lower Lambda-Rho values under the threshold cutoff for porous gas sand. (Figure 5.36). The LMR cross plot color-coded with Clay Volume (Vclay) with a range between 0 to 100%, displaying clay volume in Tarbert Formation is relatively low (about 15%) and plotting with higher Mu-Rho and lower Lambda-Rho values under the threshold cutoff for porous gas sand (Figure 5.37).

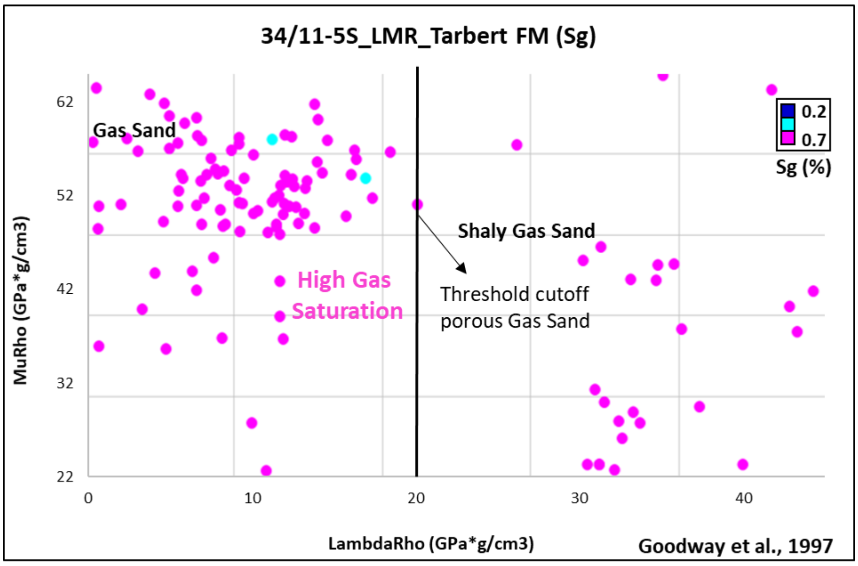

Figure 5. 36: The LMR cross plot color-coded with Gas Saturation (Sg) for Tarbert Formation illustrates high Sg in the entire formation. Data points plotting under the threshold cutoff for porous Gas Sand are the points of interest exhibiting high Sg. Few points are plotted in the shaly gas sand area.

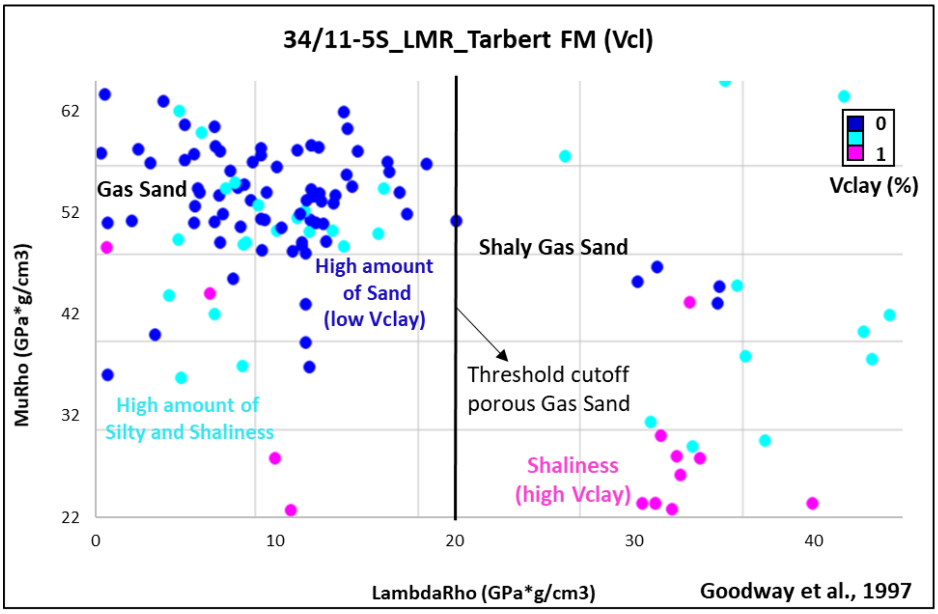

Figure 5. 37: The LMR cross plot color-coded with Clay Volume (Vclay) for Tarbert Formation show low Vclay in the formation, and data points plotting under the threshold cutoff for porous Gas Sand are the points of interest, which are shows low Vclay. Few points are plotted in the shaly gas sand area.

The LMR cross plot color-coded with Total Porosity (PhiT) with a range between 0 to 18% displays the variation of porosity in the Tarbert Formation. The formation comprises high porosity with the range of 6 to 12% and plotting with higher Mu-Rho values (Gas Sand area) (Figure 5.38).

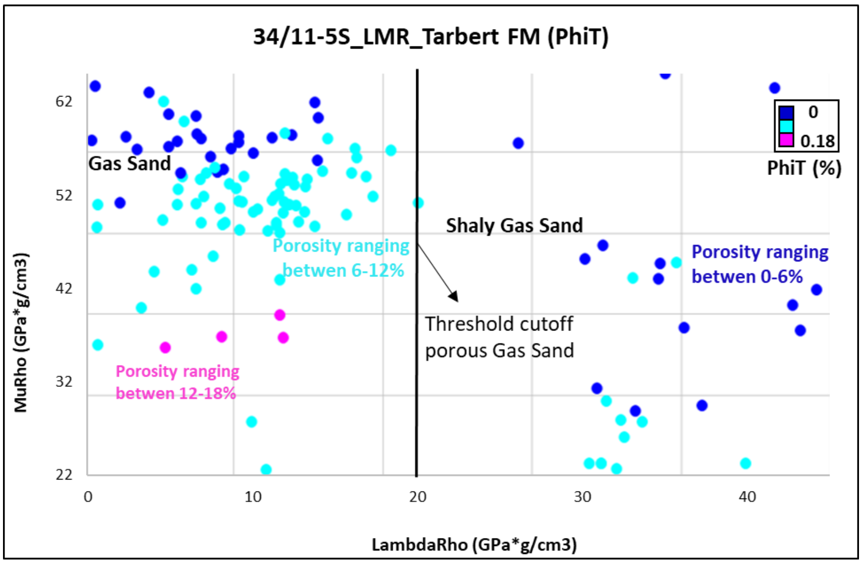

Figure 5. 38: The LMR cross plot color-coded with Total Porosity (PhiT) for Tarbert Formation demonstrate relatively high PhiT in the formation.

5.1.5.3 PhiT versus Vp cross plot

The Porosity (PhiT) vs. Vp crossplot showing Tarbert Formations present in the well 34/11-5S (Figure 5.39). The Cement Model template consists of three curves, which are Contact Cement Model (gray curve), Constant Cement Model (blue curve), and Friable Clay-Quartz curve (red curve). Moreover, this template explains the trends of sorting and the increase of cement volume.

In this well, Tarbert Formation (target reservoir) plotted under the Friable Clay-Quartz curve and Constant Cement Model. The cross plot displays the target reservoir comprising relatively low porosity, about 6-12%. In this well, Tarbert Formation is at 7086m depth. Moreover, the cross plot of PhiT vs. Vp was generated with color-coding of Gas Saturation (Sg) and Clay Volume (Vclay). The cross plot color-coded with the gas saturation (Sg) for Tarbert Formation (target reservoir) comprises high gas saturation (about 70%) at low porosity and higher P-wave velocity values (Figure 5.40).

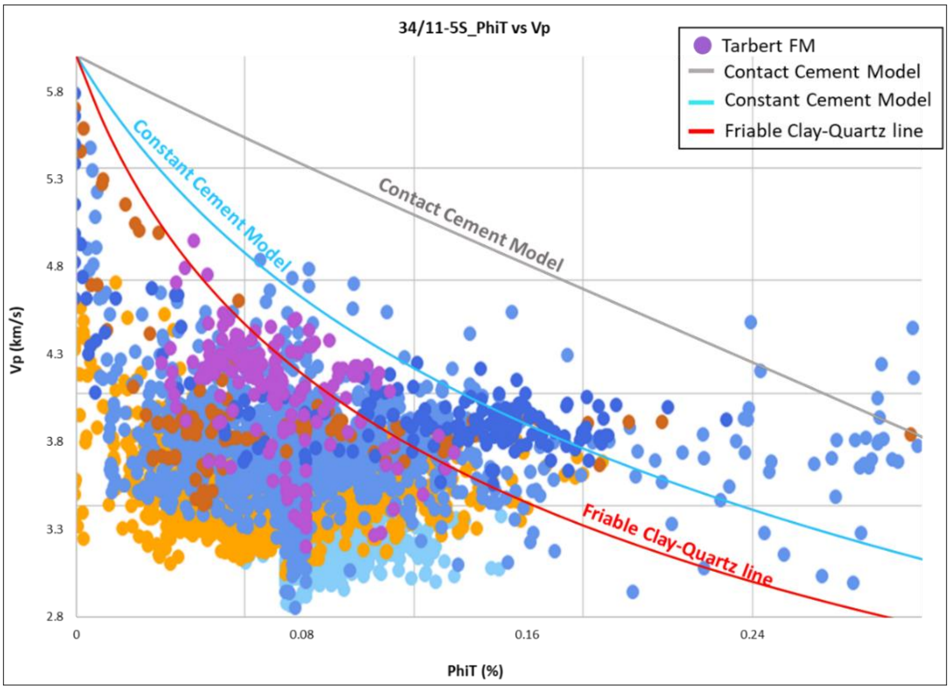

Figure 5. 39: The Porosity (PhiT) versus P-wave velocity (Vp) for all formations in the well 34/11-5S. The cross plot contains cement models that are Friable Clay-Quartz curve (orange curve), Constant Cement Model (blue curve), and Contact Cement Model (gray curve). The Tarbert Formation (target reservoir) displaying low porosity and distributed under Friable Clay-Quartz curve and Constant Cement Model.

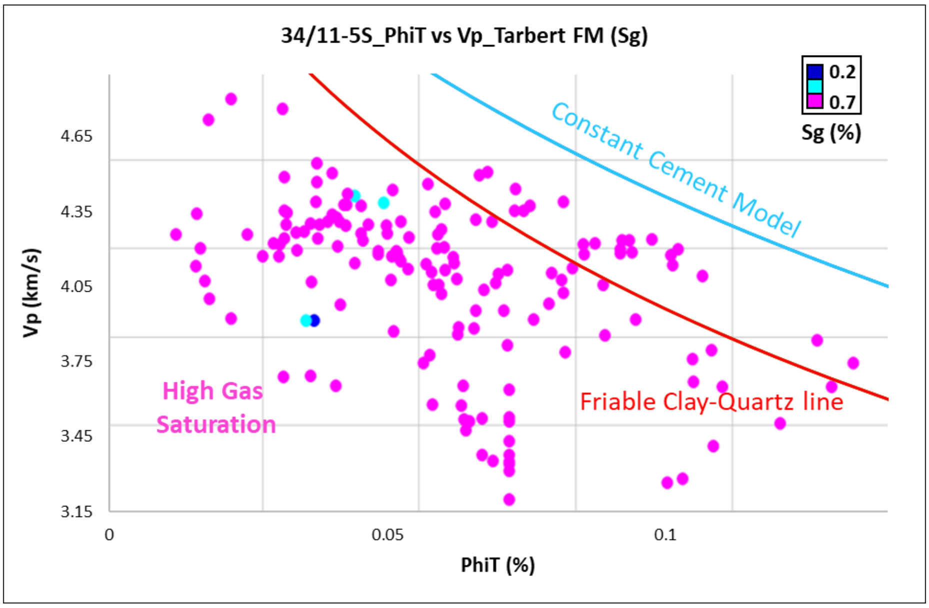

Figure 5. 40: The Porosity (PhiT) versus P-wave velocity (Vp) cross plot color-coded with gas saturation (Sg) for target reservoir show high gas saturation in the Tarbert Formation with low porosity and high Vp values.

The cross plot color-coded with the clay volume (Vclay) for the Tarbert Formation display relatively low clay volume (about 15%) which means high sand percentage is present in the Tarbert Formation (Figure 5.41).

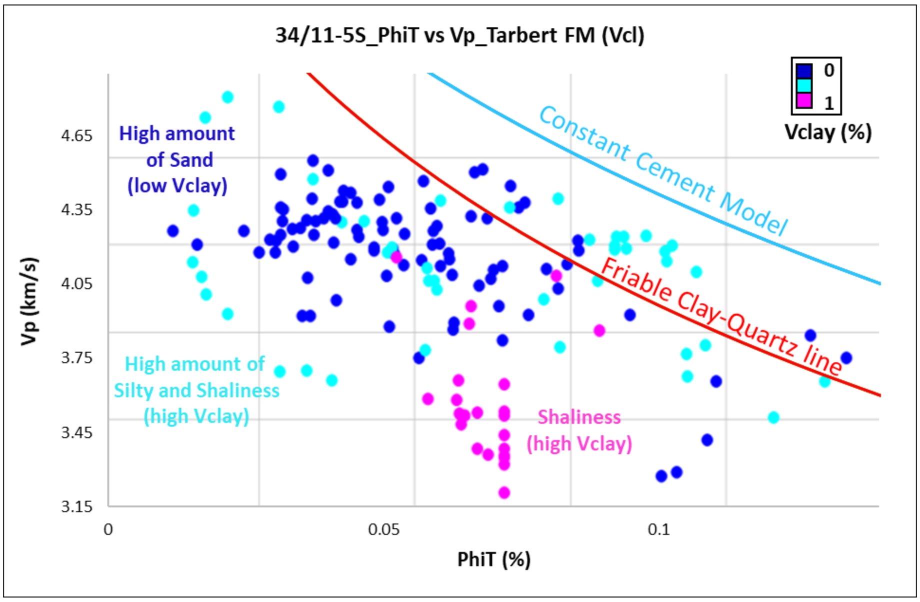

Figure 5. 41: The Porosity (PhiT) versus P-wave velocity (Vp) cross plot color-coded with Clay Volume (Vclay) for target reservoir demonstrate low clay volume in the Tarbert Formation while comprising low porosity and high Vp values.

5.1.5.4 Vp versus Vs cross plot

The Vp versus Vs crossplot template is generated from Interactive Petrophysics software (IP). The cross plot generated along with Sand and Brine saturated trend lines for the Tarbert and Formation present in the well 34/11-5S (Figure 5.42). The Tarbert Formation is plotting over the Sand line; this might be due to fluid effect. Whereas the Heather Formation is plotting on the shale line (brine saturated shale line). The range of the Vp in the cross plot is 2300 to 5800m/s. Whereas the range of Vs is 900 to 3900m/s.

The cross plot generated with color-coding of Gas Saturation (Sg) and Clay Volume (Vclay), along with Sand and Shale brine saturated trend lines for the Tarbert Formation (target reservoir zone) present in the well 34/11-5S. The color-coding of Sg shows the Tarbert Formation comprises about 70% gas saturation (Figure 5.43).

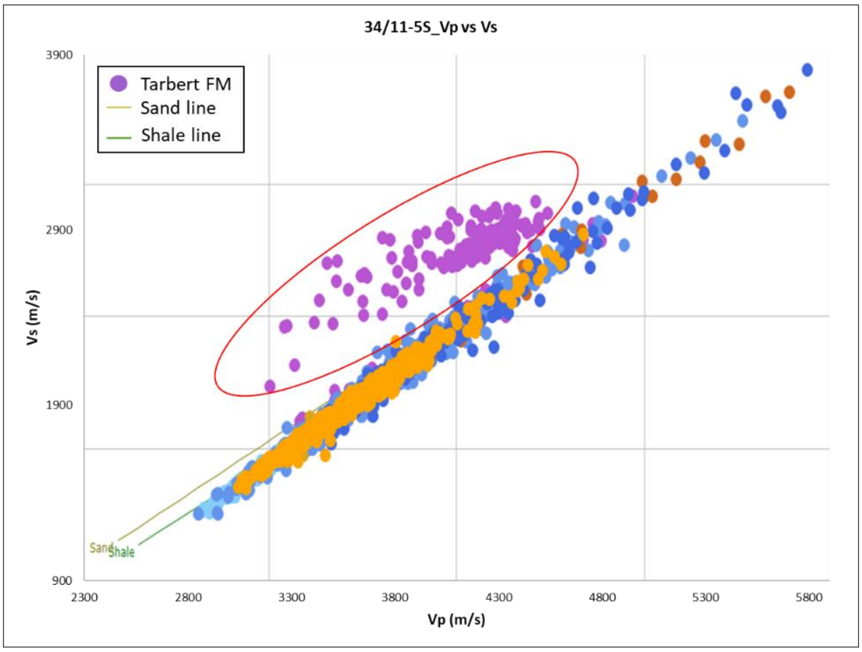

Figure 5. 42: The Vp versus Vs crossplot for the formations in the well 34/11-5S, along with the Sand and Shale brine saturated trend lines. The red circle highlights Tarbert Formation (target reservoir).

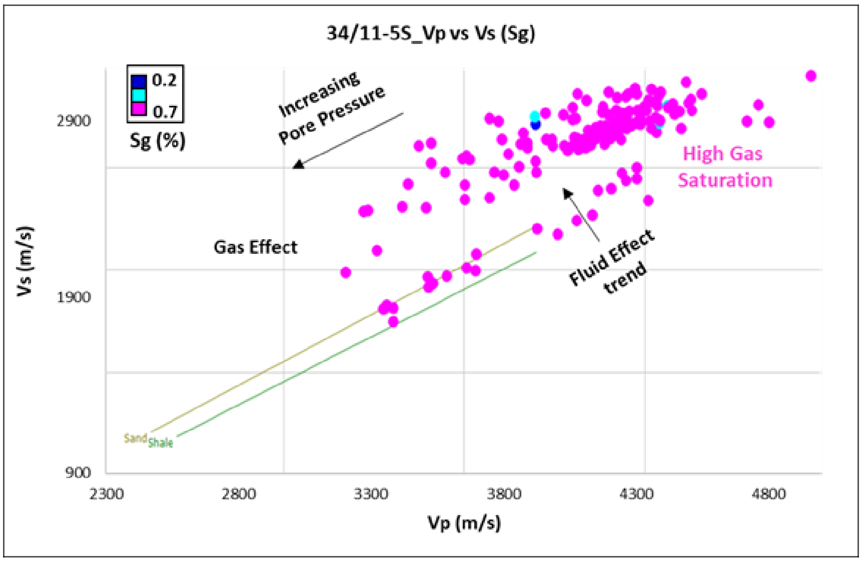

Figure 5. 43: The Vp versus Vs crossplot color-coded with gas saturation (Sg), exhibiting relatively high gas saturation in the Tarbert Formation, and due to fluid saturation, it is visible that the data points shifted from the Brine saturated Sand line (fluid effect).

The Vp versus Vs cross plot color-coded with Clay Volume (Vclay) with a range between 0 to 100% demonstrates relatively low clay volume in the Tarbert Formation, about 15% (Figure 5.44).

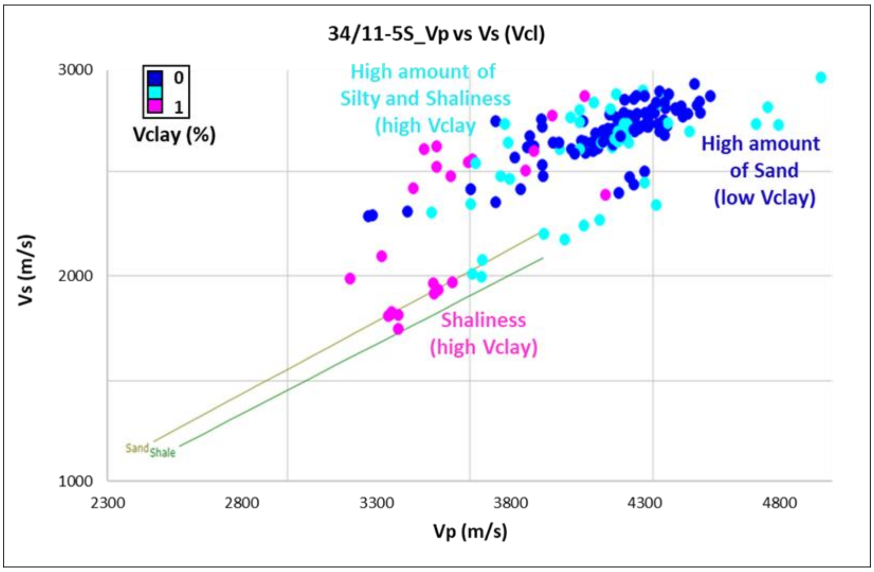

Figure 5. 44: (Top) The Vp versus Vs crossplot color-coded with clay volume (Vclay), illustrating relatively low clay volume in the Tarbert Formation. The variation of Vclay in Tarbert shows the presence of silt and shale as well; perhaps the thickness and depth of Tarbert Formation in this well might have influenced it.

The Vp versus Vs cross plot color-coded with Total Porosity (PhiT) with a range between 0 to 18% displays the variation of porosity in the Tarbert Formation. Moreover, the Tarbert Formation comprises high porosity with the range of 6 to 12% and deviating from the Sand brine saturated line, plotting near the gas effect area. (Figure 5.45).

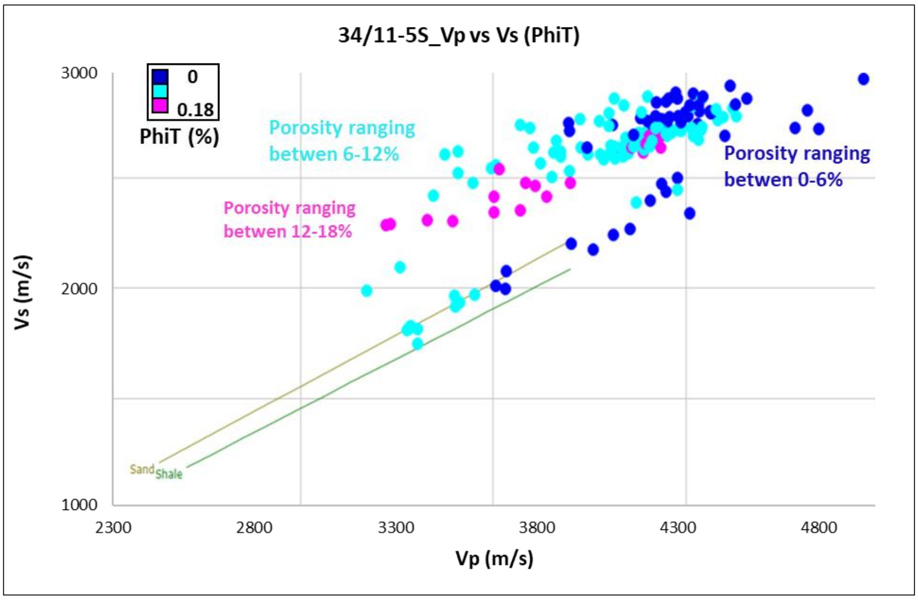

Figure 5. 45: The Vp versus Vs crossplot color-coded with Total Porosity (PhiT) display variations in the porosity but majorly contain relatively low porosity (about 6-12%) in the Tarbert Formation.

5.1.6 Results of Well: 34/11-6S

5.1.6.1 AI versus VpVsRatio cross plot

The AI versus VpVsRatio cross plot for target reservoirs (Tarbert and Ness Formations) and cap rock (Heather Formation) are present in the well 34/11-6S. In all the available wells, the Tarbert Formation is the thickest (107m) in this well, while Ness comprises relatively low thickness (89m). In the AI versus VpVsRatio cross plot, Heather Formation plotting on the Shale Background Trend (black line) and few points on the Brine Sandstone Trend.

The Tarbert and Ness Formations are plotting on the Brine Sandstone Trend, but a significant percentage of points are also plotted on the Gas Sandstone Trend (orange line) highlighted with a red circle. The range of Acoustic Impedance (AI) is between 7000 and 13500 (g/cm3*m/s) and VpVsRatio ranging between 1.45 and 2.05 (Figure 5.46-Top).

The AI vs. VpVsRatio cross plot was generated with color-coding of Gas Saturation (Sg), Clay Volume (Vclay), and Total Porosity (PhiT) in order to get a better understanding of the target reservoirs.

The AI vs. VpVsRatio cross plot color-coded with Gas Saturation (Sg) displaying the target reservoir formations Tarbert and Ness are majorly low in Sg and comprising high water saturation in the entire formation, plotting on all the three trends.

However, a small cluster of high Sg is visible in Tarbert and Ness Formations at the low VpVsRatio values on the Gas Sandstone trend. Whereas the Heather Formation comprises of high water saturation (low Sg) (Figure 5.46-Bottom).

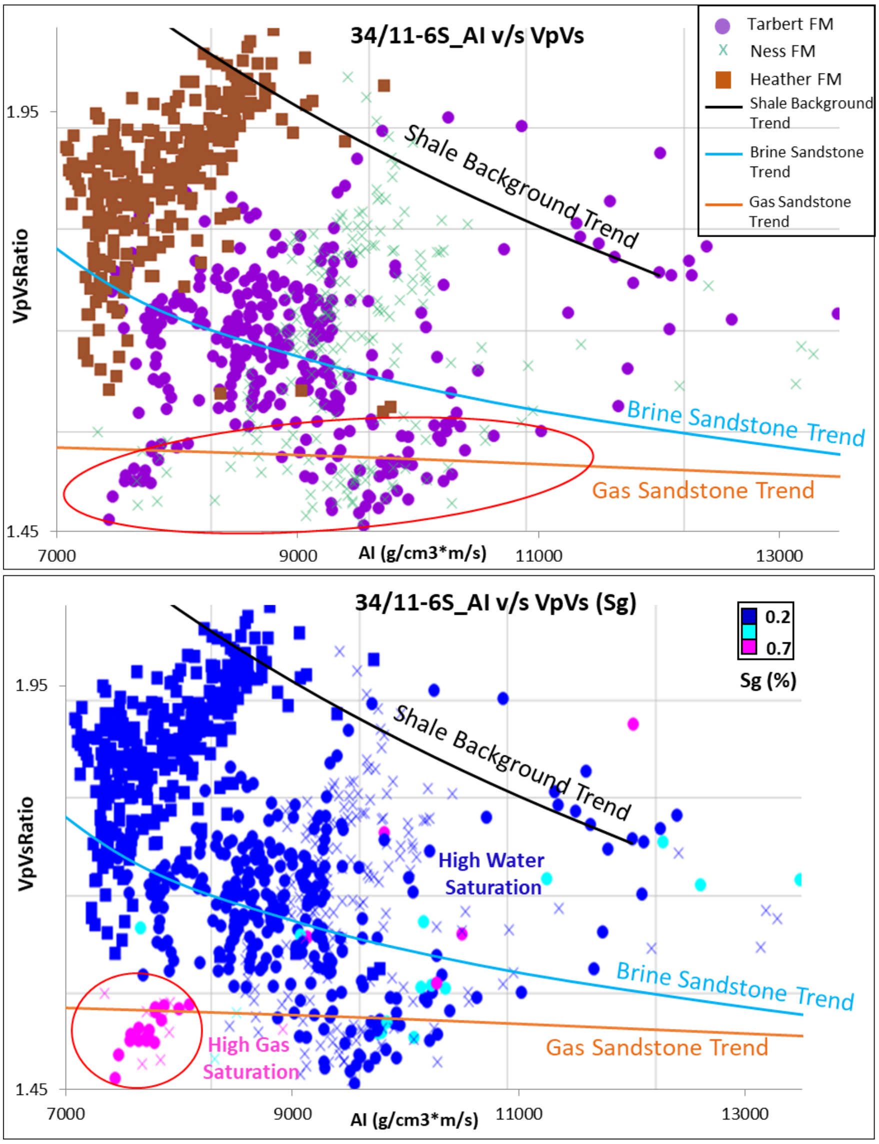

Figure 5. 46: (Top) The AI vs. VpVsRatio cross plot for the formations present in the well 34/11-6S, along with the Shale Background Trend (black line), Brine Sandstone Trend (blue line), and Gas Sandstone Trend (orange line). It is visible that the Tarbert and Ness Formations are plotting on the Brine Sandstone and Gas Sandstone Trend line. The big red oval shape represents Tarbert and Ness Formations data points plotting on the Gas Sandstone trend. (Bottom) The cross plot color-coded with Gas Saturation (Sg), illustrating a small cluster of relatively high Sg with low VpVsRatio and AI values plotting on Gas Sandstone Trend line (red circle).

The AI vs. VpVsRatio cross plot color-coded with Clay Volume (Vclay) displays that Tarbert and Ness Formations comprise relatively low Vclay. Moreover, Heather Formation is exhibiting a relatively very high Vclay (Figure 5.47-Top). The Tarbert and Ness Formations display the presence of more sand and silt in the formations, mostly at the lower VpVsRatio values. One key thing to remember here is the thickness of both the target reservoirs, because of which a variation in lithology is expected. While Heather Formation exhibits the presence of more shale along with silt at the higher VpVsRatio values and plotting on Shale Background and Brine Sandstone Trend.

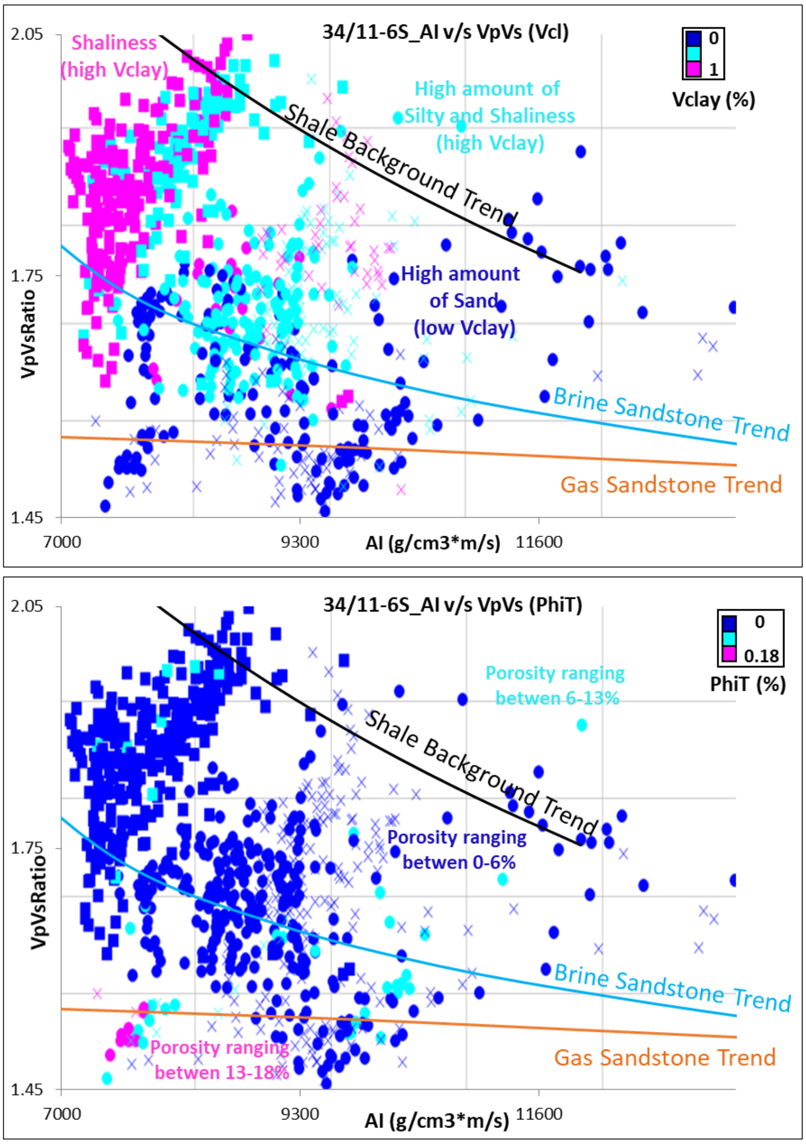

Figure 5. 47: (Top) The AI vs VpVsRatio cross plot color-coded with Clay Volume (Vclay), demonstrating relatively low Vclay in Tarbert and Ness Formations and relatively high Vclay in Heather Formation. (Bottom) The cross plot color-coded with Total Porosity (PhiT), displaying relatively high PhiT in the Tarbert and Ness Formations with low VpVsRatio values plotting exactly on Gas Sandstone Trend line where high Sg plotted.

The AI vs. VpVsRatio cross plot was generated with the color-coding of Total Porosity (PhiT), ranging between 0 to 18%. As the well 34/11-6S is deep (Heather – 6599m, Tarbert – 6873 m, and Ness - 6944m depth), the illustration of porosity for these three formations is relatively similar. The response of PhiT display by Heather Formation is relatively low (about 0 to 6%). Whereas the Tarbert and Ness Formations exhibit low porosity and show a relatively high PhiT cluster (about 10 to 18%), exactly at the same location where the formations represent high Sg on the Gas Sandstone trend with low VpVsRatio values (Figure 5.47-Bottom).

5.1.6.2 Lambda-Rho versus Mu-Rho cross plot

The LMR crossplot adapted from Goodway et al. (1997) displaying the Tarbert and Ness Formations (target reservoirs) and Heather Formation (cap rock), existing in the well 34/11-6S (Figure 5.48-Top). A threshold cutoff porous Gas Sand line is seen at 20 GPa*g/cm3 Lambda-Rho value. This threshold line demonstrates the occurrence of Gas Sand at the higher Mu-Rho values and lower Lambda-Rho values.

The Heather Formation is plotting in the LMR cross plot with relatively higher Lambda-Rho and lower Mu-Rho values. Whereas the Tarbert and Ness Formations plotting with relatively higher Mu-Rho and Lambda-Rho values. The target reservoir formations are scattered in the cross plot—relatively low data points of both formations plotting under the threshold cutoff for porous gas sand. Moreover, Tarbert Formation is of 107 m thickness in this well and exhibits a range of lower to higher Mu-Rho Lambda-Rho values (Figure 5.48-Top). The LMR cross plot color-coded with Gas Saturation (Sg), Clay Volume (Vcl), and Total Porosity (PhiT) support in understanding reservoir properties for target reservoir Tarbert and Ness Formations and the cap rock Heather Formation in the well 34/11-4.

The LMR cross plot color-coded with Gas Saturation (Sg) ranges between 20 to 70% (Figure 5.48-Bottom). The Sg color-coded cross plot demonstrates relatively low gas saturation in the Tarbert and Ness Formations, whereas a small cluster of data points highlights relatively high Sg (red circle in Figure 5.48-Bottom). This small cluster of data points plotting with relatively low Mu-Rho and lower Lambda-Rho values under the threshold cutoff for porous gas sand displays the Gas Sand zone. Perhaps, this might be due to variation in mineralogy that plotted high Sg at low Mu-Rho. Whereas the Heather Formation (cap rock) shows relatively low gas saturation (about 20%) and plotting with relatively lower Mu-Rho and higher Lambda-Rho values (Figure 5.48-Bottom).

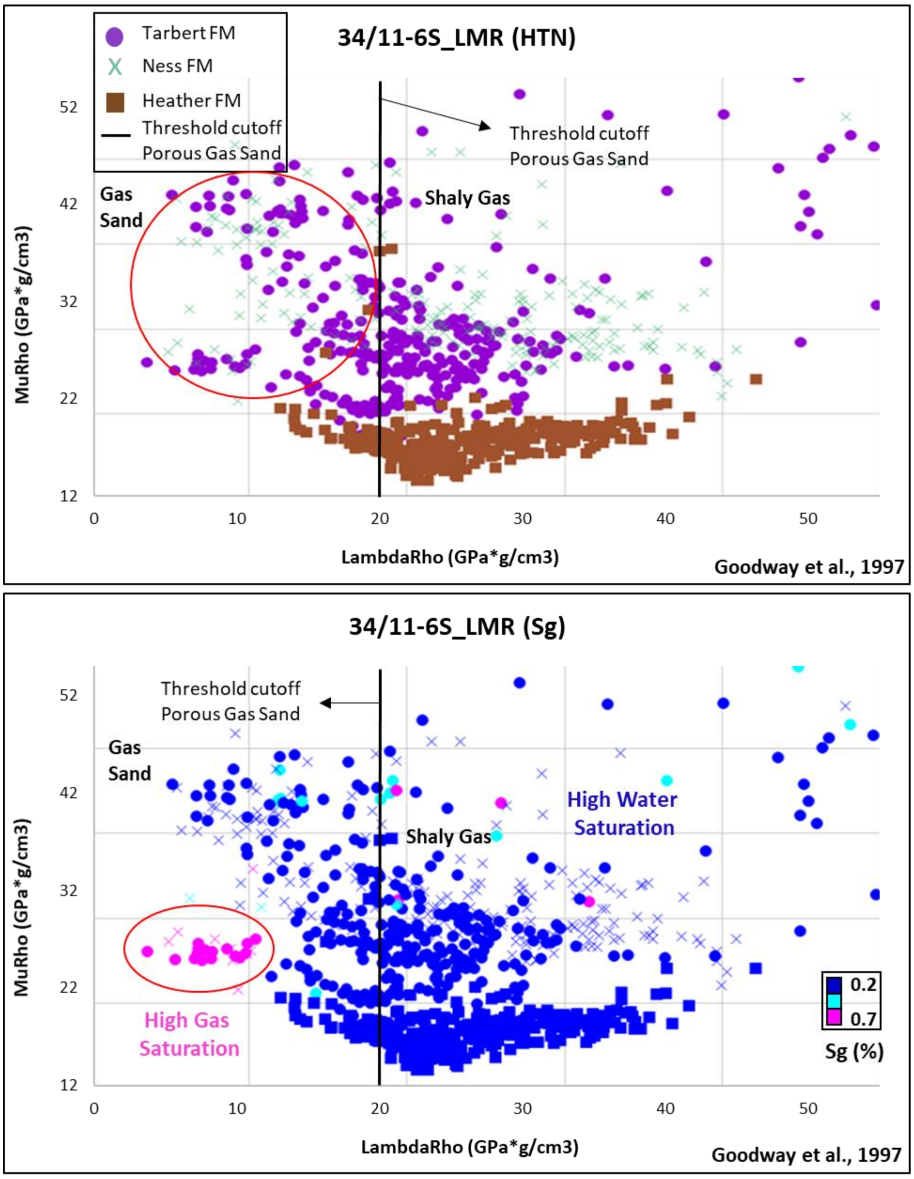

Figure 5. 48: (Top) The LMR cross plot suggested by Goodway et al. (1997) presenting Tarbert and Ness Formations (reservoir rock) and Heather Formation (cap rock) in the well 34/11-6S. The reservoir formations are plotting under and over the threshold cutoff porous Gas Sand with relatively higher Mu-Rho and Lambda-Rho values (big red circle), whereas Heather Formation is plotting with relatively high Lambda-Rho and lower Mu-Rho values under and over the threshold cutoff. (Bottom) The LMR cross plot color-coded with Gas Saturation (Sg) exhibiting a small cluster of data points with relatively high gas saturation in the Tarbert and Ness Formations, whereas relatively low gas saturation in the Heather Formation.

The LMR cross plot color-coded with Clay Volume (Vclay) exhibiting Tarbert and Ness Formations comprising relatively low Vclay, displaying Vclay variations in both formations because of its lithology and possible mineral variations, and high thickness (Tarbert – 107m and Ness – 89m). The Heather Formation is exhibiting a relatively high Vclay (Figure 5.49-Top). The LMR cross plot color-coded with Total Porosity (PhiT) demonstrated relatively low porosity in the Heather, Tarbert, and Ness Formations. Whereas Tarbert and Ness Formations comprises relatively high porosity in some places, specifically where high Sg was plotted in Tarbert and Ness on the Gas Sandstone trend line (Figure 5.49-Bottom).

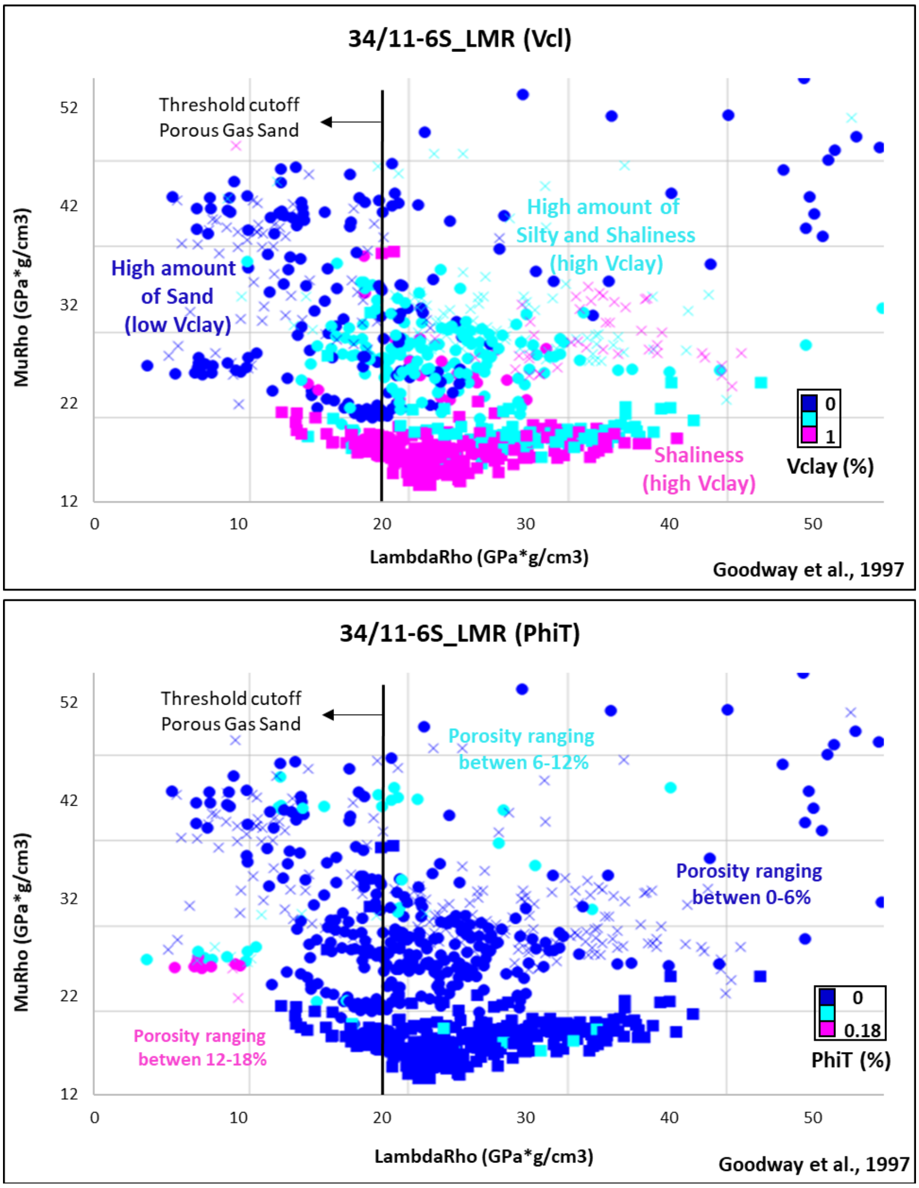

Figure 5. 49: (Top) The LMR cross plot color-coded with Clay Volume (Vclay) displaying Tarbert and Ness Formations (reservoir formations) comprising relatively low Vclay, whereas both formations display variation in Vclay due to possible mineralogy and lithology variation. The Heather Formation is exhibiting a relatively high Vclay. (Bottom) The LMR cross plot color-coded with Total Porosity (PhiT) unveiled relatively low PhiT in the Tarbert, Ness, and Heather Formations, but the reservoir formations also exhibit relatively high PhiT under threshold cutoff with low Mu-Rho values.

5.1.6.3 PhiT versus Vp cross plot

The Porosity (PhiT) vs. Vp crossplot displaying Tarbert, Ness, and Heather Formations present in the well 34/11-6S. The template is known as Cement Model, and it consists of three curves, which are Contact Cement Model (gray curve), Constant Cement Model (blue curve), and Friable Clay-Quartz curve (red curve). Moreover, this template explains the trends of sorting and the increase of cement volume. In this well, Tarbert Formation plotted under the Friable Clay-Quartz curve and Constant Cement Model, whereas Ness Formation spreading under all the three trends. The cross plot showing Tarbert and Ness Formations mainly comprises relatively low porosity, about 0 to 6% and 0-10%, respectively. The possibility of cementation in the Tarbert and Ness is present as the formations plotting on the Constant and Contact Cement Model trend. Moreover, both reservoir formations (Tarbert and Ness) are exhibiting relatively high porosity and high Vp values and plotting near Constant and Contact Cement Model curves (Figure 5.50).

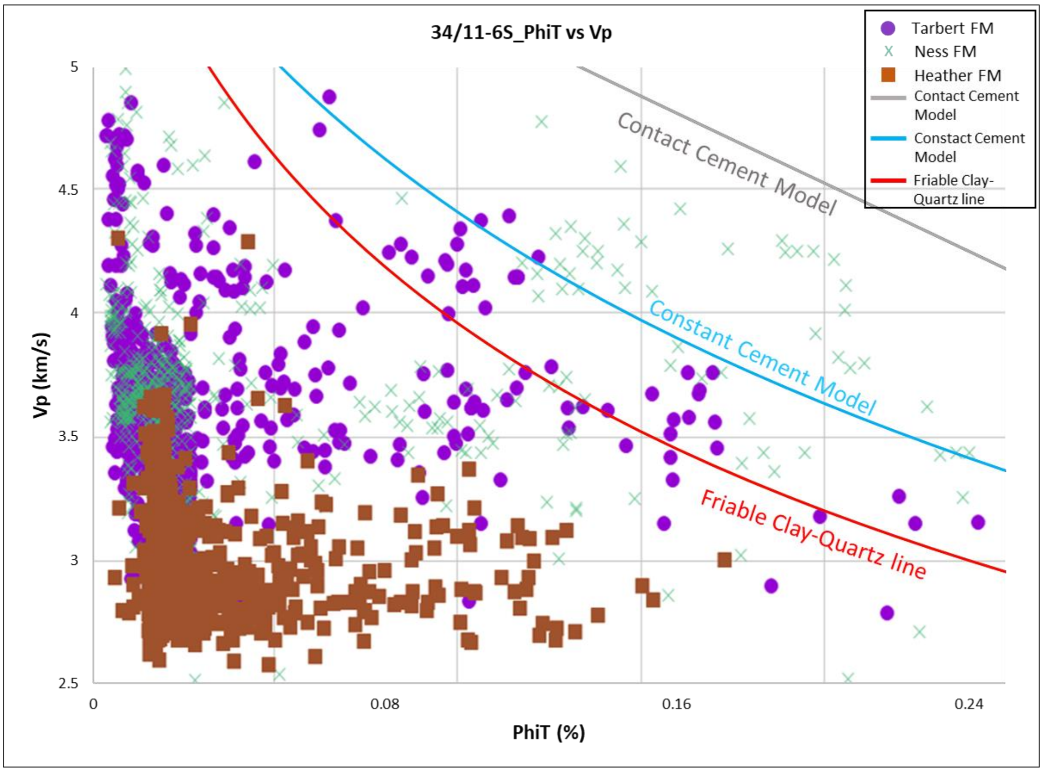

Figure 5. 50: The PhiT vs. Vp cross plot exhibiting Heather, Tarbert, and Ness Formations in the well 34/11-6S. The cross plot exhibits Heather Formation (cap rock) plotting under Friable Clay-Quartz curve and comprising relatively low porosity. The Tarbert and Ness Formations (reservoir formations) are scattered in the cross plot under Friable Clay-Quartz curve and Constant Cement Model. Ness Formation also plots between Constant and Contact Cement Models. Moreover, both the reservoir formations exhibit relatively high PhiT and Vp, perhaps, due to the presence of cementation.

The presence of high porosity at deeper depth is perhaps due to the possible variation of mineralogy and presence of cementation that might lead to porosity preservation; additionally, the Vp reflects high values (3.1 to 4.8 km/s) for such high porosity data of both formations. Moreover, the PhiT vs. Vp cross plot was generated with color-coding of Gas Saturation (Sg) and Clay Volume (Vclay) to inspect the reservoir properties in the Tarbert and Ness Formations. The cross plot color-coded with gas saturation (Sg) exhibits relatively low Sg in all the formations, whereas a small portion in Tarbert and Ness Formations illustrate relatively high Sg with relatively high porosity values (Figure 5.51-Top).

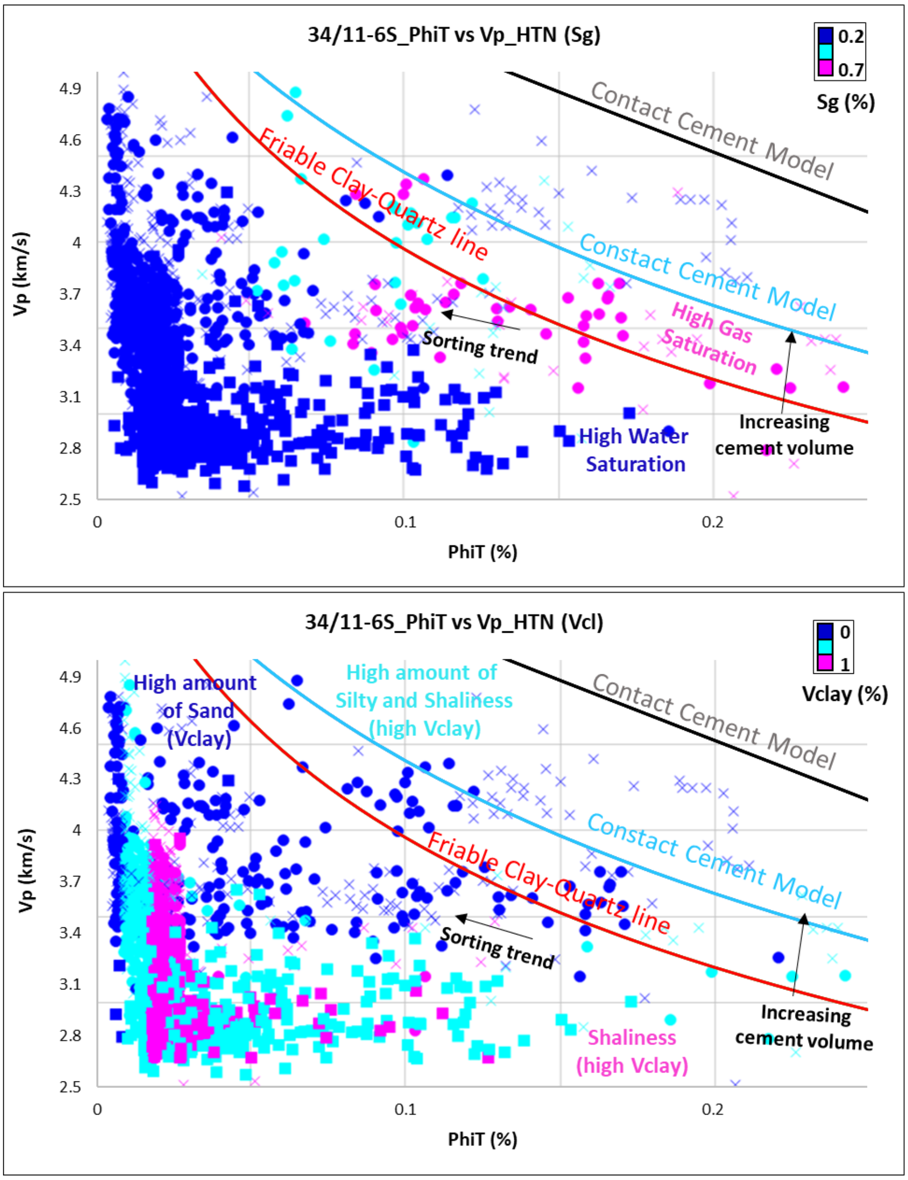

Figure 5. 51: (Top) The cross plot color-coded with Gas Saturation (Sg) shows relatively high Sg in the small part of Tarbert and Ness Formations with relatively higher PhiT and Vp values. The Heather Formation comprising relatively low Sg. (Bottom) The cross plot color-coded with Clay Volume (Vclay) shows relatively low Vclay in the Tarbert and Ness Formations, whereas, Heather Formation displays relatively high Vclay.

The cross plot color-coded with Clay Volume (Vclay) s relatively low Vclay in Tarbert and Ness Formations, whereas Heather Formation comprises relatively high Vclay (Figure 5.51-Bottom).

5.1.6.4 Vp versus Vs cross plot

The Vp versus Vs crossplot template was generated from the software Interactive Petrophysics (IP). The cross plot displays Brine Sand and Brine Shale trend lines generated by the IP software. The cross plot shows Tarbert and Ness Formations (target reservoir) and Heather Formation (cap rock) existing in the well 34/11-6S (Figure 5.52-Top).

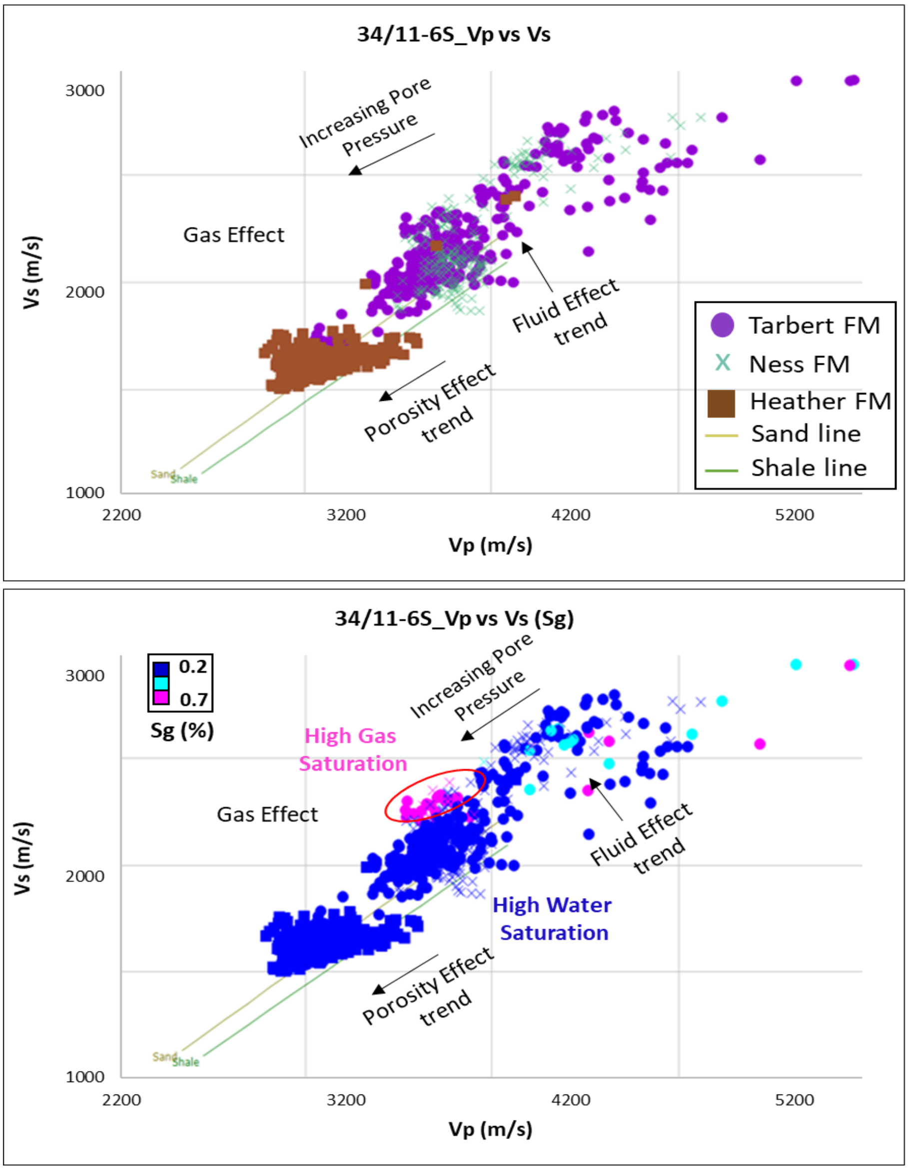

Figure 5. 52: (Top) The Vp versus Vs crossplot for Tarbert, Ness and Heather Formations in the well 34/11-6S including Brine Sand and Brine Shale trends. The Tarbert and Ness Formations deviating away from the Brine Sand trend, perhaps, due to fluid effect. (Bottom) The cross plot color-coded with gas saturation (Sg) exhibits relatively high Sg in the Tarbert and Ness Formations (a small cluster – red circle) and low Sg in the Heather Formation.

The Tarbert and Ness Formations are plotting on and over the Brine Sand line; perhaps the presence of fluid might initiate this deviation from the Brine Sand line. Whereas Heather Formation (cap rock) plotting on and above the Brine Shale line possibly shows the presence of shale, silt, and few sand percentage.

The cross plots generated with the color-coding of Gas Saturation (Sg), Clay Volume (Vclay), and Total Porosity (PhiT) for the well 34/11-6S are discussed as follows. The color-coding of Sg shows a small percentage of Tarbert and Ness Formations comprises of relatively Sg (about 70%) (Figure 5.52-Bottom). Whereas the rest of Tarbert, Ness, and the entire Heather Formations illustrate relatively high Sg (Figure 5.52-Bottom).

The Vp versus Vs cross plot color-coded with Clay Volume (Vclay) shows relatively low clay volume in the Tarbert and Ness Formations. However, both Tarbert and Ness possess Vclay variations, perhaps because of the possible change in mineralogy (Figure 5.53-Top).

Moreover, the Vp versus Vs cross plot color-coded with Total Porosity (PhiT) display relatively low porosity, about 0 to 6% and 0-10%, in the Tarbert and Ness Formations, respectively. Whereas, Ness being more in thickness than Tarbert, therefore, show porosity variations in it. The Heather Formation (cap rock) exhibits relatively low porosity (Figure 5.53-Bottom).

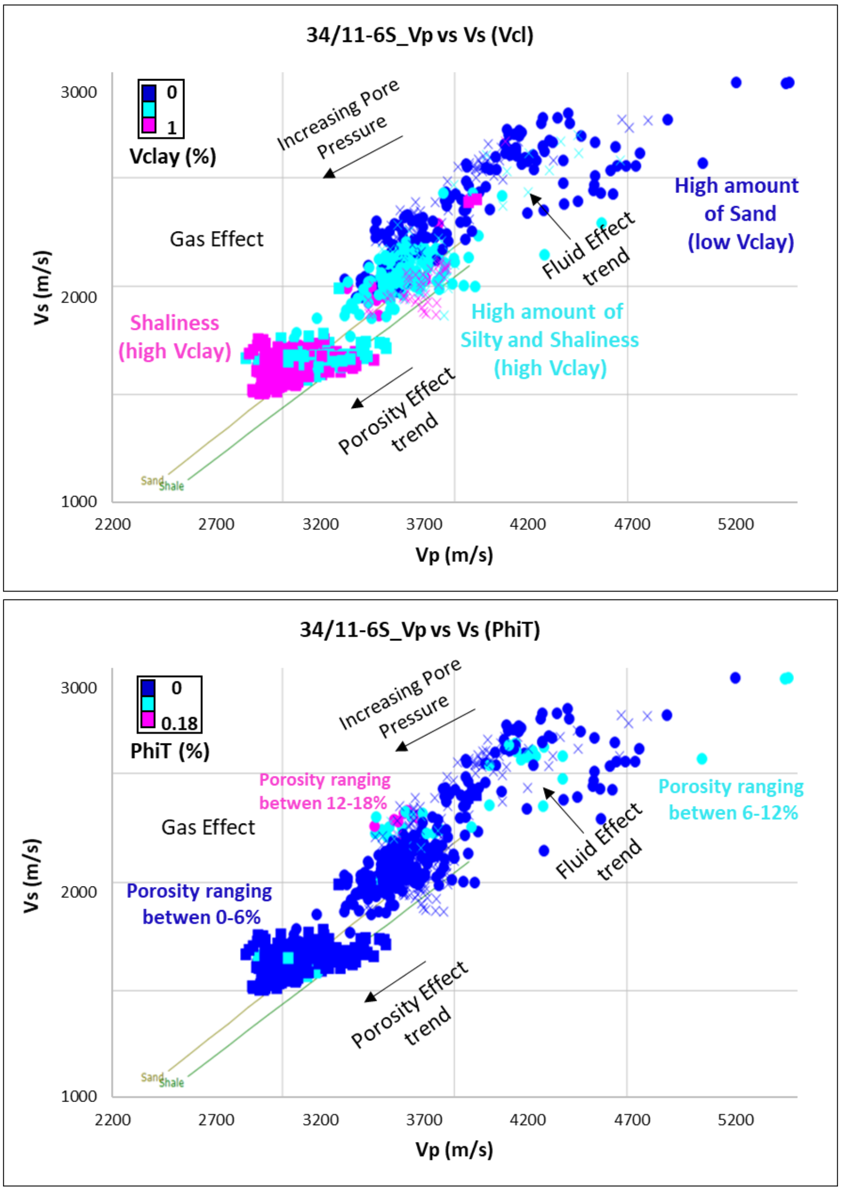

Figure 5. 53: (Top) The Vp versus Vs crossplot color-coded with clay volume (Vclay), exhibiting relatively low clay volume in the Tarbert and Ness Formations. While the Heather Formation shows relatively high clay volume (more shaly and silty). (Bottom) The Vp versus Vs crossplot color-coded with total porosity (PhiT) displaying relatively low PhiT in the Tarbert and Ness Formations, but a small cluster exhibiting relatively high PhiT is also visible at the same location where high Sg was illuminating. The Heather Formation displays relatively low porosity as of Tarbert and Ness Formations.

5.1.7 Seal Integrity

There is a need to examine the seal integrity to understand the reservoir properties and if there is a chance of hydrocarbon migration (seal failure). As this study is conducted for the fields present in Viking Graben, the chance of upliftment is very less. Therefore, t investing the seal integrity is just to examine how the caprock is behaving and out of all which cap rock could be considered one of the effective ones. The LMR template is used to plot Heather Formation for studying seal integrity. The LMR template obtained from (Perez & Marfurt, 2014), comprises four regions starting from right to left as Ductile, Less Ductile, Less Brittle, and Brittle. Subsequently, brittleness can be considered as a behavior rather than a petrophysical property because of multiple attributes such as lithology, rock strength, fluid type, texture, stress relaxation, stress regime, Total organic content, and diagenesis. The elastic properties need to be applied to the circumstance of the targeted formation and compared to lab experiments to become important for assessing seal integrity (Mondol, 2018).

The caprocks are characterized to be stiffer, which have high values of elastic properties, such as AI, E, μρ, and λρ). Several processes, like diagenetic and depositional, and minerals like stiff minerals, perhaps, improve geomechanical and acoustic properties of the caprock. Several additional factors, such as microstructure, type of clay, and mineral presence in the matrix, dominate the rock deformation. The variations present in the geomechanical properties of the caprock explain the quality of sealing nature in terms of reservoir-caprock combination. Additionally, the properties of cap rocks are not possible to explain by individual property, for instance, brittleness or stiffness. Therefore, an arrangement of several properties can be utilized to explain the cap rock properties, like matrix permeability, capillary pressure, well completion manner, pore-throat size, in-situ stress condition, etc.

Moreover, a number of rock properties, for instance, mineralogy and elastic moduli (Yang et al., 2013). Seal Integrity in all wells for the cap rock (Heather FM) is shown on the LMR crossplot (Figure 5.54). The LMR crossplot template shows, starting from lower to higher LambdaRho values, as Brittle, Less Brittle, Less Ductile, and Ductile. The cap rock Heather Formation comprises the lowest thickness in the well 34/11-1 that is 49 m, and at a depth of 3996m. The highest thickness of Heather is in the well 34/11-5S, which is 290m at a depth of 6796m. Moreover, the cap rock in the wells 34/10-23, 34/10-42S, 34/11-1, 34/11-4, and 34/11-5S are plotted in the ductile region, whereas some points of 34/11-5S well can be seen plotting in the less Ductile region. Whereas the cap rock present in the well 34/11-6S is plotting majorly in the Ductile and Less Ductile regions (Figure 5.54). Thus, it can be concluded that all the cap rocks above Tarbert Formation are displaying ductile behavior, which can be considered effective. Whereas cap rock in the well 34/11-6S can be considered less ductile. There is no evidence seen of a bad cap rock (Heather Formation) in all the wells. The objective was to assess if there are any variations in the properties of cap rocks of the Heather Formation. The low percentage of hydrocarbon saturation may also be relevant to other geological elements such as the timing of trap formation and migration.

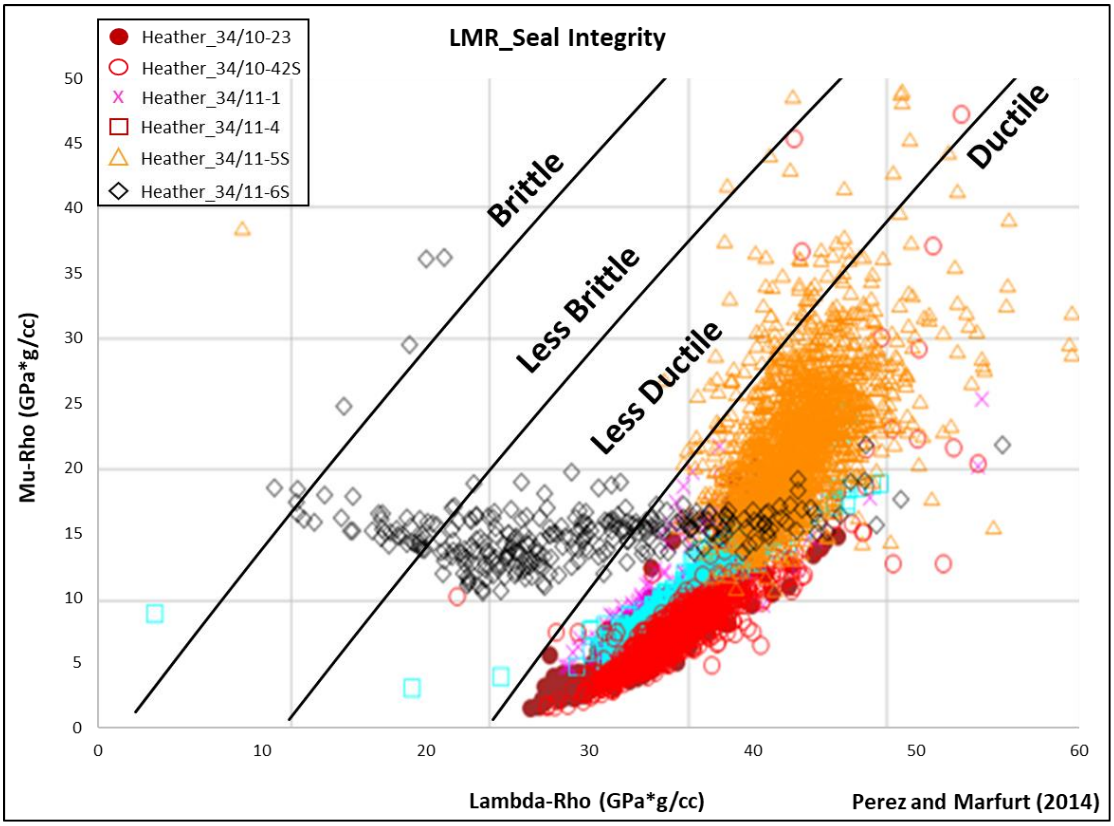

Figure 5. 54: LMR crossplot template with four regions of stiffness, starting from right to left, Ductile, Less Ductile, Less Brittle and Brittle for seal integrity of Heather Formation as cap rock in the wells 34/10-23, 34/10-42S, 34/11-1, 34/11-4, 34/11-5S and 34/11-6S. The LMR template was adopted by Perez & Marfurt, (2014).

5.2 Discussion

This chapter will discuss the petrophysical results and their importance in correlation to petrophysical analysis and reservoir quality in chapter 4. Clay volume and sorting, fluid sensitivity, and compaction, and cementation will also be reviewed with various effects in detail in chapter 6.

5.2.1 LMR Template

In the LMR (Lambda-Rho versus Mu-Rho) rock physics template, hydrocarbon-bearing reservoirs and their caprocks are plotted. The template is adapted from Goodway et al., (1997), suggesting a threshold cutoff line for porous gas sands. The main purpose of this template is to identify the fluids and lithology present in the targeted formation. The sandy and shaly intervals are effectively distinguished in the LMR crossplot. In the LMR cross plot template, the threshold cutoff line is at 20 GPa*g/cm3 Lambda-Rho that separates and makes it feasible to identify the shaly gas sand and porous gas sand. This LMR template also consists of a threshold for carbonates at 100 GPa*g/cm3 Lambda-Rho. Since no data is plotting in this range of Lambda-Rho values, that means no presence of carbonates; therefore, no clastic carbonates are discussed here.

Moreover, cemented zones and coal can also be marked in this LMR cross plot template. The complete explanation is already being discussed in chapter 3. The increase in gas saturation, thus, reduces the incompressibility. Moreover, the fluid type does not influence rigidity. Hence, the data in the cross plot shifts to the left side due to the presence of gas, and it is seen in all the LMR cross plots when the data of hydrocarbon-bearing reservoirs is plotted. The LMR cross plots are color-coded with Volume of Clay, Total Porosity, and Gas Saturation in order to study and get in-sight knowledge of the hydrocarbon-bearing reservoirs in this study.

5.2.2 PhiT vs Vp Template

The cross plot of Total Porosity (PhiT) versus P-wave Velocity (Vp) explains the presence of cementation and identifies the sorting trend. It is already completely discussed in chapter 3. The cross plots of PhiT vs. Vp were generated with the color-coding of Gas Saturation and Volume of Clay for the hydrocarbon-bearing reservoirs and their cap rocks. In the cement models, three trends are present: Friable Clay-Quartz line, Constant Cement Model, and Contact Cement Model. The Friable Clay-Quartz line exhibits a non-cemented sand model that is associated with the sorting. Moreover, the Contact Cement Model displays the presence of cementation in the sand. Whereas the Constant Cement Model explains the sorting trend in relation to constant cement value. When similar mineralogy and porosity is assumed, thus, the level of stiffness is higher in the cemented sandstone compared to the non-cemented sandstone. During the initial phase of chemical diagenesis, if the rock experiences the addition of cement thus, the porosity of the rock decreases. Moreover, the velocity of the rock experiences a significant increase in velocity.

Moreover, Marcussen, et al., (2010) generated a linear relation of cement volume and P-wave velocity. This generated linear relation is related to the shallow marine sandstones of the Etive Formation present in the northern area of the Viking Graben. This linear relation explains that the rise in P-wave velocity is the result of quartz cementation. Moreover, sorting can be determined as it ranges from 1 to 0 and when data projects on the contact cement model, the model line becomes equal to 1. Drop can be observed in sorting and an increase in the amount of low-porosity and pore-filling material. At zero porosity, sorting is equivalent to 0, and cement is not included in the pore-filling materials.

5.2.3 Vp versus Vs Template

In the dataset of all the wells, the Vs data was not available. Therefore, Vs was estimated through Hampson-Russell software. The estimated Vs is then utilized for the further processes. The Vp versus Vs crossplots are effective in identifying the gas saturation zone due to the shifting of gas-saturated data in relation to the template brine trends.

5.2.4 Volume of Clay

Through the petrophysical analysis, it is concluded that Tarbert Formation comprises relatively more sand than silt and clay in the wells 34/10-23, 34/10-42S, 34/11-1, and 34/11-4. Whereas, in the wells 34/11-5S and 34/11-6S, Tarbert Formation comprises relatively more silt and clay than sand. Considering the Ness Formation, in well 34/10-42S, containing relatively more sand than silt and clay. Moreover, in the well 34/11-1, Ness Formation constitutes comparatively more sand in the upper and lower portions, whereas, in the lower portions, relatively more clay is present. Furthermore, Ness Formation comprises sand with several shale intercalations in the well 34/11-4. Whereas, in the well 34/11-6S, Ness shows comparatively more clay and silt than sand.

The LMR rock physics template is utilized for quality control related to clay volume for Tarbert and Ness Formations. The LMR crossplot detects the Tarbert Formation data in the sand region, whereas, in the wells 34/11-5S and 34/11-6S, the Tarbert data is plotting in both sand and shaly-sand regions (Figure 5.35 and Figure 5.47-Top). Moreover, in all the wells, Ness Formation data in the LMR crossplot plotting in both sand and shaly sand regions. The Ness Formation is relatively high in clay volume, plotting with higher Lambda-Rho and Mu-Rho values. Whereas Heather Formation (cap rock) comprises a relatively higher clay volume than Ness and plotting relatively too low Mu-Rho and Lambda-Rho values. Perhaps, this fact might be due to clay volume that creates an impact on the velocity, and transformation of velocity occurs subsequently to the critical porosity. The velocity rises to the critical porosity and then falls subsequently progressing to the critical porosity. The cementation and burial in Ness and Tarbert Formations improve the velocity as compared to Heather Formation, which is cap rock. Additionally, the change in -supported matrix, i.e., Ness and Tarbert Formation to a clay-supported matrix, initiate suspension conditions that lead to the drop in the shear strength that elaborates the minimization of Mu-Rho experienced in the cap rock.

5.2.5 Compaction and Cementation

The Tarbert Formation exhibits average cement volume between 10 to 15% in well 34/10-23, whereas the Ness Formation shows the range between 0 to 20% in well 34/11-1. Moreover, the Tarbert Formation in the well 34/11-4, displays cement volume between the ranges of 0 to 8%, while the Ness Formation shows between 0 to 25% in well 34/11-4. The well 34/11-5S comprises the deepest Tarbert (7086m) with low porosity and more compaction. Moreover, no Tarbert point was plotted on the cement model lines in the cement model crossplot of well 34/11-5S (Figure 5.38). This leads to the point that the Tarbert in well 34/11-5S is not comprised of chlorite coatings; therefore, porosity becomes low and was not preserved. Whereas, in other wells at such higher depths, Tarbert and Ness Formations are display higher porosity, perhaps showing the preservation of porosity.

The Vp vs. Depth crossplot template for Mechanical Compaction (MC) Sandstone for Tarbert and Ness Formations in the wells 34/10-23, 34/10-42S, 34/11-1, 34/11-4, 34/11-5S, and 34/11-6S is plotted (Figure 5.55). The template is generated for only the mechanical compaction zone, whereas, in this study, the gas reservoirs are at deeper depths and available in the chemical compaction zone. Tarbert and Ness in the wells 34/10-23, 34/11-1, 34/11-4, and 34/10-42S is available in the range of 4 to 4.3 km depths (m RKB), whereas, in wells 34/11-6S and 34/11-5S, at deeper depths of about 6.8 km and 7.1 km (m RKB), respectively. In all the wells, it is seen that Tarbert and Ness Formations comprise higher velocity. It is evidence that with the increase of depth, velocity increases as porosity decreases.

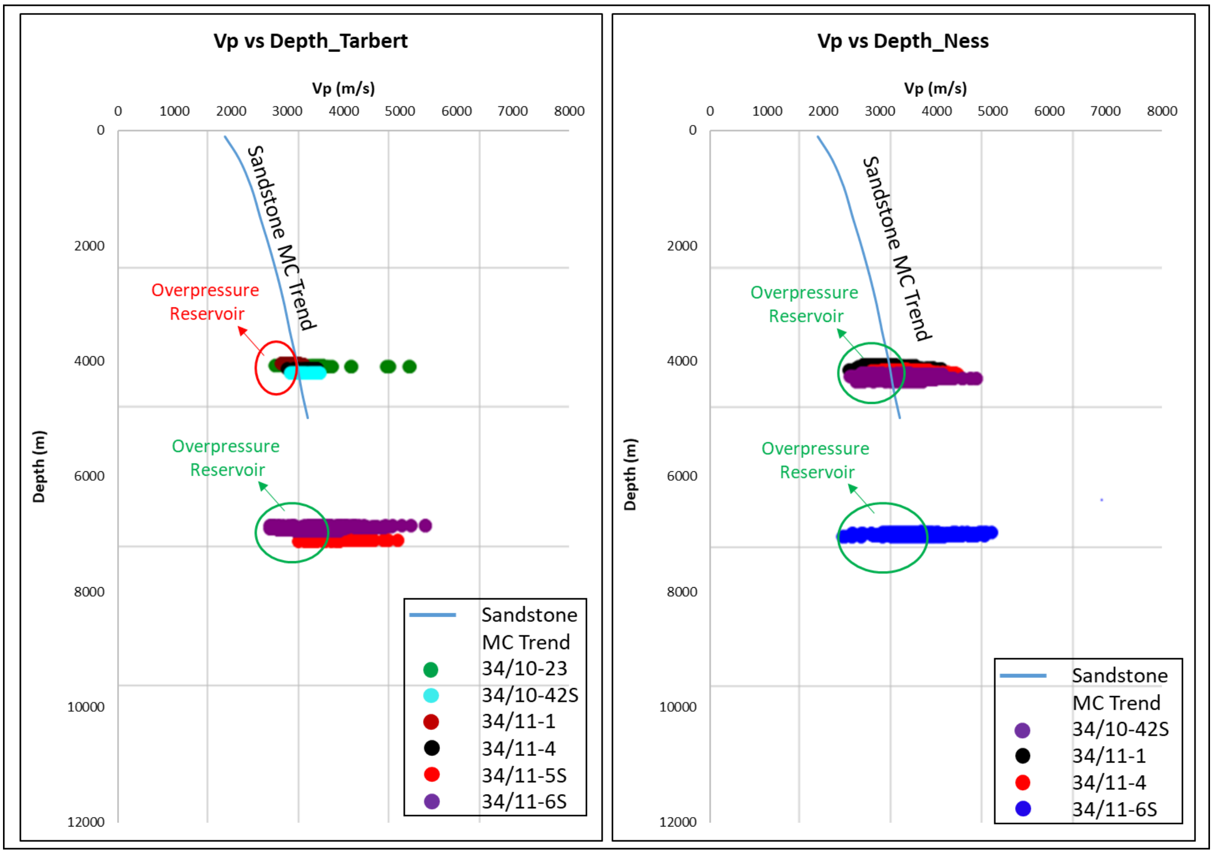

Figure 5. 55: Depth vs Vp crossplot of Sandstone Mechanical Compaction Trend for Tarbert and Ness Formations displaying overpressure reservoirs in wells 34/10-23, 34/10-42S, 34/11-1, 34/11-4, 34/11-5S and 34/11-6S. The depth is measured in (m RKB) due to which highly deviated wells (34/11-5S and 34/11-6S) are plotting on higher depths. If depth values measured from TVD, data points of deviated wells would be plotting around 4 km depth.

Tarbert and Ness in the wells at a depth of 4 to 4.3 km, also displaying clusters under the Sandstone Trend, which shows they are overpressure reservoirs. Moreover, if we increase this Sandstone Trend to the depth of 6.8 to 7.1 km (m RKB), Tarbert and Ness Formations at these depths will display a similar trend; cluster will be present under the Sandstone Trend line showing overpressure reservoirs. The quartz cementation becomes smaller when the porosity is reduced; in addition, the cementation level reduces. The process of quartz cementation is controlled by the temperature (Figure 5.56), which originates from the stylolites dissolution; moreover, it is not sensitive towards the transformation in the effective stress. Figure 5.56 shows burial and temperature history of the Tarbert Formation, present in well 34/11-1. It exhibits that Tarbert Formation experienced a rapid burial during Cretaceous age. Within this time, the temperature also rises, which initiated chemical compaction zone and thus start of quartz cementation.

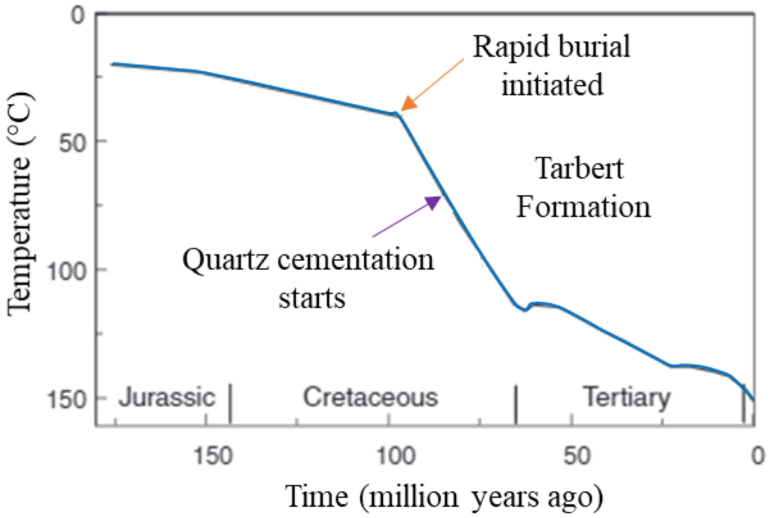

Figure 5. 56: The temperature conditions and burial history of the Tarbert Formation in well 34/11-1 (modified after Walderhaug, 2000).

5.2.6 Fluid Sensitivity

The Tarbert and Ness Formations display hydrocarbon data points deviating from the Vp versus Vs crossplot template generated brine sand trends in most wells. Moreover, in the well 34/11-6S, the same trend of plotting is found (Figure 5.52-Top), both varying from the generated brine sand trend. The effect may be related to diagenesis (cementation). Additionally, it is observed in the AI vs. Vp/Vs crossplot that a decrease in the Vp/Vs ratio value is the result of a rise in the cement volume. This is identical with the hydrocarbon saturation scenario, where Vs rises relatively more than Vp. The majority of the data from Ness Formation of the wells 34/11-4 and 34/11-6S in the Vp versus Vs crossplot (Fig. 5.29-Top and 5.52-top), is not only plotting to gas and water trends. However, it is also plotting in the area between both trends. Furthermore, considering a homogenous saturation in the formations, few data points of low hydrocarbon saturation are also plotted, which might exhibit plotting, which might exhibit less or perhaps residual gas saturation. The presence of low gas saturation might shift the data points toward the low Vp values. In the LMR crossplot related to the well 34/11-5S, a decrease in the fluid sensitivity is observed. This might result from a possible diagenesis process, as the hydrocarbon data points seen crossing over the cutoff line porous gas sand of Goodway et al., (1997) (Figure 5.35). Perhaps, it can be said that the petrophysical analysis in this study underestimated the hydrocarbon saturation being after considering the discussed results.

The fluid sensitivity is also affected by clay, which may result in low saturation than estimated through AI vs. Vp/Vs crossplot. Relatively to sand, the clays possess high incompressibility and Vp/Vs ratio values. Therefore, clay influences in the opposite direction related to hydrocarbon saturation, and an increase in the amount of clay decreases the gas sensitivity. In general, the petrophysical analysis results appear satisfying but can be critically discussed.

5.3 Limitations and Uncertainties

Possible sources of error in the rock physics diagnostics are summarized below:

- The AI vs. Vp/Vs templates rely on properties, for instance, the critical porosity and the matrix-related bulk and shear moduli, etc. For the brine-saturated sandstones, the software applies default values. In this study, the siliciclastic lithologies are supposed to be sand-shale. Still a possible mineralogical variation and the variations in elastic properties, perhaps, results in uncertainty, for example, Clay mineral types and Quartz or Feldspar variation.
- For all the target reservoirs, a homogeneous saturation is being considered, whereas, in actual the fluids perhaps, also exhibit a combination in a patchy manner.
- The unavailability of the spectral gamma ray logs in almost all the wells create a barrier in studying mineralogy present in the formations.
- Calculations related to clay volume, total porosity, saturation, and effective porosity in relation to the petrophysical analysis, might not be completely precise.
- In the Porosity vs. Vp crossplot, the Vp may experience reduction due to the residual gas, which becomes a problem when the study aims to evaluate cement and sorting trends.
- A thin section study must be carried out for all wells to verify the existence and volume of real cementation against the proposed cementation.
- Through qualitative interpretation in this study, the results are being discussed and concluded, and they are interpreter’s own biased nature to some extent. Therefore, for more detailed exact, and less biased conclusions, perhaps, quantitative approach is required.
- In terms of clay volume, saturation, and porosity, a justified correlation is generally observed. Whereas it should be considered the template applied for total porosity that leads to the underestimated effective porosity.
- The temperature and formation pressure of target reservoirs is really high, producing uncertainties while generating and interpreting the results.

Chapter 6: AVO Forward Modelling

6.1 Results

The following chapter will elaborate on the results obtained from the target reservoirs from four exploration wells (34/10-23, 34/10-42S, 34/11-1, and 34/11-5S) according to the concept of AVO Forward Modelling. The objective of AVO is to study the lithology and fluid impacts related to target reservoirs with their in-situ conditions and different fluid. The focus of the AVO analysis is the response of top target reservoirs. Though, in the study, only one base zone is examined, which is Ness Formation. The main target reservoir is the Tarbert Formation, which shows a clear boundary between sand and the upper shale of cap rock (Heather Formation). Moreover, it is seen as the primary gas-bearing reservoir zone recorded in wells 34/10-23, 34/11-1, and 34/11-5S. The top of Tarbert Formation is modeled for all the wells utilized related to AVO modeling in this study. Whereas, only in the well 34/11-1, top Ness Formation is also modelled.

6.1.1 Generating synthetic seismic

The generation of synthetic seismic is already being discussed in chapter 3. The final choice for utilizing the generated synthetic seismic initiated after examinations of many kinds of synthetic seismic wavelets. The best synthetic seismic wavelet was picked for the further process. The selection of parameters, blocking modes and size, and type of wavelet and its frequency are elaborated as follows.

6.1.1.1 Wavelet selection

For a synthetic seismic generation, the wavelet that is applied is generally the wavelet extracted statistically from the real seismic data concerning the well location. In this study, seismic data is not available; thus a linear phased Ricker wavelet is utilized (Figure 6.1). The resolution of the Ricker wavelet depends upon the selection of the dominant frequency of the wavelet. The target reservoir Tarbert Formation average P-wave (Vp) velocity estimated around 3500 to 3600 m/s.

Moreover, in Table 6.1, general real seismic data values are displayed (SEG Wiki, 2021b). The table exhibits Vp in the average of about 3500 to 3600 m/s, possibly comprising a frequency in the range of 35 to 36 Hz. Additionally, Table 6.2 defines the relation between frequency, velocity, and depth. The frequency experiences reduction as the depth increases, whereas velocity rises with depth. The table displays ranges of the frequency corresponding to the velocity as 50Hz at 2000m/s and 20Hz at 5000m/s. Furthermore, as we know, wavelength increases with the increase of depth and decrease in frequency; thus it is proportional to the Vp.

The formula of wavelength displays frequency as an inversely proportional parameter, which is as λ=Vp/frequency. The vertical resolution is estimated from wavelength as λ/4. Therefore, considering the mentioned concepts and the table, it can be concluded that the seismic resolution is high at the shallow depths. As the seismic wave penetrates deeper, the seismic wavelet loses vertical resolution.

This character makes it difficult to identify and mark the top and base of the particular formation. Considering Table 6.1, the maximum vertical resolution of the seismic wave at 2000m/s velocity and 50Hz frequency is 10m, which means a 10m thin formation can be feasibly identified with its top and base boundaries. However, at 5000m/s velocity and 20Hz frequency, the vertical resolution becomes poor and can mark the top and base of 62m thick formation.

Table 6. 1: Threshold for vertical resolution. Based on (SEG Wiki, 2021b).

Vp (m/s)	**f (Hz)**	**λ (m)**	**λ/4 (m)**
2000	50	40	10
3000	40	75	18
4000	30	133	33
5000	20	250	62

In this thesis, the dominant frequency used is 45Hz, as it is set as default in Hampson Russell Software (HRS 10.5). The utilized dominant frequency (45Hz) effectively displays minor subsurface characteristics, for instance, coal beds and low thickness reservoirs.

Thus, it is more challenging to relate synthetic seismic with real seismic waves, while correlation is not the main objective for this study. Moreover, the wavelength of the Ricker wavelet is set to 150ms, phase rotation as 0°, and sampling rate as 1ms. The mentioned values for the Ricker wavelet are utilized in generating all seismograms.

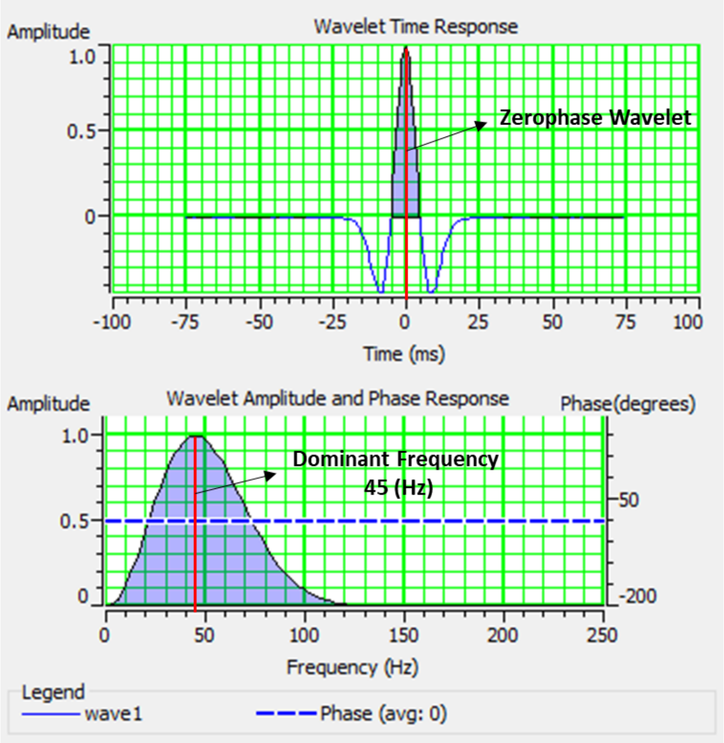

Figure 6. 1: In this study, generated Ricker wavelet was utilized. The generated wavelet has a phase rotation of 0, whereas 1 ms is the sample rate, 45 Hz is the dominant frequency, and 150 ms wavelet length. The wavelet is generated from HampsonRussell (10.5) software.

6.1.1.2 Gassmann´s fluid substitution

By using Gassmann's fluid substitution, the impacts of different fluid replacements are studied and interpreted. Fluid substitutions of 50% gas, 10% gas, 80% oil, and 100% brine are examined for the in-situ 80% gas, using the Fluid Replacement Model (FRM) in the Hampson Russell software. The transition in seismic properties can be observed as the result of fluid replacements.

Moreover, a significant transition in Poisson's ratio is observed because of the fluid replacements, and it represents the sensitivity of Poisson's ratio to fluids. The hydrocarbon saturation reduces the Poisson ratio related to brine, whereas the gas saturation causes the significant reduction. Even a minor gas saturation can bring a substantial decrease in Poisson's ratio. Thus, a 10% gas saturation display more variations relative to 100% brine saturation than variations from 80% oil. Additionally, in-situ 80% gas shows a minor difference in Poisson's Ratio relative to 50% gas. Though, it is challenging in differentiating the variations present within the high gas saturations. However, it can be said that hydrocarbon increase the shear wave (Vs) velocity and decreases the density, Poisson's ratio, and the P-wave (Vp) velocity. It is said that oil and water are heavier than gas. Therefore, the calculated density is decreased by the gas saturation. However, the fluids exhibit no impact against the shear modulus. The S-wave velocity rises to some extent because of the lower density of gas or oil against the water, as reflected in Equation 3.28. The linear trend is followed by the S-wave velocity with increasing saturation in hydrocarbon, as illustrated in Figure 6.2. Moreover, Figure 6.2 illustrates the difference in velocity response with respect to fluid dispersal and saturation.

There are two kinds in which fluids are saturated, a patchy or homogeneous condition. This study assumes the fluids present in the reservoirs are in a homogeneous fluid substitution that is a uniform arrangement of gas and brine. A patchy or heterogeneous saturation exhibit that the reservoir fluids are combined in a non-uniform manner, which might be a possible result of the difference in permeability, wettability, or perhaps, amount of shale. The estimation of rock modulus associated with uniformly fluid distribution utilizes Reuss, (1929) average, which is iso stress average. Whereas the Voigt, (1910) method or iso strain average is used in the estimation of rock modulus for a patchy fluid distribution (Avseth, 2015).

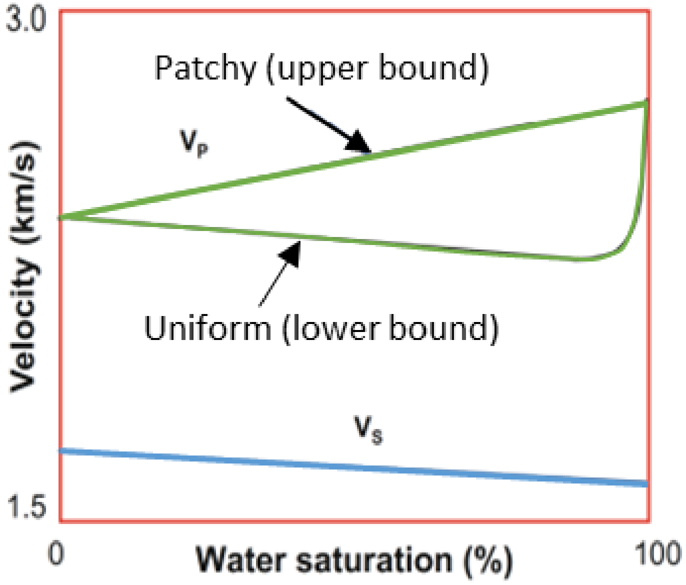

Figure 6. 2: The response of Vp and Vs against a patchy or heterogeneous upper bound and homogeneous uniform lower bound for a saturation of gas (modified after Avseth, 2015).

In the case of a homogeneous saturation, the Poisson ratio, P-wave velocity, and Acoustic Impedance get influenced by the evaluation of oil-gas saturation, illustrated in Figure 6.3 against the low temperature and pressures. A more linear relation exhibits oil relative to gas (Simm et al., 2014). The P-wave velocity increased in the presence of high gas saturation, as illustrated in Figure 6.3. Considering gas as the hydrocarbon saturation, the main reason behind it is the minor gas saturation that can reduce the bulk modulus of the gas saturated zone, which results in decreasing the velocity as reflected in equation 3.27. Moreover, the acoustic impedance exhibit decrease in the initial gas saturation percentage and rises significantly as the saturation of gas increases. The Poisson’s ratio exhibits a similar feature in the cross plot versus water saturation. Therefore, a minor amount of gas saturation perhaps exhibits a significant impact on the resultant amplitudes.

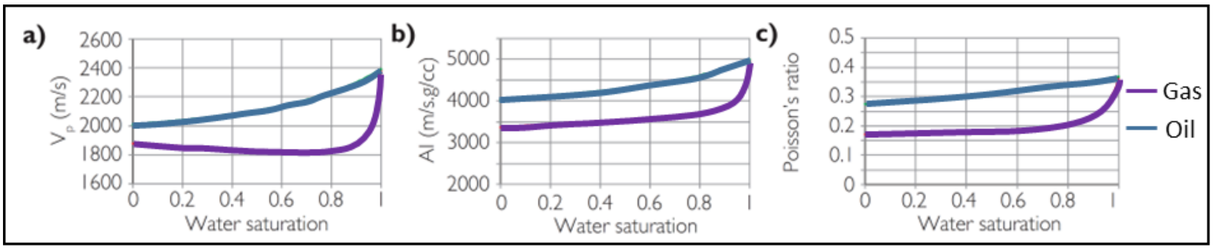

Figure 6. 3: The effects of oil and gas saturation on Vp, AI, and Poisson´s ratio. The nature of the generated curve relies on the complexity of gas and water combination that depends on the temperature and pressure (modified after Simm et al., 2014).

6.1.1.3 Blocking of well log data

Well log readings relative to seismic data possess high frequencies of 10,000Hz to 20,000Hz, comprising 2cm to 2m of vertical resolution. Thus, well log measurements record the data in large quantity. The blocking step is applied on the well log data to eliminate the smaller events; thus, the blocking step is applied on the well log data to eliminate the smaller events. This leads to help in picking the peaks or troughs for a particular feature. The blocking of density log data basically averages the log data and displays the major events. The averaging of the data depends on the size of the blocking being used. The results related to the different block sizes (2m, 5m, and 10m) and modes (Automatic Uniform, Backus Average, and Automatic Non-Uniform) applied on the density log of the well 34/10-23 are examined (Figure 6.4).

The best display of blocking is seen with 2m Backus Average blocking mode as the target reservoir (Tarbert Formation) is thin in thickness (14m). The response generated from Automatic Uniform and Automatic Non-Uniform with 2m blocking size exhibits a similar blocking trend.

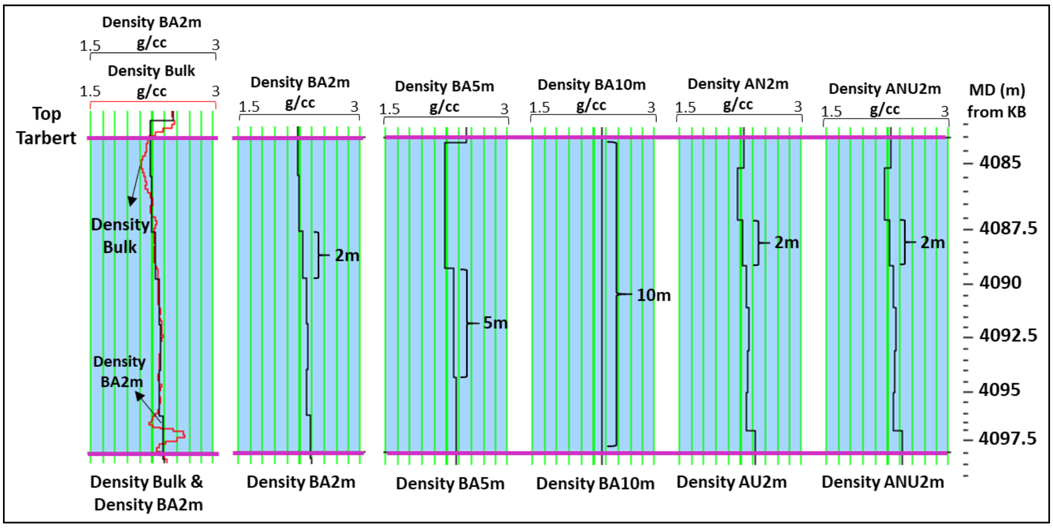

Figure 6. 4: (Left) A comparison between a measured Density Bulk log and a resultant blocked Density log. (Right) Different block sizes, such as Backus Average (BA2m, BA5m, BA10m), Automatic Uniform (AU2m), and Automatic Non-Uniform (ANU2m) applied on the Density Bulk log, and results are shown. The well 34/10-23 utilized for this example.

The applied blocking modes and sizes in generating synthetic data with different amplitudes are illustrated in Figure 6.5. For generating the symmetrical wavelets, a standard positive polarity convention is applied (Figure 6.6). The blocking modes such as Automatic Uniform (AU) and Automatic Non-Uniform display similar responses. The best synthetic wavelet through the Backus Average is 2m blocking. It can be observed that minor amplitudes are exhibited by Backus Average blocking mode with 2m size, whereas relatively more minor amplitudes can be seen with 5m blocking size.

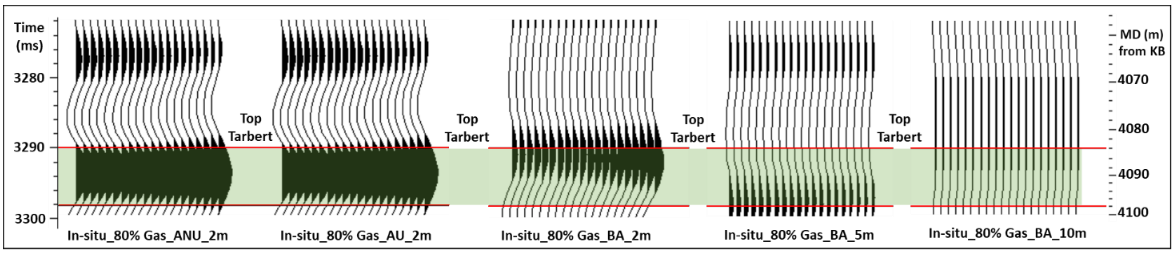

Figure 6. 5: The displaying of amplitudes (angle of 0 to 30 degrees) generated by applying various block modes and sizes, where ANU = Automatic Non-Uniform, ANU = Automatic Uniform, and BA = Backus Average. The top red line follows the peak/trough of the wavelet for TG Tarbert (Top Gas), and the bottom red line shows the base of the Tarbert Formation.

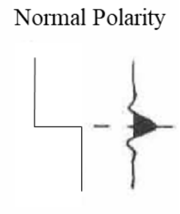

Figure 6. 6: In this study, a symmetric wavelet with a positive polarity convention is utilized. A peak generates when the upper layer is softer, and the lower is hard. The white patch is showing troughs (modified after *(Abdulateef & Al-Rahim, 2018).*

Figure 6.7 exhibits crossplots related to angle versus amplitude and Intercept versus Gradient (I-G) of the block modes and sizes utilized for well 34/10-23. The Automatic Uniform (AU) and Automatic Non-Uniform (ANU) of 2m block sizes are plotting in the same manner and comprising positive intercept and negative gradient. Whereas, Backus Average of 5m block size displays relatively higher positive gradient and negative intercept, as the thickness of Tarbert Formation in this well is about 14m and using a block size of 5m will affect the result significantly.

Moreover, the Backus Average of 2m block size exhibits a relatively lower positive gradient near zero and a relatively higher negative intercept. It is observed after many attempts that Backus Average reflects relatively a better choice as a block size for examining synthetic wavelets. All synthetic wavelets were generated through Backus Average block mode, but the blocking sizes differed depending upon the target reservoir's thickness and resolution (Tarbert Formation). In the following Table 6.3, the various block sizes utilized related to studied wells are illustrated.

Table 6. 2: Displaying the block mode and sizes utilized in all the four AVO wells.

Well	Block Size	Block Mode
34/10-23	2m	Backus Average
34/10-42S	25m	Backus Average
34/11-1	2m	Backus Average
34/11-5S	5m	Backus Average

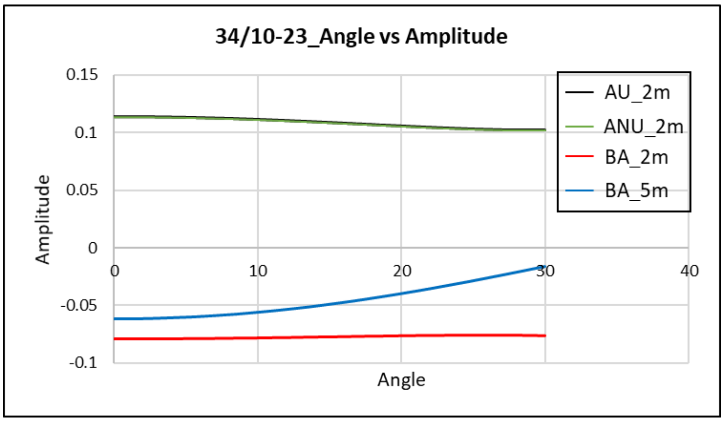

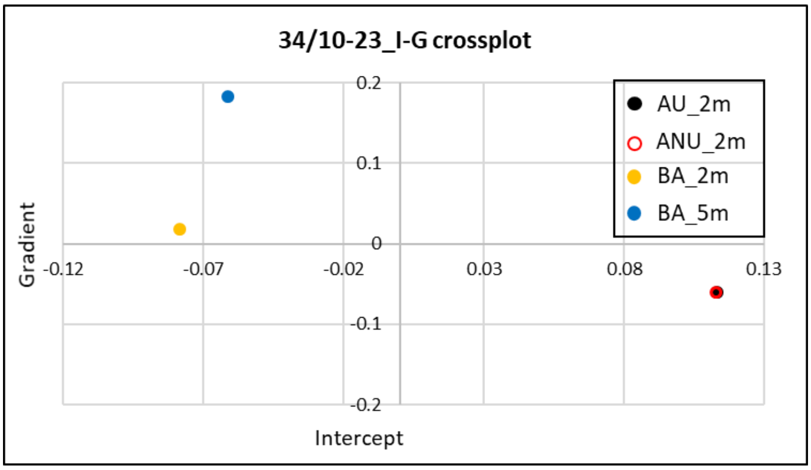

Figure 6. 7: Crossplot of Angle vs Amplitude and the resultant I-G crossplot of well 34/10-23 at the top of Tarbert Formation.

6.1.2 AVO Analysis

The AVO analysis was carried out utilizing the I-G (intercept versus gradient) crossplot. Several kinds of tests were applied on the target reservoirs with the in-situ condition and different fluid substitutions. In the three wells, 34/10-23, 34/11-1 and, 34/11-5S, the gas is contained in the top of the Tarbert Formation, where density and Vp logs are available. Whereas the Vs is predicted for every well through the fluid substitution process. Following are the different tests carried out for studying the sensitivity related to fluids, porosity, shale volume, burial and diagenesis, and comparison between hydrocarbon-bearing and brine-bearing reservoirs.

6.1.2.1 Fluid sensitivity for well 34/10-23, 34/10-42S, 34/11-1 and 34/11-5S

The well 34/10-23 exhibiting results of AVO modelling in Figures 6.8 (a) and (b), which display Angle vs. Amplitude and I-G crossplots. The main objective of these specific crossplots is to define responses occurring because of fluid substitution. Tarbert Formation with in-situ 80% gas and fluid substitution as 10% gas, 50% gas, 80% oil, and 100% brine is tested for TG (Top Gas).

For this well, 2m of Backus Average blocking is utilized. The well comprises in-situ 80% gas with 10% and 50% gas as fluid substitution having response plotted under 100% brine and 80% oil response. It is showing the Class 4 AVO I-G response. One reason for being Class 4 could be due to the deeper depth of the gas-bearing reservoir Tarbert, which is 4084m; moreover, it could be due to the smaller thickness of the Tarbert Formation, comprising 14m. Furthermore, in deeper depths vertical seismic resolution becomes poor, wavelength increases, resulting in tuning thickness. Therefore, Tarbert Formation being 14m thick and at 4084m depth, it makes Tarbert and overlying cap rock stiffer, and at this depth, the fluid sensitivity becomes low; these reasons could lead to Class 4 AVO I-G response.

The observations from the generated cross plots are that the in-situ condition plots as class 4 AVO response, which might categorize the reservoir formation as possibly compacted sandstones. Moreover, when the in-situ condition is replaced by fluid substitution with 100% brine, the data moves and crosses the background trend. The values of intercept transform from -0.07 to -0.05, and the gradient transform from 0.01 to 0.12. It corresponds to an amplitude with a lower offset, and the variation in amplitude is low as the angle of incidence increases. It reflects that shale present in the Heather Formation (cap rock) possesses relatively high impedance and Poisson’s ratio than the sand present in the Tarbert Formation (reservoir rock).

After observing the gas saturation of 10% and 50% shows that both percentages of gas saturations are plotting nearly at the same locations. Moreover, the in-situ gas saturation (80%) relative to the fluid substitution (10% and 50%) gas saturations, displaying a very minor decrease in positive gradient values. Similarly, the intercept shows a very minor decrease but in negative values. This possibly illustrates that the replacement of different gas saturations (low or high) can generate impact in AVO modelling, even if it is 10% gas saturation.

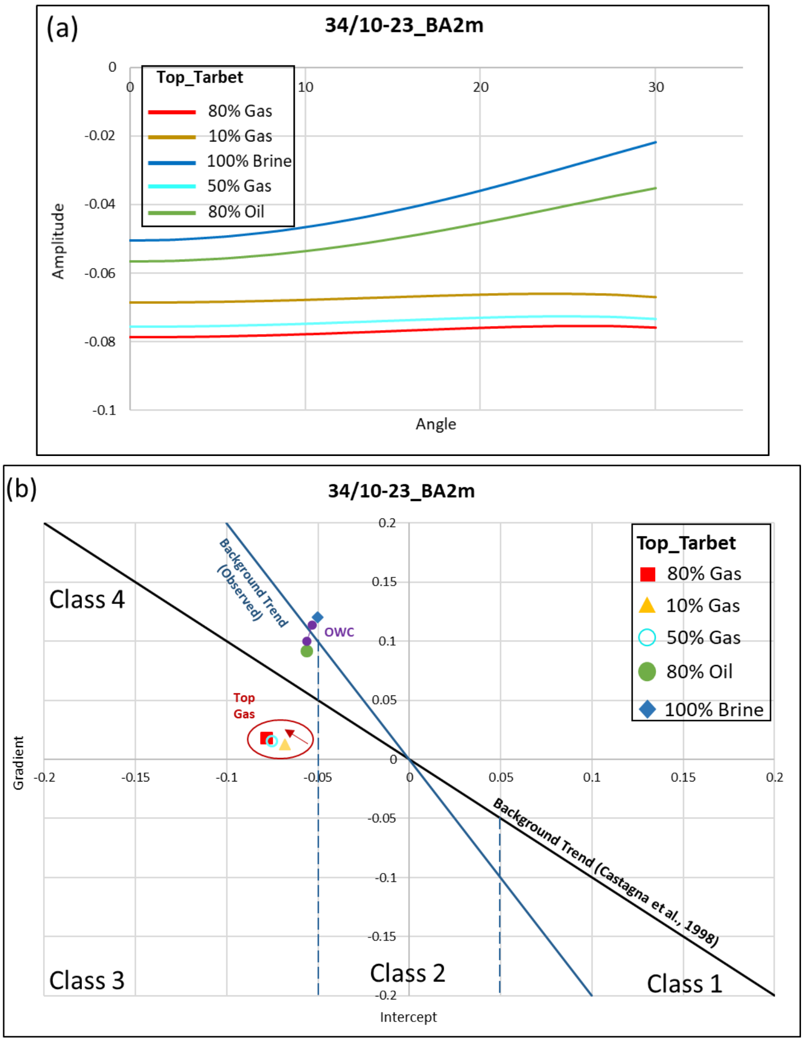

Figure 6. 8: (a) The Angle vs. Amplitude crossplot of Top Tarbert in the well 34/10-23. (b) I-G crossplot of top Tarbert Formation of well 34/10-23. The hydrocarbon saturation influence is studied for TG.

Moreover, in the well 34/10-42S, 25m of Backus Average blocking was utilized. The 100% brine in-situ, with fluid substitution 10% and 80% gas having response plotted under 80% oil response. It is showing the Class 4 AVO I-G response. The 10% oil response is slightly over 100% brine response; the reason for it is a systematic error.

This well contains Brine in the Brent Group; therefore, only Tarbert Formation is being utilized for AVO analysis. In the Brent Group, a small amount of hydrocarbon is also present, but overall, this well is considered Dry (Figure 6.9 a, b).

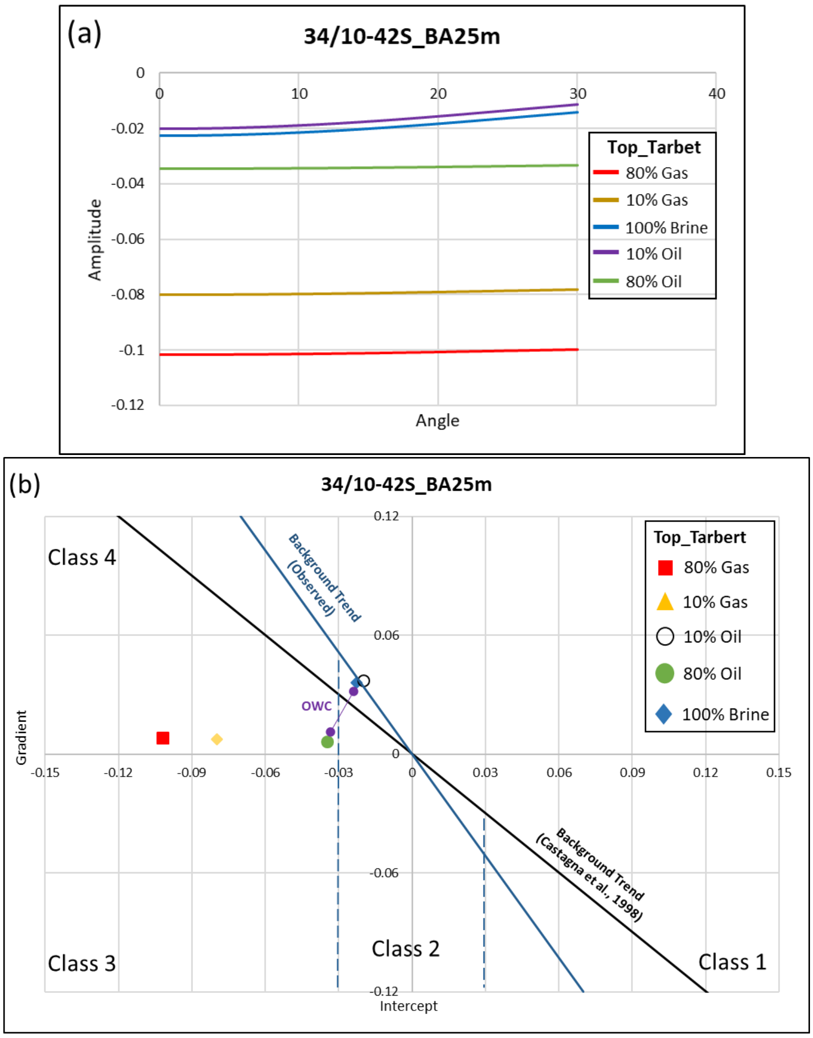

Figure 6. 9: (a) The Angle vs. Amplitude crossplot of top Tarbert (Brent Group) in the well 34/10-42S. (b) I-G crossplot of Tarbert (Brent Group) of well 34/10-42S. All the points are plotted in AVO Class 4 and this well tested to study the influence of brine-bearing Brent Group reservoirs, particularly Tarbert Formation.

In the well 34/11-1, 2m of Backus Average blocking was utilized on two Gas bearing reservoirs, Tarbert and Ness (Figure 6.10 a, b). The Tarbert with 80% gas in-situ, with 10% and 50% gas as fluid substitution having response plotted under 100% brine and 80% oil responses. It shows the Class 3 AVO I-G response. Whereas Ness comprising gas responses are positive in values compared to brine and oil, which are plotted as Class 1 and gas above to class 1, perhaps, AVO considering Ness as a Gas base.

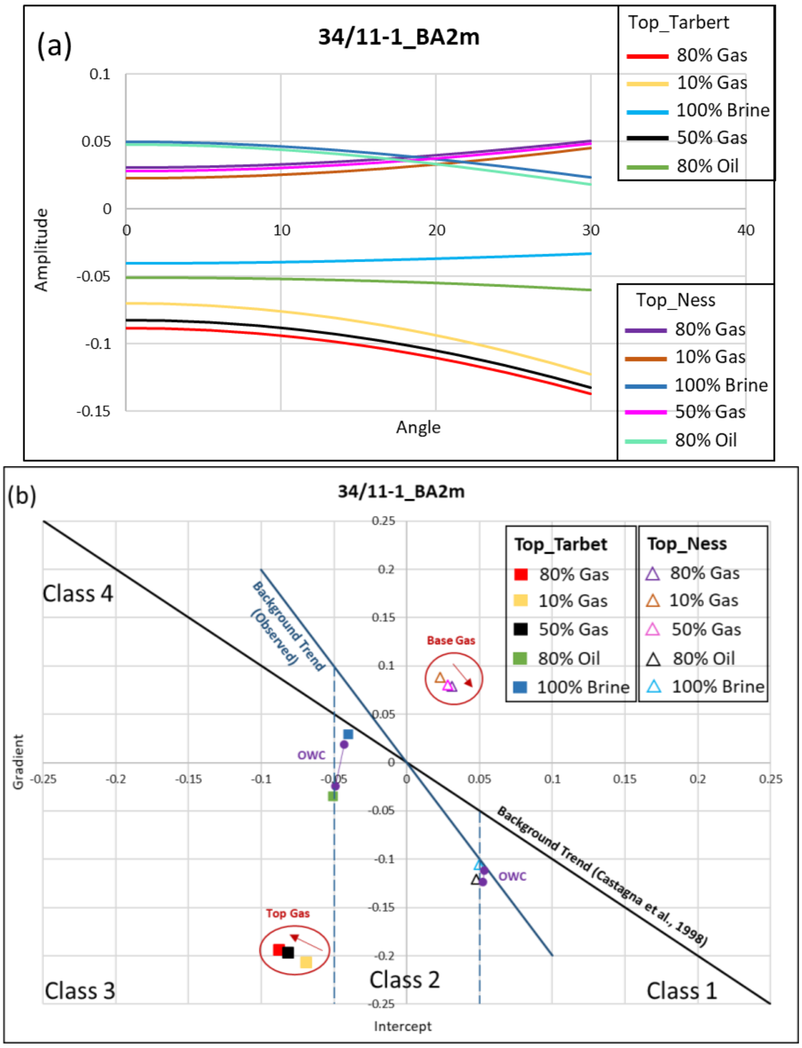

Figure 6. 10: (a) The Angle vs. Amplitude crossplot of Top Tarbert and Top Ness FMs in well 34/11-1. (b) I-G crossplot of top Tarbert and Ness Formations of well 34/11-1. The hydrocarbon saturation influence was studied for TG in Tarbert and Ness Formations.

Furthermore, in the well 34/11-5S, 5m of Backus Average blocking was utilized on Tarbert Formation (Figure 6.11 a, b). In-situ 80% gas with 10% and 50% gas as fluid substitution having response plotted under 100% brine and 80% oil response. It is showing Class 1 AVO I-G response.

Tarbert is at a higher depth (7086m) where fluid sensitivity becomes low and compaction increases; therefore, the rock becomes harder. Thus, the Class 1 AVO response might be due to these reasons. At these deeper depths, it can be concluded that AVO response has limitations with deeper depths, and therefore, it will not follow the general rule or textbooks examples.

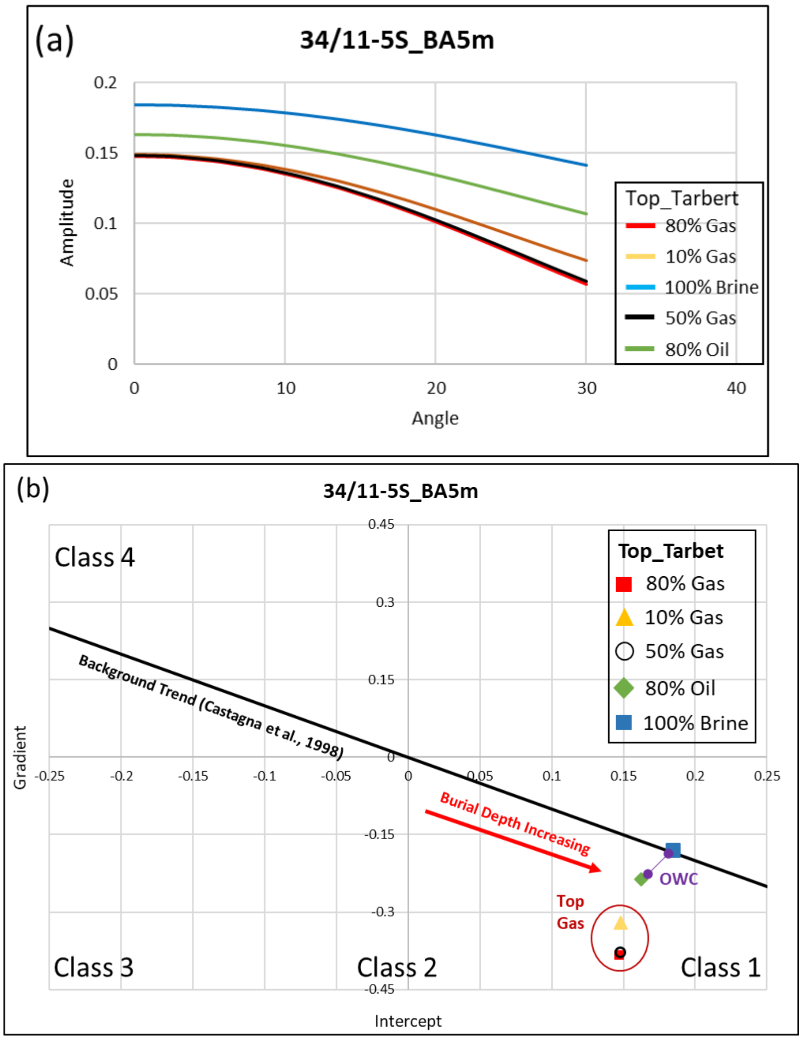

Figure 6. 11: (a) The Angle vs. Amplitude crossplot of Top Tarbert in the well 34/11-5S. (b) I-G crossplot of top Tarbert Formation in well 34/11-5S. The hydrocarbon saturation influence was studied for TG in Tarbert Formation.

6.1.2.2 Porosity and shale volume sensitivity for well 34/11-1_Tarbert (4045m)

The Porosity and Vsh sensitivity for well 34/11-1_Tarbet (4045m) being tested with different porosity and Vshale percentages on in-situ, 80% gas, and different scenarios, such as 10% gas, 50% gas, 100% brine, and 80% oil.

The resulting I-G crossplot for Porosity, and Vshale sensitivity shows that increasing the porosity and Vshale, increase the value of intercept. It follows the general rule that both the parameters are increasing with the same trend. The reason might be the decrease of compaction as porosity increases at higher depth and allows more fluid to accommodate in the pores, increasing the AVO intercept value or AVO fluid sensitivity (Figure 6.12).

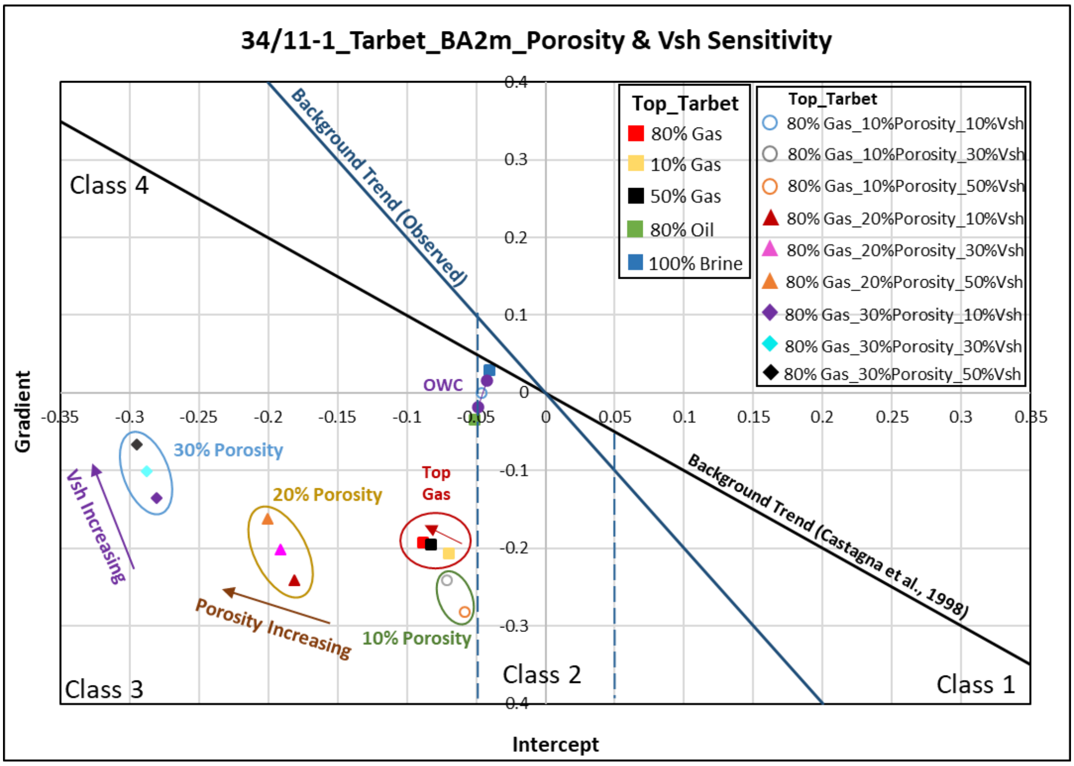

Figure 6. 12: The I-G crossplot of top Tarbert Formation in well 34/11-1. The effect of porosity, volume of shale, and water substitution studied for TG in Tarbert Formation. Two black arrows indicate increase in Porosity and Volume of Shale trends.

6.1.2.3 Sensitivity related to burial and diagenesis for well 34/11-5S

In the well 34/11-5S, the -bearing reservoir is Tarbert, the deepest reservoir in all the four AVO wells. Tarbert is at 7086m depth and consists of 24m thickness. Tarbert response plotted in Class 1 follows the general rule of AVO crossplot that in this direction higher depths AVO response is plotted. Here the sensitivity to burial and diagenesis is being tested with the parameter of different porosity percentages, such as 10%, 20% and 30%, along with the in-situ 80% gas condition. The response shows that increasing the porosity percentages increases the response towards Class 1 and decreases the intercept values, but here as the well is deeper in-depth; therefore, the impact of porosity change is less than but near to zero on intercept values.

The response of 10% porosity, which means more compacted Tarbert at 7086m depth, displays positive intercept and gradient values. This might be because Tarbert is higher in acoustic impedance (product of velocity and density) than the above cap rock Heather Formation ($Z1 < Z2$).

The response of 20% porosity means relatively less compaction at this higher depth, displays AVO response with smaller negative intercept values and increasing positive gradient values, which shows Tarbert might be less in acoustic impedance than the overlying cap rock. The response of 30% porosity at this respective higher depth (7086m) means less compaction and more porous sand, displays AVO response with smaller negative intercept values and increasing positive gradient values, which shows Tarbert might be less in acoustic impedance than the overlying cap rock (Heather Formation) (Figure 6.13).

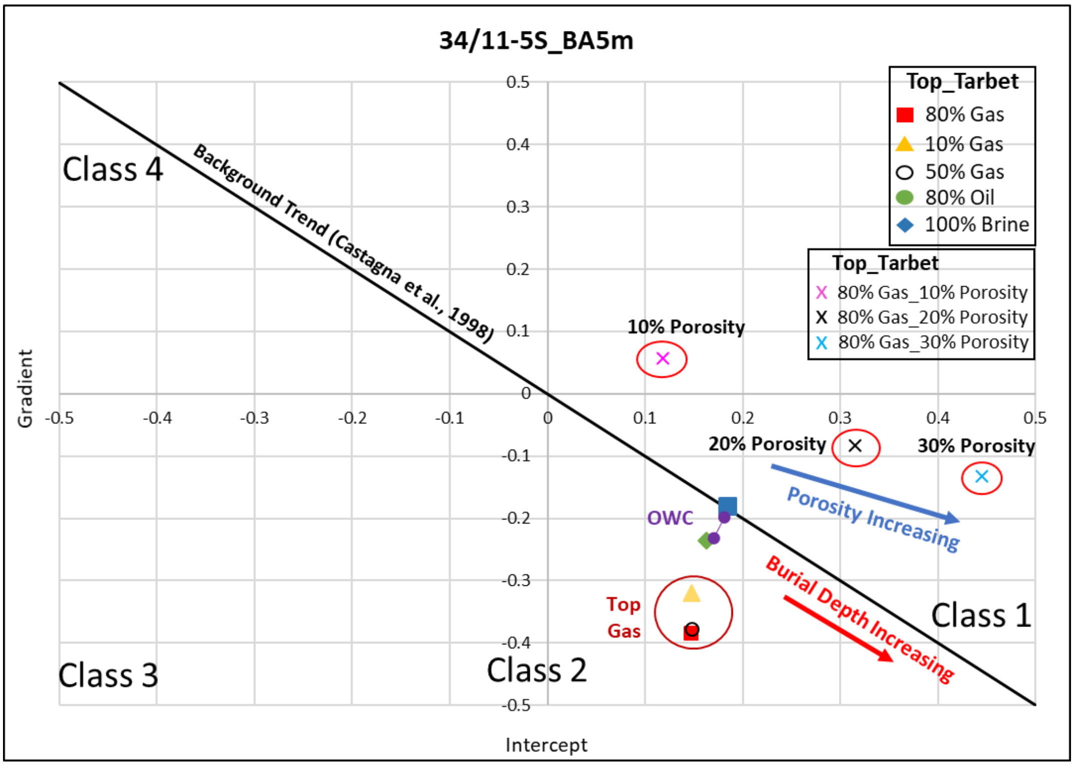

Figure 6. 13: The I-G crossplot of top Tarbert Formation in the well 34/11-5S. The effect of fluid and porosity variations shown for the top Tarbert Formation (TG). The black arrow indicates increase of burial depth trends.

6.1.2.4 *Comparison between Hydrocarbon Reservoir Well and Dry Well*

The well 34/10-23 has a response slightly above Class 3, as it is small in thickness (14m) and at greater depth (4084m); therefore, the compaction is high at this depth that plays a role in plotting the response at this point. Moreover, the effect of cap rock might be a reason as well, and at this depth, the fluid sensitivity is minimized. In addition, the presence of coating and cementation might impact the AVO response (Figure 6.14).

For the dry well 34/10-42S, Brent Group, specifically Tarbert Formation, was utilized for the AVO process. The response of this well displayed as dry can be confirmed from the I-G crossplot, in which Tarbert Formation plotted in Class 2 (Figure 6.15). Overall, the general trend of AVO is being followed by both wells that hydrocarbon is plotting under Brine response. The well 34/10-23 plotted with high gradient values as it contains gas within the reservoir (Tarbert Formation), whereas 34/10-42S contains brine and plotted with low gradient values, within and near to AVO Class 2.

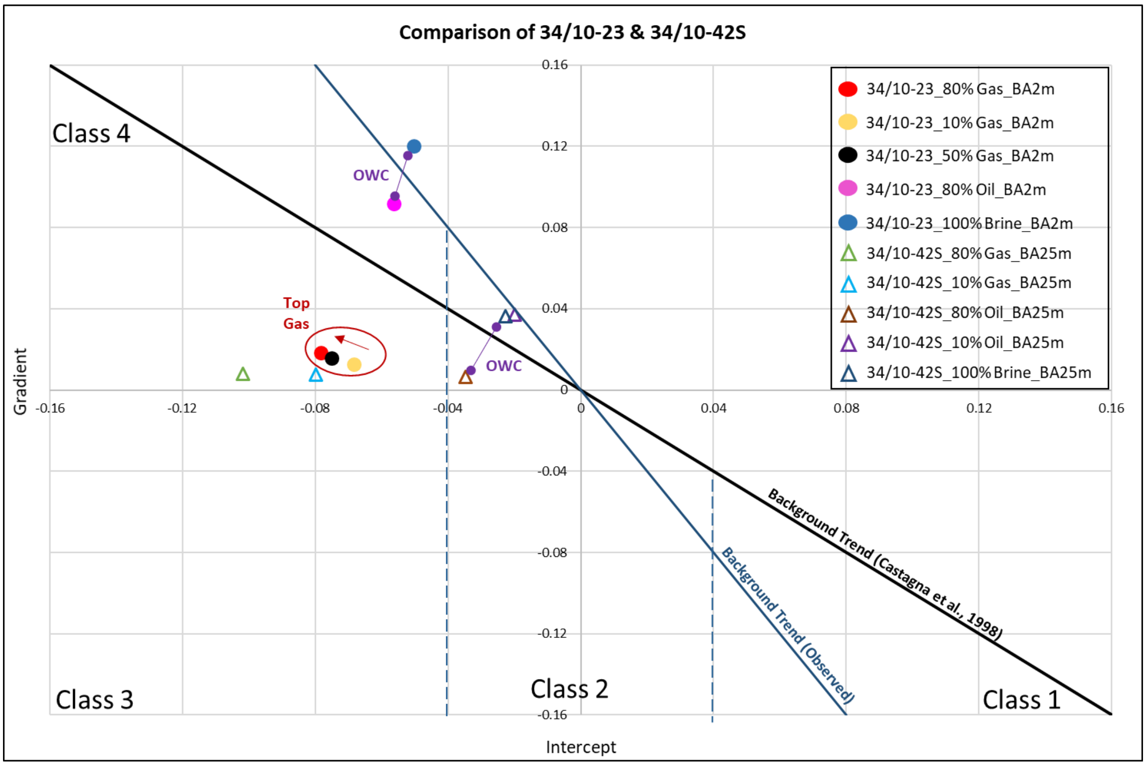

Figure 6. 14: Comparison of hydrocarbon and dry well is shown on the I-G crossplot for top Tarbert Formation in the well 34/10-23 and 34/10-42S. The hydrocarbon-bearing well is 34/10-23 with Backus Average of 2m blocking, whereas, brine bearing well is 34/10-42S with Backus Average of 25m blocking.

6.2 AVO Discussion

The main objective of carrying out the AVO modelling is to discuss the variations and uncertainties occurring in the seismic response due to the alterations in the rock and fluids. The AVO modelling can also be utilized as the direct hydrocarbon indicator for the lithologies such as, shallow depth uncompacted to moderately compacted deposits of shale and sand sequences. In this kind of lithological setting, fluid compressibility greatly impacts the compressibility of the whole rock. However, if the sandstones are compacted or existing in the presence of carbonate, the fluid compressibility impacts relatively low to the compressibility of the whole rock. Therefore, the AVO sensitivity becomes low (Simm et al., 2014).

The performing of AVO modelling on selected wells with the same target formation (Tarbert) generated several dissimilar results. In Figure 6.15, all four AVO Well comparison exhibits the reservoir response. Three wells, 34/10-23, 34/11-1, and 34/11-5S are gas-bearing reservoirs, with Tarbert being the reservoir formation, and in well 34/11-1, Ness Formation is also included as the secondary gas reservoir. The in-situ condition of these three gas-bearing reservoirs is 80% gas. The Backus Average blocking applied on all the wells, two gas-bearing wells, 34/10-23 and 34/11-1, displayed the best trend with 2m blocking. The well 34/11-5S displayed the best trend with 5m blocking. Whereas the well 34/10-42S is considered as a dry well, and its response is of 100% brine with 25m Backus Average blocking.

34/10-23: its response is slightly above Class 3, as it is small in thickness (14m) and at greater depth (4084m); therefore, the compaction is high at this depth that plays a role in plotting the response at this point. Moreover, the effect of cap rock might be a reason, and at this depth, the fluid sensitivity is minimized, which might also affect the AVO response.

34/10-42S: this is considered dry and Brent GP, specifically Tarbert Formation utilized for the AVO process. The response of this well is plotted in Class 2 and displayed as the Brine bearing well.

34/11-1: the Tarbert here is plotted in the AVO Class 3, and the Ness is plotted on the I-G crossplot as the base of gas. The saturation of gas in Tarbert is more as compared to the Ness; this might be one of the reasons for Ness being plotted as the base of gas.

34/11-5S: the reservoir in this well is the deepest reservoir in all the four AVO wells. The formation is Tarbert, at 7086m depth and consists of 24m thickness. Its response is plotted in Class 1, which follows the general rule of AVO crossplot that in this direction AVO response having higher depth are plotted.

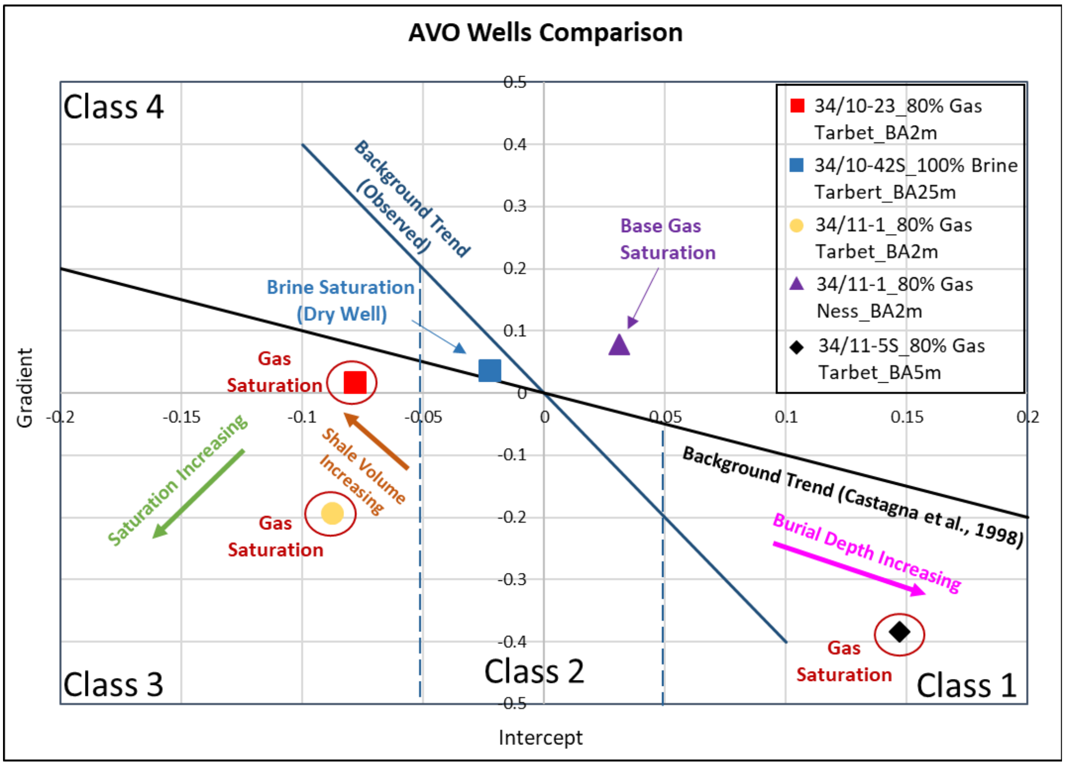

Figure 6. 15: Summary of the AVO (I-G) crossplot of the top Tarbert Formation in four wells. The effects of shale volume, saturation and burial depth (compaction & porosity loss) are illustrated.

6.2.1 Identification of Lithology

The variation in acoustic impedance (AI) between reservoir and cap rock boundary influences the intercept values. Whereas the variation in amplitude associated with the change in offset is controlled by the difference of Poisson’s ratio between the reservoir and cap rock boundary. As mentioned earlier, the relation between density and velocity is directly proportional; thus velocity increases with the increase of density in the lithology. Therefore, on the basis of different density and velocity values, lithological variation can be observed that might help in interpreting the lithology to some extent. Moreover, the relation between AI and porosity is inversely proportional; with the increase in porosity, the value of AI decreases. Furthermore, the Poisson's ratio comprises significant visible variations that help in differentiating the lithologies in a simpler manner (Simm et al., 2014).

6.2.2 Compaction of Rock

Generally, the increase in depth reflects the increase in compaction. Therefore, the porosity of a rock decreases with the increase of depth, which also influences the elastic properties of the rock. Additionally, the rise in mechanical compaction with depth reduces the rock's Poisson ratio but increases the rock's acoustic impedance. Usually, the sand at shallow depths is porous, which results in relatively low Poisson's ratio and acoustic impedance values than the shale. Moreover, at the greater depths, the porosity of sand decreases, making the sand relatively harder (stiff), resulting in the increase of Poisson's ratio and acoustic impedance values compared to shale. The change in acoustic impedance between sand and shale interfaces generates a crossover with respect to a particular depth, as shown in Figure 6.16. Moreover, this cross-over can be generated at limited or fixed depth intervals or perhaps, in several hundred meters of thickness. Additionally, the cross-over might occur more than once with increasing depth (Simm et al., 2014).

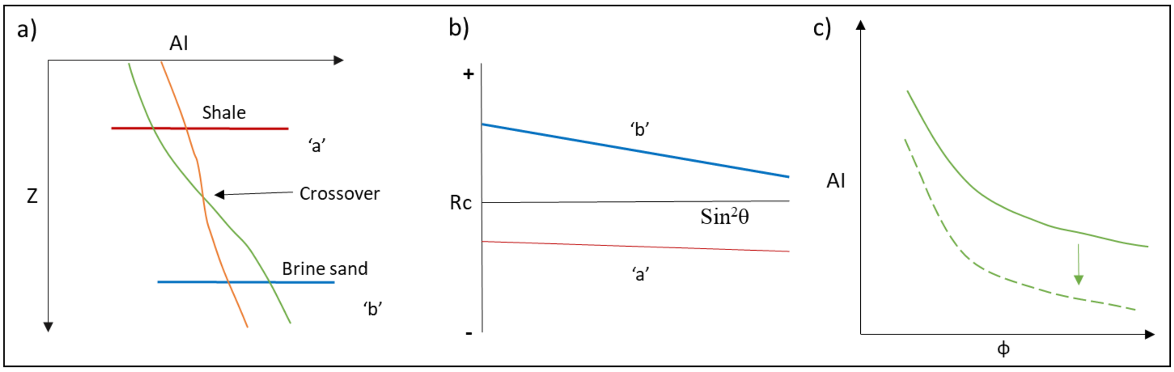

Figure 6. 16: The influence of compaction on shale and brine sand. a) Cross plot of Depth (Z) versus Acoustic Impedance (AI), where orange curve represents shale, and green curve as brine sand. b) The sand-shale boundary between the acoustic impedance cross over, generating the AVO response. c) Cross plot of Porosity of sand vs. Acoustic Impedance exhibiting brine sand (solid line) and hydrocarbon sand (dashed line) (modified after Simm et al., 2014).

In the greater depths, it is observed that the sand experiences a process of cementation. The cemented sands lower the porosity and thus increase acoustic impedance (AI) and reduce Poisson's ratio of sand. Consequently, these characteristics generate positive reflection coefficient values at both the zero offset and with increasing offsets. Therefore, this generates the AVO response as a strong negative gradient that displays as AVO Class 1, illustrated as a blue line in Figures 6.16 a) and b). This identical response is visualized in well 34/11-5S (Figure 6.11).

6.2.3 Effects related to Fluid Saturation

Generally, a decrease in the Poisson's ratio and acoustic impedance is observed due to fluid replacement, for instance, brine to hydrocarbons. Moreover, if fluid is replaced with gas, it generates a significant drop. Additionally, the condensate and light oil exhibit identical results (Simm et al., 2014). In the presence of gas sands, the AVO cross plot exhibits AVO Class 3 response. The porosity of sand gets a decrease in the presence of cementation and plots the AVO response as Class 1. The cemented sands in the AVO Class 1 reduce the brightness of positive amplitude regarding the hydrocarbon presence. Whereas cemented sands of AVO Class 3 increase, the brightness related to negative amplitude. Moreover, as the porosity comprises great influence on the AVO results, that is, with the decrease in porosity of the rock, a decrease in Poisson's ratio and acoustic impedance occurs because of the hydrocarbon saturation (Simm et al., 2014). Moreover, it is observed that the distance in the plotting of gas-bearing and brine-bearing data points is larger in the relatively shallow depth Tarbert Formation and smaller distance in the deeper depth (Tarbert Formation in well: 34/11-5S).

6.2.4 Effect of Shale

The stiffness or hardness plays a major role in the rock solid frame, influencing velocity and resultant fluid impacts. The hard (stiff) rocks comprise relatively low Poisson's ratio (PR) and high Acoustic Impedance (AI), whereas the soft nature rocks display relatively high Poisson's ratio and low Acoustic Impedance. Moreover, the stiffness in a rock depends on several factors, for instance, amount of shale, amount and type of cement, distribution of pore shape, and grain contacts quantity (Simm et al., 2014). The Tarbert Formation in well 34/11-1, tested with different shale volumes (10, 30, and 50%) (Figure. 6.12).

As the shale volume increases, the intercept values experience a decrease, whereas the gradient experiences an increase in its values. The shale volume basically exhibits the presence of clay. The clay presence in the rock can be as part of the solid framework or pore-filling or perhaps in both—this characteristic of clay results in different clay effect (Simm et al., 2014). Figure 6.12 illustrates an AVO response of Class 3, reflecting a high acoustic impedance contrast between the cap rock shale (Heather Formation) and the gas reservoir sand (Tarbert Formation) associated with the increase of shale volume. Whereas it also displays a low Poisson's ratio difference. Furthermore, the cross plot exhibits AVO response associated with shale volume sensitivity as the decrease in negative gradient values and relatively increase in negative intercept values. The different properties of shale exhibit a significant influence on the AVO response, and the shape of pores present in the rock also affects the AVO response.

The shale consists of layering that creates a flat pore in it, which is relatively high in compressibility. Whereas the different shapes of pore occurring in sandstones, for instance, triangular or rectangular or uneven, are relatively low in compressibility. The rigidity of shale becomes less due to the presence of minor cracks and flat pores (Simm et al., 2014).

6.2.5 Bed thickness and layering

The bed thickness is an important factor in AVO modelling, as the low thickness formations are difficult to examine due to AVO modelling limitations. Low-thickness reservoirs comprise low vertical resolution because the ability to separate the top and bottom of the target formation becomes less. Moreover, the thickness of Tarbert in all the wells, except well 34/11-6S, is relatively low. In this study, the target reservoir Tarbert Formation is low in thickness and at deeper depth, creating limitations for AVO modelling, as vertical resolution decreases with increasing depths. Furthermore, the effect of tuning thickness also occurs with deeper depths that additionally create AVO limitations. The boundary or interface between the formations produces variations in the amplitudes. The increase in thickness of the boundary results in an amplitude decrease. Additionally, the presence of sand that comprises depositional features such as fining upward or coarsening upward generates uneven amplitude results. Furthermore, if the interface displays sharp or even variation in the acoustic properties, this generates clear distinguish amplitudes (Simm et al., 2014) (Figure 6.17).

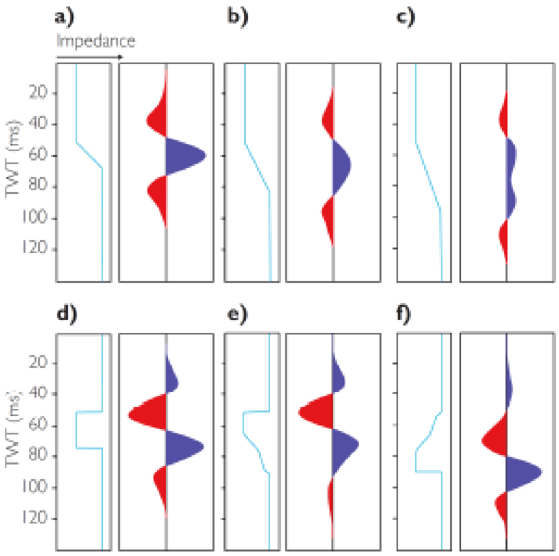

Figure 6. 17: The effect generated from boundary/interface between formations. (a to c) With the increase in thickness of the interface, resulting in amplitude decrease d) Clear and distinguish amplitudes due to sharp and even interface. (e to f) Uneven responses generated as a result of coarsening upward or fining upward successions (modified after Simm et al., 2014).

6.2.6 Pressure

The pressure in the subsurface significantly influences the acoustic properties of the rock. This pressure influence might lead to generating different AVO results. Figure 6.18 illustrates a cross plot of depth versus pressure that shows hydrostatic gradient, pore pressure, effective stress, and overburden pressure. The effective pressure is defined as the pressure zone between the reservoir pore pressure and overburden pressure, as shown in Figure 6.18.

Considering a condition in which all the subsurface rocks experience a high hydrostatic pressure. Thus, it increases velocity and effective pressure as a function of depth. One of the cases in developing an overpressured zone is the pore water that gets confined in the pore spaces during sediment deposition. This case occurs when the pore water discharge rate gets low relative to the rate of sediment deposition; consequently, it generates an overpressured zone (Simm et al., 2014).

Moreover, the compaction process might experience resistance in the presence of an overpressured zone. This possibly generates larger porosity within the rock than the standard, relative to the depth. To identify a pressure interval, the sonic log can be utilized effectively. In the presence of overpressured intervals, the sonic log will display relatively low Vp values (Simm et al., 2014).

Generally, when an overpressured reservoir is underlying a shale rock of normal pressure, this generates AVO Class 4 response. Therefore, the presence of an overpressured zone results in stiffness reduction of the rock and decreases the effective pressure due to the P-wave velocity (Vp) reduction (Simm et al., 2014). As this study is related to the HTHP reservoirs, these characteristics are observed in the AVO response of Tarbert Formation in well 34/10-23 (AVO Class 4).

Moreover, in almost all wells, the Tarbert Formation comprises chlorite coatings, which might lead to porosity preservation in the rock irrespective of the depth. The high porosity at relatively shallower depths is observed in many of the studied wells in this thesis. For instance, Tarbert Formation exhibits relatively high porosity values in the wells 34/10-23, 34/11-1, and 34/11-4.

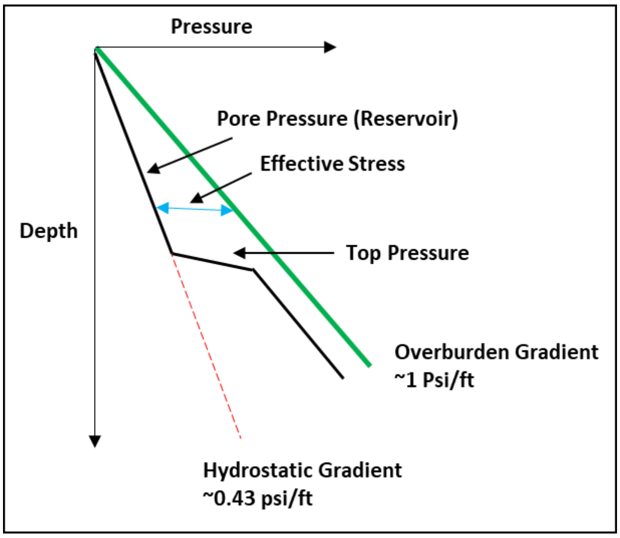

Figure 6. 18: The depth vs. pressure crossplot, displaying pore pressure, effective pressure, and overburden pressure (modified after Simm et al., 2014).

6.3 Limitations in AVO

Possible sources of error in the AVO forward modelling presented in chapter 6 are summarized below:

- The well log tools measurements comprise uncertainties due to which AVO results might have uncertainties.
- Real seismic data is not available; thus a statistical wavelet is generated (Ricker wavelet), which might not be displaying accurate and real results. Real seismic data is preferable for generating synthetic wavelets to get the most reliable and accurate AVO results.
- The vertical resolution and frequency of the wave decrease with the increase of depth. In this study, the target formation is at higher depths and comprises low thickness. Therefore, the chance of uncertainty in the AVO modelling is high.
- As the target reservoir is low in thickness and deeper in depth, the frequency is low, which possibly generates the tuning thickness effect. This results in effecting the AVO responses (Mondol, 2015).
- Because of the deeper depth of the Tarbert Formation, the fluid sensitivity possibly becomes low.
- The actual saturation of fluids present in the target reservoirs is not known. Therefore, 80% gas saturation is assumed as in-situ, which might not be exact with the real in-situ saturation. This limitation might have produced not an exact AVO response, but a sufficient one is observed in the study.
- Gassmann´s equation is applicable to clean and highly permeable reservoir rocks. Moreover, it is applied to different saturation assumptions. The possibility of Gassmann´s equation in generating uncertainties is high when it encounters a low porous and/or permeable formation and lithological variations or differences in the fluid dispersals.

Chapter 7: Conclusions

This study focuses on reservoir characterization of Early and Middle-Jurassic successions of the Valemon and Kvitebjørn fields in the northern Viking Graben, northern North Sea. The North Sea is a mature oil and gas province, which has been open for exploration since the mid-1960s. In this study, the well log data from six exploration wells 34/10-23, 34/10-42S, 34/11-1, 34/11-4, 34/11-5S, and 34/11-6S have been analyzed by utilizing three geophysical techniques: 1) Petrophysical Analysis, 2) Rock Physics diagnostics and 3) AVO Seismic Forward Modelling.

All gas-bearing reservoirs in this thesis are known as High-Temperature High-Pressure (HTHP) reservoirs. The aim is to elaborate quality of HTHP reservoirs in the Early and Middle-Jurassic successions consisting of the Cook, Rannoch, Etive, Ness, and Tarbert Formations in the study area. Generally, there are three mechanisms creating HTHP reservoirs, whereas, in this study, HTHP reservoirs could be due to the formation stress. The formation stress includes disequilibrium compaction and tectonic movement mechanisms. Moreover, the petrophysical analysis is carried out to evaluate reservoir properties, for example, saturation, clay volume, permeability and porosity, in order to classify reservoir zones and net pay in the studied well locations. The rock physics diagnostics utilized to correlate the reservoir properties from the petrophysical analysis and to evaluate cement volume. Furthermore, the AVO Modelling performed on Tarbert and Ness Formations in the wells 34/10-23, 34/10-42S, 34/11-1 and 34/11-5S to estimate the fluid generated effects and classify the AVO classes. In the thesis, different techniques were applied, and results are then integrated and associated with several phases in the thesis progress. Moreover, the limitations/uncertainties associated with the study are considered to interpret the results.

The generated results are also supported by the existing information and literature available on NPD. Due to Covid-19 restrictions that did not allow to work in the department's IT lab, which was a major barrier in starting this thesis earlier on. Moreover, the unavailability of seismic and core/cutting analysis data has limited the generated results' accuracy. The availability of the mentioned data might improve and enhance the understanding of the reservoir characterization with the related geological properties and recorded well log responses and limit the uncertainties. The cut-off values for net reservoirs for clay volume is 40%, whereas, porosity cutoff is set to 10%. Moreover, a cut-off value of water saturation in net reservoirs is set as 40%.

The generated results of this study are concluded as follows:

- The reservoir zones are recognized in the Tarbert and Ness Formations in all the available wells. Whereas the Etive and Rannoch Formations exhibit reservoir zones in all the wells, except in the well 34/10-23. Moreover, the Cook Formation comprises reservoir zones in wells 34/10-42S and 34/11-1 only. In wells 34/11-5S and 34/11-6S, Cook Formation is not penetrated by drilling.
- The Tarbert Formation is relatively a low thickness reservoir zone, consisting of a minimum thickness of 6 m in wells 34/10-42S and 34/11-4, whereas it has a high

thickness of 109 m in well 34/11-5S. Even though, being the thinnest reservoir formation in the study area, it is considered a key hydrocarbon reservoir in this study. The Tarbert Formation contains shoreline sediments (shore face or delta front). The formation yield relatively the best and satisfying reservoir properties, like the highest gas saturation and lowest clay volume. The average clay volume of the Tarbert Formation varies in a range of 5.9% to 15%. The average porosity ranges from 9% to 33%. Moreover, the well 34/11-1 holds a high net-to-gross ratio (about 92%). The pay zones in Tarbert Formation identified in wells 34/10-23, 34/11-1, 34/11-4, 34/11-5S, and 34/11-6S. Even though, at deeper depths, Tarbert Formation shows high porosity. It might be due to the presence of microquartz that perhaps led to porosity preservation.

- The Ness Formation is another good reservoir in a few wells, comprising sufficient reservoir quality. The Ness Formation is not relatively a clean sand reservoir compared to Tarbert Formation. It comprises heterolithic and irregularly thick intervals of delta-plain buried sediments. The formation contains nearly double the amount of shale as compared to Tarbert Formation in the reservoir zones. The average clay volume in the formation ranges from 13% to 26%. Moreover, the net-to-gross ratio ranges 1.3% to 60.5%. The average water saturation ranges from 12% to 30%, highest in the well 34/10-23 and lowest in the well 34/11-6S. It comprises the pay zones in wells 34/11-1, 34/11-4, and 34/11-6S. The Ness Formation is situated at deeper depths in all the wells but displays high porosity. This reason perhaps is due to the presence of microquartz, which might initiated porosity preservation.

- Etive, Rannoch, and Cook Formations are displaying good reservoir qualities where they are available but comprising water-bearing reservoirs in the studied wells. The Etive Formation shows good quality of the reservoir, but the net reservoir is relatively low in all the wells. The Etive Formation comprises sediments of upper shore face. Overall, this formation is clean but consists of few lithology variations in some wells.

- The Rannoch Formation shows properties of a reservoir zone, but the formation consists of zero net-to-gross values in most wells. Only one well (34/11-4) shows all the required information, but net pay is relatively low in it. The Density and Neutron logs did not run through the whole Rannoch Formation but a smaller portion in the well 34/11-5S; because of this reason, no water saturation and porosity estimation are performed. The Rannoch Formation possesses zero net reservoirs in three wells (34/10-23, 34/11-1, and 34/11-6S). The depositional environment of the Rannoch Formation is lower and middle shore face.

- In well 34/11-4, the Density and Neutron logs did not record the response throughout the Cook Formation. Therefore, log data is incomplete, and values for porosity and water saturation are unavailable. Moreover, Cook Formation contains high water saturation in the available wells (about 35.9% to 88%).

- The Tarbert and Ness Formations hold the main reserves in all the studied wells except 34/10-42S. The hydrocarbon content in these reservoirs is Gas and Gas/Condensate. The cap rock in each well is the same formation that is Heather Formation.

- Well 34/10-42S shows the hydrocarbon content, but all the reservoir zones are high in water saturation; therefore, this well concluded as non-economical.

- In order to display and estimate the high-pressure gas reservoirs, normal hydrostatic curve generated with the formation pressure data and formation depth acquired from NPD. Generally, it is assumed that with 1km depth, formation pressure is 10 MPa. The normal hydrostatic curve is produced for the two gas reservoirs, Tarbert and Ness Formations, for all the wells. The depth of formations is referenced from mean sea level. In all the wells, it is seen that Tarbert (gas reservoir) and Ness (gas reservoir) Formations exhibit higher formation pressure compared to the hydrostatic curve.

- The temperature of the Tarbert and Ness gas reservoirs, acquired from the well log data, exhibits relatively higher formation temperature. The formation temperature of the Tarbert Formation ranges between 138 to 154°C. Whereas the Ness Formation possesses the formation temperature range from 145 to 156°C.

- Generally, a good fit is observed for fluid content between the rock physics models and petrophysical analysis, for instance, AI versus Vp/Vs, LMR, and Vp versus Vs. The rock physics diagnostic performed with Acoustic Impedance versus P- and S-wave Velocity ratio (AI vs. VpVsRatio) crossplots comprise the Shale Background trend, Brine Sandstone trend, and Gas Sandstone trend, exhibiting Tarbert and Ness Formations plotting on the Gas Sandstone trend line with low VpVsRatio values. Moreover, a cross plot color-coded with Gas Saturation (Sg) shows Tarbert and Ness Formations comprising relatively high gas saturation in the wells where the formation is mentioned as pay zone. The Tarbert Formation shows relatively high gas saturation in wells 34/10-23, 34/11-1, 34/11-4, 34/11-5S, and 34/11-6S. Whereas Ness Formation possesses relatively high gas saturation in wells 34/11-1, 34/11-4, and 34/11-6S.

- The AI vs. VpVsRatio cross plot color-coded with Clay Volume (Vclay) shows Tarbert and Ness Formations comprises relatively low Vclay (relatively more sand) in all the wells. While the Ness Formation exhibits lithology variation as it is comparatively more in thickness than Tarbert Formation. The AI vs. VpVsRatio cross plot color-coded with Total Porosity (PhiT) display porosity variation in the Tarbert and Ness Formations. In wells 34/10-23, 34/11-1, and 34/11-4, Tarbert Formation possess relatively higher porosity (14-24%, 20-28%, and 30-40%, respectively), whereas, in wells 34/11-5S and 34/11-6S, the range of porosity variation is relatively low (5-13% and 1-18%, respectively). The Ness Formation exhibits relatively high porosity variations in wells 34/11-1, 34/11-4, and 34/11-6S as 10-35%, 15-40%, and 1-23%, respectively.

- The Lambda-Rho versus Mu-Rho (LMR) cross plot template, adapted from Goodway et al. (1997), comprises a threshold cutoff for porous Gas Sand at 20 GPa*g/cm3 of Lambda-Rho value display Tarbert and Ness Formations plotting under the threshold cutoff for porous Gas Sand line with relatively higher Mu-Rho and lower Lambda-Rho values. Whereas, in well 34/11-6S, both Tarbert and Ness Formations plot in a wide range of LMR values. Therefore, some of the data is plotting under the threshold cutoff with higher Mu-Rho and Lambda-Rho values, and relatively more data is plotting over the threshold cutoff for porous gas sand and with higher LMR values.

Perhaps, this particularly shows that formations comprising shaly gas sand and cemented tight sands. The Heather Formation plotting with high Lambda-Rho values over the threshold cutoff for porous Gas Sand.

- The LMR cross plot color-coded with Gas Saturation (Sg) display relatively high Sg in Tarbert and Ness Formations, plotting under the threshold cutoff for porous gas sand with somewhat higher Mu-Rho and lower Lambda-Rho values, whereas, Heather Formation show relatively low Sg with High Lambda-Rho values. The LMR cross plot color-coded with Clay Volume (Vclay) display relatively low Vclay in Tarbert and Ness Formations more under the threshold cutoff for porous Gas Sand line and relatively high in Heather Formation. The LMR cross plot color-coded with Total Porosity (PhiT) shows relatively high porosity in Tarbert and Ness Formations and relatively low in Heather Formation. Moreover, few data of Tarbert and Ness Formations in the well 34/11-6S, plotting in the cemented tight sand area display relatively low Vclay and high PhiT values.

- The LMR crossplot demonstrates that rigidity and incompressibility both rises because of cementation. Therefore, cemented hydrocarbon saturated sandy intervals do not plot precisely for well 34/11-6S, concerning the threshold cutoff for porous gas sands line recommended by Goodway et al. (1997).

- The rock physics diagnostic analysis with Total Porosity versus P-wave Velocity (PhiT vs. Vp) comprises a cement model. The cross plot template consists of three cement models: Friable Clay-Quartz line, Constant Cement Model, and Contact Cement Model. The Tarbert and Ness Formations comprise relatively high porosity and exhibit cement in the formation. In the well 34/10-23, 34/11-1, and 34/11-6S, Tarbert plotting on the Friable Clay-Quartz line and under Constant Cement Model line, perhaps, containing cementation, additionally, on the same locations, exhibiting relatively high Vp values (3.1-3.7 km/s, 2.9-3.3 km/s, and 4-4.9 km/s, respectively). Whereas, in the well 34/11-5S Tarbert Formation plotting only on the Friable Clay-Quartz line and not reaching to Constant Cement Model line. It also exhibits low PhiT values (about 5-13%).

- The Ness Formation in well 34/11-1, plotting on the PhiT vs. Vp cross plot on the Contact Cement Model line and comprising relatively high PhiT. The Vp of Ness data on the Contact Cement Model line is relatively high (about 2.8-3.6km/s). In well 34/11-6S, Ness Formation is plotting under the Contact Cement Model line and not reaching the Contact Cement Model line. It comprises relatively high Vp values (about 3.5-5km/s) of the formation data plotting on the Contact Cement Model line.

- In well 34/11-4, Tarbert Formation in the PhiT vs. Vp cross plot displays relatively high PhiT (about 30-40%) with relatively high Vp values (about 3.3-3.6km/s). Ness Formation plotting all over the three cement model lines with relatively high PhiT (about 15-40%) and high Vp values (about 3-4km/s).

- The PhiT vs. Vp cross plot color-coded with Gas Saturation (Sg) displays relatively high Sg in Tarbert and Ness Formation with high PhiT values. Moreover, color-coded with Clay Volume (Vclay) show Tarbert and Ness Formation comprising overall relatively low Vclay and on the data points plotting at Constant and Contact Cement Model lines.

- The P-wave versus S-wave Velocity (Vp vs. Vs) cross plot comprising Brine Sand trend and Brine Shale trend, where the gas-bearing reservoirs Tarbert and Ness Formations in all the wells plotting over the Brine Sand trend. This cross plot identifies the Gas effect when the Vs decreases relative to Vp. The gas-bearing reservoirs Tarbert and Ness Formations deflect from the Brine Sand trend and plot with high and low Vs values. On the other hand, Heather Formation plotting on the Brine Shale trend line that defines it comprising shaly formation.

- The Vp versus Vs cross plot color-coded with Gas Saturation (Sg) exhibit Tarbert and Ness Formations with relatively high Sg in the area where data points are deflecting from the Brine Sand trend and plotting with relatively low Vs. The Vp/Vs ratio displays low values when hydrocarbon saturation is present, ; in the same way, the Vp versus Vs cross plot displays the saturated and cemented sands hydrocarbon.

- The Vp versus Vs cross plot color-coded with Clay Volume (Vclay) shows a similar percentage for Tarbert and Ness Formations but where low Vclay is present, those data points display relatively high Vp values. The cross plot color-coded with Total Porosity (PhiT) exhibits relatively high PhiT in the gas-bearing reservoirs and the formations are showing variation in the PhiT. Moreover, depending on the percentage of PhiT for a particular formation in the particular well display variations in the Vp values.

- The studied reservoirs in all the wells were found below the transition zone (chemical compaction zone) and might have experienced chemical compaction for a considerable time and initiated relatively high quartz cementation. The presence of cement increases Vs more than Vp, and the Vp/Vs ratio is consequently decreased. This behavior is seen in both the gas reservoir formations (Tarbert and Ness) in almost all the wells.

- The AVO Modelling is performed on the top Tarbert Formation of wells 34/10-23, 34/10-42S, 34/11-1, and 34/11-5S. The Tarbert Formation in well 34/10-23 and 34/10-42S generated Class 4 AVO signature. Whereas the Tarbert Formation in well 34/11-1 exhibits Class 3 AVO response, and well 34/11-5S displays AVO response as Class 1. Well 34/11-1 also comprises Ness Formation as a gas reservoir and the AVO process generated response for Ness Formation as the Base Gas for Tarbert Formation.

- The well 34/10-23 exhibits Class 4 AVO I-G response, due to several reasons, for instance, being deep with a low thickness (14m), leading to tuning effect. Furthermore, in deeper depths, vertical seismic resolution becoming poor, leading to wavelength increase and tuning thickness. Therefore, Tarbert Formation being at 4084m depth, makes Tarbert and overlying cap rock stiffer due to possible quartz cementation, decreasing the fluid sensitivity; these reasons could lead to Class 4 AVO I-G response. The well 34/10-42S interpreted as non-economical through the petrophysical analysis, the AVO response of the dry well performed and displayed the AVO response as Class 2 for 100% brine in-situ and in-situ gas as Class 4, but the gas response with different fluid substitutions show negative intercept but same value of positive gradient.

- The top Tarbert Formation of well 34/11-5S exhibited Class 1 AVO response and plotted near to the background trend. The gas sand (Tarbert Formation) comprises a higher impedance compared to the above impedance of shale. The AVO Class 1 indicates the deeper burial and further substantial porosity reduction of the relevant formation. The fluid sensitivity was greatly getting limited in terms of AVO Class 1 condition, and applied fluid substitutions produced negligible response associated with the change in the AVO.

- The test for the effect of porosity and increase of shale was carried out that explains the impact of porosity influence the AVO response. The AVO response moves towards more negative intercepts and less negative gradients as the porosity increases. The AVO response being close to Class 2 moves towards the end of Class 3 due to increased porosity. Whereas the effect generated from the volume of shale is less on the AVO response. When the volume of shale is increased, which makes the rock frame softened in the sandstone reservoir of well 34/11-1, thus, the AVO response moved towards more negative intercepts and less negative gradients.

Chapter 8: References

Abdulateef, A., & Al-Rahim, A. (2018). Identification of reservoir characterization using seismic attribute and well logs for Nahr Umr Formation in Kumait oil field Supervised by. https://doi.org/10.13140/RG.2.2.29374.84801

Aki, K., & Richards, P. G. (1980). *Quantitative Seismology: Theory and Methods. San Francisco: Freeman.*

Asquith, G. B., Krygowski, D. ;, & Gibson, C. , R. (2004). *Basic well log analysis* (Vol. 16). American Association of Petroleum Geologists Tulsa.

Avseth, P. (2015). Explorational rock physics: the link between geological processes and geophysical observables. In *Petroleum Geoscience* (pp. 455–488). Springer.

Avseth, P., Jørstad, A., van Wijngaarden, A.-J., & Mavko, G. (2009). Rock physics estimation of cement volume, sorting, and net-to-gross in North Sea sandstones. *The Leading Edge*, *28*(1), 98–108.

Avseth, P. ;, Mukerji, T. ;, & Mavko, G. (2010). *Quantitative seismic interpretation: Applying rock physics tools to reduce interpretation risk*. Cambridge university press.

Avseth, P. ;, Mukerji, T. ;, Mavko, G. ;, & Dvorkin, J. (2010). Rock-physics diagnostics of depositional texture, diagenetic alterations, and reservoir heterogeneity in high-porosity siliciclastic sediments and rocks—A review of selected models and suggested work flows. *Geophysics*, *75*(5), 75A31-75A47.

Babasafari, A. A., Bashir, Y., Ghosh, D., Salim, A., Janjuhah, H., Kazemeini, S., & Kordi, M. (2020). A new approach to petroelastic modeling of carbonate rocks using an extended pore-space stiffness method, with application to a carbonate reservoir in Central Luconia, Sarawak, Malaysia. *The Leading Edge*, *39*, 592a1-592a10. https://doi.org/10.1190/tle39080592a1.1

Badley, M. , E., Price, J. , D., Dahl, C. , R. ;, & Agdestein, T. (1988). The structural evolution of the northern Viking Graben and its bearing upon extensional modes of basin formation. *Journal of the Geological Society*, *145*(3), 455–472.

Bartholomew, I. , D., Peters, J. , M., & Powell, C. , M. (1993). Regional structural evolution of the North Sea: oblique slip and the reactivation of basement lineaments. *Geological Society, London, Petroleum Geology Conference Series*, *4*(1), 1109–1122.

Bellahsen, N. ;, & Daniel, J. M. (2005). Fault reactivation control on normal fault growth: an experimental study. *Journal of Structural Geology*, *27*(4), 769–780.

Biot, M. (1956). Theory of Propagation of Elastic Waves in a Fluid-Saturated Porous Solid. II. Higher Frequency Range. *Journal of the Acoustical Society of America*.

Bjørlykke, K. ;, & Jahren, J. (2015). Sandstones and Sandstone Reservoirs. In K. Bjørlykke (Ed.), *Petroleum Geoscience: From Sedimentary Environments to Rock Physics.* (Second). Springer.

Bjørlykke, K. ;, Nedkvitne, T. ;, Ramm, M. ;, & Saigal, G. , C. (1992). Diagenetic processes in the Brent Group (Middle Jurassic) reservoirs of the North Sea: an overview. *Geological Society, London, Special Publications*, *61*(1), 263–287.

British Petroleum. (2021). *BP Energy Outlook*. BP.Com.

Brown, S. ;, Richards, P. , C. ;, & Thomson, A. , R. (1987). Patterns in the deposition of the Brent Group (Middle Jurassic), UK North Sea. *Conference on Petroleum Geology of North West Europe*. *3*, 899–913.

Budding, M. , C. ;, & Inglin, H. , F. (1981). *A reservoir geological model of the Brent Sands in southern Cormorant.*

Chamock, M. A. ;, Kristiansen, I. L. ;, Ryseth, A. ;, & Fenton, J. , P. , G. (2001). Sequence stratigraphy of the lower jurassic dunlin group, northern North Sea. In *Norwegian Petroleum Society Special Publications* (Vol. 10, pp. 145–174). Elsevier.

Christiansson, P., Faleide, J. , I., & Berge, A. , M. (2000). Crustal structure in the northern North Sea: an integrated geophysical study. *Geological Society, London, Special Publications, 167*(1), 15–40.

Clavier, C. ;, Hoyle, W. ;, & Meunier, D. (1971). Quantitative interpretation of thermal neutron decay time logs: part I. Fundamentals and techniques. *Journal of Petroleum Technology, 23*(06), 743–755.

Cornford, C. (1998). Source rocks and hydrocarbons of the North Sea. *Petroleum Geology of the North Sea: Basic Concepts and Recent Advances*, 376–462.

Coward, M. , P., Dewey, J. , F., Hempton, M., & Holroyd, J. (2003). Tectonic evolution. *The Millennium Atlas: Petroleum Geology of the Central and Northern North Sea. Geological Society, London*, *17*, 33.

Cowie, P. A., Underhill, J. , R., Behn, M. , D., Lin, J., & Gill, C. , E. (2005). Spatio-temporal evolution of strain accumulation derived from multi-scale observations of Late Jurassic rifting in the northern North Sea: A critical test of models for lithospheric extension. *Earth and Planetary Science Letters*, *234*(3–4), 401–419.

Crain, E. R. (2015). *Crain's Petrophysical Handbook Total Orgnic Carbon (TOC)*.

Dalland, A., Worsley, D., & Ofstad, K. (1988). *A lithostratigraphic scheme for the mesozoic and cenozoic and succession offshore mid-and northern norway*. Oljedirektoratet.

Dvorkin, J., & Nur, A. (1996). Elasticity of high-porosity sandstones: Theory for two North Sea data sets. *Geophysics*, *61*(5), 1363–1370.

Dvorkin, J., Nur, A., & Yin, H. (1994). Effective properties of cemented granular materials. *Mechanics of Materials*, *18*(4), 351–366.

Dvorkin, J. P. (2008). Yet another V S equation. *Geophysics*, *73*(2), E35–E39.

Ellis, D. v, & Singer, J. M. (2007). *Well logging for earth scientists* (Vol. 692). Springer.

ExxonMobil. (2017). *ExxonMobil 2017 Outlook for Energy: A View to 2040.* . Http://Oilproduction.Net/Files/2017_Outlook_for_Energy_highlights.Pdf.

Færseth, R. B. (1996). Interaction of Permo-Triassic and Jurassic extensional fault-blocks during the development of the northern North Sea. *Journal of the Geological Society*, *153*(6), 931–944.

Faerseth, R. B., Knudsen, B.-E., & Liljedahl, T. (1998). Oblique rifting and sequential faulting in the Jurassic development of the northern North Sea. *Oceanographic Literature Review*, *4*(45), 677.

Faleide, J. I., Bjørlykke, K., & Gabrielsen, R. H. (2010). Geology of the Norwegian continental shelf. In *Petroleum Geoscience* (pp. 467–499). Springer.

Fält, L. M., Helland, R., Jacobsen, V. W., & Renshaw, D. (1989). Correlation of transgressive-regressive depositional sequences in the Middle Jurassic Brent/Vestland Group megacycle, Viking Graben, Norwegian North Sea. In *Correlation in hydrocarbon exploration* (pp. 191–200). Springer.

Fazlikhani, H., Fossen, H., Gawthorpe, R. L., Faleide, J. I., & Bell, R. E. (2017). Basement structure and its influence on the structural configuration of the northern North Sea rift. *Tectonics*, *36*(6), 1151–1177.

Fjeldskaar, W., ter Voorde, M., Johansen, H., Christiansson, P., Faleide, J. I., & Cloetingh, S. (2004). Numerical simulation of rifting in the northern Viking Graben: the mutual effect of modelling parameters. *Tectonophysics*, *382*(3–4), 189–212.

Fjellanger, E., Olsen, T. R., & Rubino, J. L. (1996). Sequence stratigraphy and palaeogeography of the Middle Jurassic Brent and Vestland deltaic systems, northern North Sea. *Norsk Geologisk Tidsskrift*, *76*, 75–106.

Folkestad, A. , Odisen, T. , Fossen, H., & and Pearce, M. , A. (2014). Tectonic influence on the Jurassic sedimentary architecture in the northern North Sea with focus on the Brent Group. *Int. Assoc. Sedimentol.*, *46*, 389–416.

Folkestad, A., Veselovsky, Z., & Roberts, P. (2012). Utilising borehole image logs to interpret delta to estuarine system: A case study of the subsurface Lower Jurassic Cook Formation in the Norwegian northern North Sea. *Marine and Petroleum Geology*, *29*(1), 255–275.

Fossen, H. (1992). The role of extensional tectonics in the Caledonides of south Norway. *Journal of Structural Geology*, *14*(8–9), 1033–1046.

Fossen, H. (2010). Extensional tectonics in the North Atlantic Caledonides: a regional view. *Geological Society, London, Special Publications*, *335*, 767–793.

Fossen, H., & and Hurich, C. A. (2005). The Hardangerfjord Shear Zone in SW Norway and the North Sea: a large-scale low-angle shear zone in the Caledonian crust. *Journal of the Geological Society, London*, *162*, 675–687.

Gabrielsen, R. H., Færseth, R. B., Steel, R. J., Idil, S., & Klovjan, O. S. (1990). Architectural styles of basin fill in the northern Viking Graben. In *Tectonic evolution of the North Sea rifts* (pp. 158–179). Oxford univ, Oxford.

Gassmann, F. (1951). ELASTIC WAVES THROUGH A PACKING OF SPHERES. *GEOPHYSICS*, *16*(4), 673–685. https://doi.org/10.1190/1.1437718

Gautier, D. L. (2005). *Kimmeridgian Shales Total Petroleum System of the North Sea Graben Province*.

Gelius, L. , J., & Johansen, T. , A. (2010). Petroleum geophysics. *UniGEO*.

Giles, M. R. , Stevenson, S., Martin, S. v., Cannon, S. , J. , C., Hamilton, P. J., Marshall, J. D., & Samways, G. M. (1992). The reservoir properties and diagenesis of the Brent Group: a regional perspective. *Geology of the Brent Group. Geological Society Special Publication*, *61*, 289–327.

Glover, P. (2016). *The Spectral Gamma Ray Log*. Http://Homepages.See.Leeds.Ac.Uk/~earpwjg/PG_EN/CD%20Contents/GGL-66565%20Petrophysics%20English/Chapter%2012.PDF.

Goff, J. C. (1983). Hydrocarbon generation and migration from Jurassic source rocks in the E Shetland Basin and Viking Graben of the northern North Sea. *Journal of the Geological Society*, *140*(3), 445. https://doi.org/10.1144/gsjgs.140.3.0445

Goodway, B., Chen, T., & Downton, J. (1997). Improved AVO fluid detection and lithology discrimination using Lamé petrophysical parameters; ????,????,&??/? fluid stack?, from P and S inversions. In *SEG Technical Program Expanded Abstracts 1997* (pp. 183–186). Society of Exploration Geophysicists. https://doi.org/doi:10.1190/1.1885795

Gormly, J. R., Buck, S. P., & Chung, H. M. (1994). Oil-source rock correlation in the North Viking Graben. *Organic Geochemistry*, *22*(3), 403–413. https://doi.org/https://doi.org/10.1016/0146-6380(94)90116-3

Graue, E., Helland-Hansen, W., Johnsen, J., Lomo, L., Nottvedt, A., Rønning, K., Ryseth, A., & Steel, R. (1987). Advance and retreat of Brent Delta system, Norwegian North Sea. *Conference on Petroleum Geology of North West Europe. 3*, 915–937.

Han, D., Nur, A., & Morgan, D. (1986). Effects of porosity and clay content on wave velocities in sandstones. *GEOPHYSICS*, *51*(11), 2093–2107. https://doi.org/10.1190/1.1442062

Hansen, J. A., Mondol, N. H., Jahren, J., & Tsikalas, F. (2020). Reservoir assessment of Middle Jurassic sandstone-dominated formations in the Egersund Basin and Ling Depression, eastern Central North Sea. *Marine and Petroleum Geology*, *111*, 529–543. https://doi.org/https://doi.org/10.1016/j.marpetgeo.2019.08.044

Hashin, Z., & Shtrikman, S. (1963). A variational approach to the theory of the elastic behaviour of multiphase materials. *Journal of the Mechanics and Physics of Solids*, *11*(2), 127–140. https://doi.org/https://doi.org/10.1016/0022-5096(63)90060-7

Helland-Hansen, W., Ashton, M., Lomo, L., & Steel, R. (1992). Advance and retreat of the Brent delta: Recent contributions to the depositional model. *Geological Society, London, Special Publications*, *61*, 109–127. https://doi.org/10.1144/GSL.SP.1992.061.01.07

Henza, A. , A., Withjack, M. , O., & Schlische, R. , W. (2011). How do the properties of a pre-existing normal-fault population influence fault development during a subsequent phase of extension? *Journal of Structural Geology*, *33*(9), 1312–1324. https://doi.org/https://doi.org/10.1016/j.jsg.2011.06.010

Hilchie, D. W. (1978). *Applied openhole log interpretation (for geologists and petroleum engineers)*. D.W. Hilchie.

Hook, J. R. (2003). An Introduction to Porosity. *Petrophysics - The SPWLA Journal of Formation Evaluation and Reservoir Description*, *44*(03).

Hosken, J. W. J. (1988). Ricker wavelets in their various guises. *First Break*, *6*(1). https://doi.org/10.3997/1365-2397.1988002

Isaksen, D. , & Tonstad, K. (1989). A revised Cretaceous and Tertiary lithostratigraphic nomenclature for the Norwegian North Sea . *Norwegian Petroleum Directorate.*

Johnson, H. D., & Stewart, D. J. (1985). Role of clastic sedimentology in the exploration and production of oil and gas in the North Sea. *Geological Society, London, Special Publications*, *18*(1), 249. https://doi.org/10.1144/GSL.SP.1985.018.01.12

Jorde, K., & Diesen, G. W. (1992). The Snorre Field: A Major Field in the Northern North Sea. *Chapter 25.* .

Justwan, H., & Dahl, B. (2005). Quantitative hydrocarbon potential mapping and organofacies study in the Greater Balder Area, Norwegian North Sea. *Geological Society, London, Petroleum Geology Conference*, *6*(1), 1317. https://doi.org/10.1144/0061317

Kennedy, M. (2015). *Practical Petrophysics. : Vol. Vol 62*. Elsevier.

Ketzer, J. M. , Morad, S. , Nystuen, J. P. , & de Ros, L. F. (1999). The Role of the Cimmerian Unconformity (Early Cretaceous) in the Kaolinitization and related Reservoir-Quality Evolution in Triassic Sandstones of the Snorre Field, North Sea. *Clay Mineral Cements in Sandstones*, 361–382.

Klaja, J., & Dudek, L. (2016). Geological interpretation of spectral gamma ray (SGR) logging in selected boreholes. *Nafta-Gaz*, *72*.

Krief, M., Garat, J., Stellingwerff, J., & Ventre, J. (1990). A Petrophysical Interpretation Using the Velocities of P and S Waves (Full-Waveform Sonic). *The Log Analyst*, *31*(06).

Lafargue, E., & Behar, F. (1989). Application of a new preparative pyrolysis technique for the determination of source-rock types and oil/source-rock correlations. *Geochimica et Cosmochimica Acta*, *53*(11), 2973–2983. https://doi.org/https://doi.org/10.1016/0016-7037(89)90173-7

Larionov, V. (1969). Borehole radiometry. *Nedra, Moscow , 127.*

Livera, S. E. (1989). Facies associations and sand-body geometries in the Ness Formation of the Brent Group, Brent Field. *Geological Society, London, Special Publications*, *41*(1), 269. https://doi.org/10.1144/GSL.SP.1989.041.01.19

Mackenzie, A. S., Leythaeuser, D., Muller, P., Quigley, T. M., & Radke, M. (1988). The movement of hydrocarbons in shales. *Nature*, *331*(6151), 63–65. https://doi.org/10.1038/331063a0

Marcussen, Ø., Faleide, J. I., Jahren, J., & Bjørlykke, K. (2010). Mudstone compaction curves in basin modelling: a study of Mesozoic and Cenozoic Sediments in the northern North Sea. *Basin Research*, *22*(3), 324–340. https://doi.org/10.1111/j.1365-2117.2009.00430.x

Marcussen, Ø., Maast, T. E., Mondol, N. H., Jahren, J., & Bjørlykke, K. (2010). Changes in physical properties of a reservoir sandstone as a function of burial depth – The Etive Formation, northern North Sea. *Marine and Petroleum Geology*, *27*(8), 1725–1735. https://doi.org/https://doi.org/10.1016/j.marpetgeo.2009.11.007

Marion, D., Nur, A., Yin, H., & Han, D. (1992). Compressional velocity and porosity in sand-clay mixtures. *GEOPHYSICS*, *57*(4), 554–563. https://doi.org/10.1190/1.1443269

Mavko, G. (2005). *Effective Medium Models*. Https://Pangea.Stanford.Edu/Courses/Gp262/Notes/9.EffectiveMediumTheories.Pdf.

Mindlin, R. D. (1949). Compliance of Elastic Bodies in Contact. *Journal of Applied Mechanics*, *16*(3), 259–268. https://doi.org/10.1115/1.4009973

Mondol, N. H. (2015). Well Logging: Principles, Applications and Uncertainties. In K. Bjørlykke (Ed.), *Petroleum Geoscience: From Sedimentary Environments to Rock Physics* (pp. 385–425). Springer Berlin Heidelberg. https://doi.org/10.1007/978-3-642-34132-8_16

Mondol, N. H. (2018). Seal quality prediction using E-Poisson's ratio rock physics templet-A case study from the Norwegian Barents Sea. *GeoConvention.*

norskolje.museum.no. (2016). *Kvitebjørn Field: Oil and Gas Fields in Norway - Industrial Heritage Plan*. Https://Www.Norskolje.Museum.No/Wp-Content/Uploads/2016/02/3467_3fdf1cdb641640e1ae567d545e305730.Pdf.

Norwegian Petroleum Directorate. (2021a). *Geology of the North Sea*. Https://Www.Npd.No/En/Facts/Publications/Co2-Atlases/Co2-Atlas-for-the-Norwegian-Continental-Shelf/4-the-Norwegian-North-Sea/4.1-Geology-of-the-North-Sea/.

Norwegian Petroleum Directorate. (2021b). *The three petroleum provinces; North Sea, Norwegian Sea, and the Barents Sea in the Norwegian Continental Shelf*. Https://Www.Npd.No/En/Facts/Publications/Co2-Atlases/Co2-Atlas-for-the-Norwegian-Continental-Shelf/2-Petroleum-Activity-Age/.

Norwegian Petroleum Directorate. (2021c). *Valemon and Kvitebjørn Fields*. Https://Factmaps.Npd.No/Factmaps/3_0/.

Norwegian Petroleum/Valemon Field. (2021). *Valemon Field*. Https://Www.Norskpetroleum.No/En/Facts/Field/Valemon.

NPD.no/34-10-23. (2021). *34/10-23*. Https://Factpages.Npd.No/Nb-No/Wellbore/Pageview/Exploration/All/476.

NPD.no/34-10-42S. (2021). *34/10-42S*. Https://Factpages.Npd.No/Nb-No/Wellbore/PageView/Exploration/All/3816.

NPD.no/34-11-1. (2021). *34/11-1*. Https://Factpages.Npd.No/Nb-No/Wellbore/PageView/Exploration/All/2377.

NPD.no/34-11-4. (2021). *34/11-4*. Https://Factpages.Npd.No/Nb-No/Wellbore/PageView/Exploration/All/3314.

NPD.no/34-11-5S. (2021). *34/11-5S*. Https://Factpages.Npd.No/Nb-No/Wellbore/PageView/Exploration/All/5248.

NPD.no/34-11-6S. (2021). *34/11-6S*. Https://Factpages.Npd.No/Nb-No/Wellbore/PageView/Exploration/All/8059.

NPD.no/Etive Formation. (2021). *Etive Formation*. Https://Factpages.Npd.No/Nb-No/Strat/Pageview/Litho/Formations/35.

NPD.no/Rannoch Formation. (2021). *Rannoch Formation*. Https://Factpages.Npd.No/Nb-No/Strat/Pageview/Litho/Formations/126.

Nystuen, J. P., & Fält, L.-M. (1995). Upper Triassic-Lower Jurassic reservoir rocks in the Tampen Spur area, Norwegian North Sea. In S. Hanslien (Ed.), *Norwegian Petroleum Society Special Publications* (Vol. 4, pp. 135–179). Elsevier. https://doi.org/https://doi.org/10.1016/S0928-8937(06)80041-X

Ødegaard, E., & Avseth, P. (2003). Interpretation of Elastic Inversion Results Using Rock Physics Templates. *65th EAGE Conference & Exhibition*, cp-6-00337. https://doi.org/10.3997/2214-4609-pdb.6.E17

Odinsen, T., Christiansson, P., Gabrielsen, R. H., Faleide, J. I., & Berge, A. M. (2000). The geometries and deep structure of the northern North Sea rift system. *Geological Society, London, Special Publications*, *167*(1), 41. https://doi.org/10.1144/GSL.SP.2000.167.01.03

Perez, A. , R., & Marfurt, K. (2014). Mineralogy-based brittleness prediction from surface seismic data: Application to the Barnett Shale. *Interpretation*, *2*(4), T255–T271. https://doi.org/10.1190/INT-2013-0161.1

Phillips, T. B., Fazlikhani, H., Gawthorpe, R. L., Fossen, H., Jackson, C. A.-L., Bell, R. , E., Faleide, J. , I., & Rotevatn, A. (2019). The Influence of Structural Inheritance and Multiphase Extension on Rift Development, the NorthernNorth Sea. *Tectonics*, *38*(12), 4099–4126. https://doi.org/https://doi.org/10.1029/2019TC005756

Qu, Z. P., Wu, M. R., & Liu, Z. Y. (2013). Abnormal pressure origin analysis and seismic prediction. Science & Technology Information, 23, 35–37.

Ramberg, I. B., Bryhni, I., & Nøttvedt, A. (2007). *Landet blir til: Norges geologi*. Norsk geologisk forening.

Raymer, L. L., Hunt, E. , R., & Gardner, J. , S. (1980). *An Improved Sonic Transit Time-To-Porosity Transform*.

Reuss, A. (1929). Berechnung der Fließgrenze von Mischkristallen auf Grund der Plastizitätsbedingung für Einkristalle . *ZAMM - Journal of Applied Mathematics and Mechanics / Zeitschrift Für Angewandte Mathematik Und Mechanik*, *9*(1), 49–58. https://doi.org/https://doi.org/10.1002/zamm.19290090104

Richards, P. C. (1992). An introduction to the Brent Group: a literature review. *Geological Society, London, Special Publications*, *61*(1), 15. https://doi.org/10.1144/GSL.SP.1992.061.01.03

Richards, P. , C., & Brown, S. (1986). Shoreface storm deposits in the Rannoch Formation (Middle Jurassic), North West Hutton oilfield. *Scottish Journal of Geology*, *22*.

Roberts, A. M., Yielding, G., Kusznir, N. J., Walker, I. M., & Dorn-Lopez, D. (1995). Quantitative analysis of Triassic extension in the northern Viking Graben. *Journal of the Geological Society*, *152*(1), 15. https://doi.org/10.1144/gsjgs.152.1.0015

Rüpke, L. H., Schmalholz, S. M., Schmid, D. W., & Podladchikov, Y. Y. (2008). Automated thermotectonostratigraphic basin reconstruction: Viking Graben case study. *AAPG Bulletin*, *92*(3), 309–326. https://doi.org/10.1306/11140707009

Ryseth, A. (2001). Sedimentology and palaeogeography of the statfjord formation (Rhaetian-Sinemurian), North Sea. In O. J. Martinsen & T. Dreyer (Eds.), *Norwegian Petroleum Society Special Publications* (Vol. 10, pp. 67–85). Elsevier. https://doi.org/https://doi.org/10.1016/S0928-8937(01)80009-6

Schlumberger Limited. (1991). *Log Interpretation Principles/Applications.* Schlumberger Educational Services. .

SEG Wiki. (2021a). *Thin beds, tuning and AVO*. Https://Wiki.Seg.Org/Wiki/Thin_beds,_tuning,_and_AVO.

SEG Wiki. (2021b). *Vertical Resolution*. Https://Wiki.Seg.Org/Wiki/Vertical_resolution.

Shadravan, A., & Amani, M. (2012). HPHT 101-what every engineer or geoscientist should know about high pressure high temperature wells. *SPE Kuwait International Petroleum Conference and Exhibition*.

Sheriff, R. E., & Geldart, L. P. (1995). *Exploration Seismology* (2nd ed.). Cambridge University Press.

Shuey, R. T. (1985). A simplification of the Zoeppritz equations. *GEOPHYSICS*, *50*(4), 609–614. https://doi.org/10.1190/1.1441936

Simm, R. , and, & Bacon, M. (2014). *Seismic Amplitude: An interpreter's handbook*. Cambridge University Press.

Smethurst, M. A. (2000). Land–offshore tectonic links in western Norway and the northern North Sea. *Journal of the Geological Society*, *157*(4), 769. https://doi.org/10.1144/jgs.157.4.769

Stewart, I. J., Rattey, R. P., & Vann, I. R. (1992). Structural style and the habitat of hydrocarbons in the North Sea. In R. M. Larsen, H. Brekke, B. T. Larsen, & E. Talleraas (Eds.), *Structural and Tectonic Modelling and its Application to Petroleum Geology* (Vol. 1, pp. 197–220). Elsevier. https://doi.org/https://doi.org/10.1016/B978-0-444-88607-1.50018-8

Stieber, S. J. (1970). *Pulsed Neutron Capture Log Evaluation - Louisiana Gulf Coast*.

Ter Voorde, M., Færseth, R. B., Gabrielsen, R. H., & Cloetingh, S. A. P. L. (2000). Repeated lithosphere extension in the northern Viking Graben: a coupled or a decoupled rheology? *Geological Society, London, Special Publications*, *167*(1), 59. https://doi.org/10.1144/GSL.SP.2000.167.01.04

Tomasso, M., Underhill, J. R., Hodgkinson, R. A., & Young, M. J. (2008). Structural styles and depositional architecture in the Triassic of the Ninian and Alwyn North fields: Implications for basin development and prospectivity in the Northern North Sea. *Marine and Petroleum Geology*, *25*(7), 588–605. https://doi.org/https://doi.org/10.1016/j.marpetgeo.2007.11.007

Underhill, J. R., and, & Partington, M. A. (1993). Jurassic thermal doming and deflation in the North Sea: implications of the sequence stratigraphic evidence. *Geological Society, London, Petroleum Geology Conference*, *4*(1), 337. https://doi.org/10.1144/0040337

Varhaug, M. (2016). The defining series: Mud logging. *Oilfield Review*, *28*, 52–53.

Verbeek, C. J. R., & Focke, W. W. (2002). Modelling the Young's modulus of platelet reinforced thermoplastic sheet composites. Composites Part A: Applied Science and Manufacturing, 33(12), 1697–1704. https://doi.org/https://doi.org/10.1016/S1359-835X(02)00184-7

Vetti, V. v, and, & Fossen, H. (2012). Origin of contrasting Devonian supradetachment basin types in the Scandinavian Caledonides. *Geology*, *40*(6), 571–574. https://doi.org/10.1130/G32512.1

Voigt, W. (1910). *Lehrbuch der Kristallphysik. Leipzig: Teubner.*

Vollset, J. , and, & Doré, A. G. (1984). A revised Triassic and Jurassic lithostratigraphic nomenclature for the Norwegian North Sea, *Oljedirektoratet*.

Walderhaug, O., (2000). Modeling Quartz Cementation and Porosity in Middle Jurassic Brent Group Sandstone of the Kvitebjørn Field, Northern North Sea. Aapg Bulletin – AAPG BULL, 84.

Whipp, P. S., Jackson, C. A.-L., Gawthorpe, R. L., Dreyer, T., & Quinn, D. (2014). Normal fault array evolution above a reactivated rift fabric; a subsurface example from the northern Horda Platform, Norwegian North Sea. *Basin Research*, *26*(4), 523–549. https://doi.org/10.1111/bre.12050

Wiggins, R. , Kenny, G. S., and, & McClure, C. D. (1983). *A method for determining and displaying the shear velocity reflectivities of a geologic formation.*

Wojnar T, J. (2018). *Push and Pull: How Energy Defines Daily Life Now and Into the Future.* . Https://Energyfactor.Exxonmobil.Asia/Insights/Perspectives/Push-and-Pull-How-Energy-Defines-Daily-Life-Now-and-into-the-Future/.

Worthington, P. F., & Cosentino, L. (2005). The Role of Cut-offs in Integrated Reservoir Studies. *SPE Reservoir Evaluation & Engineering*, *8*(04), 276–290. https://doi.org/10.2118/84387-PA

Wyllie, M. R. J., Gregory, A. R., & Gardner, G. H. F. (1958). AN EXPERIMENTAL INVESTIGATION OF FACTORS AFFECTING ELASTIC WAVE VELOCITIES IN POROUS MEDIA. *GEOPHYSICS*, *23*(3), 459–493. https://doi.org/10.1190/1.1438493

Yang, Y. , Sone, H. , Hows, A. , & & Zoback, M. D. (2013). *Comparison of Brittleness Indices in Organic-rich Shale Formations*.

Yielding, G., Badley, M. E., & Roberts, A. M. (1992). The structural evolution of the Brent Province. *Geological Society, London, Special Publications*, *61*(1), 27. https://doi.org/10.1144/GSL.SP.1992.061.01.04

Zhang, H. , Liu, H. , Wu, S. , Sun, J. , Yang, C. , Xie, Y. , Chen, C. , Gao, J., & and Wang, J. (2018). Pre-Drilling Prediction Techniques on the High-Temperature High-Pressure Hydrocarbon Reservoirs Offshore Hainan Island, China . *Journal of Ocean University of China. JOUC*, *17*, 72–82.

Ziegler, P. A. (1975). *Geologic evolution of North Sea and its tectonic framework*. *59:7*. https://www.osti.gov/biblio/6921173

Ziegler, P. A. (1992). European Cenozoic rift system. *Tectonophysics*, *208*(1), 91–111. https://doi.org/https://doi.org/10.1016/0040-1951(92)90338-7

Zoeppritz, K. (1919). VIIb. Über Reflexion und Durchgang seismischer Wellen durch Unstetigkeitsflächen. *Göttinger Nachrichten*, *1*, 66–84.

Appendix 1 – Abstracts

Abstract – 1:
Characterization of HTHP Reservoir in the northern North Sea, Offshore Norway

Shahid, A.A,[1*], Fawad M.[1], Rahman M.J.[1*], & Mondol N.H.[1,2]

[1]Department of Geoscience, University of Oslo (UiO), Norway
[2]Norwegian Geotechnical Institute (NGI), Norway
*Email: aliasha@student.geo.uio.no

This study focuses on characterizing the high temperature high-pressure (HTHP) Tarbert Formation reservoir sandstones in the northern North Sea. A suite of well log data from two gas discovery wells [34/10-23 (Valemon) and 34/11-1 (Kvitebjørn)], from the Viking Graben, utilize to evaluate the reservoir quality. Middle Jurassic Tarbert formation's depth is 4084 and 4045m, respectively, in wells 34/10-23 and 31/11-1. In the study area, the depositional environment of the Tarbert Formation is marginal marine. It comprises moderately massive fine to medium-grained, gray to brown sandstone, with a minor amount of thin siltstone, coal beds and shale, and few calcareous bands (NPD, 2020). Petrophysical analyses carry out to calculate the clay volume (V_{clay}), porosity (φ_t), and gas saturation (S_g). Moreover, rock physics diagnostics performed to evaluate the target reservoir sandstones. A comparison of Gamma Ray Log responses of the Tarbert Formation in both wells indicates that well 34/10-23 has cleaner sand than well 34/11-1.

The cross plot of density (RhoB) and P-wave velocity (Vp) shows that the Tarbert Formation in well 34/10-23 exhibits relatively high P-wave velocity and increases with increasing density. However, in the other well, there is not that much P-wave velocity variation with the increase in density. The cross plot color-coded with V_{clay} shows that the Tarbert Formation in both wells generally consists of low clays; however, the clay percentage is relatively high in well 34/10-23. The RhoB-Vp cross plots color-coded with total porosity (φ_t) and gas saturation (S_g) represent that porosity in well 34/10-23 is relatively high (about 25%), compared to the other well (about 15%). The gas saturation (S_g) is relatively high (about 70%) in well 34/11-1, whereas the gas saturation in other well varies from 20% to 70%.

The comparison of Tarbert Formation in both wells shows a similar physical behavior as the formation depths are approximately the same, and the temperature variation is not significant, either assuming no exhumation in the study area. Well 34/10-23 documented high velocity and high density compared to the other well due to calcite's presence. In well 34/11-1, the P-wave velocity in Tarbert Formation is not changed with the increase of density values due to the preservation of porosity by chlorite coatings warrants further investigations.

Abstract – 2:

Rock-Physics analysis & AVO modeling of HTHP reservoirs in the northern North Sea, Offshore Norway

Shahid, A.A,[1*], Fawad M.[1], & Mondol N.H.[1,2]

[1]Department of Geoscience, University of Oslo (UiO), Norway
[2]Norwegian Geotechnical Institute (NGI), Norway
*Email: aliasha@student.geo.uio.no

This study focuses on rock-physics analysis and AVO (amplitude versus offset) modeling of the high-temperature high-pressure (HTHP) Middle-Jurassic reservoir marginal-marine sandstones in the Valemon field, northern North Sea (Fig.1). A suite of well-log data in wells 34/10-23 and 34/10-42S, from the Viking Graben, is utilized to evaluate the reservoir quality. The target reservoir is Tarbert Formation at two different depths at 4084 and 4211m, in wells 34/10-23 and 34/10-42S, respectively. We carried out Rock-Physics diagnostics to relate the clay-volume (V_{clay}), total-porosity (φ_t), and gas-saturation (S_g) with elastic properties to evaluate the reservoirs. Moreover, AVO forward modeling utilizes to generate AVO Intercept-Gradient (I-G) crossplots.

The Acoustic Impedance (AI) versus P-to S-wave velocity-ratio (Vp/Vs), Lambda-Rho ($\lambda\rho$) versus Mu-Rho ($\mu\rho$), and porosity (φ_t) versus Vp show that the Tarbert Formation in well 34/10-23 exhibits a relatively low Vp/Vs-ratio and plotting within the gas-bearing sandstone trend. However, in the well 34/10-42S, the Tarbert Formation data exhibits a relatively high Vp/Vs-ratio plotting along with the brine-saturated sandstone trend. On the other hand, $\lambda\rho$ versus $\mu\rho$ cross-plot shows relatively high Mu-Rho and low Lambda-Rho values for the Tarbert Formation in well 34/10-23 plotting within the gas-saturated sandstone zone. The other well (34/10-42S) data possess relatively low Mu-Rho and high Lambda-Rho values for the Tarbert Formation and plotting out of the threshold cutoff for gas-saturated sandstone. The cross-plot of φ_t, versus Vp with cement models demonstrates that the Tarbert Formation in both wells has a relatively similar trend and plotting at the high porosity range. The Tarbert Formation in well 34/10-23 is reasonably thick (14m), displaying variations in porosity (0-25%) and plotting in the region between the Friable Clay-Quartz line and Constant-Cement model line (with no cementation?). Whereas Tarbert Formation in well 34/10-42S is only 6m thick, comprising high porosity (~21-36%), and plotting within the Constant-Cement model area.

AVO modeling is performed with in-situ 80%-gas and 100%-brine conditions in wells 34/10-23 and 34/10-42S, respectively. The fluid substitution with 10%-gas, 50%-gas, 100%-brine, and 80%-oil were carried out in well 34/10-23. Whereas the other well (34/10-42S) was modelled with 10%-gas, 80%-gas, 10%-oil, and 80%-oil. The I-G cross plot displaying AVO class 4 for the Tarbert Formation for both wells. The cross-plots color-coded with V_{clay}, φ_t and S_g show that the Tarbert Formation in both wells generally consists of low clays (~33%); however, the clay percentage is relatively high in the well 34/10-42S. Moreover, porosity in well 34/10-23 is relatively low (~25%), compared to well 34/10-42S (~37%). The gas-saturation is relatively high (~70%) in well 34/10-23, whereas in well 34/10-42S, the gas presence is non-commercial (~31%-S_g).

The comparison of the Tarbert Formation in both wells indicates that well 34/10-42S is dry, owing to high porosity due to porosity preservation, possibly by chlorite coatings. The gas-bearing Tarbert

Formation in well 34/10-23 shows an AVO class-4, perhaps, due to several reasons, being deep with a low thickness (14m), leading to tuning effect. Moreover, Tarbert and overlying cap rock become stiffer due to possible quartz cementation, decreasing the fluid sensitivity.

Appendix 2 – Remaining well logs

Tarbert Formation in well 34/10-42S

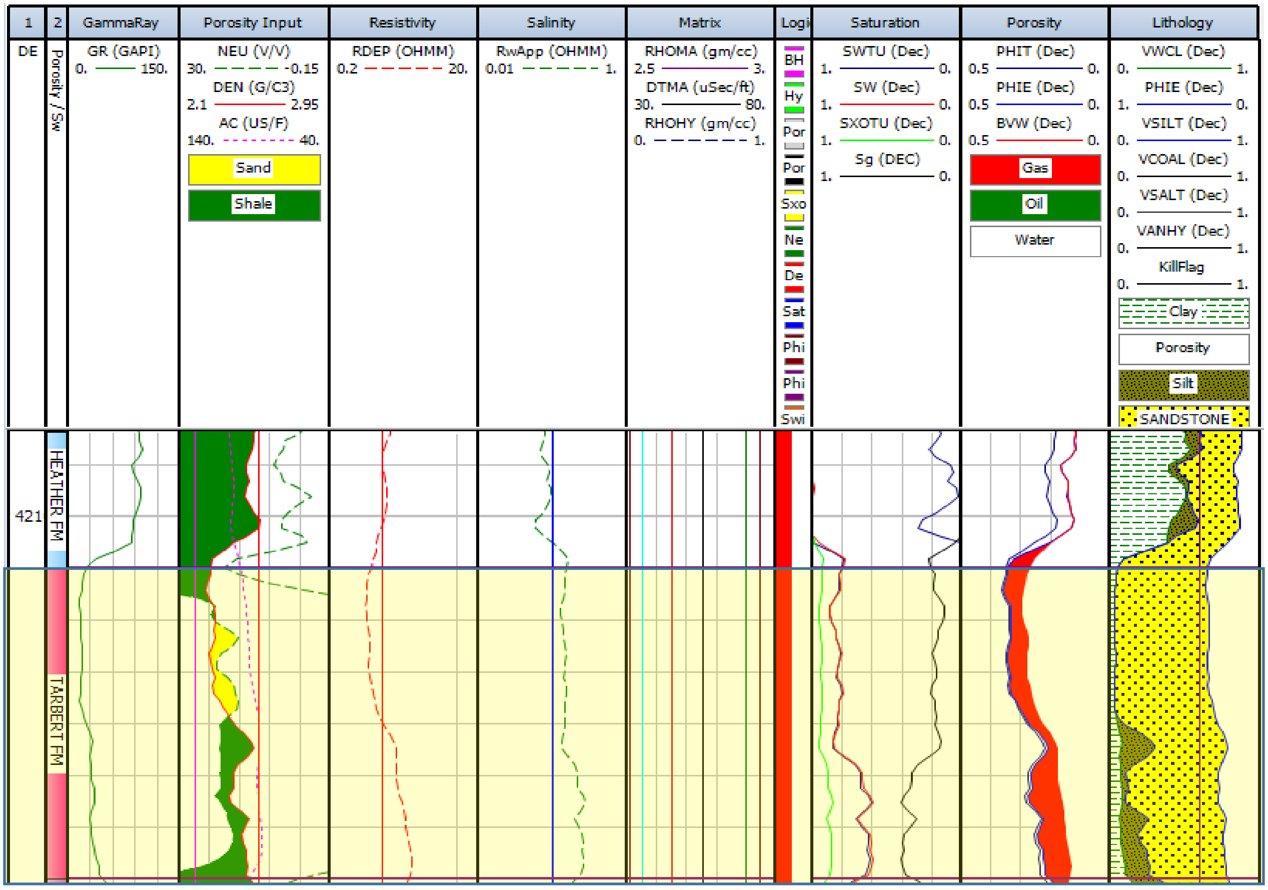

Tarbert Formation in well 34/11-1

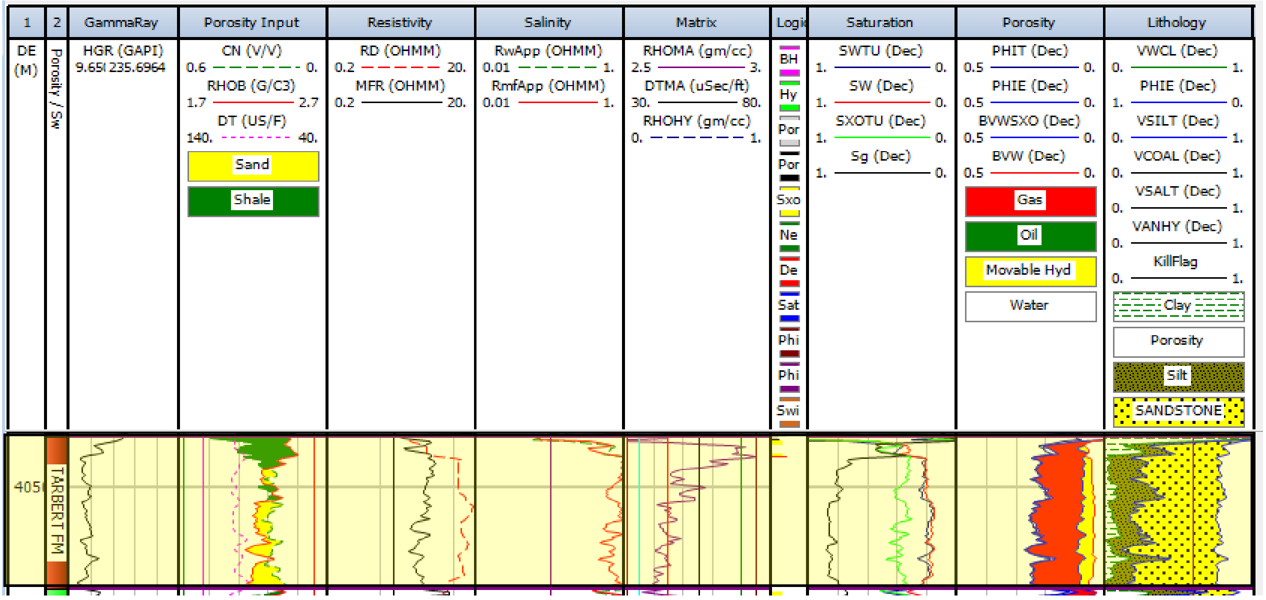

Tarbert Formation in well 34/11-4

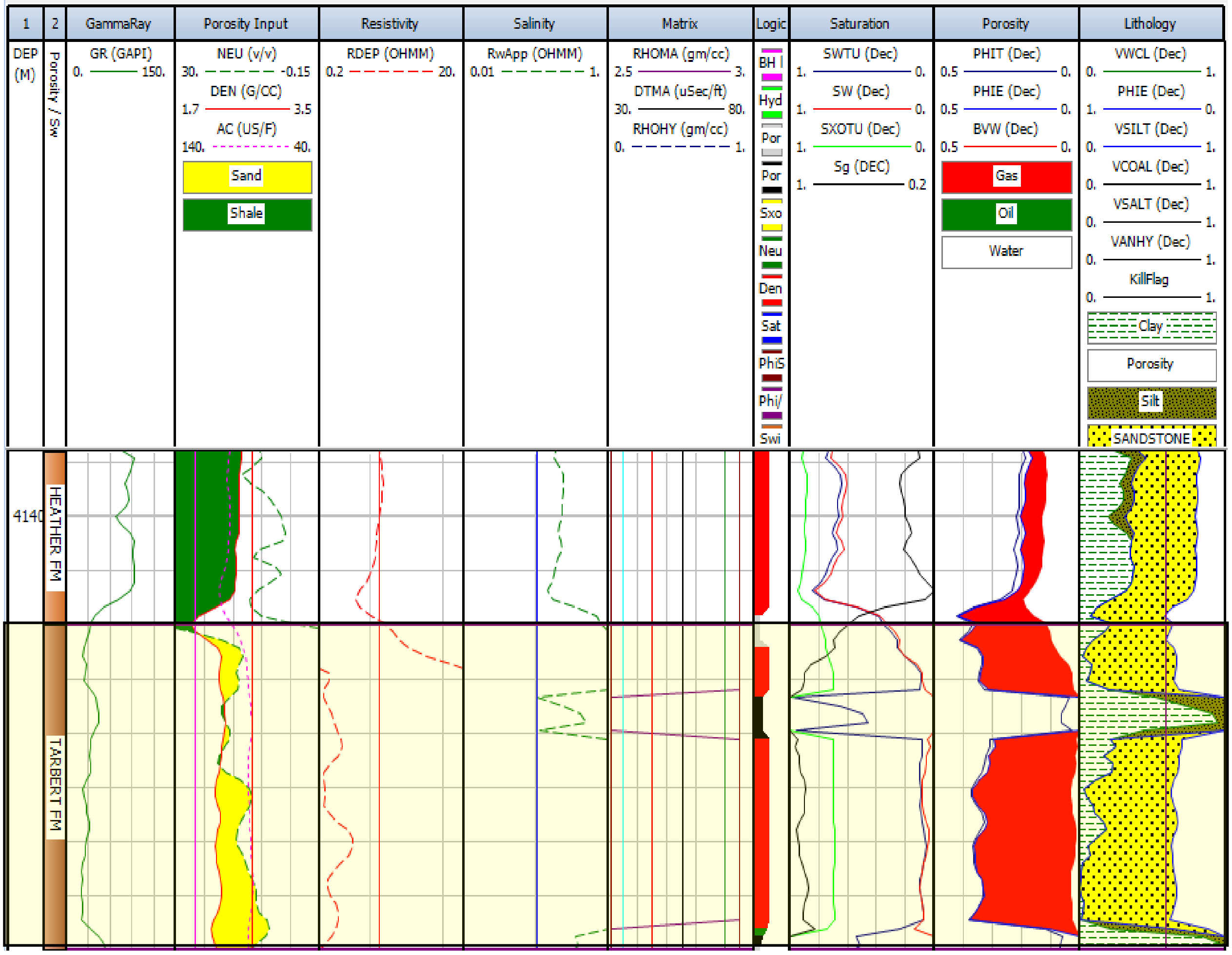

Tarbert Formation in well 34/11-5S

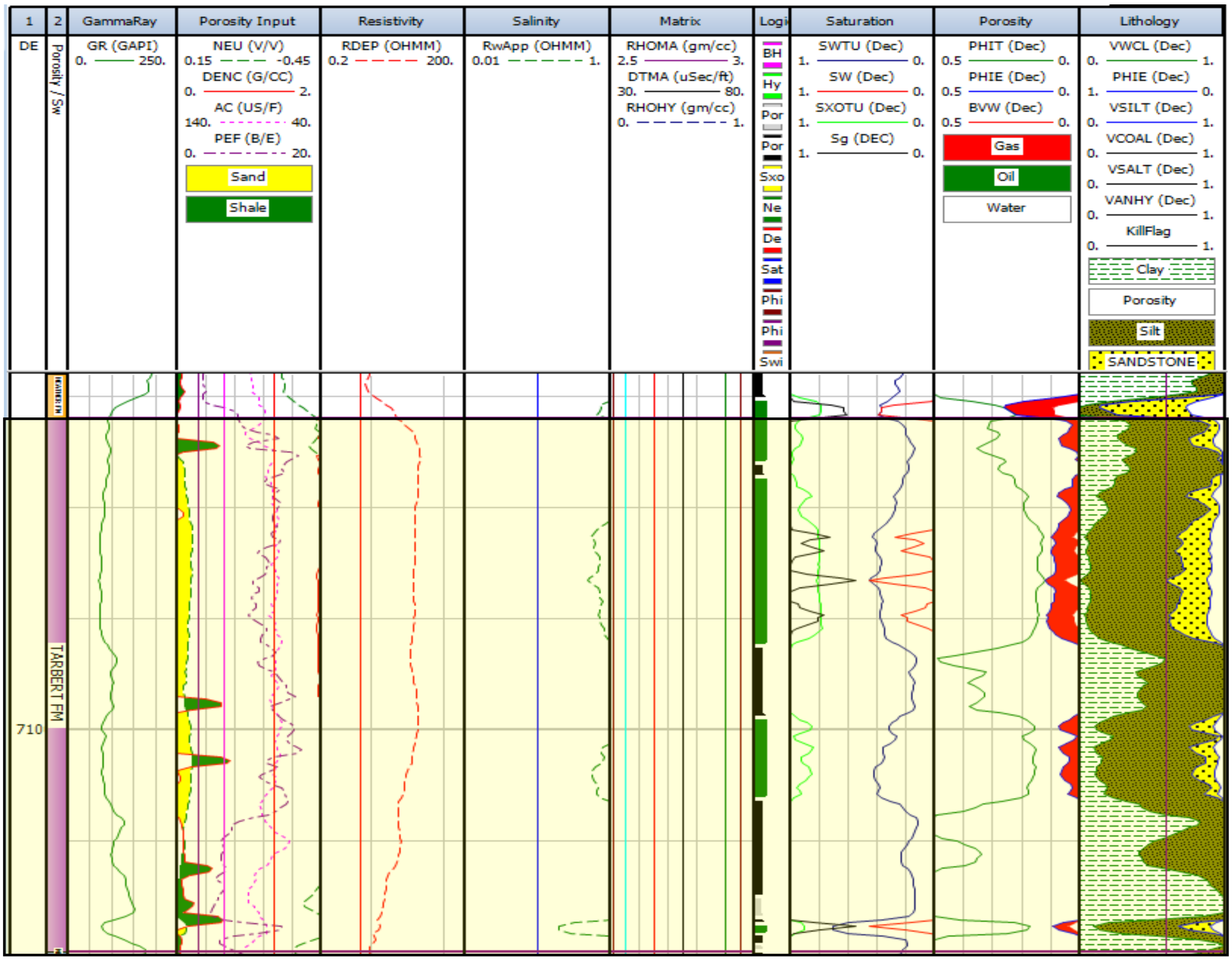

Tarbert Formation in well 34/11-6S

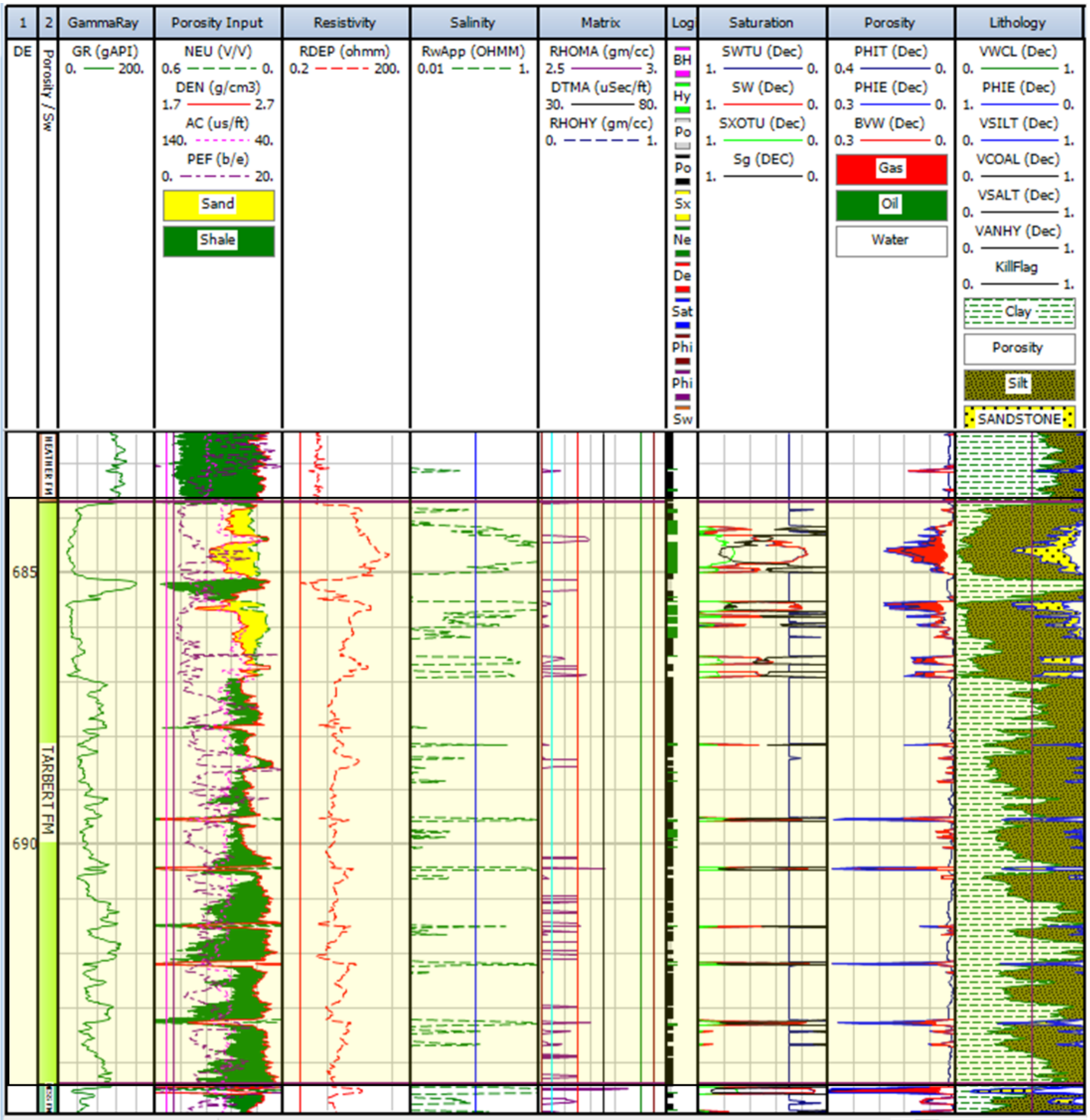

Ness Formation in well 34/11-4

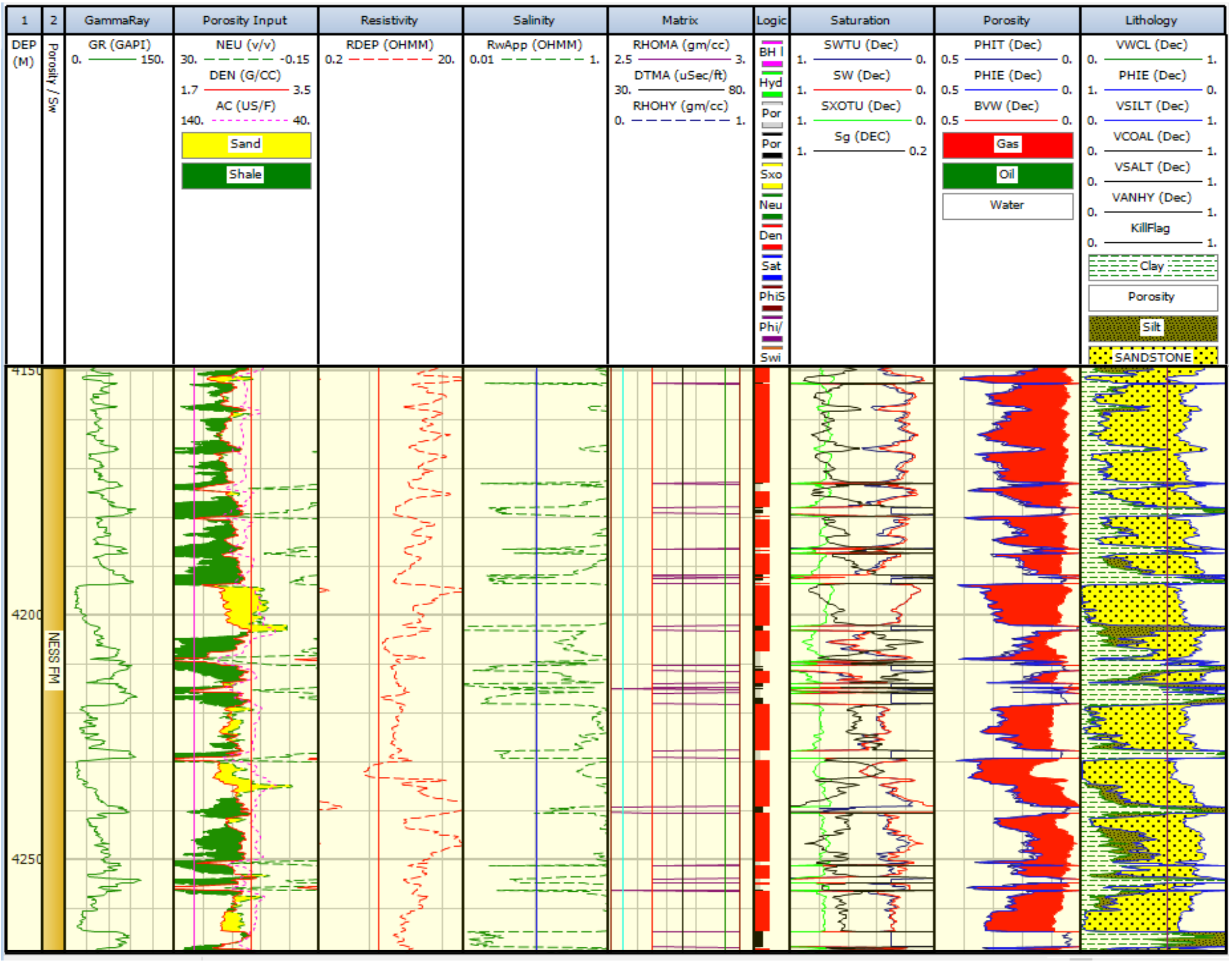

Ness Formation in well 34/11-6S

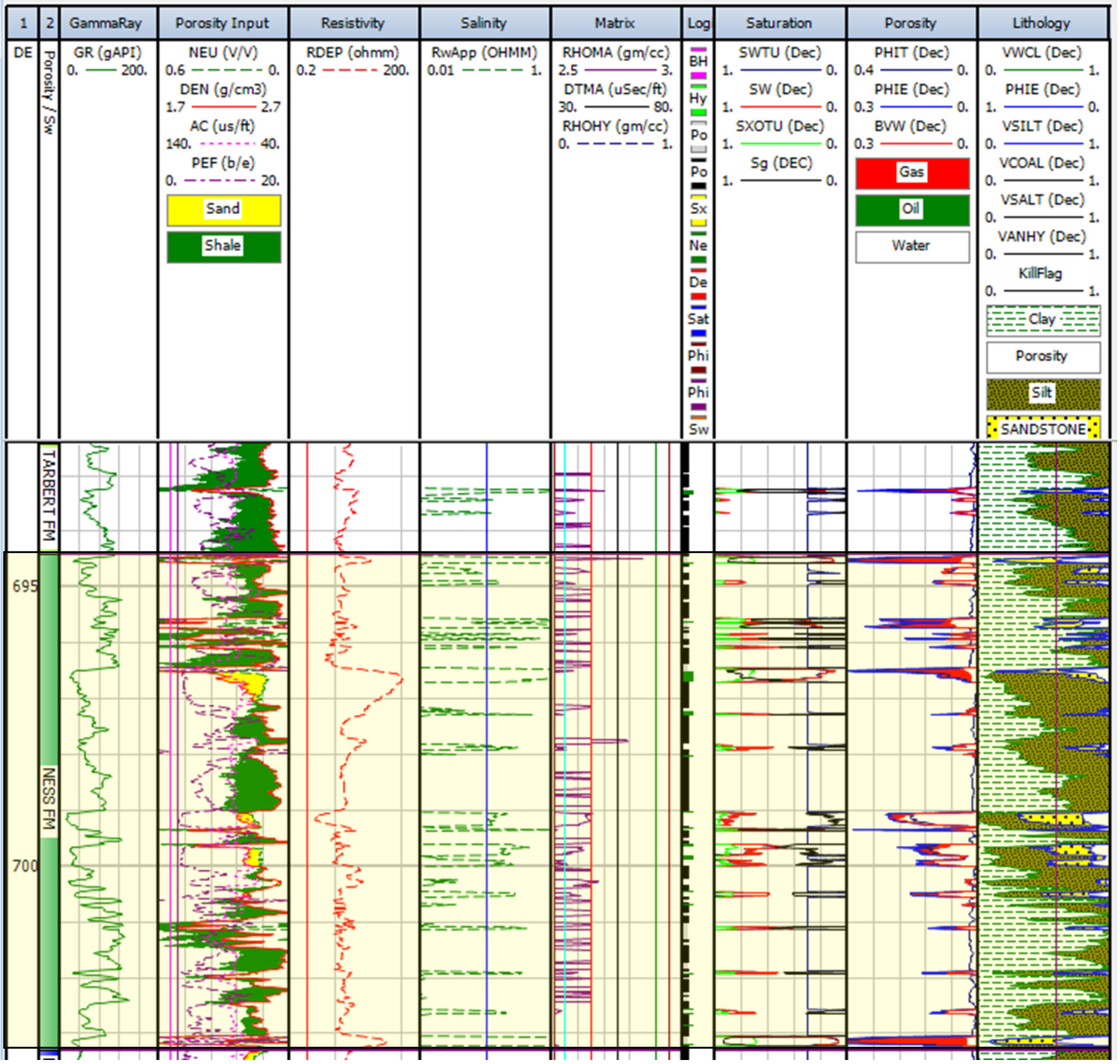
1
2
GammaRay
Porosity Input
Resistivity
Salinity
Matrix
Log
Saturation
Porosity
Lithology
DE
Porosity / Sw
GR (gAPI) 0. 200.
NEU (V/V) 0.6 0.
DEN (g/cm3) 1.7 2.7
AC (us/ft) 140. 40.
PEF (b/e) 0. 20.
Sand
Shale
RDEP (ohmm) 0.2 200.
RwApp (OHMM) 0.01 1.
RHOMA (gm/cc) 2.5 3.
DTMA (uSec/ft) 30. 80.
RHOHY (gm/cc) 0. 1.
BH
Hy
Po
Po
Sx
Ne
De
Sat
Phi
Phi
Sw
SWTU (Dec) 1. 0.
SW (Dec) 1. 0.
SXOTU (Dec) 1. 0.
Sg (DEC) 1. 0.
PHIT (Dec) 0.4 0.
PHIE (Dec) 0.3 0.
BVW (Dec) 0.3 0.
Gas
Oil
Water
VWCL (Dec) 0. 1.
PHIE (Dec) 1. 0.
VSILT (Dec) 0. 1.
VCOAL (Dec) 0. 1.
VSALT (Dec) 0. 1.
VANHY (Dec) 0. 1.
KillFlag 0. 1.
Clay
Porosity
Silt
SANDSTONE
TARBERT FM
NESS FM
695
700